Advanced Methodologies for the Synthesis and Characterization of Polymer Networks

Zur Erlangung des akademischen Grades einer

DOKTORIN DER NATURWISSENSCHAFTEN

(Dr. rer. Nat.)

von der KIT-Fakultät für Chemie und Biowissenschaften
des Karlsruher Instituts für Technologie (KIT)

genehmigte

DISSERTATION

von

M. Sc. Federica Cavalli

aus Crema, Italien

1. Referent: Prof. Dr. Manfred Wilhelm

2. Referent: Prof. Dr. Leonie Barner

Tag der mündlichen Prüfung: 25. Juli 2019

“if we knew what it was we were doing,
it would not be called research,
would it?”
Albert Einstein

Die vorliegende Arbeit wurde von Februar 2016 bis Juni 2019 unter Anleitung von Prof. Dr. Leonie Barner und Prof Dr. Manfred Wilhelm am Karlsruher Institut für Technologie angefertigt.

Erklärung

Ich erkläre hiermit, dass ich die vorliegende Arbeit im Rahmen der Betreuung durch Prof. Dr. Leonie Barner und Prof. Dr. Manfred Wilhelm selbstständig verfasst und keine anderen als die angegebenen Quellen und Hilfsmittel verwendet habe. Wörtlich oder inhaltlich übernommenen Stellen sind als solche kenntlich gemacht und die Satzung des Karlsruher Instituts für Technologie (KIT) zur *Sicherung guter wissenschaftlicher Praxis* wurde beachtet.
Des Weiteren erkläre ich, dass ich mich derzeit in keinem weitern laufenden Promotionsverfahren befinde und auch keine vorausgegangenen Promotionsversuche unternommen habe.

_____ _____

Ort, Datum Federica Cavalli

Abstract

Polymer networks are a particular class of materials composed of polymer chains which are three-dimensionally connected to each other.[1] In an ideal simplified scenario, polymer networks are represented as a net in which the space between the crosslinking points, also called elastic chain length, is equal throughout the whole structure. In reality, the presence of defects such as unreacted moieties and loops alters the length of some of the elastic chains, and therefore the pore size distribution.[2]

Recent literature shows the negative impact of structural defects on the elasticity of the network.[3-5] Aware of this fact, and considering that polymer networks are part of our everyday life in diapers,[6] contact lenses[7] and materials for waste water treatment,[8] one of the current key challenges lies in the development of novel synthetic strategies for the achievement of more homogenous networks, with maximized application potential.[4]

With this in mind, the presented study is oriented towards the investigation of advanced synthetic approaches for the formation of well-defined polymer networks. In particular, the synthesis of poly(acrylic acid) hydrogels with application as separation agent in a membrane-free process for the desalination of salt water was envisaged in the present work.[9]

For this purpose, the network formation was controlled by reversible addition-fragmentation chain transfer (RAFT) polymerization of acrylic acid as monomer in the presence of *N,N´*-methylenebisacrylamide as crosslinking agent. Importantly, the employment of the RAFT agent had a significant impact on the crosslinking process when compared to the conventional free radical polymerization (FRP). According to size-exclusion chromatography (SEC), in the RAFT-mediated process it was possible to identify first the formation of linear chains, and thereafter the incorporations of an increasing number of equivalent chains until gelation. The resulting networks were characterized by higher degrees of swelling compared to those obtained *via* FRP. However, independently from the synthetic approach, the networks exhibited heterogeneity in the mobility of the elastic chains as observed in ^{1}H NMR relaxometry experiments. This is associated with the presence of defects in the network microstructure, underpinning the need of advanced characterization techniques for the identification of the type of structural defect.

For this reason, a novel synthetic and analytical technology platform for the precise design of polymer networks is developed in the second part of the presented work. The proposed strategy enable the introduction of traceable defects within the network microstructure by locating

heteroatoms such as fluorine, detectable *via* NMR spectroscopy, precisely at the crosslinking points. The incorporation of heteroatoms was achieved by synthesizing networks *via* the end-linking strategy using the *para*-fluoro–thiol reaction (PFTR) as a ligation tool during the crosslinking process. Initially, an in-depth mechanistic study of the reaction was conducted to gain further insights into the ligation technique. Potential side reactions such as disulfide bond formation or multiple substitutions on the fluorinated aromatic ring were successfully suppressed and the reaction parameters were carefully optimized.

Finally, a series of networks was obtained *via* PFTR upon reaction of a well-defined bifunctional precursor and a three- or four-armed linker. A library of reaction conditions was identified to expand the approach to different types of polymers, e.g. polystyrenes and polymethacrylates. The mesh size distribution, and so the degree of crosslinking, was precisely tuned by using bifunctional precursors with different molecular weights. For all networks, the quantification of the number of unreacted moieties was determined *via* ^{19}F NMR spectroscopy without degradation of the network, proving the analytical power of the proposed strategy.

In conclusion, the current work reveals a first step towards a deeper understanding of the structure–performance relationship, while an outlook into potential future research is provided in the final part of the current thesis.

Zusammenfassung

Polymernetzwerke sind eine besondere Klasse von Materialien, die aus dreidimensional miteinander verknüpften Polymerketten bestehen.[1] Im vereinfachten Idealfall werden Polymernetzwerke als ein Geflecht dargestellt, bei dem der Abstand zwischen den Vernetzungspunkten, auch elastische Kettenlänge genannt, über die gesamte Struktur gleich ist. In Wirklichkeit jedoch verändert das Vorhandensein von Defekten, wie beispielsweise unreagierte funktionelle Gruppen oder Polymerschlaufen, die Länge einiger elastischer Ketten innerhalb des Netzwerkes und beeinflusst somit die Porengrößenverteilung.[2]

Aktuelle Literaturergebnisse heben den negativen Einfluss von strukturellen Defekten auf die Elastizität von Netwerken hervor.[3-5] In Anbetracht dieser Tatsache, und unter Berücksichtigung, dass Polymernetzwerke Verwendung in unserem alltäglichen Leben finden, wie zum Beispiel in Windeln,[6] Kontaktlinsen,[7] sowie als Materialien zur Abwasserbehandlung,[8] liegt eine entscheidende Herausforderung heutzutage in der Entwicklung neuartiger Synthesestrategien, um homogenere Netzwerke mit maximiertem Anwendungspotential realisieren zu können.[4]

Dementsprechend ist die vorliegende Arbeit auf die Untersuchung moderner Syntheseansätze zur Darstellung von wohldefinierten Polymernetzwerken ausgerichtet. Insbesondere ist die Synthese von Poly(acrylsäure)-Hydrogelen zur Anwendung als Trennmedium in einem membranfreien Prozess zur Entsalzung von Salzwasser in der vorliegenden Arbeit ins Auge gefasst worden.[9]

Zu diesem Zweck wurde die Polymernetzwerkbildung mittels einer reversiblen Additions-Fragmentierungs-Kettentransfer (RAFT) Polymerisation von Acrylsäure als Monomer in der Gegenwart von *N,N´*-Methylenbisacrylamid als Vernetzer kontrolliert. Hierbei hatte besonders der Einsatz des RAFT-Agenz einen signifikanten Einfluss auf den Vernetzungsprozess im Vergleich zu Netzwerken, die mittels einer herkömmlichen freien radikalischen Polymerisation (FRP) hergestellt worden sind. Anhand der Größenausschlusschromatographie (SEC) war es möglich, zunächst die Bildung von linearen Ketten und danach den Einbau einer zunehmenden Anzahl von äquivalenten Ketten bis zur Gelierung nachzuvollziehen. Die entstandenen Netzwerke wiesen im Vergleich zu FRP-synthetisierten Netzwerken einen höheren Quellungsgrad auf. Unabhängig von der Syntheseroute zeigten die Netzwerke jedoch eine Heterogenität in der Mobilität der elastischen Ketten auf, welches anhand von ^{1}H NMR-Relaxometrie-Experimenten bewiesen wurde. Dieses Verhalten ist dem Vorhandensein von Defekten in der Netzwerk-

Mikrostruktur geschuldet, was wiederum die Notwendigkeit erweiterter Charakterisierungsmethoden zur Identifizierung der Art des Strukturdefekts veranschaulicht.

Aus diesem Grund wurde im zweiten Teil der vorliegenden Arbeit eine neuartige Synthese- und Analysetechnologieplattform für die präzise Darstellung und Charakterisierung von Polymernetzwerken entwickelt und dargestellt. Die vorgeschlagene Synthesestrategie ermöglicht die Einführung von nachweisbaren Defekten innerhalb der Netzwerk-Mikrostruktur, indem Heteroatome wie Fluor, die mittels NMR-Spektroskopie nachweisbar sind, extakt an den Vernetzungspunkten eingebaut werden. Der Einbau von Heteroatomen in Polymernetzwerke wurde mit Hilfe der Endgruppen-Kopplungsstrategie unter Anwendung der *para*-Fluoro–Thiol Reaktion (PFTR) als Ligationswerkzeug während des Vernetzungsprozesses erreicht. Zunächst wurde eine detaillierte mechanistische Studie der PFT-Reaktion durchgeführt, um weitere Erkenntnisse über die Ligationstechnik zu gewinnen. Mögliche Nebenreaktionen, wie zum Beispiel Disulfidbrückenbildung oder Mehrfachsubstitutionen am fluorierten aromatischen Ring, wurden erfolgreich unterdrückt, und die Reaktionsparameter wurden sorgfältig optimiert.

Schließlich wurde eine Vielzahl an Netzwerken mittels PFTR hergestellt, indem ein wohldefinierter bifunktionaler Vorläufer mit einem drei- oder vierarmigen Linker zur Reaktion gebracht wurde. Eine Reihe von Reaktionsbedingungen wurde identifiziert, um das Verfahren auf verschiedene Arten von Polymeren, z. B. Polystyrole und Polymethacrylate, erweitern zu können. Die Größenverteilung der Maschen, und damit der Vernetzungsgrad, wurde durch den Einsatz von bifunktionellen Vorläufern mit unterschiedlichen Molekulargewichten exakt abgestimmt. Bei allen Netzwerken wurde die Anzahl der nicht reagierten Einheiten mittels ^{19}F NMR-Spektroskopie ohne Zersetzung des Netzwerks quantifiziert, was das analytische Leistungsvermögen der vorgeschlagenen Strategie hervorhebt.

Schlussfolgernd lässt sich festhalten, dass die vorliegende Dissertation einen ersten, wichtigen Schritt zu einem tieferen Verständnis der Struktur-Leistungs Beziehung aufzeigt. Die Arbeit schließt mit einem Ausblick auf zukünftige Forschungsvorhaben.

Table of Contents

Abstract ..... **I**

Zusammenfassung ..... **III**

Table of Contents ..... **V**

1 Introduction **1**

2 Theoretical Background **5**

2.1 Modern Polymerization Techniques 5

2.1.1 Free Radical Polymerization 7

2.1.2 Reversible-Deactivation Radical Polymerization 10

2.2 *para*-Fluoro–Thiol Reaction 19

2.3 Network 25

2.3.1 Network Topology 26

2.3.2 Equation of State for Network Systems 27

2.3.3 Synthetic Strategies 31

2.3.4 Current Challenges 36

2.4 Hydrogels 42

2.4.1 Polyelectrolytes 42

2.4.2 Desalination based on Polyelectrolyte Hydrogels 45

3 RAFT-mediated Network Formation **49**

3.1 Model System 51

3.2 Poly(sodium acrylate) 59

3.2.1 Effect of the RAFT Agent 59

3.2.2 Effect of the Degree of Crosslinking 67

3.3 Salt Rejection Experiments 71

3.4 Summary 74

4 In-depth Investigation on the *para*-Fluoro–Thiol Reaction **75**

4.1 Small Molecule Thiol Derivatives 77
4.1.1 Model Reaction 77
4.1.2 Kinetic Study 81
4.1.3 Presence of Ester Bonds 88
4.2 Polymeric Thiol Derivatives 92
4.2.1 Kinetic Study 92
4.2.2 Investigation on Disulfide Bond Formation 100
4.3 Self-propagated PFTR 106
4.4 Summary 113
5 Network Formation *via para*-Fluoro–Thiol Reaction 115
5.1 Networks from Small Molecules 117
5.2 Networks from Polymers 125
5.2.1 Polymeric Thiol Derivatives 126
5.2.2 Polymeric Fluorinated Derivatives 147
5.3 Summary 159
6 Conclusion and Outlook 161
7 Experimental Section 165
7.1 Materials 165
7.2 Methods 167
7.3 Synthetic Protocols for Chapter 3 177
7.4 Synthetic Protocols for Chapter 4 180
7.5 Synthetic Protocols for Chapter 5 188
Bibliography 196
8 Appendix 203
8.1 Appendix for Chapter 4 203
8.2 Appendix for Chapter 5 218
List of Abbreviations 227
List of Figures 231
List of Scheme 243

List of Tables **245**

Publications **247**

Conferences **248**

Acknowledgements **249**

1 Introduction

Polymeric networks are three-dimensional assemblies of crosslinked polymer chains with characteristic and unique material properties including permanent porosity, elastic behavior, and insolubility when placed in contact with solvents.[1] Accordingly, polymer networks are widely applied in many fields such as: rubbers,[10] medical devices,[11, 12] health care,[6] adhesives, cosmetics[13] or as separation agent for desalination in a membrane-free process.[9] The latter is of high impact as it offers an attractive strategy to recover potable water upon swelling of the hydrogel in salt water. Moreover, the insolubility of the networks allows for an easy 'recover and reuse' upon regeneration, increasing its application potential.

The macroscopic behavior of the network is strictly dependent on its microstructure and its chemical composition.[1] The composition is determined by the choice of the starting materials, e.g. monomer, while the microstructure refers to how the polymer chains are interconnected within the network, e.g. mesh size distribution. Several theoretical models have been developed for the description of the structure–performance relationship, however they often refer to an ideal polymer system that does not present any structural defects, such as polymer loops or the presence of unreacted crosslinking points.[14] However, the existence of the above-mentioned defects significantly influences the overall material properties as their presence affects the elasticity and the mesh size distribution.[2, 3, 15]

For example, poly(acrylic acid) (PAA) networks have been used in earlier works as separation agent for the desalination of salt water.[9] Starting from an aqueous solution containing 10 g L^{-1} of NaCl, the amount of salt rejected reached levels of approximately 20% when using PAA

networks with a degree of crosslinking equal to 5%.[9] The reported PAA networks were synthesized *via* conventional free radical polymerization (FRP), which is by far the easiest method to produce such materials but does not allow for a precise structural control over the microstructure of the final network. Thus, the synthesis and manufacturing of defect-free networks is nowadays highly desirable in order to understand whether a more homogeneous structure leads to a higher charge distribution, which in turn results in a better salt rejection. Driven by this urge, the networks were synthesized *via* RAFT-mediated copolymerization of a mono- and a bifunctional monomer to achieve a better control over the crosslinking process (Figure 1.1, **Chapter 3**). The influence of the RAFT agent was evaluated during the crosslinking process and afterwards on the resulting networks. The advantage of this approach consists in the simplicity of the reaction set-up, the direct synthesis of polymer network using a wide variety of functional monomers, including acrylic acid, and the possibility of a gram scale production, which is beneficial for potential application in the desalination of salt water.

In addition, due to the complexity of the network microstructure, it is also beneficial to develop new synthetic strategies that allow for the traceability of defects if present. A direct and precise quantification of the previously listed defects is important for correlating the differences observed in the behavior of a material to the presence of a specific defect.[4] This concept is extensively discussed by the group of Olsen and Johnson, which elucidated the impact of primary and secondary loops, quantified *via* network disassembly spectroscopy (NDS), in the elastic properties of a given polymer network.[3, 5, 16-18] However, while their approach involves the disassembly of the networks, in this thesis the focus was set on the development of a direct, nondestructive method for the quantification of defects, e.g. the number of unreacted functionalities within a polymer network system. Moreover, since an equimolar ratio between the functional groups is required during network formation, assessing the percentage of unreacted functionalities also gives an indication on the amount of existing dangling ends. For this purpose, the recently emerging *para*-fluoro–thiol reaction (PFTR)[19] has been selected as a highly suitable ligation technique for the crosslinking process (Figure 1.1, second and third panel).

Initially, the PFTR was investigated for the synthesis of star-shaped polymer structures to avoid the analytical limitations associated with the insolubility of polymer networks while still representing the chemistry of the crosslinking points (Figure 1.1, **Chapter 4**). The reaction was examined in terms of side reactions such as multiple substitutions at the fluorinated aromatic ring or disulfide bond formation of the thiol derivative, as their presence will lead to defects during network formation. Moreover, different reaction parameters that influence the nucleophilic substitution, such as the chemistry of the thiolate, the polarity of the solvent as well as the type and the amount of base were considered.

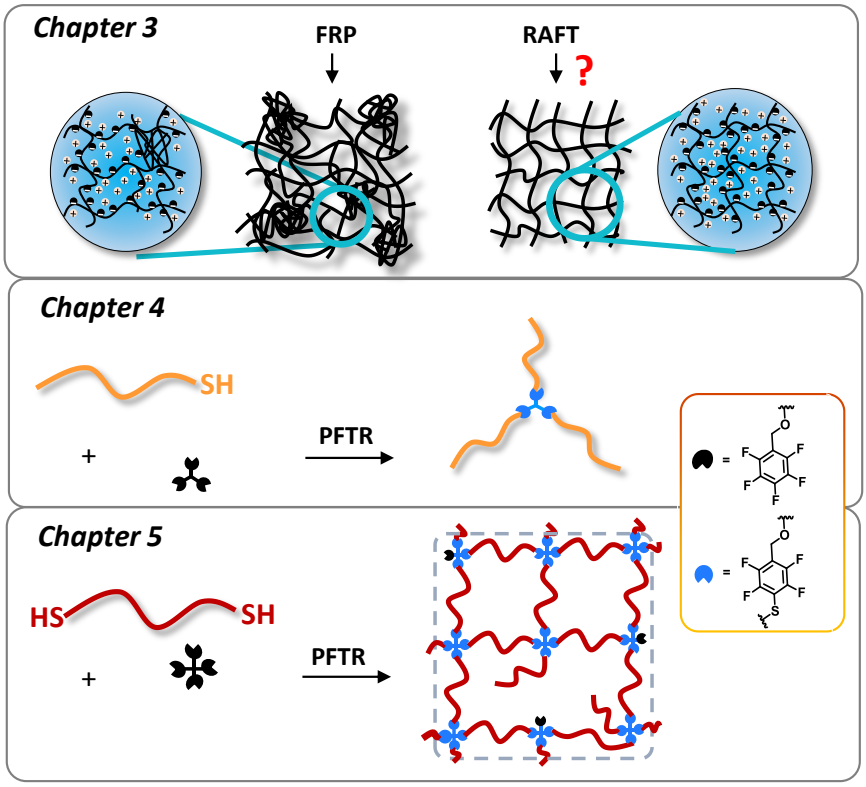

Figure 1.1 – General overview of the projects presented in the current thesis. Chapter 3: RAFT-mediated network formation as an advanced synthetic route for the control of the crosslinking process (compared to conventional polymer network formation via FRP). Chapter 4: In-depth investigation on PFTR for optimizing the reaction conditions using a (simplified) polymer model system. Chapter 5: Network formation via PFTR with precise characterization of PFTR-related traceable defects.

Finally, a variety of networks was synthesized *via* end-linking approach using PFTR as ligation during the crosslinking process (Figure 1.1, **Chapter 5**). Thus, bifunctional polymeric thiols derivatives were reacted with a three- or four-armed linker containing pentafluoro benzyl groups. Subsequently, the use of bifunctional fluorinated linker in combination with thiol based crosslinker was optimized to provide a library of reaction conditions, which choice is mainly driven by the type of polymer employed. The molecular weight of the bifunctional precursor determines the mesh size and so the degree of crosslinking within the final network. Thus, a series of networks possessing a high and a low degree of crosslinking were synthesized. For each system, the fluorinated atoms, strategically located at the crosslinking points, could be easily detected *via* ^{19}F NMR spectroscopy using standard routine measurements. In detail, the resonances of the fluorine atoms before and after ligation appear at different position in the ^{19}F NMR spectrum and thus, are facile to distinguish. The comparison of the two sets of resonances allows for a thorough quantification of the unreacted functionalities. Assessing the amount of unreacted moieties is crucial since their presence affects the pore size distribution

(see Figure 1.1, bottom panel) and thus the macroscopic properties, e.g. swelling behavior.[20] Moreover, it provides a tool for the identification of defects at the nanometer scale.

Overall, the present thesis is driven by the current need of new chemical strategies for controlling polymer network formation and the development of new ligations, which allow structural elucidation and a clearer structure–performance relationship. Two main synthetic approaches are presented in the current thesis. First, the RAFT-mediated polymer network formation was used for the fabrication of polymer networks with potential application in the desalination of salt water. Second, the end-linking strategy using PTFR as ligation was introduced as a new methodology for the precision design of polymer networks with the advantage of gaining detailed insights into the network microstructure by detecting and quantifying the amount of defects where present.

2 Theoretical Background

The current chapter provides the theoretical background necessary for understanding the concepts, methods and instrumentations used within this thesis. Firstly, an overview of some of the most relevant modern polymerization techniques is described, specifically distinguishing between conventional free radical polymerization (FRP) and reversible-deactivation radical polymerization (RDRP). Next, the thiol-based ligation reaction termed "*para*-fluoro-thiol reaction" (PFTR) is highlighted as a powerful synthetic tool for building a variety of complex architectures. Further, an insight into network formation including the origin of structural defects and a critical description of the different synthetic routes, along with their advantages and disadvantages, is discussed. Eventually, a special class of network named polyelectrolyte hydrogels and their application in a membrane-free desalination process is proposed.

2.1 Modern Polymerization Techniques

The word "polymer" derives from the Greek words "poly" (many) and "meros" (parts). According to the International Union of Pure and Applied Chemistry (IUPAC), a polymer (macromolecule) is a "molecule of high relative molecular mass, the structure of which essentially comprises the multiple repetition of units derived from molecules of low relative molecular mass", generally called monomers.[21] In other words, a polymer is composed of either one or a combination of different monomers chemically linked together during a synthetic process

called “polymerization”. The number of monomeric units present in a macromolecule is referred to as a degree of polymerization (X_n) and plays a key role in determining the thermal and mechanical properties of the final polymer.[22] Contrary to monomers, synthetic polymers do not possess a specific, easily accessible, molecular weight. Rather, the nature of polymerization leads to a statistical distribution of molecular weights depending on the length of each polymer chain in a mixture. In particular, two distributions are commonly referred to: the number average molar mass M_n and the mass average molar mass M_w. Simply, M_n is the arithmetic mean molecular weight of all polymer chains in a sample. Compared to M_n, M_w accounts for the fact that bigger chains contain more of the total mass of a polymer sample than smaller chains do, it is often defined as weight average molar mass.[22] The ratio between M_n and M_w determines the dispersity index ($Đ$), which is used as an indication of the distribution width. The higher the value of $Đ$, the more diverse the chains lengths are within the polymer sample. Accordingly, a polymer with $Đ = 1$ is a monodisperse polymer, where M_n is equal to M_w. Usually, this is feasibile only for natural macromolecules such as proteins and *DN*A, while it is not the common case for synthetic polymers.

Indeed, each polymerization technique leads to polymers with varying ranges of dispersity index, mainly due to their different synthetic pathways. Accordingly, the polymerization processes can be divided into two main categories: step-growth polymerization or chain-growth polymerization. For the former, monomers contain complementary functionality and react with each other stepwise, creating first dimer, then trimer and only at high conversion a polymer with high molecular weight.[22] In contrast, chain-growth polymerization – utilized in this work – generates an active species during an initial step (initiation) and the polymerization proceeds by repetitive insertion of a monomer unit at a time. [23] This category can be further divided into ionic and radical polymerizations. In ionic polymerization, the propagating species is either a cation or an anion, the reaction is performed at relative low temperatures and is characterized by high reaction rates.[22] Furthermore, high degrees of polymerization and stereochemical control can be achieved. Because ionic polymerizations involve the propagation of charged species, repulsion of chain-ends leads to less termination or transfer reactions, giving ionic polymerization the character of “living polymerization”, which have a number of favorable characteristics. These include a linear increase of the molecular weight with conversion, the possibility of achieving a target molecular weight by adjusting the monomer/initiator ratio and a narrow molecular weight distribution. This ultimately allows higher control over the polymer architecture, starting from end-group fidelity. Despite this, ionic polymerizations are extremely sensitive towards impurities, and can be utilized only for a restricted range of monomers, e.g.

no free carboxylic acid groups. Conversely, radical polymerization allows for a broader monomer selection, is less sensitive to impurities and boasts a much simplified reaction set-up. With the ultimate aim of synthesizing poly(acrylic acid) network for the desalination of salt water, the emphasis is placed on the radical polymerization process, given the aforementioned advantages in comparison to the ionic polymerization.

2.1.1 Free Radical Polymerization

Free radical polymerization (FRP) is by far the most used polymerization technique in industry.[24] The FRP mechanism, summarized in Scheme 2.1, consists of a sequence of three fundamental steps: initiation, propagation and termination. During the initiation step, an initiator molecule is decomposed allowing the production of free radicals. The initiator is often an organic peroxide or an azo- or diazo-type compound, which can be thermally decomposed. Photoinitiators, which degrade upon UV or visible irradiation, or redox systems are also a suitable option.[25] Generally, each initiator is categorized according to its "half-life" ($t_{1/2}$), which is the time necessary for the concentration of initiator to reach half of its original value.

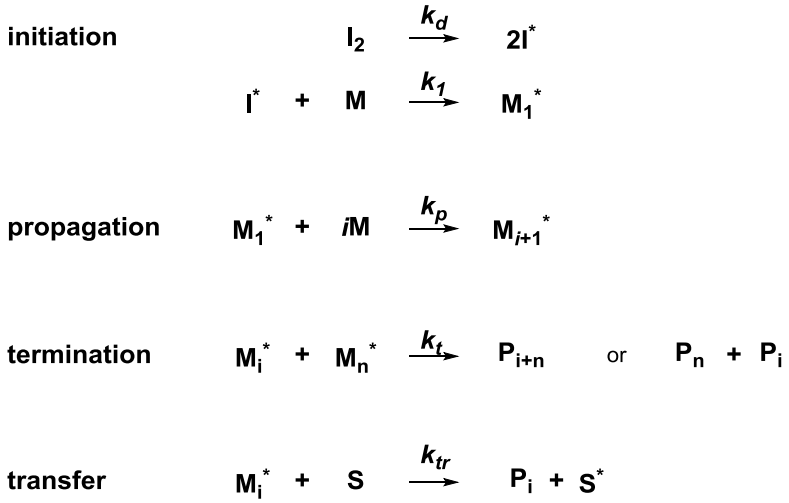

Scheme 2.1 – The free radical polymerization (FRP) process includes: i. the initiation, which generates active radicals; ii. the propagation, where the radical can grow in size after sequential addition of a monomer unit, and iii. the termination and/or transfer reactions, where the final polymer chain is produced.

Independently from the degradation pathway, the initiation rate is described as the disappearance of initiator over time or, in other words, as the production of radicals capable of initiating the polymerization over time. The rate of decomposition, R_d, is directly proportional to the initiator concentration and its efficiency. The efficiency is defined as the amount of radicals formed able to initiate the polymerization. It is determined by comparing the amount of initiator

decomposed to the amount of polymer chain produced (M^*, refer to Scheme 2.1) and can assume values between 0 and 1. Respectively, the mentioned parameters are related according to the following equations:[25]

$$-\frac{d[I]}{dt} = k_d[I] \tag{2.1}$$

$$R_d = \frac{d[I^*]}{dt} = -2f_i\frac{d[I]}{dt} = 2f_i k_d[I] \tag{2.2}$$

where k_d the rate coefficient for the decomposition of the initiator into radicals, [I] the concentration of initiator, and f_i is the efficiency of the initiator.

After initiation of the polymerization, the propagation proceeds *via* addition of a monomer unit to a reactive radical chain, ultimately growing to a macroradical. It is assumed that the propagation rate is independent from the length of the chain (monomer conversion), meaning that all the chains can grow at an equal rate.[22] Furthermore, since the consumption of monomer is significant in this step and negligible during the initiation, the rate of polymerization (R_p) is described as the amount of monomer consumed over time. Thus, the concentration of monomer (M) and the propagating polymer chains (M^*) are directly proportional to R_p as follows:

$$R_p = -\frac{d[M]}{dt} = k_p[M][M^*] \tag{2.3}$$

where k_p is the rate coefficient for the propagation step. Nevertheless, the quantification of [M^*] is difficult to achieve. To overcome this, a steady-state assumption is applied, which assume that the concentration of radicals increases until it reaches a constant value throughout the polymerization.[23] Eventually, two reactive species (radicals) react with each other leading to an unreactive chain called polymer. This event is named termination and can occur *via* combination or disproportionation. The former is a direct coupling of two macroradicals (i.e. M_i and M_j) to form a single dead macromolecule (polymer) of chain length $i+j$. While in the latter case, a hydrogen is transferred from one chain to another yielding two polymer chains, one containing a saturated chain end and the other one an unsaturated chain end. Independently from the specific termination process, the termination event is a bimolecular process and its reaction rate is expressed by the disappearance of the growing chain (M^*) over time, hence it is proportional to the concentration of macroradicals in solution as below:

$$R_t = -\frac{d[M^*]}{dt} = 2k_t[M^*]^2 \quad (2.4)$$

An additional type of termination event is called "transfer reaction", and it refers to the interaction of a growing radical with another molecule, which can be the monomer, the solvent, the initiator or a transfer agent intentionally added to decrease the degree of polymerization (X_n). During the transfer process, a macroradical interacts with any of the aforementioned molecules by abstracting a weakly bonded atom (e.g. hydrogen or halogen). The results of this interaction are a dead polymer and the formation of a newly generated radical, which can continue the polymerization. Usually, the influence of the transfer reaction is quantified by the transfer constant (C):[23]

$$C = \frac{k_{tr}}{k_p} \quad (2.5)$$

where the rate coefficient for the transfer (k_{tr}) and the propagation (k_p) reactions are compared. To conclude, the degree of polymerization is defined as the ratio between the propagation rate and the sum of the rates of all the aforementioned termination events as expressed in the following equation:

$$X_n = \frac{R_p}{R_t + R_{tr}} \quad (2.6)$$

In terms of its use, FRP is worldwide employed in industry for the production of important products such as low- density polyethylene (LDPE), poly(vinyl chloride) (PVC), fluoropolymers (e.g. polytetrafluoroethylene, PTFE), polystyrene and acrylic- or methacrylic- based polymers.[22, 24] However, despite its multi-billion dollar industry, polymers obtained *via* FRP process suffer from limitations such as a lack of control over the molar mass and the dispersity index. Even though these parameters may be irrelevant for many industrial applications, the inability to more precisely control their synthesis represents a major restriction in fundamental research and advanced material design. Indeed, the achievement of well-defined structures is a key feature for a comprehensive structure–performance relationship. To overcome this, the development of controlled radical polymerization techniques (CRP) has been a long-standing goal for polymer chemists. Eventually, starting from 1982 when Otsu *et al.* proposed and described a possible mechanism to achieve control over FRP, new synthetic routes have been exploited, opening the door for the synthesis of new materials with specific, targeted features.[26, 27] Here,

the term CRP or reversible-deactivation radical polymerization (RDRP) is used instead of "living polymerization" because termination reactions are limited but cannot be completely avoided. In satisfying the main aims of this thesis, RDRP was utilized in the synthesis of narrow-disperse polymers with precise end-group functionality for use as precursors in network synthesis, and also as an additive to mediate polymer growth in free radical network formation.[28] Such RDRP techniques will thus be the focus of the next section.

2.1.2 Reversible-Deactivation Radical Polymerization

For years scientist have been screening new reaction conditions and pathways in order to merge the easy set-up associated with the free radical polymerization and the control over the molecular weight typical of an ionic polymerization.[29] In the latter case, the low polydispersity of the generated polymer is the result of the livingness character of ionic polymerization, which implies that, in absence of impurities, the propagating chain can continue growing until all the monomer is consumed.[30] This will lead to the formation of polymer, which molecular weight M_n is defined as:

$$M_n = M_0 \frac{[M]_0}{[I]} x + M_{TA} \tag{2.7}$$

where M_{TA} is the molecular weight of the transfer agent used for introducing control, M_0 is the molecular weight of the monomer, $[M]_0$ is its initial concentration, $[I]$ the concentration of initiator, and x is the conversion, respectively. As previously mentioned, the first inspiring work in this context was the one reported by Otsu and coworkers in 1982.[26, 27] The idea is based on the use of specific "controlling agents" able to react with the propagating radical by pushing the growing chain into a "dormant state" in a reversible manner. Since the reaction is reversible, the newly formed species can dissociate one more time and restart the polymerization. Ideally, upon breakage of the newly formed bond, one monomer unit is inserted, resembling the character of living polymerization. Reactions fulfilling this propagation criteria are referred to as "reversible-deactivation radical polymerization" (RDRP), and allow for the synthesis of macromolecules with narrow molecular weight distribution, low dispersity index, linear increase of the molecular weight over time and precise architectures (e.g. α,ω-functionalized polymers).[31] The main goal is to prolong the lifetime of the macroradicals, from milliseconds to hours, and hence drastically diminish the termination events.

The controlling agent that allows RDRP can be either a stable radical, which does not initiate the polymerization, (Nitroxide-Mediated Polymerization, NMP)[32, 33] or a metal complex

(Atom Transfer Radical Polymerization, ATRP)[34-37]. In both cases, the equilibrium between dormant and active species is highly shifted towards the "dormant species". Indeed, ATRP and NMP polymerizations base their concept on the remarkable reduction of the propagating radicals upon addition of high concentration of dormant species. Alternatively, when the controlling agent is a di- or trithiocarbonate molecule, the polymerization is called Reversible Addition-Fragmentation chain Transfer (RAFT) polymerization.[38] In this case, the concentration of radicals is the same as in FRP, and the control is induced by an activation/deactivation mechanism. RAFT polymerization is more versatile, proceeds in organic as well as in aqueous media and it is less sensitive to diverse functional groups compared to NMP and ATRP. Among others, particularly relevant for the work developed in this thesis is the polymerization of acrylic acid, which is why the RAFT polymerization approach is chosen and critically discussed.[39]

Reversible Addition-Fragmentation Chain Transfer (RAFT) Polymerization

As mentioned, the RAFT process differs from other RDRP techniques because it does not involve a drastic reduction of the radical concentration, rather a reversible addition-fragmentation of the growing macroradical to a particularly designed chain transfer agent (CTA), also named "RAFT agent".[40] The concept of forming C-C bonds upon radical addition-fragmentation has been reported as reaction step for organic synthesis.[23] However, in order to translate this idea to polymeric systems, a CTA needs to be able to undergo propagation in a similar fashion to the monomer. The term RAFT polymerization was introduced in 1998 by Rizzardo, Thang and Moad, when the mechanism was proposed and its effectiveness highlighted for the polymerization of methyl methacrylate (MMA).[38]

Similar to the conventional free radical polymerization, the RAFT process starts with the initiation step, where an external initiator (e.g. azo-compound) generates the first radicals. Next, the initiator reacts with a monomer unit generating a growing radical (P_n^*). Immediately, the RAFT agent traps the newly formed radical and the "pre-equilibrium" is established, as shown in Scheme 2.2.[31] Subsequently, the CTA undergoes β-scission, resulting in the release of R^*, able to continue the polymerization. Once R^* has incorporated monomer units (re-initiation), it becomes a macroradical (P_m^*) and the main equilibrium is established.[41] Afterwards, the reaction proceeds until desired conversion. The above mentioned steps are visualized in Scheme 2.2, where it becomes clearer how the RAFT equilibrium itself does not alter the radical concentration.[42] Furthermore, the overall process can be summarized as in the bottom box reported in Scheme 2.2. Particularly, it demonstrates the possibility to achieve α,ω-telechelic polymers, as for living polymerizations, *via* RAFT approach, where the R and the Z group

represents the α and the ω group, respectively. The molecular weight of the synthesized polymer is calculated as follows:

$$M_{\mathrm{n}}^{\mathrm{theo}} = x\frac{[M]_0}{[CTA]_0}M_{\mathrm{monomer}} + M_{\mathrm{CTA}} \tag{2.8}$$

where x is the conversion, $[M]_0$ and $[CTA]_0$ the initial concentration of monomer and CTA, respectively, while M is the molecular weight of the monomer or the CTA, according to the subscript.

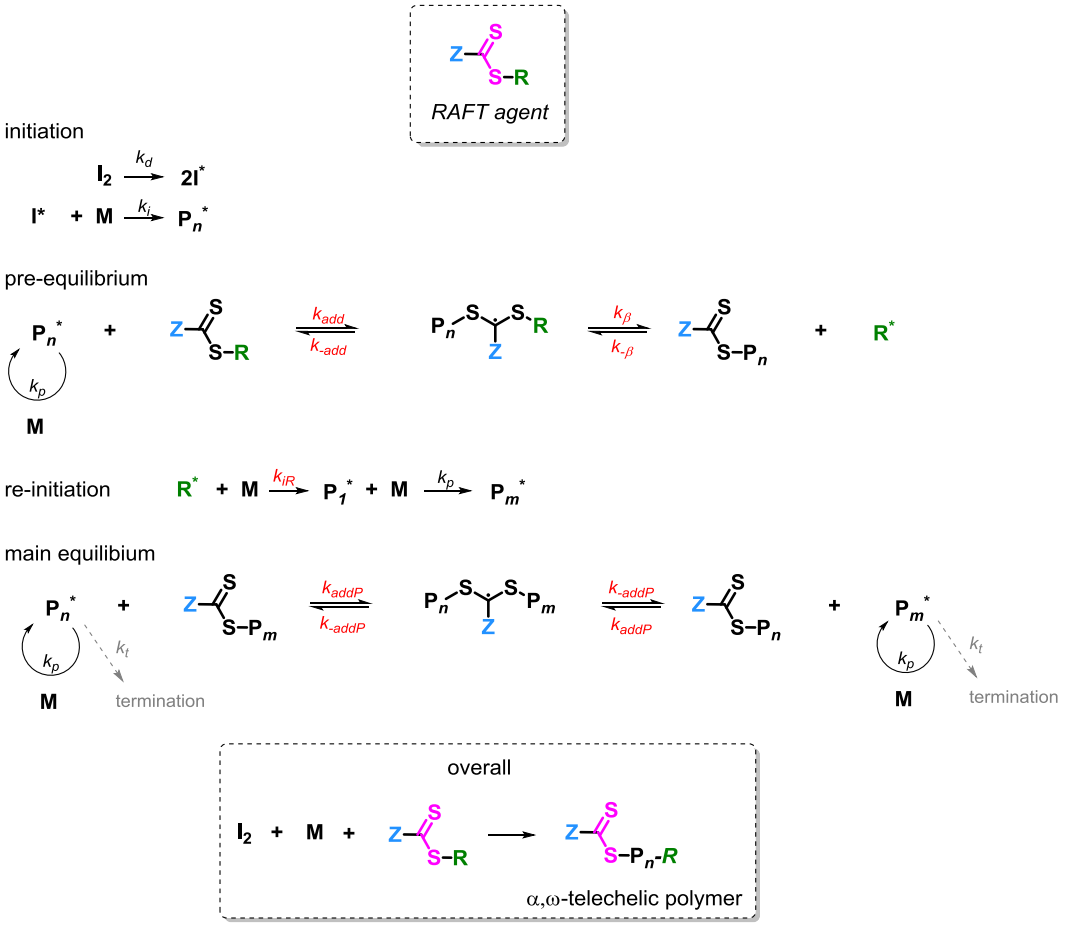

Scheme 2.2 – Detailed overview of the RAFT mechanism. The initiation includes the decomposition of the initiator and the formation of the growing radical. The pre-equilibrium is established between the previously formed radical and the RAFT agent. The re-initiation refers to the incorporation of monomer units by the leaving R group of the RAFT agent. During the main equilibrium the propagating radical chain P_n is added to the RAFT unit and the polymer radical P_m is eliminated. The termination steps are drastically limited, yet not completely avoided. In the top box the general representation of a RAFT agent is depicted, while in the bottom box the overall reaction scheme is shown.

For a better understanding of the importance of the RAFT agent selection, it is necessary to focus on the pre-equilibrium step. Indeed, here, it is fundamental that the propagating radical preferentially interacts with the RAFT agent rather than propagating independently. This is

quantified by two transfer coefficients C_{tr} (= k_{tr}/k_p) and C_{-tr} (=k_{-tr}/k_{iR}), and the partition coefficient (ϕ).[42] These parameters are defined as follows:

$$k_{tr} = k_{add}\frac{k_\beta}{k_\beta + k_{-add}} = k_{add}\phi \quad (2.9)$$

$$k_{-tr} = k_{-\beta}\frac{k_{-add}}{k_\beta + k_{-add}} = k_{-\beta}(1-\phi) \quad (2.10)$$

$$\phi = \frac{k_\beta}{k_\beta + k_{-add}} \quad (2.11)$$

where all the rate coefficients are shown in Scheme 2.2. The partition coefficient (ϕ) represents the preference of the intermediate radicals involving the RAFT agent to return to starting materials or to fragment to products.[43] Therefore, for a RAFT agent to effectively participate in the polymerization, the partition coefficient during the pre-equilibrium, ϕ, should be > 0.5.[43] Later on, once the main equilibrium is established, k_β is replaced by k_{-addP} and k_{add} by k_{addP} and ϕ will be equal to ~0.5.[43]

The choice of the RAFT agent is not universal but needs to be optimized according to the monomer and is a vital consideration for achieving narrow disperse macromolecules. Given this, the specific role of the Z and the R group is explained in the following section.

RAFT agent design

Generally, all conventional RAFT agents present two common features: a reactive double (C=S) and a weak S-R bond.[44] However, depending on the chemistry surrounding the dithiocarbonyl group, RAFT agents can be categorized as follows: dithioester (alkyl-), trithiocarbonates (S-), dithiocarbamates (NR_2-) and xanthates (OR-), as shown in Figure 2.1.

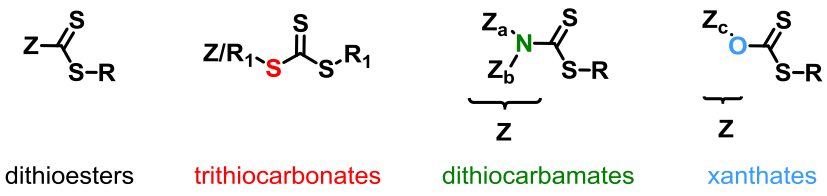

Figure 2.1 – Classification of RAFT agents in four different classes according to their chemical structures: dithioesters, trithiocarbonates, dithiocarbamates and xanthates.

Where Z is considered the "stabilizing group" and R is the "leaving group". Certainly, the choice of both is critical for an effective CRP.[44]

The role of the stabilizing group (Z) is to ensure the reactivity of the main double bond, C=S (high k_{add}). Accordingly, if the stabilizing effect is excessively high, the fragmentation is not

efficient (low k_β), and the polymerization is delayed (retardation). Whereas, in the opposite case, no addition of polymer chains to the RAFT agent occurs (low k_{add}), resulting in a loss of control over the polymerization.[42] It has been observed that the most promising RAFT agents are those where Z is either a carbon (dithioesters) or a sulfur derivative (trithiocarbonate), while xanthates and dithiocarbamates show significant lower reactivity.[38] This is because the nearby oxygen or nitrogen participates in resonance structures with the C=S double bond, lowering its reactivity. An exception are dithiocarbamates where the nitrogen is part of an aromatic ring, thus not available for interaction with the adjacent double bond.[45] In this case, the reactivity of the CTA is comparable to that of dithioesters and trithiocarbonates.

In contrast, the S-R bond must be weak and R a good leaving group. This is important in order to ensure that its scission from the RAFT agent is more probable compared to the one of the propagating radical ($\phi > 0.5$).[31] Furthermore, its ability to re-initiate the polymerization has to be comparable to that of the monomer ($k_{iR} > k_p$). Indeed, only when these two criteria are fulfilled, the size of the growing chains are similar to each other. Typically, R is chosen to mimic the monomer structure.[44]

For an easier monomer to RAFT agent selection, general guidelines have been established for both groups (R and Z) independently, and are depicted in Figure 2.2.[46]

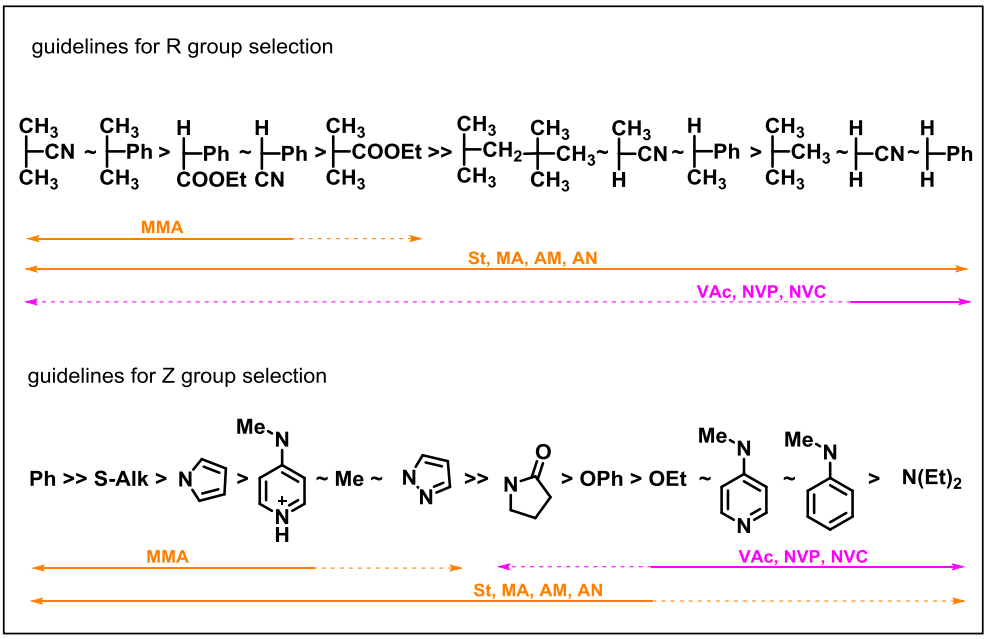

Figure 2.2 – Guidelines for an appropriate RAFT agent selection, divided into the selection for R and Z groups, seperately. Solid lines represent good control over the polymerization, while dotted lines indicate poor control. List of abbreviations: MMA (methylmethacrylate), VAc (vinyl acetate), NVP (N-vinylpyrrolidone) and NVC (N-vinyl carbazole). The figure is adapted from "S. Perrier, Macromolecules ***2017****, 50, 7433-7447".*[46]

Polymerization of acrylic acid

Several fundamental studies led to the development of accurate guidelines for many monomers, (Figure 2.2), however, they mostly do not include more complex monomers such as acrylic acid. Nevertheless, RAFT represents the only example of controlled polymerization for the direct polymerization of such monomer.[47] Acrylic acid can be polymerized, also on industrial scale, *via* conventional free radical polymerization. In contrast, the polymerization methods based on ionic or reversible-deactivation radical polymerization to achieve narrow disperse acrylic acid based polymers are still challenging. The latter is due to the low tolerance of such techniques towards the carboxylic acid functionality.[47]

In details, since acrylic acid is a protic monomer, the anionic polymerization process is suppressed by the monomer itself. Moreover, the use of methacrylates monomers is preferred over the analogous acrylate derivatives.[48] In ATRP the main problem is associated with the reaction between the carboxylic group with the metal complex.[49] Eventually, the polymerization of (meth)acrylic acid monomers *via* NMP is prevented or slowed down by the accumulation of nitroxide radicals, and their respective partial decomposition in acidic medium.[50] To overcome these issues, usually an analogous monomer (e.g. *tert*-butyl acrylate or benzylic acrylate) is polymerized and the corresponding PAA is achieved after deprotection of the ester group *via*, for instance, acidic hydrolysis.[51] The general strategy is depicted in Scheme 2.3.

Contrary to the above listed methods, RAFT allows for a controlled polymerization of acrylic acid without the need of any protecting group. This is because the trithiocarbonate group is not affected by acidic environment. RAFT agents suitable for the purpose are 1-phenylethyl dithiobenzoate, dibenzyl trithiocarbonate,[52] bis(1-phenylethyl) trithiocarbonate[52] and 4-cyano-4-(phenylthioylthio)-pentanoic acid (the latter is depicted in Figure 2.3 as CTACOOH).[53] Last but not least, the polymerization of acrylic acid is proved to be feasible upon irradiation of the reaction mixture with UV radiation at ambient temperature, highlighting the power of the RAFT polymerization approach.[39]

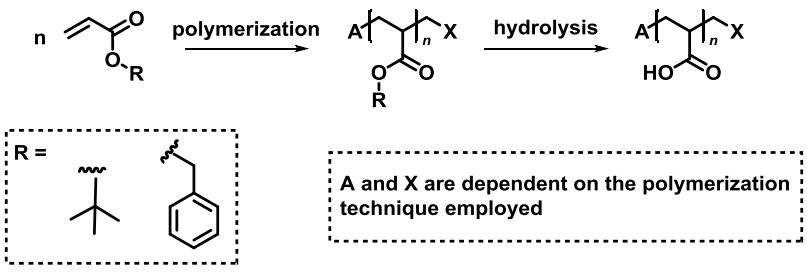

Scheme 2.3 – Reaction scheme for an alternative synthetic route towards the achievement of poly(acrylic acid) polymers. In the scheme, R corresponds to the protecting group, while A and X are the two chain ends, which nature is dependent on the polymerization approach employed.

RAFT agent functionalization and post-modification

It has been discussed that well-controlled polymers can be achieved *via* RAFT polymerization. This refers not only to the narrow molecular weight distribution ($Đ < 1.5$) but also to the possibility of obtaining α-ω telechelic polymer, where the chemistry of the end groups is strictly related to the RAFT agent employed, as shown in Scheme 2.2. Here, two strategies can be followed: i. the synthesis of a CTA already containing the desired end groups[42, 54] or ii. the post-modification approach, where the RAFT agent is modified after polymerization.[55] The former group is further divided into two subcategories, being them the synthesis of the RAFT agent from raw materials or the modification of RAFT agents containing carboxylic groups pre-polymerization. Indeed, several CTAs presenting this feature are commercially available on research scale, while the two RAFT agents used in this thesis are depicted in Figure 2.3.

*Figure 2.3 – Chemical structure of the two commercially available RAFT agents possessing a carboxylic acid group employed in **Chapter 5**.*

Among different strategies for the synthesis of a RAFT agent,[43] the reaction between carbodithioate salt and an alkylating reagent is adopted in **Chapter 5** for the synthesis of a bifunctional RAFT agent carrying pentafluorobenzyl groups at both ends (**biPFB**). This strategy is often commonly used due to its simplicity and its versatility. Indeed, it can be adopted to all the classes of RAFT agent (Figure 2.1) for introducing primary or secondary R groups[43] or for the synthesis of both symmetric[56] and asymmetric RAFT agents.[57]

Following a different approach, RAFT agents containing a carboxylic group, such as those reported in Figure 2.3, can be modified through esterification or amidation mostly *via* carbodiimide coupling reaction.[58, 59] Following this procedure, hundreds of RAFT agents have been synthesized and utilized for a wide variety of purposes, e.g. grafting of polymers onto a surface,[60] bioconiugation[61] or introducing ATRP initiator for the synthesis of block copolymers.[62] Different reviews summarizing all the CTAs produced are available in literature.[42, 43]

In **Chapter 5**, the above discussed synthetic approaches are used in order to achieve bifunctional RAFT agents for the synthesis of homotelechelic polymer to be used as precursors for network formation.

A general feature of polymers made *via* RAFT polymerization is that the polymers, as well as the RAFT agent itself, are inherently colorful (from pink to yellow) and that the labile dithiocarbonate moiety is still present in the final polymer. Since both features can rise limitations for certain applications or further reactions (e.g. those involving strong nucleophiles), several post-modification routes involving the thiocarbonyl moiety have been established. A brief overview is given in Scheme 2.4, and more detailed insights are available in dedicated reviews.[55] Herein, the aminolysis and the photo-induced hetero-Diels–Alder reactions are described in more detail, as they have been used in **Chapter 4** and **Chapter 5** for material design.

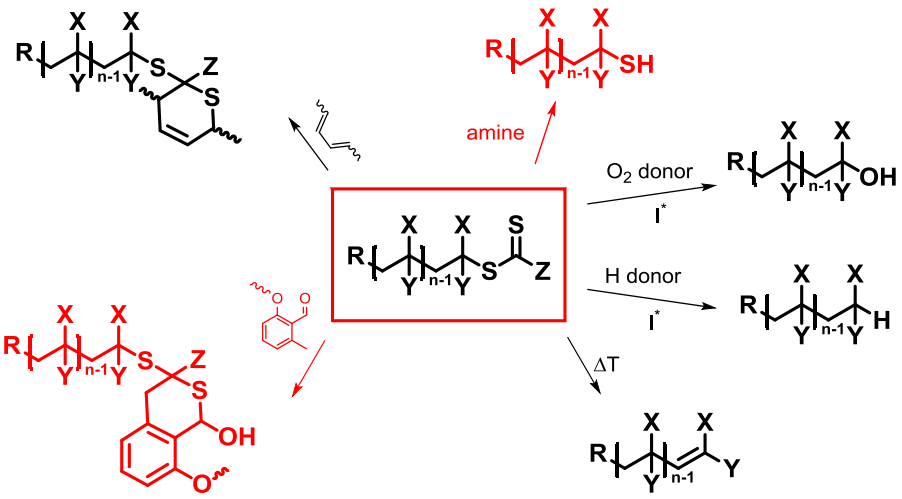

Scheme 2.4 – Schematic representation of some possible modification reactions involving a typical RAFT end-group (red box). In red are highlighted the reaction used in this thesis.

Aminolysis

The process of aminolysis utilizes the sensitivity of the dithiocarbonate group towards nucleophiles. It is a versatile and widely used approach because the polymer containing a thiol end-group can be further reacted in a series of a well-established thiol-X reactions such as the *para*-fluoro–thiol and thiol-Michael reactions.[63] The power of aminolysis lies in the easy set-up, fast reaction rates and quantitative yields. Any primary or secondary amine having nucleophilic character can be employed for the purpose. However, it is necessary to consider the inherent reactivity of thiols to form disulfide bonds during the reaction set-up. Thus, fundamental is the removal of oxygen from the reaction mixture prior addition of the amine. Several papers reported in literature suggest the direct addition of a suitable substrate for the thiol to react with, e.g. activated double bonds (thiol-ene) or gold surfaces.[55, 63] However, if the aim is the achievement of polymeric thiols as such, the intrinsic tendency to form disulfide can be limited

or completely blocked by the use of reducing agents during aminolysis, e.g. tris(2-carboxyethyl)phosphine (TCEP).[64] The cleavage of the thiocarbonyl group leads to loss of color typical of RAFT polymers, and the yielded macrothiol can be isolated by precipitation.

Hetero-Diels–Alder reaction

The hetero-Diels–Alder reactions (*h*DA) utilizes the electron-deficient dienophile in a [4+2] cycloaddition with a suitable diene.[65] The term "hetero" refers to the presence of heteroatoms in the chemical structure of the dienophile, in this case sulfur. Starting from seminal works of Barner-Kowollik *et al.*[66, 67], the applicability of such reactions has been shown to be feasible with several RAFT agents *via* both photo-induced[68, 69] and thermal activation.[70, 71] Herein, the photo-activated reaction between the dithiocarbonate (dienophile) and a custom designed photocaged diene (photoenol) is used for incorporating the desired functionality onto the polymer and the removal of the sensitive RAFT group at the same time.[69] Similar to aminolysis, *h*DA reactions proceed in high yield and short reaction times at ambient temperature. Moreover, contrary to the other Diels–Alder reaction, the herein reported photoenol cycloaddition is irreversible. Nevertheless, one disadvantage of this ligation is the time-consuming synthesis of the custom made photoenol, which is obtained after five reaction steps.

2.2 *para*-Fluoro–Thiol Reaction

The *para*-fluoro–thiol reaction (PFTR) is a highly appealing ligation chemistry that has recently found extensive application.[72] The presence of fluorine atoms within the molecule usually allows for materials with unique properties.[73] Particularly, due to the fact that the fluorine is the most electronegative atom, and therefore capable to form very strong bonds with other elements.[74] Herein, the C-F bond, which is the strongest single bond to carbon, is of significant relevance.[73] Due to the difference in electronegativity between the two atoms, C-F bond is highly polarized, with the partially positive charge being located on the carbon. This is of high importance for the understanding of ligation such as PFTR, where an aromatic fluorinated group is involved. Indeed, contrary to most of the fluorocarbon compounds, perfluoroarenes are highly reactive.[75] The replacement of six H atoms with six more electron-withdrawing F atoms, changes the reactivity of the aromatic ring completely, which becomes susceptible to nucleophilic, rather than electrophilic, substitutions.[76, 77] Some pioneering works on this topic date around the 1950´s, when compounds such as hexafluorobenzene became available on a large scale. At that time, reactions of hexafluorobenzene with hydroxides, alkoxydes and organolithium compounds led to products such as pentafluorophenol, pentafluoroanisole, pentafluorotoluene and many more derivatives that are nowadays commercially available.[78]

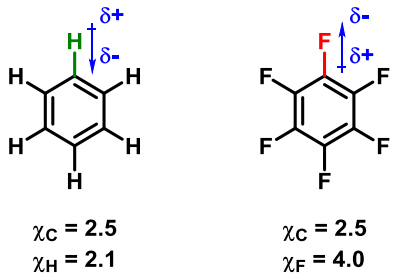

Figure 2.4 – The influence of the different electronegativity of H and F on the electron density of the aromatic ring. In example benzene (left) and hexafluorobenzene (right). The electronegative values are in agreement with the relative scale of electronegativity of Pauling.[79]

However, the pentafluoro group has gained increasing attention for material scientists in the late 2000s, when Ott *et al.* incorporated pentafluorostyrene in a polymer scaffold.[80] In their work, the fluorinated group was reacted with an amine in order to obtain graft polymers upon nucleophilic substitution. Despite the great importance of this and previous reports, the findings of Becer *et al.* just a year later are particularly relevant for the current thesis.[81] Indeed, here, a thiol was used as a nucleophile and the reaction, for the first time, proceeded quantitatively at ambient temperature within few hours. The reaction was performed in *N*,*N*-dimethylformamide

(DMF) using triethylamine as a base.[81] These mild reaction conditions are feasible due to the higher acidity and nucleophilicity of thiols compared to amine and hydroxyl derivatives of similar structure.[82] Furthermore, the employment of thiol derivatives gives the ligation more attractive application potential. In fact, thiol-chemistry is one of the most investigated type of coupling reactions, due to the high abundance of sulfur and the wide variety of commercially available thiol derivatives.[83-85] Moreover, as mentioned in the previous section, polymeric thiols are easily accessible *via* RAFT polymerization followed by aminolysis of the thiocarbonate group (Scheme 2.4).[55, 63] Finally, since cysteine is a thiol-containing amino acid, peptides can be used as ligation counterpart, expanding the use of PFTR to biological systems.[86, 87] Thus, as stated in the name, the term PFTR refers to a reaction between a pentafluoro phenyl (PFP) moiety and a thiol derivative, as depicted in Scheme 2.5.

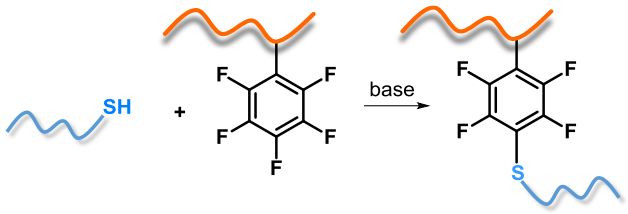

Scheme 2.5 – General scheme for the para-fluoro thiol reaction (PFTR). The moieties involved are a thiol and a fluorinated aromatic ring. A base is used for the deprotonation of the thiol to generate the thiolate and promote the aromatic nucleophilic attack.

As summarized in recent review articles,[19, 72] it has been shown that in principle any thiol can undergo PFTR, and that the reaction can be conducted in both organic and aqueous media.[86] Depending on the type and amount of base and solvent used, the ligation is completed within minutes or hours, as shown in more detail in **Chapter 4**, where an in-depth kinetic study is proposed. The term "*para*" in the PFTR acronym refers to the position where the nucleophilic attack takes place. On this topic, Kvíčala *et al.* extensively discussed the reaction pathway and the selectivity of nucleophilic substitutions on perfluorinated aromatic rings.[88] In simple words, one can consider a general structure of the PFP moiety as the one reported in Scheme 2.6, where Y can be any desired substituent.

Similar to the equivalent benzene derivatives, when a substituent is present on the aromatic ring, the regioselectivity of the following substitution is influenced or regulated by the nature of the substituent itself. This observation was introduced for the first time in 1937 by Louis Hammet.[89] The quantification of the substituent effect for a nucleophilic substitution was obtained by comparing the rate constant of a selected reaction in the case where Y (Scheme 2.6) is the desired substituent (k) with the case where Y is a hydrogen atom (k_0), according to the formula:

$$\log\frac{k}{k_0} = \sigma\rho \tag{2.12}$$

where σ and ρ are two constants. In detail, σ depends on the type of substituent (substituent constant) and ρ on the reaction itself (reaction constant). In principle, the term σ can be determined for any position of the ring, but for the PFTR only the value of the substituent constant for the atom in *para*- position is relevant (σ_p). This is because the nucleophilic substitution takes place in *para*- position respect to the position of the substituent Y. Accordingly, Kvíčala *et al.* reported that for σ_p larger than -0.20, the nucleophilic substitution in *para*- position is favored because of a better delocalization of the charges, as depicted in the mesomeric structures in Scheme 2.6, pathway A.[88] This is in agreement with Burton *et al.*, who observed this behavior for not electron-withdrawing or not powerful electron-donating groups.[90] Due to the electro-donating effect of the newly introduced nucleophile, no further substitutions are observed after the one in *para*- position. Similarly, the fluorine in *para*- is the more electron-poor and less sterically shielded than the position in *ortho*- to the non-fluorinated substituent (Y), which is why this is the main position involved.[91]

In contrast to the previous case, if σ_p is smaller than -0.20, the nucleophilic substitution will proceed according to pathway B (Scheme 2.6, bottom). This is valid for powerful electron-donor substituents (e.g. oxygen). In general, the values for σ_p are available in literature.[92]

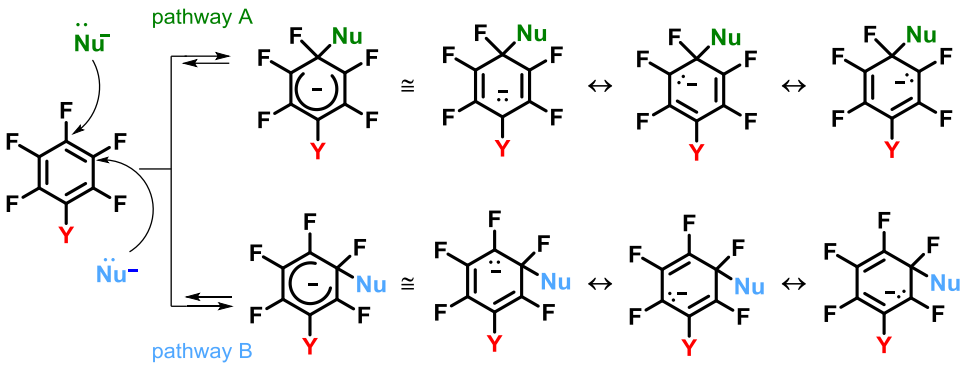

*Scheme 2.6 – Schematic representation of the resonance structures for the nucleophilic substitution in mono-substituted perfluoraromatic compounds. According to the nature of the substituent Y either pathway A or B is followed. Mostly, pathway A occurs with the exception of strong electron donor group.[90] The figure is adapted from "J. Kvíčala, M. Beneš, O. Paleta, V. Král, J. Fluorine Chem., **2010**, 131, 1327–1337".[88]*

In agreement with what above reported, the different selectivity of two different PFP moieties during nucleophilic attack has been recently reported in literature.[69] In one case, PFP is directly attached to an oxygen belonging to an ester group (activated ester), i.e. strong electron-donor. In the second case, the substituent Y on the PFP moiety is an aliphatic chain (polymer

backbone). The results depict *para*-substitution in the latter case and multiple substitutions involving both *para*- and *meta*- position in the first case as depicted in Scheme 2.7. The reactivity of pentafluoro-activated esters is also of high relevance,[93] yet not a topic of this thesis.

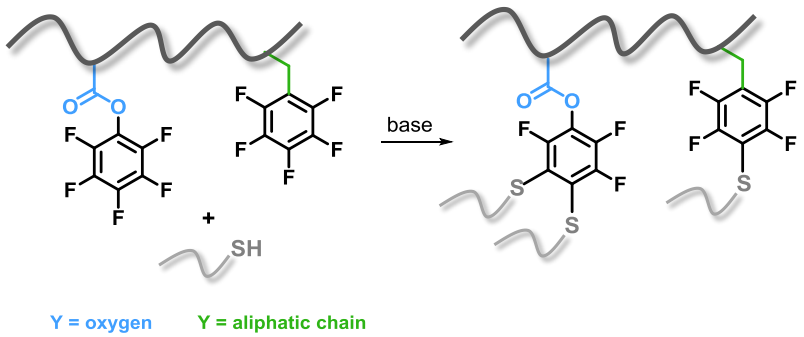

Scheme 2.7 – PFTR reaction performed in the presence of two different substituents (Y), an oxygen and an aliphatic chain. The different reactivity is highlighted in the final product.

Aside studies related to the selectivity of the nucleophilic attack, other fundamental studies available in literature address the possibility of a "click"-like behavior for PFTR. In this context, the orthogonality between PFTR and copper-catalyzed azide-alkyne cycloaddition (CuAAC) or thiol-ene reactions have been explored.[94-97] In the first case, if the PFP moiety and the triple bond are present on the same molecule, CuAAC needs to be performed first as the thiol is reactive towards the triple bond as well.[96] This is not an issue if the azide group is present on the polymer rather than the triple bond.[97] For what concern the competition between PFTR and thiol-ene reactions instead, no interference has been detected between PFP moieties and not-activated double bonds (e.g. allylic groups), independently from the reaction order. Ultimately, orthogonality was demonstrated in case of thiol derivatives containing hydroxyl[69, 98] or carboxylic groups (**Chapter 4**). However, the criteria to define a ligation as "click reaction" are rather strict,[99] and it has been discussed that the term "click" reaction has been misapplied in the recent literature over the more realistic "high efficient reaction". Furthermore, the reactivity of different small molecule thiol derivatives towards PFTR has been explored by Noy *et al.*. In agreement with their relative pK_a values, the reactivity follows the order of aromatic, glycosidic > primary > secondary > tertiary thiol.[98] An extended version of this study covering polymeric thiols and the impact of potential side reactions such as disulfide bond formation is discussed in **Chapter 4**.

Finally, more relevant is the application of PFTR for material design. Interestingly, PFP moieties show stability under several polymerization conditions, such as anionic polymerization,[100] FRP[96] and the previously mentioned types of RDRP[69, 80]. This allows the easy incorporation of PFP moiety in the polymer chain as end-group or pendant functionality, which resulted in

the synthesis of jelly-fish like[101] and glycopolymers[81, 102] along with the extensive use of PFTR as post-modification technique.[69, 94, 95, 98, 103] In similar way, the functionalization of both flat and microsphere surfaces has been reported.[104-109] The last examples take particularly advantage of the fluorine atoms present in the PFP group. Accordingly, the unique analytical power of fluorine permits broader characterization methods such as X-Ray Photoelectron Spectroscopy (XPS), Time-of-Flight Secondary Ion Mass Spectroscopy (ToF-SIMS), and mostly the possibility to follow the reaction *via* routine analysis such as ^{19}F Nuclear Magnetic Resonance spectroscopy (^{19}F NMR). The latter is discussed in the following section.

^{19}F NMR Spectroscopy

As shortly mentioned before, the fluorine atom is the most electronegative compound and as such bears advantages and disadvantages. Among the advantages, is the added value of organofluorine compounds, such as thermal stability and improved chemical stability as demonstrated in different products in the medical,[110, 111] agricultural[112] and material sector.[113] Next, ^{19}F has a spin nucleus of ½, a high gyromagnetic ratio (γ = 40.1 MHz·T^{-1})[114] and a natural abundance of 100%, which makes ^{19}F an extremely suitable atom for NMR investigations since the precession of the nuclei in an external static magnetic field (B_0) is described by the Larmor frequency (ω_L) as follows:

$$\omega_L = \gamma B_0 \tag{2.13}$$

The intensity of the resonances in fluorine NMR spectroscopy can be accurately related to the number of fluorine atoms responsible for it, allowing the integration of the resonances similar to ^{1}H NMR and in contrast to ^{13}C NMR.[115] Moreover, since nine electrons surround the nucleus, compared to a single one in the case of hydrogen, the range of the chemical shifts of ^{19}F extends over a range of approximately 500 ppm compared to the 13 ppm of the proton.[115] It follows that the chemical shifts in ^{19}F NMR spectroscopy are more sensitive to changes in the local environment, providing an extremely valuable tool for structure recognition.[115] In particular, the sensitivity increases in the order –CF_3 < -CF_2 < -CF.[115] Indeed, the single carbon to fluorine bond, which includes aliphatic, vinylic and aryl derivatives, expands in the range from −70 to −238 ppm.[115] In contrast, -CF_2 and -CF_3 derivatives have a range of about 50 and 30 ppm, respectively.[115] Additionally, the resonances of fluorine atoms do not overlap with those of carbon or proton, avoiding tedious purification procedure or solvent removal prior to analysis. In a similar way, the absence of ^{19}F atoms in naturally occurring biomolecules or in most of the commercially available products, allows for a targeted insertion of such atoms in

custom made position, e.g. the crosslinker molecule for network formation (refer to **Chapter 4** and **Chapter 5**), the ligand or the protein in chemical biology[110]. Due to the listed reasons, attention on the ^{19}F NMR is constantly increasing in the area of chemical biology. One interesting example, is the possibility of investigating intermediate structures during the protein folding thanks to the extremely short resolution times (seconds).[110] On the other hand, two disadvantages can be faced when using ^{19}F NMR: First, the lack of intrinsic reference peaks arising from the residual solvent signal such as $CHCl_3$ for spectra recorded in $CDCl_3$ in a routine ^{1}H NMR. This leads to the fact that not all the spectra are recorded using $CFCl_3$ as internal reference, which can cause confusion and misinterpretation of the data when comparing different ^{19}F NMR spectra with each other. Second, even though it is possible to record ^{19}F NMR spectra by using the same probes for proton spectroscopy, the probe is made of fluorocarbons polymer. This results in a distortion of the baseline, which needs to be taken in account when this affects the area of interest in the spectrum.[115] However, the distortion of the baseline can be overcome by increasing the concentration of the sample in the NMR tube and *via* multipoint baseline corrections post-analysis.

In **Chapter 4** and **Chapter 5**, ^{19}F NMR spectroscopy is used for monitoring of the *para*-fluoro-thiol reaction. The high sensitivity of fluorine NMR spectroscopy to the local environment allows for a clear distinction between *ortho*-, *para*- and *meta*- resonances before the reaction from each other and from the *ortho*- and *meta*- resonances after PFTR. Additionally, the possibility of integrating the resonances allows for the quantification of the residual starting material compared to the desired PFTR product. In detail, ^{19}F NMR spectroscopy is used in **Chapter 4** for an in-depth analysis of the selected *para*-fluoro-thiol–reaction, while in **Chapter 5** the performances of the same reaction are evaluated after its employment, for the first time, during network formation. The chemical modification of the fluorinated aromatic ring before and after reaction is strategically used to gain information on the crosslinking efficiency. In the case of polymer network a gel-phase ^{19}F NMR spectroscopy was used. With the term gel-phase one refers to the situation where the sample is constituted of few mg of resin (gel) swollen in the desired deuterated solvent. The term gel-phase is used to differentiate the analytical method from the solid-state ^{19}F NMR, and allow the use of routine NMR spectrometers, avoiding the change of the probe prior to analysis. Positively, few reports have proven the comparability of the spectra obtained by gel-phase and solid-state NMR, both qualitatively and quantitatively.[116-118] The signal-to-noise ratio is optimized by increasing the amount of resin in the probe, insuring a minimum concentration of fluorine atoms of 0.01 $mol \cdot L^{-1}$ in the NMR tube, and the relaxation time up to few seconds, typically 3s.

2.3 Network

The term "network" refers to a three-dimensional assembly of polymeric chains linked together by physical or chemical crosslinking points, as displayed in Figure 2.5 (right).[119] The properties of the obtained material differ significantly compared to their linear or branched counterparts having the same chemical composition (Figure 2.5).[120] For instance, polymer networks have a large deformation elasticity (rubber-like behavior) and in contact with a solvent swell instead of dissolving.[1] The elasticity and the ability to swell, induced by the crosslinking process, is particularly relevant on the industrial scale for disparate applications. Furthermore, their insolubility allows for an easy recovery and eventual re-use of the material itself after regeneration.[121] Accordingly, polymer networks have found applications as contact lenses,[7] drug delivery systems,[12, 122] scaffolds for tissue engineering,[11] rubber tires,[123] agricultural products,[124] adhesives,[125] superabsorbents[6] and many more.

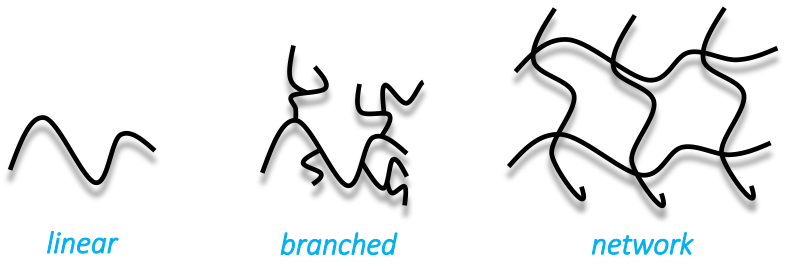

Figure 2.5 – Examples of different polymer architectures: a linear chain (left), a branched polymer (middle) and a polymer network (right).

The applicability of networks at industrial level demands a full understanding of the structure/performance relationship. In details, two parameters play a major role: chemical composition and topological structure.[126] The former mainly refers to the monomer selection, and reflects, for instance, on the swelling behavior, which depends on the polymer/solvent interaction and the degree of crosslinking.[127] Concerning the topology, the schematic representation of a network shown in Figure 2.5 depicts an ideal scenario, where the distance between each crosslinking points is equal throughout the matrix. In reality, this is usually not the case and a series of so-called ´structural defects´ can be present, which change the microstructure of the network and as a consequence its macroscopic properties. Different theories, presented in Section 2.3.2, have been proposed to describe the impact of these structural changes.[1] However, this is not a straightforward process due to the challenges associated with the characterization of insoluble polymer networks and the complexity of such systems.[4] Nonetheless, it is well known that the

preparation conditions such as synthetic strategy, temperature, monomer concentration and chemical nature of the crosslinker play a major role in determining the microstructure of the formed network, as discussed in Section 2.3.3.[120]

2.3.1 Network Topology

The microstructure of any network is composed of a series of structural elements. To begin with, a polymer network is described as an assembly of polymer chains connected by cross-linking points, or junctions, which divide the primary chain into meshes. In an ideal network, as the one depicted in Figure 2.6 (left), all the meshes possess the same length, and the same functionality at the connecting points, *f*, which is the number of elastic chains per junction.[1] Therefore, the resulting three-dimensional structure is characterized by a monodisperse pore size distribution. However, ideal networks cannot be synthetically achieved.[120] The direct consequence is an irregular distribution of the meshes due to a random distribution of the junction points along the polymer chains. Hence, a real network will present domains, or regions, having different crosslinking densities. Additionally, other structural defects may occur such as: i. dangling ends, where the polymer chain is connected to the network structure only by one end, ii. cyclic loops, where both ends of the polymer chain are connected to the same junction or iii. permanent intermolecular entanglements of elastic chains between different crosslinking points.[120] All the listed structural defects are depicted in Figure 2.6 (right).

Pioneering studies on polymer networks led to the development of equations for describing the relationship between the different elements present within the network microstructure. However, these equations are only valid for ideal networks, and do not take in account any defect.

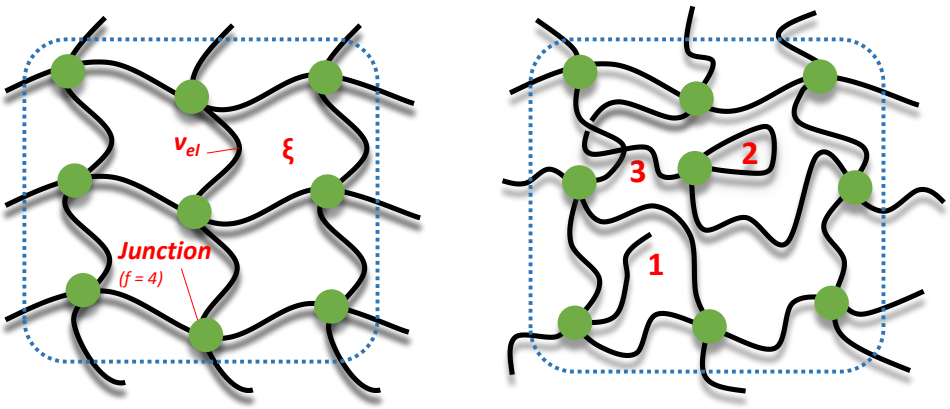

Figure 2.6 – Left: the definition of elastic chain (ν_{el}), cycle rank (ξ) and junction having functionality f are depicted for an ideal network. Right: defects such as dangling chains (1), cyclic loops (2) and intermolecular entanglements (3) are highlighted for a real network.

For instance, the amount of crosslinking is calculated as concentration of elastic chains per volume of dry network (v_{el}/V_0) or as number of crosslinks per volume of dry network (μ_{el}/V_0). The cycle rank (ξ), which is the number of independent circuits in a network[128] can be derived as

$$\xi = v_{el} - \mu_{el} \tag{2.14}$$

Moreover, μ_{el} and v_{el} are related with each other through the functionality of the crosslinking point as shown by[129]

$$\mu_{el} = \frac{2}{f} v_{el} \tag{2.15}$$

Eventually, the (average) molecular weight of the elastic chains between the crosslinking points, M_c, is defined as

$$M_c = \rho \frac{V_0 N_A}{v_{el}} \tag{2.16}$$

where ρ is the gel density, N_A the Avogadro number and V_0 the volume of the network.
The combination of the previous equations, allows the relationship between the crosslink functionalities, the cycle rank and the elastic chain length as reported in equation 2.17.[128]

$$\xi = v_{el}\left(1 - \frac{2}{f}\right) = \frac{\rho V_0 N_A}{M_c}\left(1 - \frac{2}{f}\right) \tag{2.17}$$

Once defined the relationship between the structural elements, it is important to understand how a given microstructure affects the macroscopic properties of the material or, vice versa, how an external stimulus modifies the microstructure of the network. For this purpose, the equation of state for the network before and after a structural change needs to be written.[1]

2.3.2 Equation of State for Network Systems

To start with an example of structural changes caused by an external stimulus, one can consider that the direct consequence of a gel in contact with a solution is the expansion of its microstructure (mixing term). However, due to physical constraints (crosslinking points), the network cannot expand to infinite (elastic term). Thus, these two opposite forces will balance until an equilibrium is achieved.[130] These changes can be expressed in terms of variation of the Gibbs

free energy (ΔG) between the gel and the surrounding solution. In a first approximation, known as the Frenkel-Flory-Rehner hypothesis, the variation of the total free energy, or more practically of the chemical potential (μ), can be considered as the sum of the variation of these two terms, and at the equilibrium [131, 132]

$$\Delta\mu_1 = \Delta\mu_{1,\mathrm{mix}} + \Delta\mu_{1,\mathrm{el}} = 0 \tag{2.18}$$

where the subscript 1 refers to the variation in the chemical potential of the solvent in the gel phase, and the chemical potential is the partial derivative of the free energy with respect to the moles of solvent, n_1, at a given temperature T and pressure p.

$$\Delta\mu_1 = \left(\frac{\partial \Delta G}{\partial n_1}\right)_{T,p} \tag{2.19}$$

The mixing term

The mixing term, $\Delta\mu_{\mathrm{mix}}$, refers to the interaction solvent/polymer and it is described by the Flory-Huggins theory.[133] This theory is commonly used for describing non-crosslinked polymer in solution, however it can also be applied to networks.[134] The free energy of mixing can be expressed by the sum of the enthalphic (H) and entropic (S) components. The formula follows the liquid-lattice model, meaning that the polymer segments and the solvent molecules are considered randomly distributed on a lattice. The variation of entropy is a consequence of the increased number of possible conformations that a polymer chain can assume in a diluted system.[133] The variation in enthalpy is mainly represented by the quality of the solvent by the Flory-Huggins parameter χ. In general, χ is larger than 0.5 for a bad solvent, and it is smaller for a good solvent. After statistical treatment, the chemical potential of mixing results in [133]

$$\Delta\mu_{\mathrm{mix}} = RT(ln(1 - v_2) + v_2 + \chi v_2^2) \tag{2.20}$$

where v_2 is the volume fraction of polymer, R is the gas constant, and T is the temperature.
Even though the assumption that the free energy in a swollen network is identical to the one of a polymer in solution is made, the Flory-Huggins theory describes quite successfully the mixing energy in non-polar environments, but fails in case of polar systems, where interactions such as hydrogen bonds are present.[1]

The elastic term

The elastic term relates to how the stress, responsible for the macroscopic deformation, is reflected on a macromolecular level in the typical microstructure of a network, where chains are connected to each other. This term is derived from the theory of rubber elasticity.[131, 133] First, it is important to define how all the polymeric chains are connected within the network by introducing a new parameter, $\vec{r}$, which is the end-to-end distance of an elastic chain. For a polymer network, the end-to-end vector $\vec{r}$ for elastic chains follows a Gaussian type function. Second, it is assumed that the elastic free energy of the polymer network is equal to the sum of the elastic free energy of each elastic chain.[133]

Several theories have been developed to interpret the phenomenon, with the affine and the phantom theory being the most used ones.[135] In the affine model, developed by Flory, the deformations are the same at each length scale as the network can only transform "affinely". In this model, the positions of the junctions are fixed and fluctuations are not allowed due to intermolecular entanglements.[131, 133] In contrast, in the phantom network, developed by James and Guth, the elastic chains are free to move and the crosslinking points fluctuate around their mean position. It is the mean position of the junction points that deforms affinely with the strain. However, the magnitude of the fluctuation of each junction around its mean position is strain invariant.[136, 137] Both theories describe the chemical potential for the elastic term as

$$\Delta\mu_{\mathrm{el}} = A\frac{v_{\mathrm{el}}}{V_0 N_{\mathrm{A}}} V_1 RT v_2^{1/3} q_{\mathrm{c}}^{-2/3} \tag{2.21}$$

where q_c is the degree of swelling during the crosslinking process and A is a constant, which value depends on the adopted theory. In details, A is equal to 1 for the affine model and to $(1 - 2/f)$ for the phantom model, where f is the functionality of the crosslinker. By comparing the two theories, one could observe that for a network having a crosslinker with $f = 3$, the variation in the elastic energy predicted by the affine theory is three times higher compared to the phantom theory. The difference gets smaller with increasing the crosslinker functionality and tends to 0 for $f \to \infty$. Despite these two models are the most widely used, none of them perfectly describes a real network. These two models are more considered as "case-limit", and the actual fluctuation of the crosslinking points in a real network will assume values in between these two extremes. This is because in a real network (Figure 2.6) the junction can be connected to either short or long chains, with the latter exercising lower constraints.

Starting from these models, other theories such as the constrained junction model[138] or the tube model,[139] which account for defects in the microstructure, have been considered but the complexity of their mathematical solution make them less applicable.[1] Nonetheless, it has

been shown that the phantom network is a good approximation for networks with an intermediate degree of swelling (up to ~10),[1] and it is by far the most used model to interpret experimental data. Thus, it will be used in **Chapter 5** for the interpretation of the swelling behavior of polystyrene networks.

Practical use of the equation of state

From a practical point of view, the equation of state, commonly referred to as Flory-Rehner theory, is used to compare the predicted and the experimental swelling behavior of a polymer network given its chemical composition, crosslinking density and the type of solvent the network is swollen in. The deviation of both values is used as a rough indication for estimating the amount of defects in the synthesized networks. On the one hand, the presence of defects such as primary loops and unreacted functionality will results in higher degree of swelling as they contribute to the existence of bigger meshes. On the other hand, the swelling is reduced by defects such as entanglements since they act as additional crosslinking points. The swelling degree refers to the amount of solvent the network can incorporate in its structure compared to the amount of dry gel.[14] The experimental swelling degree ($Q_{eq,exp}$) can be expressed as mass ratio according to equation 2.22.

$$Q_{\mathrm{eq,exp}} = \frac{m_s - m_0}{m_0} \tag{2.22}$$

where m_s is the mass of swollen network and m_0 is the mass of dry polymer. In order to compare the experimental and the theoretical value, the equilibrium between the two phases needs to be reached. The equilibrium is reached when no variation in the mass of swollen network can be recorded for longer swelling time. The theoretical swelling is the value of q for which the elastic and the mixing term are equal to each other ($\Delta\mu = 0$, Equation 2.18). Alternatively, q is identified as the crossing point between the elastic and the mixing term in Figure 2.7.

Q_{eq} and q are related by the density of the polymer (ρ_0) and the solvent ($\rho_{solvent}$) as follows:

$$Q_{\mathrm{eq,theo}} = (q-1)\frac{\rho_{\mathrm{solvent}}}{\rho_0} \tag{2.23}$$

The impact of the solvent/polymer interaction is visualized by varying the χ parameter. In detail, for a given network the better the polymer/solvent interaction the higher the swelling. The elastic term is determined by the density of the elastic chain, the degree of swelling during the crosslinking process (q_c, Equation 5.2) and the model used for interpreting the data (phantom or affine model). Hence, when increasing the degree of crosslinking the swelling decreases and,

in general, lower degrees of swelling are predicted for the affine model compared to the phantom one. In Figure 2.7 the effect of the solvent/polymer interaction (dashed lines) and the degree of crosslinking (solid lines) is highlighted.

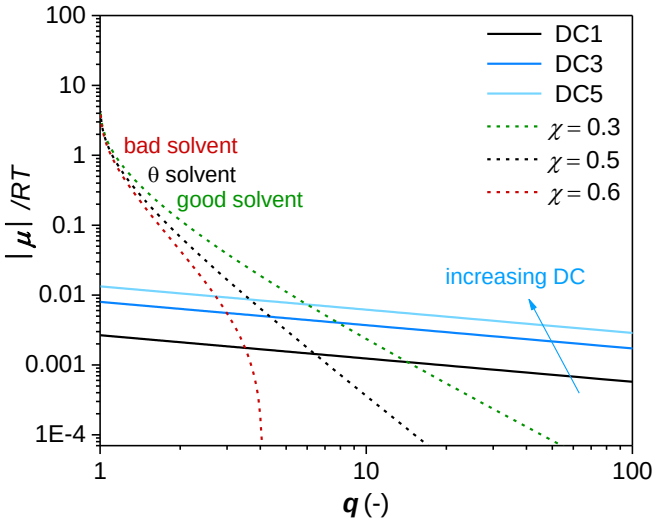

Figure 2.7 – The mixing (dashed lines) and the elastic term (solid lines) for polystyrene networks are depicted. For the mixing term (equation 2.20) the χ value is varied according to the legend. For the elastic term (equation 2.21) f = 4, so that A = 0.5 (phantom model), while q_c = 4 and the density of the elastic chain is determined by the degree of crosslinking (DC), which is varied according to the legend.

2.3.3 Synthetic Strategies

Networks are synthesized starting from solutions composed of monomer, crosslinker and solvent.[120] Some important synthetic parameters are the degree of crosslinking (*DC*), which refers to the molar ratio between the crosslinker and the monomer:

$$DC = \frac{n_{\text{crosslinker}}}{n_{\text{monomer}}} * 100 \tag{2.24}$$

and the concentration of monomer during the synthesis, also referred to as the swelling ratio during the synthesis, and can be expressed as mass ratio Q_{syn}. In this thesis Q_{syn} is calculated as

$$Q_{\text{syn}} = \frac{m_{\text{solvent}}}{m_{\text{monomer}}} \tag{2.25}$$

Independently from the adopted synthetic strategy, the network formation proceeds through consecutive crosslinking events, which connect different macromolecular chains with each other, rapidly increasing the molecular weight of the polymer. The network is formed when its

microstructure expand through the whole volume of solvent available (Q_{syn}). This moment is also named gelation point.[140] The crosslinking points prevent the polymer from dissolution in the solvent. Indeed, after gelation two phases can be identified: the sol fraction, indicating the amount of polymer which is still soluble, and the gel fraction, which refers to the insoluble part.[141] Inhomogeneities are the direct consequence of side reactions, unreacted functionalities or statistical events occurring during network formation. In this regard, each synthetic strategy presents advantages and disadvantages, which will be critically discussed.

In any case, it has to be defined whether the network is physically or chemically corsslinked. In the former, the dissolution is avoided due to physical interaction, such as hydrogen bonding or π–π interactions between the polymer chains,[142] and the linkage is usually reversible. In the latter, covalent bonds are present between elastic chains and crosslinking points. In this thesis, only chemically crosslinked networks are considered. Accordingly, a polymer network can be synthesized *via* conventional free radical polymerization, reversible-deactivation radical polymerization (RDRP) or by using polymer precursor, e.g. curing and end-linking strategy, as summarized in Figure 2.8.[120]

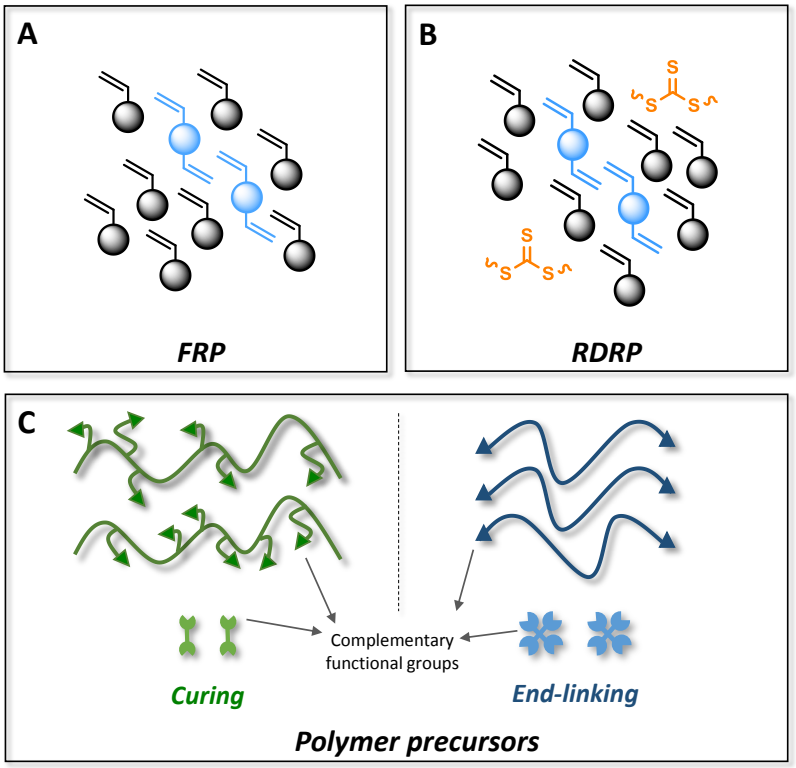

Figure 2.8 - Overview of the different strategies for the synthesis of polymer networks. In details, polymerization of a mono- and bi- unsaturated monomer via (a) free radical polymerization or (b) reversible-deactivation radical polymerization (RDRP), e.g. RAFT polymerization. (c) Synthesis of networks starting from pre-made polymer precursors: curing and end-linking approach. In both case the polymer chain is reacted with a small molecule acting as a crosslinking agent.

Free Radical Polymerization

Free radical copolymerization is by far the easiest and most extensively used method to achieve polymer networks. One of the first and most studied system involves the copolymerization of a mono and bifunctional vinyl system such as styrene and divinylbenzene (DVB).[143] The initiator is added in order to start the process, whether the solvent may or may not be present. In the mentioned example, the styrene forms the elastic chains and the DVB the crosslinking points. After the initiation step, the growing radicals are present in a solution of monomer or monomer plus solvent. At this stage, due to the high dilution of growing radicals, the overlap of different polymer chains is more difficult, favoring intramolecular reactions of the pendant double bond (cyclization) over intermolecular crosslinking.[120] This seems to result in the occurring of gelation at a nanoscale level (nanogels).[144] However, as the polymerization continues and new polymer chains are formed, the concentration of polymer chains and so the probability of intermolecular reactions increases.[2] The intermolecular reactions between the pendant double bond belonging to either a nanogel or a new polymer chain result in the formation of microgels. The agglomeration process continues and eventually complete gelation is achieved. The process can be seen as the results of the agglomeration of different nano- and microgels, each of them having its own crosslink history.[120] Therefore, the network will be constitute of highly crosslinked domains in the initial stage and less crosslinked domain in the final stage. It follows that the free radical crosslinking process is based on a random process and as such does provide limited control over the network architecture. However, the advantage of forming network *via* FRP is the easy set-up, the scalability and the versatility of the concept, which can be translated to a wide variety of systems composed of a mono- and a biunsaturated monomers (Figure 2.8a). The incorporation of structurally different monomer units in the gel microstructure is achievable simply by changing the initial feed. This allows for a one-step synthesis of a network with different properties, which are the combination of those of the monomers used.

RDRP-mediated network formation

As mentioned in Section 2.1.2, the reversible-deactivation radical polymerization (RDRP) techniques emerged as a powerful tool towards the synthesis of more defined polymer chains. Since their development in the mid−1990s, not only linear chains but also more complex architectures have been synthesized by RDRP, including polymer networks. Indeed, in a pioneering work, Ide and Fukuda investigated the use of RDRP on the crosslinking process of styrene with divinylbenzene.[145] Starting from this study, many more were reported in the following year,[146] including kinetic studies performed both experimentally and *via* kinetic Monte Carlo (*k*MC)

simulation.[147] Practically, some differences have been observed when networks are synthesized *via* RDRP such as delay in the gelation point and higher degrees of swelling. The general claim is that when the network is synthesized *via* RDRP, there is no formation of nanogels in the initial phase of the polymerization, thus leading to more homogeneous networks compared to conventional FRP.[2, 148-150] This hypothesis arises from the fact that in RDRP the termination events are mostly suppressed and the growth of the radicals is constant throughout the polymerization. Moreover, during the so-called "dormant period", when the radical is not active, the polymer chain has time for diffusion, process that might favor inter- over intramolecular reactions.[120] However, it has to be mentioned that cyclization are not completely avoided and some degree of heterogeneity are still present in the network microstructure. Indeed, despite the growing number of publications and investigations employing different analytical tools such as quantification of the chemical conversion,[145] rheology[149] and light scattering,[144] several contradictive opinions can be found in literature regarding the mechanism of network formation *via* RDRP and FRP.[2, 146] Mostly, none of the previous studies allow for a certain conclusion on whether the mechanism is truly beneficial.[146] Additional information on this topic are discussed in **Chapter 3**.

Polymer precursors

Herein, the formation of the network is achieved *via* a two-steps approach. Firstly, the polymer chains are synthesized, and subsequently the crosslinking event occurs by mixing the precursor polymer and the crosslinking agent. Within this context, two strategies have been developed, named ´curing´ and the ´end-linking´ approach.

Curing

The term ´curing´ refers to the crosslinking process occurring between a linear polymer chain, containing functional groups randomly distributed along the polymer chain, and a crosslinking agent (Figure 2.8c).[120]

The crosslinking agent is an additional molecule, which is able to react with the abovementioned reactive functional groups. The reaction between the complementary functionalities present one on the polymer chain and the other on the crosslinking agent leads to ´curing´ and the generation of networks. One of the most common examples within this class is the vulcanization of rubbers.[123, 151] In this case, the polymer precursor is an elastomer, e.g. polybutadiene (PB) or polyisoprene (PI), containing unreacted double bonds along the polymer backbone and elemental sulfur (or a sulfur based compound), which acts as a crosslinking agent. A different

polymer precursor can be obtained by the copolymerization of two monomers, only one of which is reactive towards the crosslinking agent.

In terms of their microstructure, it has to be noted that in both synthetic approaches, the crosslinking points are random distributed along the polymer. This means that the length of the elastic chains (mesh) is not constant throughout the gel, leading to an inhomogeneous pore size distribution.[120]

End-linking

In contrast to the curing process, the precursor polymer suitable for the end-linking approach contains functional groups solely at the end of the chain itself (i.e. α,ω-homotelechelic polymer). These specific polymer chains are usually synthesized *via* RDRP or anionic polymerization in order to achieve well-defined linear polymers having a narrow molecular weight distribution and, explicitly, high end-group fidelity. In a second step the α,ω-homotelechelic polymers are reacted with a multifunctional linker ($f \geq 3$), as shown in Figure 2.8c (bottom right).[120, 152] The linker constitutes the junction point in the final network, while the polymer precursor reflects the elastic chains. Ideally, the mesh distribution and the crosslinking density is constant throughout the gel.[152] Thus, the end-linking strategy is often the strategy of choice for fundamental studies on polymer networks.[3, 5, 18] In an ´end-linked´ network the average molar mass of the elastic chain (M_c) is calculated as[153]

$$M_c = 2\left(\frac{M_A}{f_A} + \frac{M_B}{f_B}\right) \tag{2.26}$$

where M is the molecular weight and f is the functionality of the polymer (A) and the crosslinker (B), respectively.

The advantage of this technique is that both, the polymer and the crosslinker, are well-defined (macro)molecules. However, during the crosslinking process, each chain does not always react with its complementary functional unit on the crosslinker molecule, resulting in dangling chains and unreacted functionalities (Figure 2.6). In addition, it is possible that both the functionalities of a given elastic chain react with the same crosslinker molecule, originating a primary loop (Figure 2.6). Nonetheless, it is widely accepted that the end-linking strategy is the most suitable method to achieve model networks, which is an intermediate system between an ideal and a real network.[152]

2.3.4 Current Challenges

Current challenges in the field of polymer network concern not only the exploration of methods to obtain defects-free networks, but also methods that facilitates the quantification of defects where present, as well as the crosslinking efficiency. Herein, a selected overview of few examples published in the last couple of years is presented.

From parent gels into diversely functionalized daughter gels

The group of Jeremiah Johnson published in early 2017 about the practicability of tuning the mechanical, thermal and swelling properties of a gel by insertion of monomers or monomer and crosslinker into an already existing polymer network.[154] The living character is introduced into the network system by the trithiocarbonate moiety present on the elastic chain of the polymer network. The parent network is obtained *via* azide-alkyne cycloaddition reaction between a four-armed polyethylene glycol polymer terminated with dibenzocyclooctyne and a bis-azide RAFT agent. Subsequently, the network is immersed in a solution containing the new monomer and a photocatalyst. After irradiation of the solution with LED light, the daughter gel is generated (Figure 2.9).

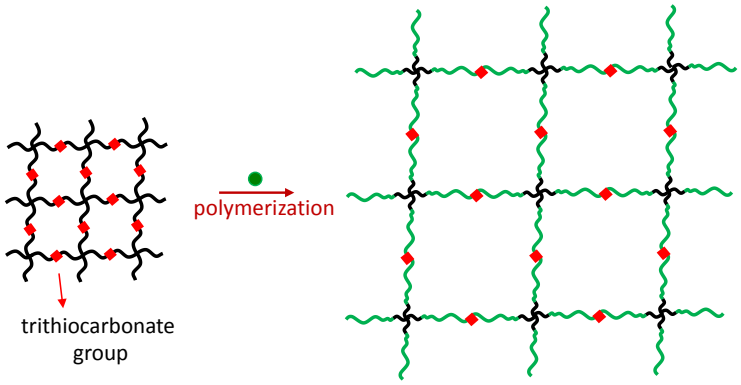

*Figure 2.9 – Left: parent gel obtained via crosslinking reaction between the polymer containing the thrithiocarbonate moiety and the complementary linker. Right: newly synthesized network obtained after introduction of the new monomer (green) in the parent gel via RAFT polymerization. The figure is adapted from reference "M. Chen, Y. Gu, A. Singh, M. Zhong, A. M. Jordan, S. Biswas, L. T. J. Korley, A. C. Balazs, J. A. Johnson, ACS Central Science, **2017**, 3, 124−134."[154].*

The presence of the photocatalyst is necessary to ensure a homogeneous growth of the network. By varying the exposure times, different networks were obtained, which elasticity decreased as the monomer conversion and the swelling degree increased. To overcome this effect, in a parallel experiment, the parent gel was exposed to a solution containing monomer, photocatalyst and a crosslinker. By tuning the ratio of crosslinker to monomer, eventually a network with

similar mechanical properties, but different chemical composition, compared to the parent network was obtained. Finally, the study was further expanded by generating stimuli-responsive and healable materials. Even though this study did not investigated the homogeneity of the newly formed networks, it provides an exciting example of reprogrammable materials, highlighting the applicative power of polymer networks.

Quantification of the crosslinking efficiency

A commonly reported strategy for the quantification of the crosslinking efficiency is the degradation of the network microstructure, either chemically or photochemically, and the subsequent analysis of the obtained soluble fractions.[18, 155-157]

In 2018 Estupiñán *et al.* reported a strategy for the quantification of the crosslinking efficiency in fluorescent polymer network.[157] Here, the nitrile imine mediated tetrazole-ene cycloaddition (NITEC) reaction is used as a crosslinking ligation.[158] The polymer network is synthesized *via* end-linking approach between α,ω-tetrazole-capped polystyrene and a trimaleimide linker upon UV irradiation. The idea is based on the fact that each ligation point produces a fluorescent pyrazoline ring. Thus, quantification is possible *via* fluorescence analysis upon comparison of the results with a pre-determined calibration curve (Figure 2.10).

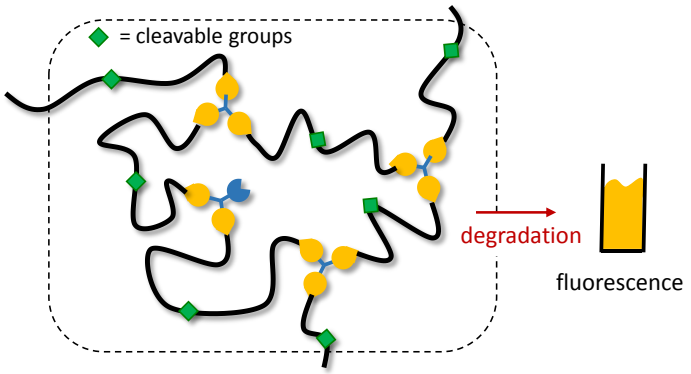

Figure 2.10 – Fluoroscent network and susbsequent cleavage of the network after degradation of the trithiocarbonate moiety present on the elastic chain (green square). The quantification of the crosslinking point is achieved by measuring the fluorescence of the resulting solution and comparison with an appropriate calibration curve. The figure is adapted from reference "D. Estupiñán, C. Barner-Kowollik, L. Barner, Angew. Chem. Int. Ed. ***2018****, 57, 5925-5929.".*[157]

Eventually, two different sets of elastic chains, short and long, were used for network formation. The results suggest that higher percentages of soluble fraction were obtained if short elastic chains were employed. Accordingly, for short elastic chains the network is more highly crosslinked, probably leading to a less efficient penetration of the UV light necessary for promoting the crosslinking reaction.

Despite the approach provides an excellent example of topological insight, an accurate quantification of the number of crosslinks is possible only after cleavage of the network *via* aminolysis of the trithiocarbonate moiety, which is still present on the elastic chain, since solid-state fluorescence did not provide reliable measurements. Moreover, the authors reported that the reagents used for the aminolysis step, such as TCEP, butylamine and in a minor measure acrylates, affect the fluorescence intensity and need to be considered when performing the calibration curve.

In the current thesis the *para*-fluoro–thiol reaction (PFTR) is suggested as ligation for the crosslinking reaction during network formation *via* end-linking approach. Here, the fluorine atoms are specifically located at the crosslinking points. Thus, the identification and quantification of the unreacted moieties was performed upon comparison of the intensity of the resonances associated to the fluorine atoms before and after ligation upon ^{19}F NMR measurements without the need of disassembly the network. More details on the PFT reaction and on the resulting networks are given in **Chapter 4** and **Chapter 5**.

Counting the loops in polymer networks

Aside unreacted functionality, the quantification of topological defects such as primary loops is desirable. Primary loops are indeed not elastically active chains, and their presence affects the mechanical properties of the resulting network.[1] However, the quantification of primary loops is not achievable simply from the quantification of the reacted, or unreacted, groups. This is because both the end-groups of a primary loop are reacted with two complementary functionality in the crosslinker. The problem is that their rearrangement in the space is not ideal, since both the chain ends are connected to the same junction point rather than to two different ones (Figure 2.6). For the purpose, a work in collaboration between the laboratories of Johnson and Olsen at Massachusetts Institute of Technology (MIT) established the network disassembly spectrometry (NDS) strategy as a tool for accessing the number of primary loops, and thus examine the impact of these defects on the mechanical properties of the resulting materials.[18] In a similar fashion to the work of Estupiñan *et al.*, after reaction of the elastic chains with a three functional crosslinker, the network is disassembled *via* cleavage of the labile group. The difference, however, is that the position of the labile group is not in the middle of the chain. This is because the goal is to obtain two distinguishable products named a short and a long fragment (S and L, respectively) upon cleavage. The necessity of an asymmetric cleavage is depicted in Figure 2.11, and based on the fact that a fully reacted junction can originate the combination LLL, SSS, SSL and LLS but a loop can only rise LLS and SSL fractions. Thus,

the ratio [LLL]:[LLS] relates a quantity only possible for an ideal network (LLL) with one possible to both an ideal network and primary loops (LLS). The higher the amount of loops, the higher is the LLS fraction, the lower is the above defined ratio. It follows that the value of the [LLL]:[LLS] ratio can be correlated to the amount of primary loops, as depicted in the graph in Figure 2.11 (right). Their findings revealed that the higher the dilution of the monomer during the synthesis, the higher the probability of forming primary loops, and that the gel is not formed if the network junctions contain more than 30% of primary loops.

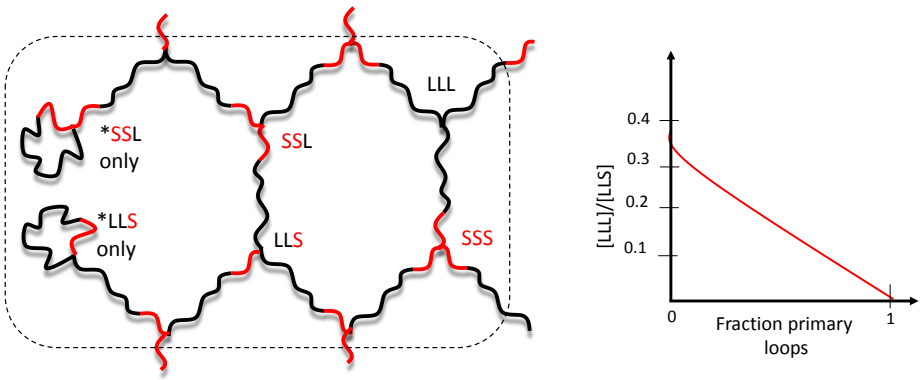

*Figure 2.11 – Left: Representation of the concept used for the quantification of the amount of primary loops within the network. Right: Plot correlating the value of the [LLL]:[LLS] ratio to the fraction of primary loops based on the statistical analysis of the soluble fractions after degradation. The figure is adapted from "H. Zhou, J. Woo, A. M. Cok, M. Wang, B. D. Olsen, J. A. Johnson, PNAS, **2012**, 109, 19119–19124".*[18]

Later on, the two working groups expanded their approach to the quantification of secondary loops, with a revised version of the NDS strategy.[17] Moreover, they developed a new elasticity theory termed "real elastic network theory" (RENT), which accounts for the presence of topological defects.[4] As previously mentioned, primary loops affect the elasticity of the network, as they are not elastically active. However, they suggested that the impact of defects on the elasticity is lower when increasing the loop order (e.g. secondary instead of primary loops) or the distance of a considered chain from the loop itself.[17] In addition, they correlated the crosslinker functionality (*f*) to the amount of loops formed. The results suggest that a crosslinker possessing odd functionality is more likely to generate primary loops, while for even values of *f* the secondary loops were more probable.[5] Ultimately, it was proposed that a step-wise addition of the crosslinker during network formation is an efficient synthetic approach to minimize the amount of loops in the final product.[16]

^{1}H NMR relaxometry

An alternative strategy to analyze the network topology is to investigate the network mobility *via* ^{1}H NMR-relaxometry. Contrary to the NDS proposed in the previous examples, ^{1}H NMR

measurements are performed on the network and do not require any additional synthetic step, e.g. no disassembly. The driving force for the use of ^{1}H NMR relaxometry is that the transverse relaxation decay (T_2) is sensitive to the mobility of the protons.[159] Since a network is composed of structural elements presenting different mobilities, e.g. elastic chains (the mobility depends on the chain length: the longer the more mobile), dangling ends (mobile) and crosslinking points (rigid), T_2 relaxation measurements appear to be a suitable method for this purpose.[159] The applicability of the concept is shown, for example, in the work of Höpfner and coworkers, where low-field ^{1}H NMR is employed for the analysis of cross-linked polyelectrolytes.[160] Typical values for T_2 are in the scale of seconds for fluids, and of μs to ms for polymers. Thus, a general procedures for this specific NMR measurements require the use of echo techniques, MSE and CPMG/XY16 sequences in order to track the full relaxation decay.[160] After subtraction of the solvent signal from the raw data, and normalization of the data points, a typical transverse relaxation decay for a poly(sodium acrylate) hydrogel having *DC* = 3 is reported in Figure 2.12. Since the networks are a complex matrix, the relaxation decay (Figure 2.12, left) are often deconvoluted by using an Inverse Laplace Transformation (ILT, Figure 2.12, right) for a better visualization of the T_2-times distribution.[160]

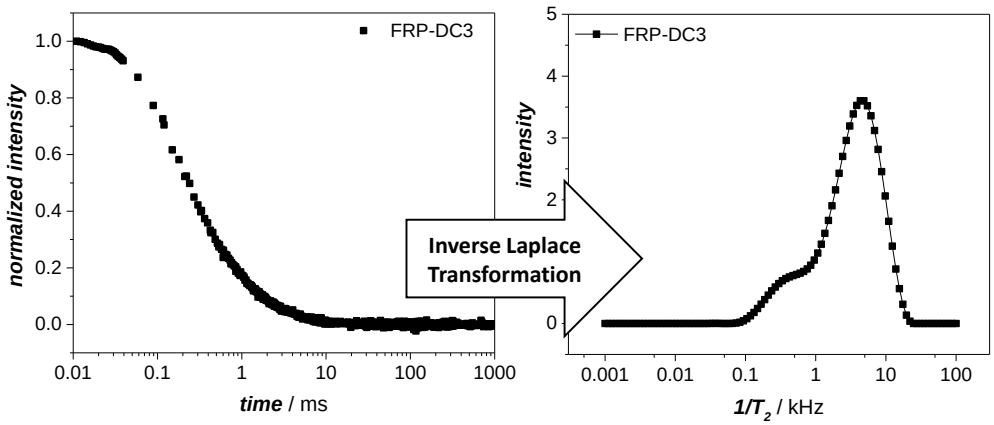

Figure 2.12 – Left: Full T_2-relaxation curve for a poly(sodium acrylate) network with DC = 3. Right: Deconvolution of the relaxation decay by using Inverse Laplace Transformation (ILT) showing the distribution of the relaxation rates $1/T_2$.

In their work, the effect of the crosslinking degree and the swelling ratio during the synthesis were investigated.[9, 161]. It was found that, the higher the crosslinking degree the shorter is the relaxation time. This is in line with the expectations as the higher *DC*, the higher the junction density and thus the more are the constraints, which limits the mobility of the chains. Similarly, reducing the amount of solvent during the crosslinking process led to a more rigid material, probably due to a higher percentage of entanglements. Later on, Arens *et al.* observed a bimodal

distribution of the relaxation decay for surface crosslinked and interpenetrating networks, in agreement with the two main domains present within the sample, each of them having a different *DC*. The latter example clearly displays the potential of the analytical method.[161]

In the current thesis, ^{1}H NMR relaxometry was used to investigate the mobility of the networks synthesized *via* RAFT mediated polymerization of acrylic acid and *N,N´*-methylenebisacrylamide (MBA) to tackle some of the still open questions regarding the differences between FRP and RDRP mediated network formation starting from a mono- and bifunctional monomer. The experimental procedure and the equation used for processing of the raw data can be found in Section 7.2

2.4 Hydrogels

Hydrogels are a particular class of polymer networks able to swell in water. A breakthrough in the history of hydrogel is the discovery of Wichterle and Lim in 1960.[162] In their report, poly (2-hydroxyethyl methacrylate) (PHEMA) was crosslinked in water yielding a soft, clear, elastic gel able to swell in water. The gel revealed compatibility with living organisms, opening the venue for the modern contact lenses and suggesting the application of hydrogels in the biomedical field.[7]

The ability to swell in water is guaranteed by the presence of functional groups such as –OH, -NH_2, -COOH, -$CONH_2$ and –SO_3H within the gel.[163] The crosslinking process can occur *via* physical or chemical interaction. In principle, all the synthetic strategies mentioned in Section 2.3.3 can also be applied for hydrogels. Common synthetic polymers used for hydrogels fabrication are the previously mentioned PHEMA, poly(vinyl alcohol) (PVA) and poly(ethylene glycol) (PEG).[164]

Next, hydrogels able to change their structure as a response to environmental stimuli have been developed and defined as stimuli responsive hydrogels. In details, light, temperature and magnetic fields are considered physical stimuli, while pH or ionic factor are termed chemical stimuli.[165] Furthermore, the response to biochemical stimuli such as enzyme or antigen is of high interest for pharmaceutical, and in general biomedical, applications.[166]

Concerning the application, hydrogels that contract or relax upon electrochemical stimuli are investigated for functioning as human muscle and tissue.[167, 168] Moreover, hydrogels can be applied for the removal of highly toxic heavy metal ions from water, [8] for food packaging[169] and in the cosmetic industry.[13] Finally, several reports that critically reviewed the use of hydrogels as drug delivery system are available in the literature,[122] where important factors are the drug loading, and the time over which the drug is released.

Eventually, superabsorbent polymers (SAPs) represent a special class of hydrogels.[6] Hydrogels belonging to this subclass are mostly composed of crosslinked polyelectrolytes such as poly(sodium acrylate), which will be discussed in the following section.

2.4.1 Polyelectrolytes

The term polyelectrolytes refers to a polymer having fixed charges along the chains. The presence of these charges allows for the absorption of large amount of water, up to 1000 times the weight of the network itself.[170] The charges can be introduced prior or post synthesis, by using

charged monomers or changing the pH of the surrounding solution. For example, when using poly(acrylic acid) (PAA) networks, the fixed charged are obtained by neutralization of the carboxylic acid group present on the repeating unit.[171] The first synthesis of crosslinked poly(sodium acrylate) (PSA) is reported by Kern in 1938. Later on, several studies regarding the synthesis and properties of such materials were proposed by Kuhn and Katchalsky.[172, 173]
The biggest market of polyacrylates is their use as absorbents in diapers, which were commercialized first in Japan in the early 1980´s.[171] The global market of superabsorbent polymers reached value of around USD 6 billion in 2017, with sodium acrylate covering over three-fifth of it (USD 3.5 billion).[174]
In the current thesis, the use of PSA network as separation agent for the desalination of salt water is considered.

Equation of state for polyelectrolytes

Before moving to the application, it is important to highlight some key differences when dealing with polyelectrolytes rather than not charged networks. Accordingly, the equation of state for hydrogels needs to be adjusted in order to consider the effect of the charges. Therefore, the variation of the free energy is now given by the sum of the mixing, the elastic and additionally the electrostatic term ($\Delta\mu_{\text{ionic}}$). At the equilibrium,

$$\Delta\mu = \Delta\mu_{\text{mix}} + \Delta\mu_{\text{el}} + \Delta\mu_{\text{ionic}} = 0 \qquad (2.27)$$

The mixing term

The mixing term as described in Section 2.3.2 is mostly capable to describe network in a non-polar environment, but it fails in polar protic system having oriented interactions such as hydrogen bonds.[1] This limit can be overcome by including several new parameters in the equation. Nevertheless, the mixing term contributes in a minor measure to the overall variation of the free energy when $\Delta\mu_{\text{ion}}$ is present. For this reason, the Flory-Huggins theory is still a good estimation for describing the mixing term.[134]

The elastic term

The high degree of swelling and the presence of charges associated with polyelectrolytes reflects to more stretched and stiff chains, respectively. However, this is not considered by the Gaussian distribution model of the end-to-end vector distance.[175] A more accurate interpretation of the experimental values is possible when more complex models, which account for the finite extensibility of the chain and a non-Gaussian distribution, are considered e.g. Langevin

chain statistics.[130, 175] Due to the complexity of the term, which is not straightforward to compute, the experimental data obtained for polyelectrolytes will not be compared with the theory, which is why this problem is herein approached only qualitatively.

The electrostatic term

This term describes the effect of the charges, having them a major role when considering macroscopic deformation such as swelling (Figure 2.13). Indeed, when a charged network is placed in contacted with a solution with a salt concentration c_s, the mobile charges present in solution redistribute themselves between the two phases.[173, 176] The equation for the electrostatic potential can be written as[177]

$$\Delta\mu_{\text{ion}} = -RTV_1\left[\sum c_{\text{i}}(g) - c_{\text{i}}(l)\right] \tag{2.28}$$

where c_i is the concentration of the considered ions (i), while g and l are the solution inside and outside the gel, respectively. In Equation 2.28 the approximation of diluted solutions is applied and the concentrations, easily measurable experimentally, are used instead of the activities. Even though the gel is a semi-dilute system, this approximation is still considered valid.[132]

In the case of PSA in contact with a NaCl aqueous solution (1:1 electrolyte), at the equilibrium the electro-neutrality principle is respected and

$$c_{\text{Na}^+}(l) * c_{\text{Cl}^-}(l) = c_{\text{Na}^+}(g) * c_{\text{Cl}^-}(g) \tag{2.29}$$

with

$$c_{\text{Na}^+}(l) = c_{\text{Cl}^-}(l) = c_{\text{s}} \tag{2.30}$$

$$c_{\text{Na}^+}(g) = c_{\text{Cl}^-}(g) + \frac{\rho v_2}{M_2} \tag{2.31}$$

where ρ is the density of the dry polymer, v_2 the volume fraction of the polymer in the gel and M_2 the molar mass of polymer per free counter ion. Critically, the value of M_2 is not equal to the molecular weight of the monomer as it is not possible to charge every unit. Indeed, due to the so-called Manning condensation, a minimum distance needs to be present between two charged species, [178, 179] which for monovalent ion in water is equal to 7 Å.[180] This characteristic distance is called Bjerrum length.[178]

It follows that, the combination of Equations 2.30 and 2.31 with Equation 2.29 results in

$$\Delta\mu_{\text{ion}} = 2RTV_1\left[c_s - \sqrt{c_s^2 + \left(\frac{\rho v_2}{2M_2}\right)^2}\right] \tag{2.32}$$

2.4.2 Desalination based on Polyelectrolyte Hydrogels

The term desalination literally means "removal of salt from".[181] The importance of desalination is associated with the high demand of fresh water by the growing population and the high availability of seawater (97% of the total water in the world).[181] In the last decades numerous studies on the desalination have been performed, which led to the development of efficient large-scale used methods. The main classification concerns thermal and membrane-based processes, with the latter presenting a lower energy consumption and a simpler set-up. Indeed, the process using reverse osmosis membranes covered 63% of the global market in 2011, while the thermal multi-stage flash distillation 23%.[181] From the material point of view, the main problems associated with the thermal process is corrosion, while the one associated with the membrane is fouling.

Herein, a relative new application for poly(sodium acrylate) (PSA) networks is discussed. In detail, in a pioneering work of Höpfner *et al.*, PSA networks have been proved to be a suitable material for the desalination of salt water (NaCl solution) in a membrane-free forward osmosis process.[182, 183] In the mentioned application, not only the ability of these hydrogels to absorb huge amounts of water is beneficial, but the charges present on the polymer chains play a key role for the realization of the process.[182] Thus, when a dry gel containing fixed charges is placed in contact with a salt solution, the equilibrium established between the two phases is qualitatively described by the Donnan effect.[176] Because of the charges present on the elastic chain of the polymer network the ion concentration is different inside and outside the gel. It follows that uncharged water molecules can freely enter the network structure, while the mobile ions are partially rejected due to presence of the fixed charges. The principle is depicted in Figure 2.13. It has to be noted that, when the network starts swelling, its microstructure expands, resulting in a lower charge density. Thus, a new Donnan equilibrium is established and more mobile ions enter the gel.[177] Nonetheless, as a result of these ion-interactions, the supernatant phase will be enriched in salt concentration, while the water within the gel will have a lower salt content compared to the starting solution used for swelling.

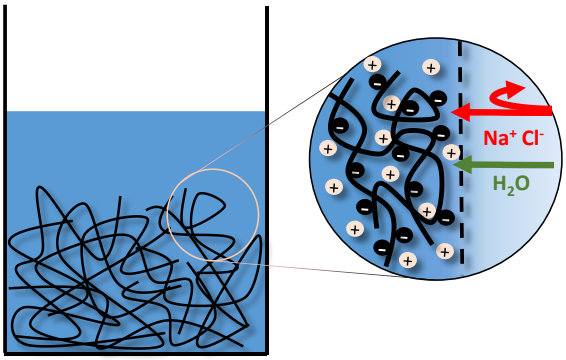

Figure 2.13 – Swelling for polyelectrolytes in contact with a salt solution. Herein, the uncharged water molecules can freely enter the network but the mobile ions are partially rejected due to the fixed charges present on the network structure (electrostatic repulsion). The figure is adapted from "Höpfner et al., Prog. Coll. Polym. Sci. ***2013****, 140, 247".* [183]

The practical realization of the desalination is achieved by a discontinuous three-step approach, as depicted in Figure 2.14. [182] First, the dry PSA gel is mixed with salt water and it is allowed to swell. In the current thesis, the salt solution used as initial feed is characterized by an initial salt content $c_{s,0}$ = 10 g·L^{-1} (Figure 2.14, step 1). After swelling, the supernatant phase characterized by $c_s > c_{s,0}$ is removed (Figure 2.14, step 2). Finally, the water within the hydrogel, which by contrast has $c_s < c_{s,0}$, is squeezed-out by applying an external pressure (Figure 2.14, step 3). In a typical experiment, the relative ratio between the swollen polymer and the supernatant phase (Q_{rel}) is kept equal to 2. By doing so, the solution is equally distributed (half and half) between the gel and the supernatant phase.

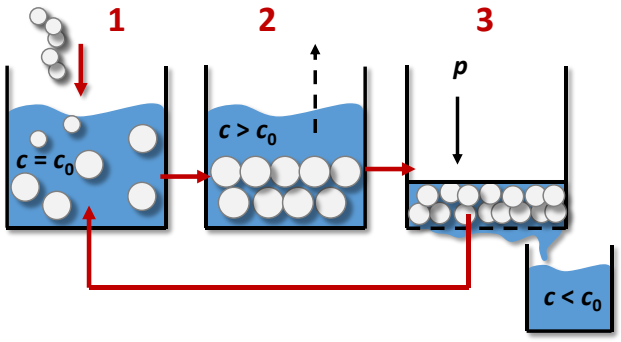

Figure 2.14 - Practical realization of the desalination based on a discontinuous three step approach using polyelectrolyte networks. 1. The dry hydrogel is placed in contact with the solution to swell until equilibrium is reached. 2. Removal of the supernatant phase enriched in salt content. 3. An external pressure is applied to recover the desalinated water from within the hydrogel matrix. The figure is adapted from "Höpfner et al., Prog. Coll. Polym. Sci. ***2013****, 140, 247".* [183]

State of the art

The preliminary work of Höpfner *et al.* was focused on establishing the proof of concept for the realization of the above described process. The PSA hydrogels were synthesized *via* free radical polymerization with different degrees of crosslinking (*DC*, from 0.5 – 5 mol%) and neutralization (*DN*, from 0 to 75%). Their findings revealed that the higher *DC* and *DN*, the better is the salt rejection, qualitatively in agreement with the Donnan theory.[9]

Later on, Arens *et al.* studied the impact of different network architectures on the desalination performances. The investigation included surface crosslinked PSA networks and interpenetrating networks and the influence of significantly higher *DC*, e.g. 30%. Furthermore, quasi-model networks obtained *via* physical crosslinking were synthesized to produce network with different pore size or possessing dangling chains.[161] Next, thermally responsive networks were developed by introducing monomers such as *N*-isopropylacrylamide into the microstructure as a copolymer in the elastic chain or by generating interpenetrating networks, one composed of sodium acrylate (SA) and one of *N*-isopropylacrylamide (NIPAm) as repeating unit. The idea is to (partially) recover the desalinated water inside the gel (Figure 2.14, step 3) by inducing the structural collapse of PNIPAm networks upon temperature changes. The main results derived from this complex and exhaustive study are:[161]

i. PSA networks are more suitable for the process compared to the analogous poly(sodium methacrylate).
ii. Interpenetrating networks present better performances compared to the equivalent single PSA network obtained *via* FRP, mostly when the first network is characterized by a high *DC* = 5% and the second by *DC* = 1 % (higher charge density).
iii. The presence of dangling chain is beneficial as it increases the charge density.
iv. The thermal response of PNIPAm networks vanished if more than 10% of SA is used as comonomer, while it is preserved in case of interpenetrating networks.

Additional work was performed to optimize the energetic consumption,[161] which is not discussed here as the main topic of this thesis is centered on the investigation of different approaches for network formation with the aim of generating a more homogeneous microstructure.

Accordingly, two approaches are investigated: the RAFT-mediated network formation to achieve PAA network in a one-step process (**Chapter 3**), and the end-linking strategy involving the use of the *para*-fluoro-thiol reaction, to allow the quantification of unreacted moieties (**Chapter 4** and **Chapter 5**).

3
RAFT-mediated Network Formation

A recent publication of Olsen and Johnson discussed the negative impact of structural defects such as loops on the elastic properties of networks.[17] These findings changed the view of synthetic polymer chemists, which are nowadays focused on the development and understanding of synthetic pathways for the achievement of more homogenous networks, with the aim of maximizing its application potential. Accordingly, the current chapter aims towards the development of more defined poly(sodium acrylate) (PSA) networks, which are used as separation agent for the desalination of salt water in a membrane-free process.[182]

On a large scale, both in industry and in laboratories, PSA networks are synthesized *via* conventional free radical polymerization (FRP).[6] While this strategy is often selected for its simplicity, the synthetic process allow only limited control over the microstructure. According to the literature, network synthesized *via* FRP present both highly crosslinked domains (nanogels) and less crosslinked domains.[2] Compared to an ideal network microstructure, this might affect the distributions of the fixed charges along the polymer backbone as well as the swellability, even if ideal and FRP networks present a similar degree of swelling (refer to Figure 3.1). Charge distribution and swellability determine the charge density, and thus the performance of the network towards salt rejection. Therefore, it is of high importance to investigate whether a more homogenous microstructure allows for a higher charge density, as depicted in Figure 3.1.

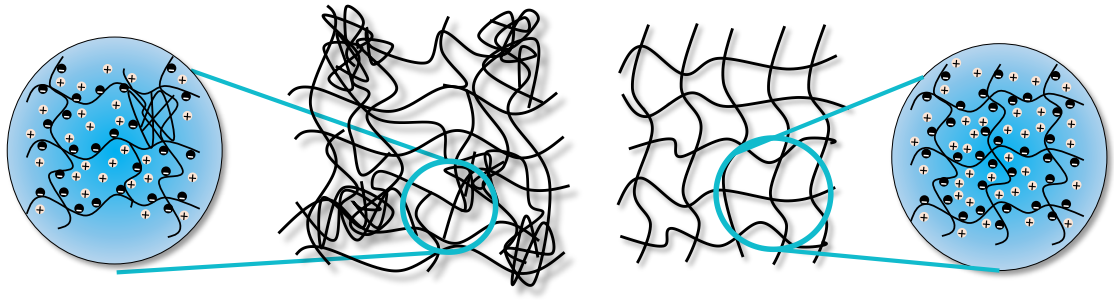

Figure 3.1 –Theoretical charge distribution in a network having an inhomogeneous (left) and homogeneous (right) microstructure.

For this purpose, in **Chapter 2**, several approaches have been listed for a more precise synthesis of polymer networks (refer to Section 2.3.3): the curing process, the end-linking strategy and the reversible-deactivation radical polymerization (RDRP) mediate network formation.

The RDRP approach is of particular interest, since only minimal changes compared to FRP are necessary during the polymerization to obtain the final network. The difference lies solely in the addition of an appropriate controlling agent such as a suitable nitroxide, metal complex or RAFT agent to the reaction mixture,[120, 148, 184] thus gram scale production, beneficial for the application, is still possible. Since the application demand poly(acrylic acid) based networks, the RAFT polymerization is, at present, the most suitable RDRP approach (refer to Section 2.1.2).

Accordingly, the influence of a RAFT agent on the crosslinking process, still argued in literature,[146] was studied in detail. Thereafter, the networks resulting from the RAFT-mediate copolymerization of acrylic acid (AA) with *N,N´*-methylenebisacrylamide (MBA) were characterized *via* ^{1}H NMR relaxometry and rheology to investigate the mobility of the microstructure and the mechanical properties of the network, respectively. Finally, the networks were tested in salt rejection experiments.

The results presented in this Chapter are part of a joint publication with Christoph Pfeifer (AK Wilhelm), currently in preparation. The ^{1}H NMR relaxometry measurements were performed by Christoph Pfeifer (KIT). The rheological measurements were performed by Dr. Lukas Arens (KIT). The RAFT agent S,S-di((2-methyl)propionic acid) trithiocarbonate (TRITT) was provided by Dr. Thomas Gegenhuber (KIT).

The project was supervised by Prof. Dr. Leonie Barner and Prof. Dr. Manfred Wilhelm.

3.1 Model System

The interest towards RDRP-mediated network formation arise from the established positive impact that controlling agents have on the synthesis of linear polymer chains, as they allow a linear increase of the molecular weight of the polymer with conversion due to the drastic reduction of termination and transfer reactions of the propagating chains. In contrast, the propagating chains in FRP are characterized by high and broad molecular weight distribution at any stage of the polymerization.

While the difference in the mechanism of polymerization between RAFT and FRP polymerization is well known for the synthesis of linear polymer chains, the impact of the controlling agent, here a RAFT agent, on the crosslinking process is still debated.[146] Few literature reports have already discussed the topic and propose the formation of highly crosslinked nanogels at the early stage of the polymerization in case of FRP. [2, 120, 149] Subsequently, the nanogels react with each other, leading to an inhomogeneous network characterized by multiple domains having different degree of crosslinking (see Figure 3.2). On the other hand, during RDRP mediated copolymerization the polymer is expected to grow gradually, generating first highly branched chains and eventually turning into a gel. The latter process is claimed to allow for better diffusion of the chains and thus a more homogeneous microstructure in the final network.[144, 149] The aforementioned situation can be summarized as depicted in Figure 3.2.

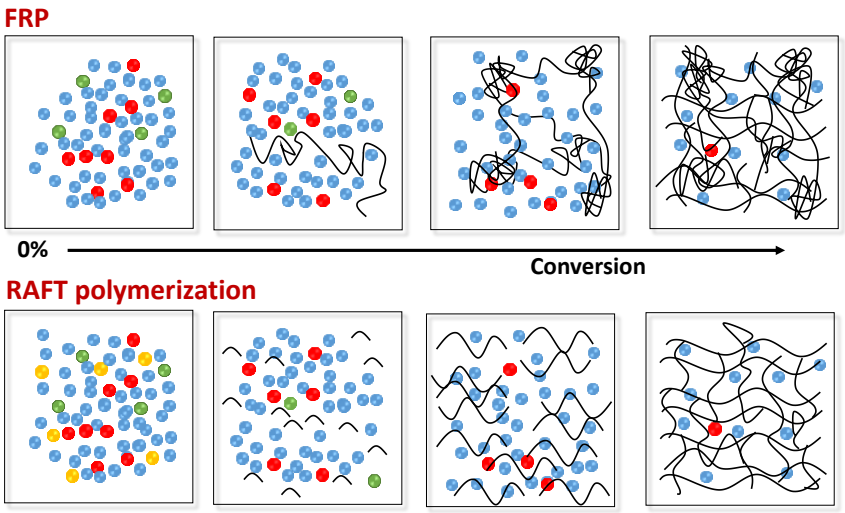

Figure 3.2 – Representation of the crosslinking process via FRP (top) or RAFT (bottom) polymerization between a mono- (blue) and a bifunctional (red) monomer, in the presence of initiator (green). The RAFT agent is represented by a yellow circle (bottom) but for simplicity not reported in the growing chains, while the polymer by the solid black lines. In a first approximation the overlap between the polymer chains is considered as a crosslinking point, independently of its nature (backbiting reaction, entanglement or crosslinking agent). The figure is adapted from "Henkel R., Vana P., Macromol. Chem. Phys. ***2014****, 215, 182–189". [149]*

In the first step, the validity of the aforementioned assumption was herein investigated. For this purpose, one possibility is the analysis of the crude mixture *via* size-exclusion chromatography (SEC), specifically at early stage of the polymerization, as the growing chains are still soluble (Figure 3.2, second box). Thus, the crosslinking process was performed with and without the presence of the RAFT agent, while keeping all the other parameters constant. Noteworthy, in order to perform this study on poly(acrylic acid), the use of an aqueous SEC is necessary because of the hydrophilicity of the polymer. However, due to instrument limitations, only the analysis of polymer with $M_n < 10^5$ g·mol^{-1} is meaningful (refer to Section 7.2). This is a limitation for the study of the crosslinking process where the molecular weight of the polymer is expected to reach higher molecular weight as a consequence of the crosslinking reaction. Accordingly, to allow measurements of a broader range of molecular weight, the crosslinking process was studied on a model system, which can be analyzed *via* THF SEC.

The herein reported model system involved the copolymerization of methyl acrylate (MA) with 1,3-butanediol diacrylate (DAc). Moreover, regardless whether the polymerization refers to linear or crosslinked chains, an accurate choice of the RAFT agent in relation to the monomer is fundamental for the RAFT polymerization to be efficient (as discussed in Section 2.1.2). To test the accuracy of the RAFT agent selection, linear chains were synthesized first, avoiding insolubility issues associated with networks. DoPAT was used as RAFT agent for the polymerization of MA, which was performed at 70 °C for 6 h using different molar ratio of MA:DoPAT (from 1:100 to 1:1000, refer to Section 7.3). The reaction scheme and the SEC traces recorded at the end of the polymerization are reported in Figure 3.3, while a summary of the molecular weight and the dispersity index (*Đ*) of the obtained polymers is reported in Table 3.1.

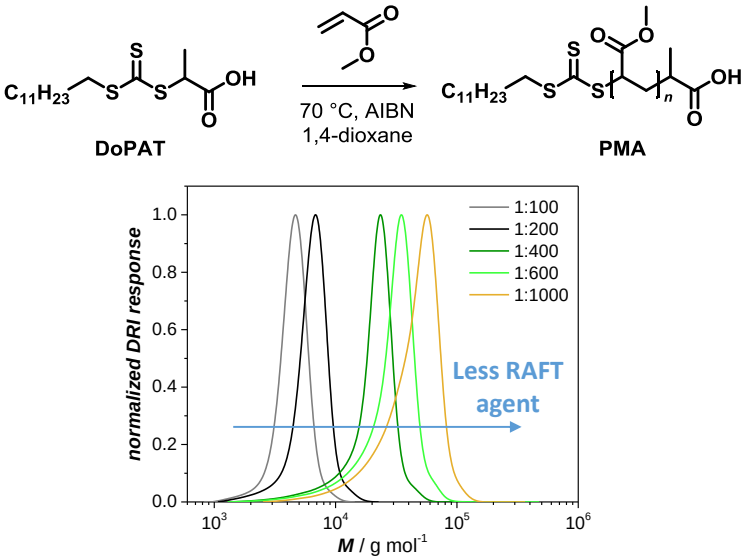

Figure 3.3 – Top: Reaction scheme for the synthesis of poly(methyl acrylate) via RAFT polymerization. Bottom: SEC traces after polymerization using different molar ratios of RAFT agent (DoPAT) to monomer. The molar ratio used in each case is stated in the legend.

Table 3.1 – Overview of the linear poly(methyl acrylate) polymers synthesized, displaying the amount of RAFT agent used during the polymerization (molar %), and the molecular weight ($M_{n,PMA}$) and the dispersity index (Đ) of the resulting polymer.

DoPAT:MA	DoPAT (mol%)	$M_{n,PMA}$ [(a)] (kg·mol^{-1})	Đ[(a)]
1:100	1.00	4.6	1.1
1:200	0.5,	6.6	1.1
1:400	0.25	20	1.2
1:600	0.17	30	1.3
1:1000	0.10	48	1.4

[(a)]as determined *via* SEC based on poly(methylmethacrylate) calibration.

From Table 3.1 and Figure 3.3, it can be concluded that the molecular weight is influenced by the amount of the RAFT agent, whereas the dispersity index of the polymer is narrow in each case ($Đ < 1.5$). The dispersity index slightly increases at low molar percentage of RAFT (0.1 %), which is expected as the control is reduced for longer chains. Overall, the data indicate an accurate choice of the RAFT agent respect to the selected monomer.

Thus, in the next step, the crosslinking process between MA and DAc was investigated with and without the presence of DoPAT as RAFT agent. In addition, in order to evaluate the impact of the RAFT agent on the final network, the use of two different concentrations of RAFT agent during synthesis were tested. In detail, 0.10 and 0.17 mol%, which correspond to a molar ratio of 1:1000 and 1:600 (RAFT agent:MA, respectively). In both cases (FRP and RAFT), the polymerization was performed using a molar ratio of 1:100 (DAc:MA, corresponding to a network having $DC = 1$) in dioxane (20 % w/w).

The reaction scheme is depicted in Scheme 3.1, while more details on the experimental procedure are provided in **Chapter 7** (Section 7.3).

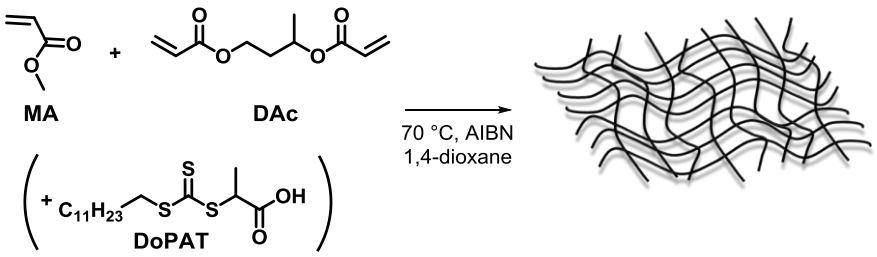

Scheme 3.1 – Reaction scheme for the synthesis of polymeric networks using methyl acrylate as monomer and 1,3-butanediol diacrylate (DAc) as crosslinking agent. The polymerization was performed at 70 °C with and without the presence of the RAFT agent (DoPAT).

To investigate the polymerization kinetics, the reaction mixture was divided into several vials and the reaction was stopped at selected intervals of time. Subsequently, the vials were twisted upside down to have a visual feedback for the network formation. Here, the gelation was defined by the moment in which no percolation of the solution was observed after twisting of the vial, as displayed in Figure 3.4 (top: FRP, bottom: RAFT with 0.10 mol% RAFT agent). The gelation was observed after 40 min for FRP, after 3.5 h for RAFT polymerization using 0.10 mol% DoPAT, and after 7 h when using 0.17 mol% DoPAT. Hence, a delay in the gelation is noticeable for the RAFT process but no particular information concerning the molecular weight of the chains are associated with it.

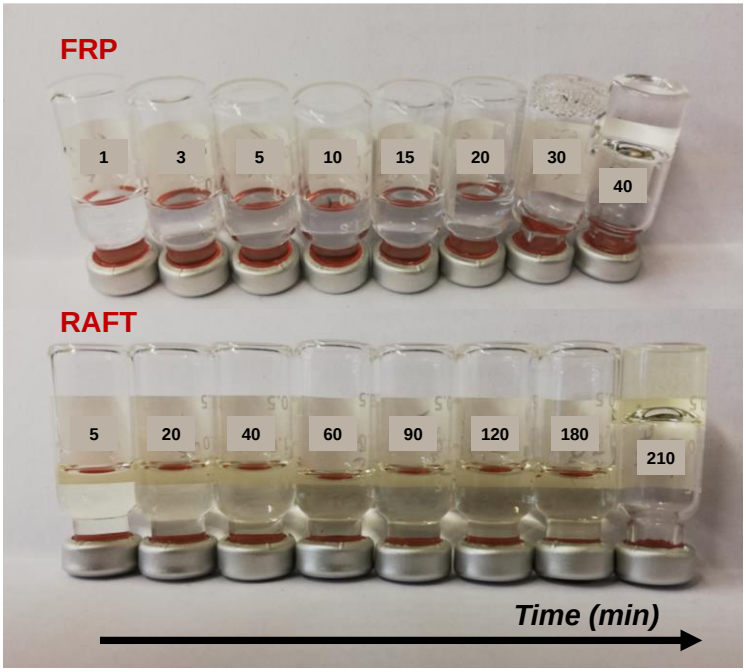

Figure 3.4 –The visual feedback for the network formation during the crosslinking reaction was obtained by twisting the vial upside down at selected intervals of time. The number on the vial corresponds to the reaction time (in minutes) at which the polymerization was stopped. Top: conventional free radical polymerization (FRP). Bottom: RAFT-mediated polymerization using 0.10 mol% of RAFT agent (DoPAT).

In order to further investigate the crosslinking process, the vial was opened to determine the conversion at each reaction time (refer to Section 7.3, Equation 7.11). After evaporation of the residual monomer and dioxane, the reaction mixture was analyzed *via* SEC.
The results for the free radical polymerization are depicted in Figure 3.5.

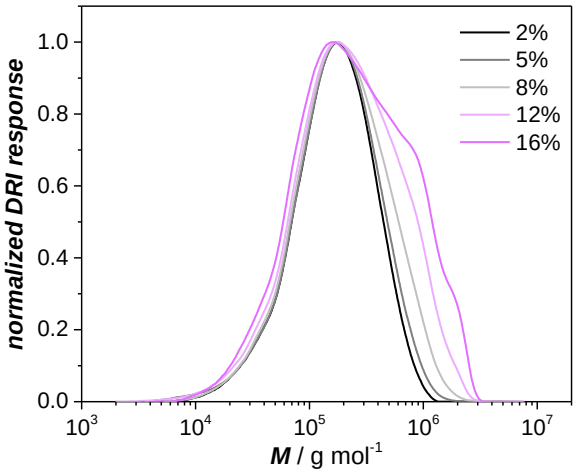

Figure 3.5 – SEC traces obtained at different conversion values for the crosslinking reaction between MA and DAc via FRP.

According to the SEC trace obtained after 2% conversion (Figure 3.5, black), the polymer is defined by a molecular weight equal to $1.5 \cdot 10^5$ g·mol^{-1} and $Đ$ = 2.4. These are typical values for FRP, where long chains are produced at early stage of the polymerization, here at t = 3 min. After 5 min, the conversion is equal to 5% and the SEC trace of the polymer is identical to the previous one, confirming the hypothesized crosslinking process represented in Figure 3.2 (top, second box). At higher conversion values, the SEC traces show a higher and broader molecular weight distribution, as a consequence of the crosslinking and termination reactions. The SEC analysis of the polymeric sample corresponding to a reaction time of 30 min, which presented a conversion of 32%, was not possible since the significant degree of branching lowered the solubility of the product. Finally, the gelation was observed after 40 min. Notably, the gelation is not associated with the end of the polymerization, as the polymerization can continue to polymerize within the formed network microstructure.

In the next step, the crosslinking reaction was repeated in the presence of 0.10 mol% of RAFT agent. Analogous to the FRP reaction, the samples were analyzed *via* SEC, and the corresponding SEC traces at different conversion values are reported in Figure 3.6.

Comparing Figure 3.6 with Figure 3.5 shows a significant difference between the two crosslinking process (FRP and RAFT mediated). At 3% conversion, achieved here after 5 min, the reaction mixture is mainly composed of polymer chains with a molecular weight of 4500 g·mol^{-1} and $Đ$ = 1.3 (Figure 3.6, gray line), in contrast to $M_n = 1.5 \cdot 10^5$ g·mol^{-1} ($Đ$ = 2.4) for FRP. Next, the reaction was stopped after 20 min, corresponding to 16% conversion, similar to FRP. According to SEC, at this stage the solution is formed by narrow dispersed linear chains having a molecular weight equal to 18 000 g·mol^{-1} and $Đ$ = 1.3 (Figure 3.6, black line).

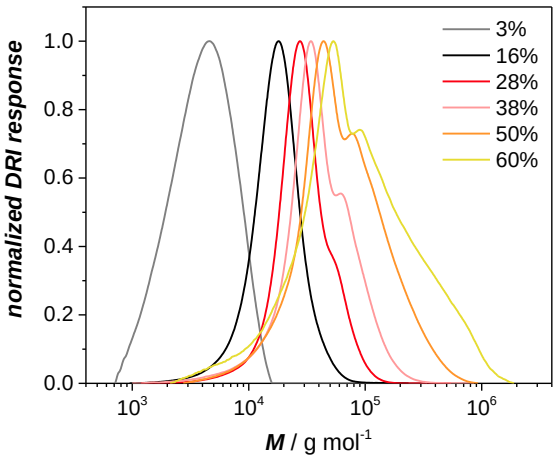

Figure 3.6 – SEC traces obtained at different conversion values for the crosslinking reaction between MA and DAc via RAFT polymerization using 0.10 mol% of DoPAT.

After a reaction time of 40 min and a conversion of 28%, it is possible to notice a shoulder in the SEC traces (Figure 3.6, dark red line). The shoulder indicates the presence of a fraction of polymer chains with higher molecular weight. Since the bifunctional monomer is present within the reaction mixture, the shoulder is a consequence of the crosslinking process, and thus of the presence of branched chains. At longer reaction time, no conclusive information is gained from the SEC traces. However, it is noticeable that the crosslinking process continues to occur and an increasing number of growing chains connect with each other. The gelation occurred after 3.5 h (Figure 3.4, bottom), at approximately 75% conversion.

In the last step, the effect of the RAFT agent concentration on the crosslinking process was investigated by performing the same reaction using 0.17 mol% of DoPAT. The SEC traces for the latter reaction are reported in Figure 3.7.

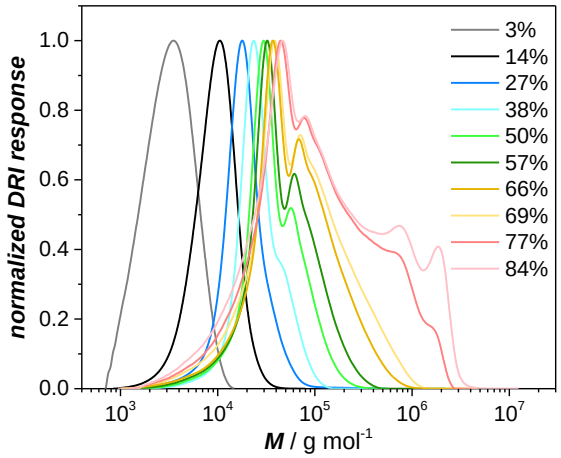

Figure 3.7 – SEC traces obtained at different conversion values for the crosslinking reaction between MA and DAc via RAFT polymerization using 0.17 mol% of DoPAT.

The first SEC trace in Figure 3.7 (gray line) corresponds to a conversion of 3% and displays growing chains having a molecular weight of 3500 g·mol^{-1} and $Đ$ = 1.3. Despite the similar conversion, the polymer chains have a lower molecular weight compared to the previous case, which is expected as the amount of RAFT agent was increased. Subsequently, the gradual growth of the propagating chains continues. For example, a molecular weight of 18 000 g·mol^{-1}, previously achieved at 16% conversion (20 min), is now reached at 40 min and 27% conversion (Figure 3.7, blue line). As before, a shoulder is visible in the SEC trace when the main peak presents a molecular weight of ~24 000 g·mol^{-1} (Figure 3.7, light blue line). This value is achieved here at 38% conversion, while the gelation occurred at ~85% conversion.

The results obtained so far confirm the reaction pathway proposed in Figure 3.2. It was demonstrated that during the FRP process long chains are present from the early stage of the polymerization (e.g. 3% conversion), while for the RAFT mediated process, only short chains having a low and well-defined molecular weight could be detected *via* SEC analysis, as shown in Figure 3.8 (left). At approximately 35% conversion, a visual feedback for gelation was observed for FRP (Figure 3.4, top), while the branched chains are still soluble in case of RAFT polymerization (Figure 3.4, bottom). Moreover, according to SEC analysis, for a given conversion (e.g. 50%) the lower the amount of the RAFT agent, the higher is the molecular weight of the growing branched chains Figure 3.8 (right).

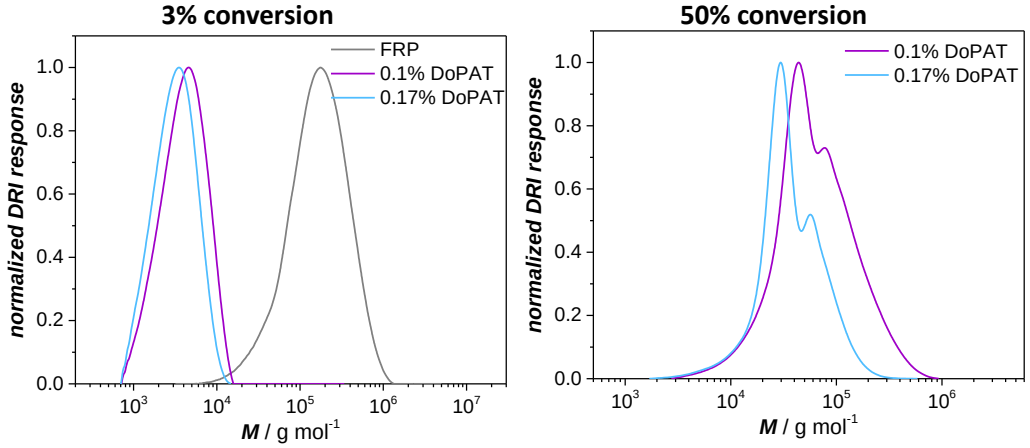

Figure 3.8 – Comparison of the SEC traces obtained at 3% (left) and 50% (right) conversion during the crosslinking reaction between MA and DAc via FRP (gray) and RAFT polymerization with 0.10 (violet) and 0.17 (light blue) molar percentages of RAFT agent (DoPAT).

Lastly, for the RAFT mediated crosslinking process the gelation is observed after ~75% and ~85% conversion when 0.10 and 0.17 mol% of RAFT agent were used, respectively.

Assuming at any stage an equal conversion of the crosslinking agent, a higher number of crosslinking points occurs in solution in case of RAFT polymerization, because the gelation occurs at higher conversions. It follows that a better diffusion between the growing chains during the crosslinking process is achievable in the presence of the RAFT agent. The low dispersity index of the polymer chains synthesized *via* RAFT polymerization indicate that the presence of backbiting and termination reactions is limited.

In the next step, the aim is to verify whether the difference in the crosslinking process, and the gradual growth of the chains, leads to a more homogeneous network structure (Figure 3.2, fourth box). For the purpose, it is assumed that the observed differences in the crosslinking process are associated with the presence of the controlling agent and are independently from the monomer used, as long as the selected RAFT agent is able to control the growth of the desired monomer. Thus, the analysis on the final network was performed directly on the targeted poly(acrylic acid) (PAA) networks synthesized *via* RAFT polymerization, as shown in the next section.

3.2 Poly(sodium acrylate)

In this section the RAFT-mediated process is adapted to the synthesis of poly(sodium acrylate) networks, suitable for the salt rejection experiments. As before, first the ability of the selected RAFT agent (i.e. TRITT) to control the polymerization of the desired monomer was evaluated upon synthesis of linear chains. Subsequently, the PSA networks were synthesized using different amount of RAFT agent but the same degree of crosslinking (*DC*), to focus on the effect of the RAFT agent on the final network. Thereafter, the amount of RAFT agent was fixed to a desired value and the *DC* was varied during the synthesis to obtain a variety of PSA networks for testing in salt rejection experiments.

3.2.1 Effect of the RAFT Agent

Synthesis of linear poly(acrylic acid)

The synthesis of narrow disperse poly(acrylic acid) is achievable using S,S-di((2-methyl)propionic acid) trithiocarbonate (TRITT) as RAFT agent.[39] Herein, the polymerization was performed at 70 °C using distilled water as solvent (20% w/w) and 4,4'-Azobis(4-cyanovaleric acid) (V-501) as water soluble thermal initiator (Figure 3.9, top). In order to verify the range of conditions under which the RAFT agent is able to control the polymerization of acrylic acid (AA), different RAFT agent:AA molar ratios, from 1:100 to 1:1000, were tested. After 3 h of reaction time, the polymer was analyzed *via* aqueous SEC, as displayed in Figure 3.9 (bottom).

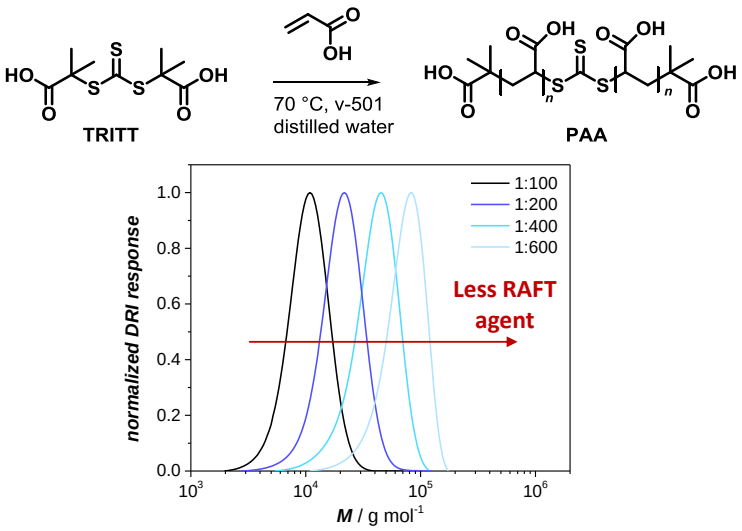

Figure 3.9 – Top: Reaction scheme for the RAFT polymerization of acrylic acid (AA) employing TRITT as RAFT agent. Bottom: SEC traces after RAFT polymerization performed using different molar ratio of TRITT:AA (reported in the legend). The results refer to a reaction time of 3 h (full conversion).

The SEC traces, reported in Figure 3.9, present a narrow molecular weight distribution ($Đ < 1.5$) for each of the synthesized polymers, indicating that TRITT is a suitable RAFT agent for the polymerization of AA as reported in Table 3.2.

Table 3.2 – Overview of the poly(acrylic acid) synthesized using different molar percentage of RAFT agent (%TRITT), including the molecular weight ($M_{n,PAA}$) and the dispersity index (Đ).

TRITT:AA	%TRITT	$M_{n,PAA}$ [(a)] (kg/mol)	$Đ$[(a)]
1:100	1	9	1.2
1:200	0.5	20	1.2
1:400	0.25	33	1.3
1:600	0.17	70	1.3
1:1000	0.1	N/A[(b)]	N/A[(b)]

[(a)]as determined *via* aqueous SEC, using poly(sodium acrylate) calibration.

[(b)]not measurable due to instrument limitations

Synthesis of poly(sodium acrylate) based networks

The achievement of poly(sodium acrylate) networks is based on a two step process: first the synthesis of PAA network, and thereafter the neutralization of the carboxylic acid group for the introduction of fixed charges.

As previously mentioned, it is important to first evaluate the impact of the RAFT agent on the network formation. Thus, a series of poly(acrylic acid) based networks were synthesized using acrylic acid as monomer, and *N,N´*-methylenebis(acrylamide) (MBA) as crosslinker. The molar ratio MBA:AA (expressed as percentage) defines the degree of crosslinking (*DC*) of the final network, according to Equation 2.24. Thus, a series of PAA networks having $DC = 1$ were synthesized using zero (FRP) and different molar percentage of RAFT agent. The reaction scheme is reported in Scheme 3.2, while more details about the reaction procedure are available in Section 7.3.

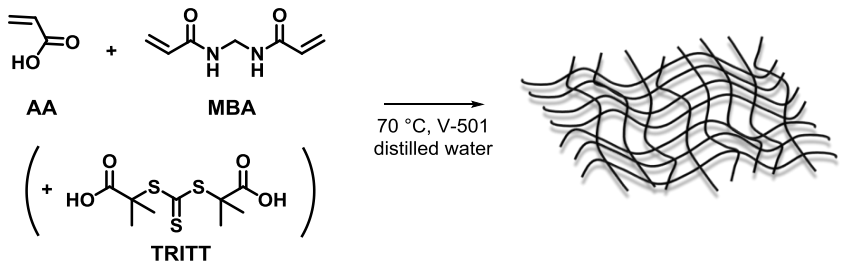

Scheme 3.2 – Reaction scheme for the synthesis of poly(acrylic acid) networks using N,N´-methylenbisacrylamide (MBA) as crosslinker and TRITT as RAFT agent. The polymerization was performed in water (20% w/w) at 70 °C in presence of V-501 as initiator, with and without the presence of the RAFT agent (TRITT).

Except for concentrations of RAFT agent higher than 0.25%, thus for the 1:100 and 1:200 molar ratio, the network formation was successfully achieved in all cases. The network formation is visualized in Figure 3.10, where each vial was twisted upside down after polymerization.

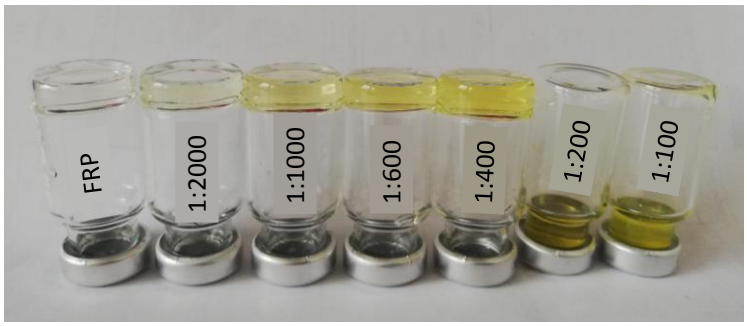

Figure 3.10 – Reaction mixture after the polymerization of AA (t = 16 h) in the presence of the crosslinking agent (MBA, 1 molar %) either via conventional free radical (FRP, first vial on the left side) or RAFT polymerization using different amount of RAFT agent (yellow solutions). The molar ratio of RAFT agent:monomer used is reported on the vials.

It is known that the higher the amount of RAFT agent, the lower is the degree of polymerization, and thus the lower is the molecular weight of the final polymer, as shown in **Chapter 2**, (Section 2.1.2, Equation 2.8). However, if the number of monomer units per chain decreases, also the average number of crosslinking points per chain decreases. For example, when considering the 1:100 molar ratio of RAFT agent to monomer, the maximum theoretical length of the polymer chain is approximately 100 monomer units. Hundred monomer units in turn means an average of one crosslinking agent per chain. Thus, the formation of a branched polymer rather than a polymer network is more likely to occur (refer to Figure 3.11), which is why no gelation was observed for the 1:100 molar ratio. A similar scenario occurred for the 1:200 molar ratio but not for the 1:400 molar ratio when targeting *DC* = 1.

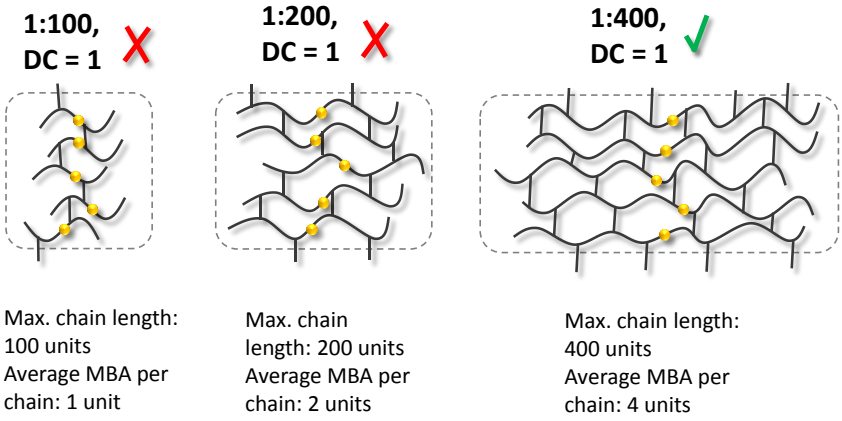

Figure 3.11 – Theoretical number of crosslinking points per chain when using a molar ratio (TRITT:AA) of 1:100 (left), 1:200 (middle) and 1:400 (right). The crosslinking points are represented by vertical solid lines, while the RAFT agent is represented by the yellow circle.

To further investigate this phenomenon, an additional network was synthesized using a molar ratio of 1:200 (RAFT agent:AA) but double the amount of crosslinker (*DC* = 2). Since the amount of crosslinking points per chain would be equivalent to the network synthesized with a 1:400 molar ratio and *DC* = 1, network formation is expected. After polymerization, the network was successfully achieved, indicating the necessity of a minimum number of crosslinking points per chain to yield the desired polymer network, as visualized in Figure 3.12. The theoretical minimum is achieved, in this case, when the ratio RAFT agent (mol %) to *DC* is equal to 0.25.

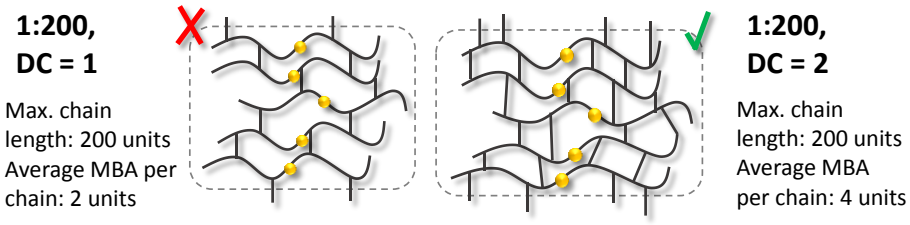

Figure 3.12 – Increased number of crosslinking points per chain when using a molar ratio (TRITT:AA) of 1:200 and DC = 1 (left) or DC = 2 (right). The crosslinking points are represented by vertical solid lines, while the RAFT agent is represented by the yellow circle.

Subsequently, all the networks having *DC* = 1 were extensively washed with water to remove the extractables and thereafter dried to calculate the relative amount of network obtained, as summarized in Table 3.3.

Table 3.3 – Summary of the PAA networks synthesized in the current section including the molar ratio of RAFT agent:AA, the molar % of TRITT, the % of network achieved and the relative reaction code.

TRITT:AA	%TRITT	Code	%Network
0 (FRP)	0	FRP-DC1	98
1:2000	0.05	RAFT005-DC1	98
1:1000	0.1	RAFT01-DC1	97
1:600	0.17	RAFT017-DC1	91
1:400	0.25	RAFT025-DC1	80

From Table 3.3 it is visible that increasing the amount of RAFT agent leads to a lower amount of network. This can be related to the gradual incorporation of the growing chains towards network formation in the case of the RAFT polymerization, as described in Section 3.1. Moreover, since at a higher concentration of RAFT agent the number of crosslinking points per chain is lower, it is more probable that a larger fraction of branched chains is not incorporated in the microstructure, lowering the overall yield.

In summary, it was observed that a minimum amount of crosslinking points per chain is necessary to achieve network formation. Since the amount of RAFT limits the maximum length of the polymer chains, and thus the amount of crosslinker per chain, the network formation was successfully achieved for concentration of RAFT agent lower than 0.25%. This is not a disadvantage as the RAFT agents are typically expensive, thus lowering the necessary amount will lower the impact of the approach on the cost of the material.

Subsequently, the networks were converted into superabsorbent hydrogels by introducing permanent charges upon neutralization of the carboxylic acid group. The presence of charges strongly influences the ability of the network to absorb water. The neutralization was performed by mixing the network with a solution of $NaHCO_3$ ($[NaHCO_3] = 0.1\ mol \cdot L^{-1}$, see Section 7.3). The ratio Na^+:AA, expressed as percentage, determines the degree of neutralization (*DN*).

In principle, the higher the degree of neutralization, and so the amount of charges, the higher is the degree of swelling, until the theoretical limit is reached (Manning condensation).[178] In order to estimate the effect of charges on the swelling ability, the **FRP-DC1** network was swollen using a different Na^+:AA ratio, targeting a 25%, 50%, 75% or, ideally, 100% degree of neutralization. The swellability was evaluated against a solution of sodium chloride ($[NaCl] = 10\ g \cdot L^{-1}$) after a swelling time of 16 h (overnight), as these are the condition in which the salt rejection will be performed. The degrees of swelling at equilibrium are reported in Figure 3.13.

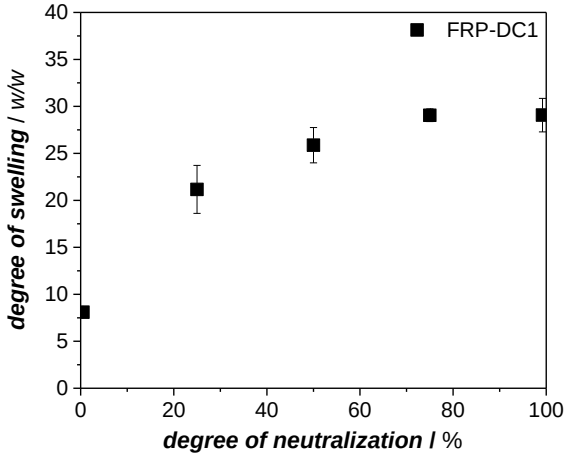

*Figure 3.13 – Influence of the degree of neutralization (DN) on the swellability. The effect was studied on **FRP-DC1** as representative network.*

As already observed in previous works,[9, 161] an increase in the swellability is visible up to a value of $DN \approx 75\%$, thereafter the increment is negligible. Thus, for the other PAA network

synthesized in the current section, only the degree of swelling ($Q_{eq,exp}$) before and after neutralization (targeted *DN* = 100%) is reported in Table 3.4. The values are expressed as mass ratio, according to Equation 2.22.

Table 3.4 – Summary of the degree of swelling, at DN = 0 or 100, for poly(acrylic acid) networks synthesizing via FRP or RAFT polymerization.

Network	Swelling (*DN* = 0)	Swelling (*DN* = 100)
FRP-DC1	7.1 ± 0.2	29.1 ± 1.8
RAFT005-DC1	8.5 ± 0.3	33.3 ± 0.3
RAFT01-DC1	9.3 ± 1.0	34.0 ± 1.0
RAFT017-DC1	10.5 ± 0.2	35.9 ± 0.4
RAFT025-DC1	15.0 ± 0.5	39.2 ± 1.0

As expected, the Q_{eq} is significantly higher (three times) in case of charged network compared to the analogous before neutralization, due to the presence of fixed charges along the polymer chains. The swelling degrees of the network synthesized *via* RAFT polymerization are higher compared to those made *via* FRP for both, the charged (*DN* = 100) and uncharged (*DN* = 0) state. In detail, the water absorbency experiments (Table 3.4) showed that the lower the amount of RAFT agent, the lower are the differences in the degrees of swelling between the samples synthesized using the FRP or the RAFT polymerization approach. Moreover, despite the low amount of RAFT agent used for the synthesis of **RAFT005-DC1** (0.05 molar %), the impact of the RAFT agent on the swellability is still evident (Table 3.4, second entry).

An increase in the swellability is associated with variation of the network microstructure, e.g. larger mesh size or lower number of entanglements and of highly crosslinked regions, in agreement with the initially proposed reaction pathway (Figure 3.2). However, while it was possible to elucidate the difference between the two approaches (FRP and RAFT) at the early stage of the polymerization (model system in Section 3.1), precise information about the microstructure are difficult to obtain, and cannot be assessed by swelling experiments. Moreover, due to the insolubility of complex materials such as polymer networks, the analytical methods available for the characterization of the material are limited.

Despite its insolubility, it is known that a polymer network is composed of more rigid (junction points) and more mobile (elastic chains) parts, and that the mobility of the chains is dependent on its length with longer chains being more flexible. It follows that, not all protons present within the microstructure are equivalent, and as such analyzing the dynamics of the network can be an efficient analytical tool to gain insights into the network microstructure. The analysis

of the dynamics of the network can be performed *via* ^{1}H NMR relaxometry, in particular upon T_2 measurements, since transverse relaxation decay (T_2) is sensitive to the mobility of the protons.[185] Moreover, this possibility was demonstrate also for poly(electrolyte) networks in previous works.[9, 160] Thus, the RAFT-mediated network as well as the FRP reference were analyzed *via* ^{1}H NMR relaxometry, adopting a similar procedure to the one reported in the literature (refer to Section 7.2),[160] and the results are compared in Figure 3.14.

More rigidity leads to faster relaxation decay and it is usually associated with a higher degree of crosslinking. Here, despite the same amount of crosslinker was used for each network (*DC* = 1), the relaxation decay (Figure 3.14, left) is faster for the network synthesized *via* FRP compared to those synthesized in the presence of the RAFT agent, indicating a more crosslinked structure for the FRP sample. Moreover, differences in rigidity are observed also within the RAFT polymerized samples. As noticeable from the deconvoluted decay plot (Figure 3.14, right), the higher the amount of RAFT agent, the higher is the contribution of the mobile parts to the relaxation decay.

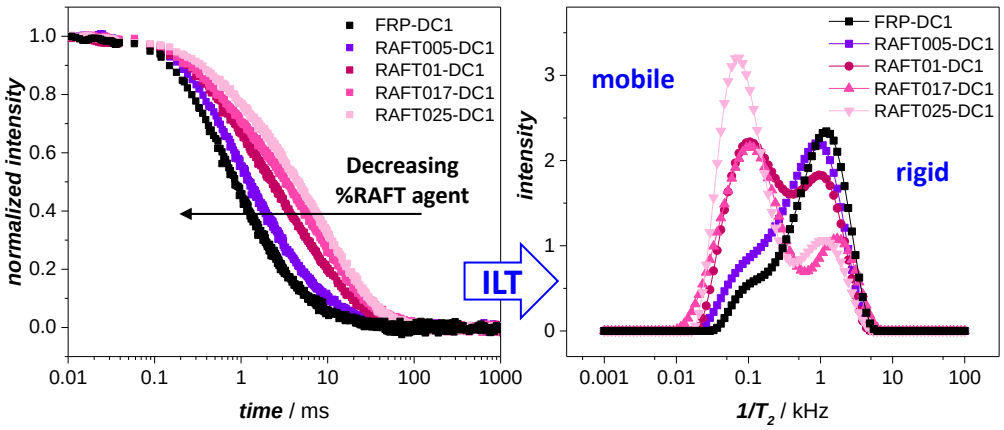

Figure 3.14 - T_2 relaxation curve (left) and deconvoluted decay, using the Inverse Laplace Transformation, (ILT, right) for PSA hydrogels having DC = 1 and synthesized either via FRP or RAFT polymerization using different amount of RAFT agent (see legend).

As observed during the study of the crosslinking process (Section 3.1), in the presence of larger amount of RAFT agent, the chains have a lower amount of crosslinking point per chains, and a higher amount of crosslinking points occur in solution (before gelation), due to the reduced molecular weight of the chains. Thus, the networks is most likely to present a less densely knotted structure, and a higher amount of dangling ends. Independently from the synthetic approach, each network presents a certain level of heterogeneity in the mobility indicating the presence of structural defects.

Lastly, the mechanical properties of the synthesized networks were tested to verify whether the RAFT agent has a negative impact to the overall rigidity of the network. For this reason, rheological measurements were performed (according to the procedure described in Section 7.2) to obtain: the complex modulus (G^*), which indicates the overall resistance of the hydrogel to deformation, and the loss factor tan(δ), which indicates the loss in the elastic behavior due to viscous contributions (e.g. dangling ends). Accordingly, low value of tan(δ) are desirable.
The samples were measured in the "*as prepared*" state (no purification), using the strain-controlled rheometer Ares G2 and disk-shaped specimens. The measurements were performed in the linear viscoelastic regime (LVE), where G^* is independent from the applied strain (constant values, see Section 7.2). The reproducibility of the method is demonstrated in Section 7.2, while herein the absolute value of the complex modulus ($|G^*|$) at 1 rad/s and 0.1% strain was selected as representative quantity to compare different samples with each other.
In order to evaluate the effect of the RAFT agent on the mechanical properties of the network, a stock solution of monomer, crosslinker and solvent (DC = 1, 20% w/w monomer in distilled water) was prepared and divided in vials. Afterwards, different amounts of TRITT and initiator (molar ratio of TRITT:initiator = 1:0.15) were added and the samples placed at 70 °C overnight to perform the crosslinking reaction, and achieve the desired networks. The rheological properties of the synthesized networks are reported in Figure 3.15.

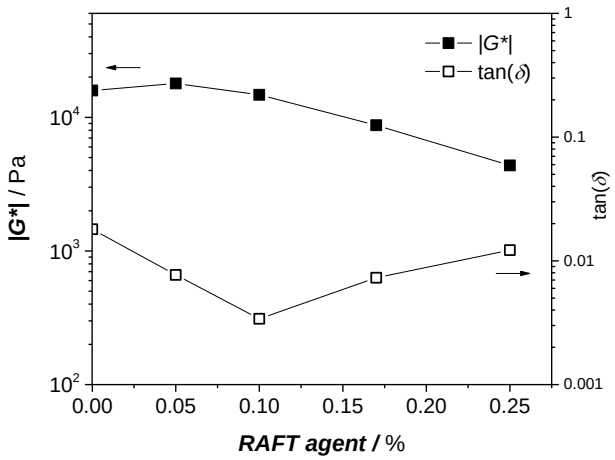

Figure 3.15 – Absolute value of the complex modulus $|G^*|$(filled symbols) and the loss factor (tan (δ)) (empty symbols) for poly(acrylic acid) hydrogels in the "as prepared" state, synthesized via FRP (0% RAFT agent) or RAFT polymerization using different molar percentage of RAFT agent, as indicated along the x axis.

The value of $|G^*|$ is similar for the PAA networks synthesized using 0, 0.05 and 0.1 molar % of RAFT agent, indicating that at these concentrations the presence of RAFT agent does not negatively affect the mechanical properties of the network. However, the values of $|G^*|$ decreases from $\approx 1.5 \cdot 10^4$ Pa to $\approx 5 \cdot 10^3$ Pa when higher percentage of RAFT agent (0.25 molar %) were

employed (Figure 3.15), while the values of the loss factor (tan (δ)) are similar in all samples and within the expected range for hydrogel (0.01-0.1).[186] The decrease of the $|G^*|$ values are ascribed to the higher percentage of soluble fractions still present in the specimens, as the measurements were performed in the "*as prepared*" state. Accordingly, the reduced mechanical properties are not necessarily related with the microstructure of the network but more with the higher percentage of extractables.

Overall, the swelling tests, the relaxation decay and the mechanical properties indicate a more rigid structure for the FRP samples, partially arising from termination reactions but also from a higher number of crosslinking points per chain. Accordingly, increasing the amount of RAFT agent leads to network with higher mobility and higher swellability. In order to investigate whether this is a positive feature for the application, a library of polymer networks having different degree of crosslinking was synthesized.

3.2.2 Effect of the Degree of Crosslinking

Herein a variety of PSA networks having different degrees of crosslinking (*DC* = 0.6 – 5) was synthesized in order to vary the macroscopic properties of the networks, e.g. swellability and rigidity, before performing the salt rejection experiments. More specifically, a series of poly(acrylic acid) networks having a *DC* equal to 0.6, 1.5, 3 and 5 mol% was synthesized *via* FRP or RAFT polymerization using either 0.1 or 0.25 mol% of TRITT. The different degrees of crosslinking are stated in the code of the considered poly(sodium acrylate) network. For example, **FRP-DC3** indicates a network synthesize *via* free radical polymerization with a *DC*= 3. After network formation, the swelling degree for the fully charged network (*DN* = 100%) against an aqueous solution of 10 g·L^{-1} of NaCl was investigated, as depicted in Figure 3.16.

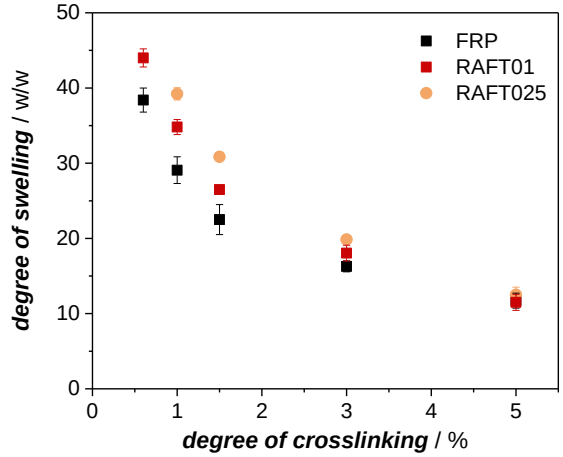

Figure 3.16 – Degrees of swelling, expressed as mass ratio, for poly(acrylic acid) hydrogels presenting different degree of crosslinking (DC) and synthesized via FRP polymerization (black symbols) or RAFT polymerization using 0.1 (red symbols) or 0.25 (orange symbols) molar percentage of RAFT agent.

The degrees of swelling for three different series of PSA networks are plotted in Figure 3.16. In each series, the degrees of swelling decrease with increasing the degree of crosslinking (DC). Starting from the FRP series (Figure 3.16, black symbols), the degree of swelling (Q_{eq}) varies from ~38 to 12 w/w ratio, moving from *DC* = 0.6 to 5 mol%, in agreement to previously reported literature data and to the higher amount of junction points.[9, 161] The networks containing 0.1 mol % of RAFT agent (Figure 3.16, red symbols) present higher Q_{eq} for *DC* = 0.6, 1 and 1.5 mol% compared to the FRP samples (increment of 10-20%), whereas the values are rather similar at *DC* = 3 mol% and identical for *DC* = 5 mol%. Moreover, for a fixed degree of crosslinking (e.g. *DC* =1.5 mol%) the swellability increases when higher concentration of RAFT agent were used during the synthesis. In detail, the value of Q_{eq} varied from ~20 to 30 for 0 and 0.25 mol% of RAFT agent. For the PSA networks synthesized using 0.25 mol% of RAFT agent (Figure 3.16, orange symbols), the differences between the swelling experiments are significant up to *DC* = 3 mol%, while they are negligible for *DC* = 5 mol%.

Subsequently, the networks were analyzed *via* ^{1}H NMR relaxometry, as shown in Figure 3.17 In detail, the samples presenting 0.1 (top) and 0.25 mol% (bottom) of RAFT agent are compared with the analogous FRP sample having the same targeted *DC*.

Similar to the swelling experiments, the differences in mobility are pronounced until *DC* = 3 and 5 mol% when using 0.1 and 0.25 molar percentages of RAFT agent, with the RAFT-mediated network being more mobile than the analogous FRP sample (Figure 3.17). As previously discussed, an increase in the mobility is associated to a less densely crosslinked structure. Moreover, it is observed that for high degree of crosslinking the networks present a similar relaxation decay. It follows that, the difference in mobility associated with lower amount of crosslinking points per chain becomes negligible when higher percentage of crosslinker are used during the synthesis.

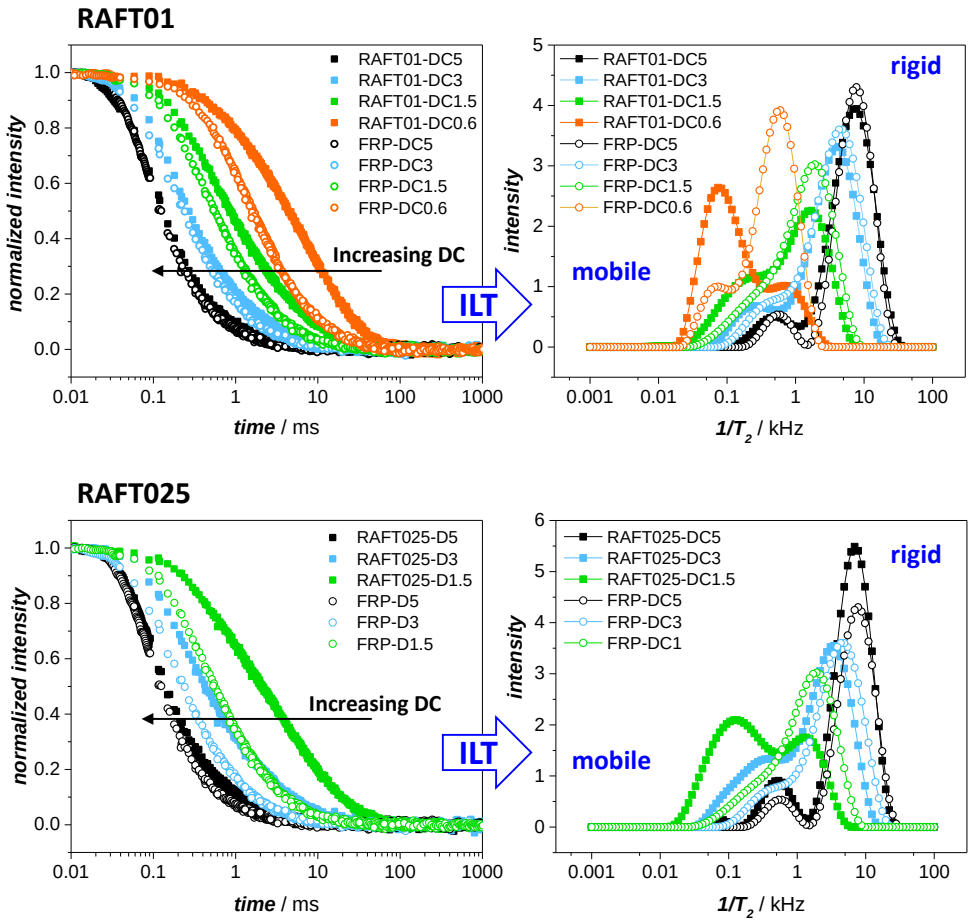

Figure 3.17 – Left: T_2 relaxation curve (left) and deconvoluted decay using the inverse Laplace Transformation, (ILT, right) for poly(acrylic acid) hydrogels synthesized via RAFT polymerization (filled symbols) using 0.1 (top) or 0.25 (bottom) mol % of TRITT. In both cases the results are compared with an analogous network (same DC) but synthesized via FRP (empty symbols).

As a final characterization, the mechanical properties of the networks were tested *via* rheological experiments. According to the ^{1}H NMR relaxometry measurements, the rigidity of the networks is expected to increase for more rigid elastic chains, thus for networks with higher degrees of crosslinking. The rheological data obtained for the poly(acrylic acid) hydrogels synthesized using a concentration of 0.10 mol% RAFT agent are displayed in Figure 3.18, and compared to the analogous FRP samples. Here, the value of $|G^*|$ increase from $\approx 1 \cdot 10^4$ Pa to $\approx 5 \cdot 10^4$ Pa when moving from *DC* = 0.6 to 5 mol%, regardless the type of polymerization used during the synthesis. Moreover, for *DC* = 0.6 mol% the $|G^*|$ of the poly(acrylic acid) network synthesized *via* RAFT polymerization (red symbol) is lower compared to the FRP analogous (black symbol), with values equal to $\sim 8 \cdot 10^3$ Pa to $\sim 1.1 \cdot 10^4$ Pa for RAFT and FRP networks, respectively. The differences in the mechanical properties are negligible at the other degrees of crosslinking tested.

The higher rigidity is associated with the increased number of constrains (junction points) introduced by the higher concentration of crosslinking agent when moving from left to right of the graph reported in Figure 3.18. Lastly, the value of the loss factor (tan(δ)) are smaller in case of RAFT mediated network formation. In principle, this indicates a lower dissipation of energy, thus a more ideal behavior of the networks in case of RAFT-mediated polymerization, however the differences are minimal and no final conclusion about homogeneity can be made by solely evaluating the single values.

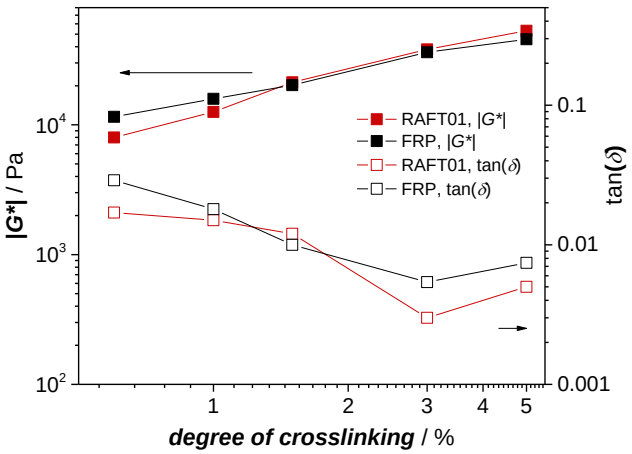

Figure 3.18 – Absolute value of the complex modulus $|G^*|$(filled symbols) and the loss factor (tan (δ)) (empty symbols) for networks synthesized either via FRP (black) or RAFT polymerization using 0.10 mol% of TRITT (red).

In summary, for the studied system, increasing the degree of crosslinking minimizes the differences in swellability, mobility and mechanical properties between samples obtained *via* FRP compared to those obtained *via* RAFT polymerization. Moreover, for a fixed degree of crosslinking, the differences in the abovementioned properties were more pronounced with increasing the amount of RAFT agent used during the synthesis.

In order to evaluate how this affects the desalination performances, it is necessary to perform salt rejection experiments.

3.3 Salt Rejection Experiments

Salt rejection experiments serve as preliminary data to evaluate the performance of a given network during desalination (as explained in Section 2.4.2). The pioneering work of Höpfner *et al.* showed that a high degree of crosslinking is beneficial for the salt rejection as it increases the charge density. On the other hand, a low *DC* reduces the energy necessary to recover the water from inside the hydrogel, and the amount of material needed and increases the amount of water that can be collected at the end of each cycle.[9] In a complementary work of Arens *et al.*, different polymer architectures have been investigated. The results showed that interpenetrating networks and networks presenting dangling ends led to an improved salt rejection ability.[161]

Here, a library of networks synthesized *via* FRP and RAFT-mediated polymerization were tested to evaluate whether the synthesis has a beneficial impact on the charge distribution density, and thus on the salt rejection ability. The experiments were performed using a Q_{rel} = 2 (determined from Equation 7.5), so that the brine is equally divided between the gel and the supernatant phase. The amount of dry network necessary to achieve these conditions was calculated from Equation 7.6 (refer to **Chapter 7**, Section 7.2). Next, the poly(sodium acrylate) network in its charged state (targeted *DN* = 100%) was allowed to swell overnight in salt water, before analyzing the supernatant phase. The expectation is that, as a result of the salt partition, the supernatant phase is enriched in salt content as qualitatively described by the Donnan effect.[187] Independently from the network microstructure (mean-field model), the performance of different gels can be compared according to the percentage of salt rejected as follows:

$$\%\ salt\ rejected\ (SR) = \frac{c_{s,final} - c_{s,0}}{c_{s,0}} * 100 \qquad (3.1)$$

where $c_{s,final}$ is the concentration of salt in the supernatant phase after swelling, and $c_{s,0}$ is the concentration of the initial salt solution used for the experiments. For consistency with previous works, the initial salt concentration was equal to 10 $g \cdot L^{-1}$ of NaCl in water. [9, 161] The salt concentration after swelling experiment is evaluated by conductivity measurements, as detailed in Section 7.2 (**Chapter 7**). In general, the salt rejection is expected to increase for high charge density,[176] thus for low Q_{eq}, and high *DC*.

Firstly, the series of networks synthesized in Section 3.2.1 having the same degree of crosslinking (*DC* = 1 mol%) but different amount of RAFT agent was tested, and the results are compared in Table 3.5.

Table 3.5 – Percentage of salt-rejected (% SR) for a series of poly(sodium acrylate) networks having DC = 1 but a different amount of RAFT agent. For clarity, the values of the swelling at equilibrium are reported (Q_{eq}).

Network	% RAFT agent	%SR	Q_{eq}
FRP-DC1	0	11.9	29.1 ± 1.8
RAFT01-DC1	0.1	11.9	34.0 ± 1.0
RAFT017-DC1	0.17	12.6	35.9 ± 0.4
RAFT025-DC1	0.25	12.2	39.2 ± 1.0

In terms of absolute values, the percentage of salt rejected is ≈12% for all networks (Table 3.5). However, it has to be mentioned that the salt rejection ability was expected to be higher for sample with lower Q_{eq}, as, assuming an identical charge distribution, the charge density is higher.[176] Thus, when looking at the first two entries (**FRP-DC1** and **RAFT01-DC1**), even though the salt rejection percentage is identical, the network synthesized *via* RAFT polymerization is a better candidate for the final application. The same 12% of salt rejected in fact is associated to a higher Q_{eq}, which means that less material is needed for an equivalent desalination of the same amount of salt water in case of **RAFT01-DC1**. An identical situation is visible for the last two entries, where even less material would be necessary according to the higher values of Q_{eq}.

Afterwards, the library of PSA networks synthesized *via* FRP or RAFT polymerization employing 0.1 or 0.25 mol% of TRITT were analyzed. For an easier comparison of the data, the %SR is plotted against the Q_{eq}, as depicted in Figure 3.19. In the same graph, the results are compared to theoretical values obtained from the Donnan theory (Figure 3.19, dashed lines).[176, 183] The experimental details and the calculation of the theoretical values are reported in Section 7.2.

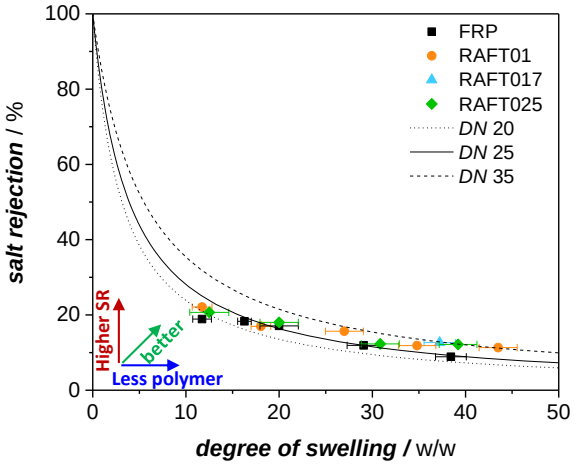

Figure 3.19 – Salt rejection experiments for networks synthesized via FRP or RAFT polymerization. The experimental results (symbols), expressed as percentage of salt rejected, are compared to theoretical values obtained from the Donnan theory (lines).

The salt rejection experiments reported in Figure 3.19 shows that no major differences are observed between the networks, independently from the selected synthetic approach except for few data points. In detail, small differences are noticed at higher degree of swelling ($Q_{eq} \approx 35–40$), where the networks synthesized *via* RAFT mediated polymerization show an improvement in the salt rejection performance. The absolute %SR are approximately 5% higher with respect to the FRP samples. This increment can arise either from a better charge distribution or from a higher content of dangling ends, already proven to be beneficial to the salt rejection, in case of the RAFT-mediated network. However, from the salt rejection experiments it is not possible to discriminate between the two cases.

The dashed lines in Figure 3.19 represent the theoretical values as calculated form the Donnan theory. In detail, each line correspond to a membrane with a different degree of neutralization, as stated in the legend. Accordingly, from the comparison between experimental with theoretical data, it results that the synthesized hydrogels behave similarly to a membrane having a degree of neutralization of 25 for most of the samples, and of *DN* = 35 for the networks that showed a better salt rejection (RAFT at high degree of swelling). In each case, the obtained degree of neutralizations are lower than the theoretical value. The deviation can be ascribed to the Manning condensation and thus to the fact that not all the carboxylic acid groups can be neutralized.[178]

3.4 Summary

In the current chapter, the influence of the RAFT agent on the network formation was examined in detail. It resulted that the addition of a RAFT agent to the crosslinking process of a mono- and a bifunctional monomer led to remarkable differences at early stage of the copolymerization. In detail, the presence of the RAFT agent led to the formation of well-defined polymer chains ($Đ$ = 1.3), a better diffusion of the chains in the reaction mixture, and a gradual incorporation of chains towards gelation, which occurred at ~75% conversion, differently to the conventional FRP where the gelation was observed already at ~30% conversion.

Concerning the macroscopic properties, the RAFT-mediated network presented a higher swellability and mobility of elastic chains within the network microstructure compared to the FRP networks. In detail, for a given *DC*, the differences between the two set samples (FRP and RAFT) decreased for lower molar percentage of RAFT agent, while for a fixed amount of RAFT agent (e.g. 0.1 mol%), the differences became negligible at high degree of crosslinking (e.g. *DC* = 3 mol%). Independently from the synthetic approach, the mobility of the networks presented a certain level of heterogeneity according to the ^{1}H NMR relaxometry measurements. However since no ideal network was reported in the literature so far, there is no indication on how its relaxation decay should appear, and more fundamental research is necessary in this direction.

Notably, the studied macroscopic properties (e.g. swellability, mobility and rigidity) are the result of the average properties of the whole sample, and do not give precise information on the presence, the identity and the amount of defects within the microstructure. For this purpose, the idea of tracing, in the final network, the presence defects occurred during the synthesis is proposed in the next chapters as advanced synthetic and analytical platform for the identification and quantification of structural defects.

4

In-depth Investigation on the *para*-Fluoro–Thiol Reaction

One possibility for achieving the traceability of defects consists in the use of the recently emerging *para*-fluoro–thiol reaction (PFTR) as ligation during the crosslinking process for the synthesis of networks *via* the end-linking approach. The location of the fluorine atoms solely at the crosslinking points indeed arises the possibility to identify and quantify the presence of unreacted moieties *via* ^{19}F NMR spectroscopy.

In order to achieve the final goal however, it is important to understand whether the reaction is suitable for the purpose. For this reason, particular attention was given to potential side reactions, as they will translate in structural defects during network formation. The side reactions investigated involved multiple substitutions on the fluorinated aromatic group, disulfide bond formation and potential interference of specific functional groups, for instance the carboxylic acid group to mimic the acrylic acid pendant moiety. Furthermore, the effect of the solvent polarity and the type and the amount of base, from equimolar to under-stoichiometric amounts, on the nucleophilic substitution was considered. As the proposed crosslinking reaction (PFTR) should be of broad application, the reaction was studied using different thiol precursors spanning a wide range from small molecule to polymeric thiol derivatives. For a better understanding of the reaction events, as well as for assessing the rate coefficients of the main (PFTR) and

side (disulfide) reactions, the experimental data were complemented by kinetic Monte Carlo (*k*MC) simulations.

All the listed reaction conditions were investigated using a simplified model system, i.e. a trifunctional linker and a monofunctional thiol (star shape architecture), to avoid characterization limits associated with the inherent insolubility of polymer networks.

Parts of this chapter are adapted or reproduced from Ref. [188] with permission from The Royal Society of Chemistry.[188] The project was supervised by Prof. Dr. Leonie Barner.

Parts of this chapter are adapted or reproduced from Ref. [189] with permission from The Royal Society of Chemistry.[189] The *k*MC simulations were performed by Lies De Keer (Ghent University). The project was supervised by Prof. Dr. Leonie Barner and Prof. Dr. Dagmar R. D´Hooge.

Parts of this chapter are adapted or reproduced from Ref. [190] with the permission from John Wiley & Sons.[190] Fabian Blößer (Queensland University of Technology, QUT) was involved in the development of the concept and in the scientific discussions. The project was supervised by Prof. Dr. Leonie Barner and Prof. Dr. Christopher Barner-Kowollik.

4.1 Small Molecule Thiol Derivatives

4.1.1 Model Reaction

First, an overview of the analytical techniques used to investigate the progress of the *para*-fluoro–thiol reaction (PFTR) is presented on a model system composed of a three-armed fluorinated linker and a monofunctional thiol (dodecanethiol, aliphSH). The model system is based on a 3+1 reaction to mimic at best the chemistry of the crosslinking points within the network, while avoiding characterization limits arising from the insolubility of the network. Since a previous literature report showed that multiple substitutions have occurred when ester bonds were present in the vicinity of the fluorinated group,[69] the fluorinated linker used in the current study was explicitly designed without any ester bonds (**3PFB,** Scheme 4.1).

As depicted in Scheme 4.1 the thiol (3 eq.) was reacted with the fluorinated linker (**3PFB**, 1 eq.) in THF. In order to start the reaction, 1,8-diazabicyclo[5.4.0]undec-7-ene (DBU, 3 eq.) was added to the reaction mixture. The reaction was carried out at ambient temperature, using an initial concentration of functional groups equal to 0.15 mol·L^{-1}. At t = 0 and t = 5 min, aliquots of the reaction mixture were analyzed *via* ^{19}F and ^{1}H NMR spectroscopy, size-exclusion chromatography (SEC) and high-resolution electrospray ionization mass spectrometry (ESI-MS) to confirm the proposed reaction pathway. The reaction is stopped by neutralizing the base with an excess of benzoic acid (BA, 6 eq).

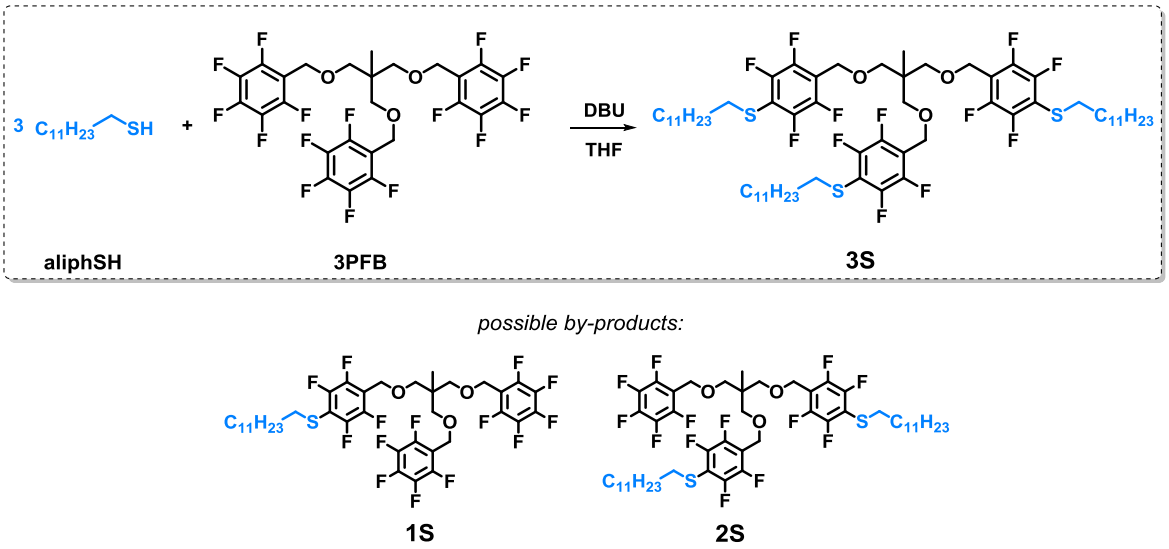

*Scheme 4.1 – Reaction scheme for the para-fluoro–thiol reaction (PFTR) between dodecanethiol (aliphSH) and a fluorinated three-armed linker (**3PFB**). Top: The main reaction is displayed together with the targeted trisubstituted product (**3S**). Bottom: Possible by-products such as the mono- and disubstituted linker (**1S** and **2S**, respectively).*

At first, the crude mixture was analyzed *via* SEC and ESI-MS to identify the number and type of species formed during the reaction and to perform an internal calibration of the SEC for further kinetic studies presented in Section 4.1.2. The SEC traces as well as the ESI-MS spectrum are depicted in Figure 4.1. At t = 0, the thiol and the linker could be unambiguously assigned to the SEC traces with aliphSH appearing at lower molecular weights and **3PFB** at higher molecular weights. After 5 min of reaction, the peaks corresponding to the thiol and the linker decrease in intensity, and simultaneously, new peaks arise at higher molecular weights indicating the formation of various PFTR adducts. ESI-MS analysis of the crude reaction mixture after t = 5 min was then conducted in order to identify the products. The main products were identified as $[M+Na]^+$ adducts. In the spectrum (Figure 4.1), the mono- (1S), bi- (2S) and trisubstituted (3S) linker could be identified. In particular, the targeted $[3S+Na]^+$ appears at m/z(exp) = 1229.5774, which is in excellent agreement with m/z (theo) equal to 1229.5753 (Δm = 0.0021). A comparison of the experimental and simulated spectra for each adducts is reported in Appendix (Figure 8.1).

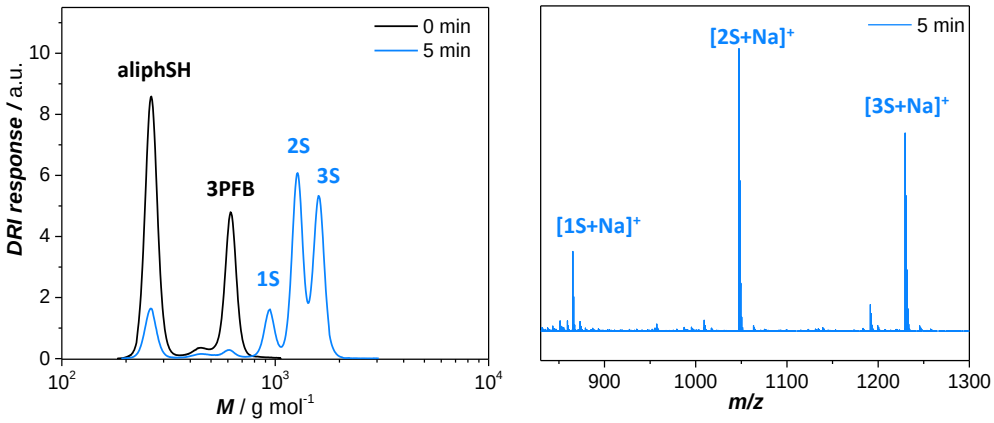

Figure 4.1 – Left: SEC traces of the crude reaction mixture at t = 0 (black) and t = 5 min (blue). Right: (+)ESI-MS spectrum of the reaction after 5 min is depicted. The peak were assigned according to the products shown in Scheme 4.1. The figure is adapted from Ref. [188] with the permission of The Royal Society of Chemistry.

Hence, in the selected sample, the most abundant peak in the SEC trace (Figure 4.1, left, blue line) is the one corresponding to the disubstituted linker (**2S**), suggesting that reaction times longer than 5 min are necessary for the conversion to be quantitative. However, due to the excellent agreement between the experimental and the simulated spectra (see Appendix, Figure 8.1), the ESI-MS spectrum shows that only one thiol is present on each fluorinated aromatic ring, excluding the presence of multiple substitution on the same moiety. Nonetheless, neither

the SEC nor the ESI-MS spectrum gave precise information on the exact conversion or on the exact position of the aromatic ring (e.g. *para*) the nucleophilic attack took place.

In order to further elucidate the above-mentioned reaction characteristics, ^{1}H NMR and ^{19}F NMR spectra were recorded. For an accurate assignment of the resonances, an aqueous work-up of the crude mixture was performed to remove the excess of benzoic acid (BA), used for neutralizing the base, and the DBU-BA salt.

In the ^{1}H NMR spectrum a resonance shift from δ = 2.68 ppm to δ = 2.95 ppm was observed for the protons adjacent to either the thiol group or to the newly formed C_{arom}–S bond (Figure 4.2, topmost and bottommost panels, labeled in magenta). In a similar fashion, the protons belonging to the CH_2 group in β-position with respect to the sulfur presents a shift in their resonance from δ = 1.67 to 1.56 ppm before and after reaction (refer to Figure 4.2). The resonances of the other protons of the thiol derivative did not vary significantly due to their distance in respect to the fluorinated ring.

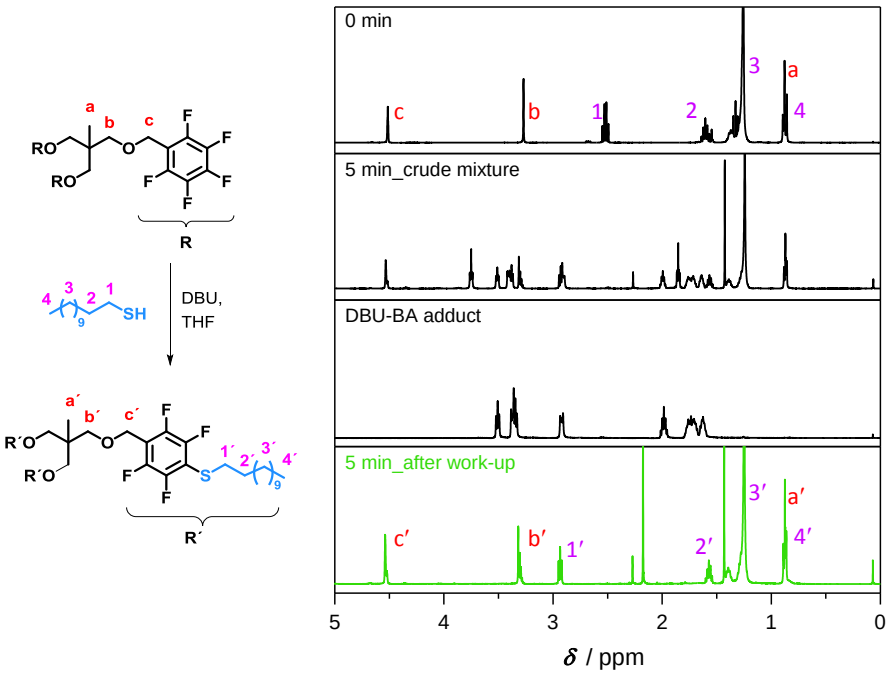

Figure 4.2 – ^{1}H NMR spectra ($CDCl_3$*, 400 MHz) of the reaction mixture at t = 0 and t = 5 min. The spectrum after 5 min of reaction is shown as crude reaction mixture (second panel) and after purification (bottom panel). Additionally, the ^{1}H NMR spectrum for the DBU-BA adduct is reported as guideline for the peak assignment. Mainly the shift of the resonance identified as **1** from δ = 2.68 ppm to δ = 2.95 ppm implies the success of the PFTR. The figure is adapted from Ref. [188] with the permission of The Royal Society of Chemistry.*

More structural insights were gained when ^{19}F NMR spectra were recorded. A comparison of the ^{19}F NMR spectra of the 3PFB linker before and after PFTR is depicted in Figure 4.3. In

detail, the resonances for the *ortho*-, *para*-, and *meta*-fluorine atoms of the pristine **3PFB** linker appear at δ = −143.7, −154.2 and −162.3 ppm, respectively.[69] After PFTR, the intensity of the previously mentioned resonances decreased, while new resonances at δ = −134.7 (*m*′) and δ = −143.3 (*o*′) ppm appeared, which can be ascribed to those of the new *ortho*- and *meta*-fluorine atoms. Their chemical shifts are in agreement with literature-reported values, confirming that the substitution has taken place at the *para*- position.[69] The variation in the chemical shifts of the new resonances is due the replacement of an electron withdrawing group (i.e., a fluorine atom) by an electron donating group (i.e., the sulfur atom)[115]. Moreover, as for protons, the fluorine resonances can be quantified, allowing an accurate calculation of the conversion.[115] At any reaction time, the conversion is obtained by comparing the integral of the resonances before and after reaction as follows:

$$conversion\ (\%) = \frac{0.5m'}{0.5m' + p} * 100 \tag{4.1}$$

The resonances of the parent linker need to be in a ratio 2:1:2 (*o:p:m*), while those of the product in a ratio 1:1 (*m*′:*o*′). Importantly, one of the main advantages of using ^{19}F NMR spectroscopy is that the resonances do not overlap with those arising from the protons of other compounds present in the reaction mixture such as solvent, base or polymer backbone, thus no work-up is necessary when recording ^{19}F NMR spectra.

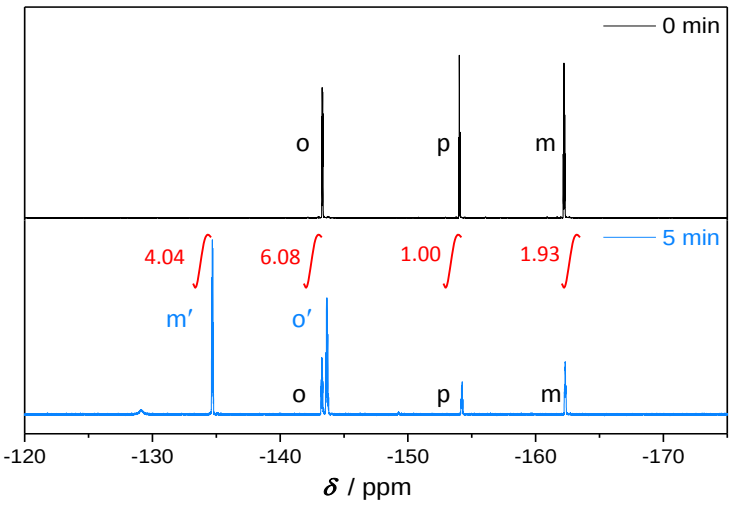

Figure 4.3 –^{19}F NMR spectra ($CDCl_3$*, 377 MHz) of the fluorinated aromatic ring before (black) and after (blue)PFTR. Before reaction (black, **3PFB**) the resonances for the meta- (m), para- (p) and ortho- (o) fluorine atoms are present. After PFT reaction (blue) the new ortho- (o′) and meta- (m′) resonances appear. The comparison of the intensity of the resonances before and after reaction is used for calculating the conversion according to Equation 4.1. The figure is adapted from Ref. [188] with the permission of The Royal Society of Chemistry.*

4.1.2 Kinetic Study

General remarks

Given the same reaction, two important parameters that influence the conversion are the reaction time and the concentration of the species participating to the reaction. This is because the reaction rate (R_{PFTR}) is directly proportional to the rate coefficient (k_{PFTR}) of the reaction and the concentration of the species involved (thiol and PFB groups).

$$R_{PFTR}(t) = k_{PFTR}[SH][PFB] \tag{4.2}$$

Thus, for higher concentrations the reaction is faster, leading to higher conversion in shorter reaction times. Similarly, as the conversion increases over time, the longer the reaction time, the higher the conversion.

The influence of time and concentration is briefly presented for the model reaction. As before, the molar ratio between the starting materials and the base is kept equal to 1:1:1 (SH:PFB:base). Aliquots of the reaction mixture were taken at multiple time intervals and the base was removed by passing the crude mixture through a short column of basic alumina prior to SEC analysis. The conversion of the PFTR reaction was calculated from the recorded ^{19}F NMR spectrum according to Equation 4.1. The corresponding SEC traces for PFTR performed using an initial concentration of thiol groups equal to 0.15 mol·L^{-1} are depicted in Figure 4.4 (left). Similarly, the effect of the concentration was evaluated after a reaction time of 5 min for different concentrations of functional group, e.g. $[SH]_0$ = 0.075 mol·L^{-1}, 0.15 mol·L^{-1}, 0.30 mol·L^{-1} and 0.50 mol·L^{-1} as shown in Figure 4.4 (right).

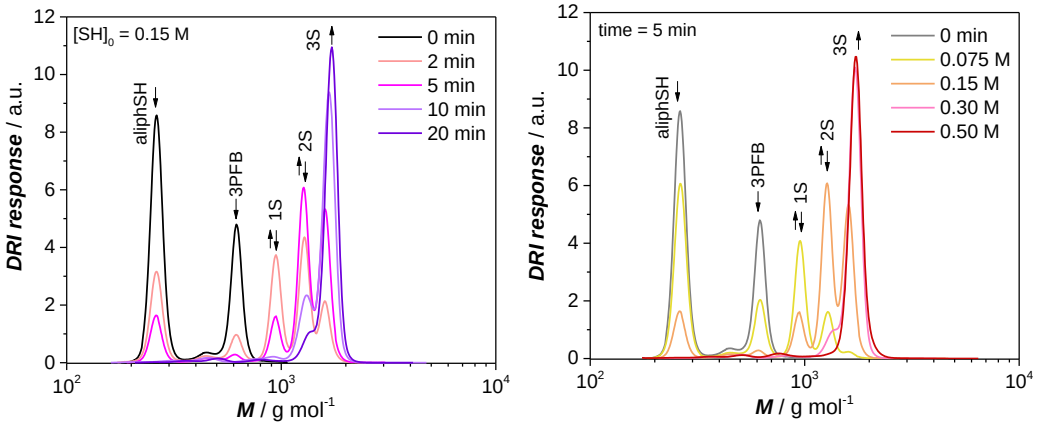

Figure 4.4 – Influence of time and concentration on the PFTR performed using an initial molar ratio of SH:PFB:DBU equal to 1:1:1. Left: The initial concentration is equal to 0.15 M in THF and the time is reported in the legend. Right: The reaction time is set to 5 min and the different concentrations tested are reported in the legend. The figure is adapted from Ref. [188] with the permission of The Royal Society of Chemistry.

The effect of time and concentration can be seen not only in terms of functional group conversion but also as product distribution in the SEC traces (refer to Figure 4.4). At longer reaction times or higher concentrations, the peak with the highest intensity corresponds to the trisubstituted product (**3S**). Accordingly, the peaks corresponding to **1S** and **2S** disappear faster at higher concentrations. In each case, the reaction starts with the appearance of the monosubstituted species, followed by an increase of the di- and trisubstituted species, parallel to a decrease of the **1S**. Eventually, the amount of the **2S** decreases as all intermediates are transformed in the **3S** species towards the end of the presented mechanistic study.

During network formation, reactions are usually performed at high concentrations, which means that a fluorinated aromatic group is more likely surrounded by more than one equivalent of thiol at a time. Thus, it is important to investigate the reaction outcome when mimicking such conditions in order to exclude potential side reactions. Accordingly, PFTR was carried out using an excess of thiol compared to the PFB groups (molar ratio of 1:1.5:1.5 = PFB:SH:base) in THF and at ambient temperature. In the presented case, the initial concentration of PFB groups was equal to 0.50 mol·L^{-1} to mimic the high concentration of both species during network formation. After 1 h, ^{19}F NMR spectrum and SEC trace are recorded in order to evaluate the presence of multi-substituted species. The results are compared in Figure 4.5.

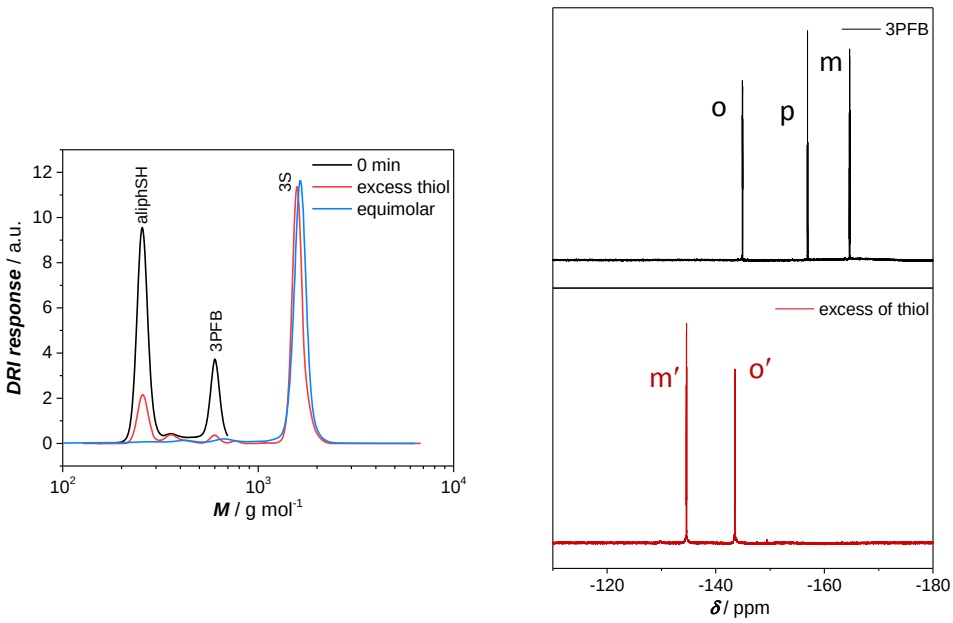

Figure 4.5 – SEC (left) and ^{19}F NMR spectra (right, $CDCl_3$*, 377 MHz) before and after PFTR employing 3PFB and either an equimolar (blue) or an excess (red) of aliphSH. The molar ratio of SH:base is kept equal to 1:1 and the $[PFB]_0$ = 0.5 M in both cases. The reported data refer to the analysis of the reaction mixture after 1 h of reaction time. The figure is adapted from Ref. [188] with the permission of The Royal Society of Chemistry.*

Here, the ^{19}F NMR spectrum, recorded after PFTR is performed using an excess of thiol (Figure 4.5, bottom), shows the typical resonances for PFTR (*o′* and *m′*) and a ratio 1:1 between the new *ortho*- and the *meta*- resonances. This indicates that no additional atoms were involved in the reaction except for the fluorine atoms in *para*- position. As support for this assumption, the SEC traces show no peak at a higher molecular weight than the one corresponding to the **3S** product. The results obtained from ^{19}F NMR spectroscopy and SEC analysis are of high relevance as it proves that the pentafluoro benzyl (PFB) group is also a suitable functional group for a selective PFTR, regardless the presence of an oxygen nearby, as no side reactions occurred.

Assessing the rate coefficient via kinetic Monte Carlo (kMC) simulations

In this subsection, the *para*-fluoro–thiol reaction was characterized both experimentally and by kinetic Monte Carlo (*k*MC) simulations in order to assess the rate coefficient. Briefly, *k*MC is a computer simulation based on a stochastic method. During the simulation, a representative number of molecules is followed throughout the studied process, and each reaction event is selected according to the reaction probability. For numerical accuracy, it is important to have a sufficiently high number of initial molecules.[191]

Mechanistically, the PFTR begins with the deprotonation of the thiol by a base generating a reactive thiolate. At this point, the thiolate can either undergo nucleophilic substitution with the fluorinated aromatic ring (PFTR), or it can react with a second thiol molecule generating a disulphide bond (side reaction). Importantly, the thiolate is not available anymore for PFTR after disulfide bond formation has taken place. The disulfide bond formation lowers the yield of the main reaction and causes defects when applied to polymer network formation. Therefore, in order to understand the impact of the disulfide bond formation on PFTR, the side reaction is first studied in an isolated way, e.g. only thiol and base, without a fluorinated linker. The reaction was performed using a molar ratio of SH:base equal to 1:1 and a concentration of thiol ($[\text{thiol}]_0 = 0.15\ \text{mol}\cdot\text{L}^{-1}$). At specific time intervals, aliquots of the crude reaction mixture were analyzed *via* SEC. The progress of the reaction was monitored by comparing the relative intensity of the peak assigned to the thiol with the one of disulfide, distinguishable in a SEC chromatogram. Furthermore, the raw data were used for subsequent *k*MC simulations and the determination of the rate coefficient of the reaction. As output, the simulated SEC traces are compared to the experimental one, as shown in Figure 4.6. The simulated SEC traces are obtained after tuning of the rate coefficient to match with the experimental data. For clarity reasons, it must be mentioned that the x- and y-axis of both graphs are changed when the experimental

SEC traces are compared to the simulated ones due to the absence of a DRI detector or elution volume when simulating the data (see also Appendix, Figure 8.2).

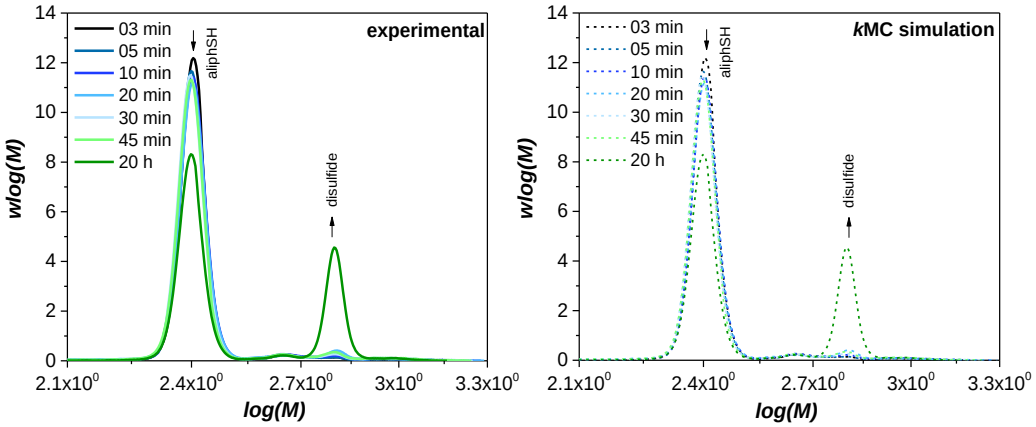

Figure 4.6 – Experimental (left) and simulated (right) SEC traces for the disulfide bond formation for aliphSH. The reaction is performed with an initial ratio SH:DBU = 1:1 in THF ($[thiol]_0$ = 0.15 mol·L^{-1}). The fluorinated linker was not included in the reaction mixture in order to exclusively assess the rate coefficient of the side reaction. The figure is adapted from Ref. [189] with the permission of The Royal Society of Chemistry.

The results show that for aliphSH, long reaction times, e.g. 24 h, are needed to assess the rate coefficient, which is found to be equal to $1.0 \cdot 10^{-5}$ L·mol^{-}1·s^{-1}, indicating that the disulfide bond formation reaction is not promoted in the adopted reaction conditions. Next, the same thiol was reacted with the three-armed fluorinated linker (**3PFB**). The PFTR was performed using an equimolar ratio between the thiol and **3PFB**, using $[thiol]_0$ = 0.075 mol·L^{-1}. Similar to the disulfide bond formation, the reaction was followed both experimentally and by *k*MC simulations. Starting from the experimental data, the conversion of the PFB group is obtained *via* ^{19}F NMR spectroscopy and the data were used as input for the *k*MC calculations, together with the information previously obtained regarding the side reaction. The comparison between experimental and simulated results is presented in detail in Figure 4.7 to highlight different aspects of the reaction.

Firstly, the simulated functional group conversion over time (Figure 4.7a, full line) is fully comparable to the experimental data, indicating the capability of the model to describe the reaction. Next, in Figure 4.7b, is reported the simulated product spectrum, which depicts the absolute concentration of each specie over time. According to Figure 4.7b, the effect of the side reaction (disulfide) seems to be negligible in the studied conditions. To further confirm this hypothesis, the SEC traces showing the evolution of the **1S**, **2S** and the targeted **3S** species as extrapolated from the reported product spectrum are compared to the experimental SEC traces.

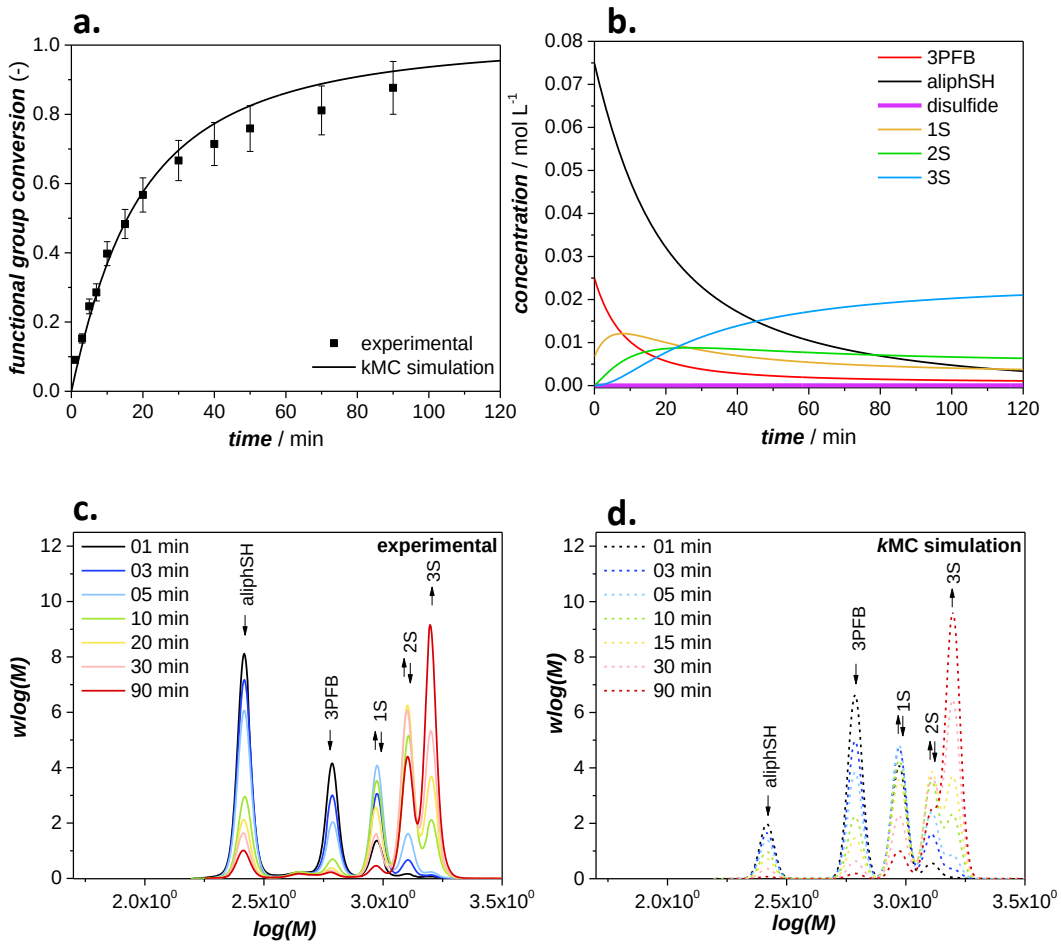

Figure 4.7 – a. Experimental and simulated data are compared in terms of functional group conversion over time. b. Simulated product spectrum showing the variation of the absolute concentration of each species over time during PFTR c. Experimental and d. Simulated SEC traces at selected intervals of time showing the evolution of each specie according to the product spectrum (b). The PFTR reaction was performed at ambient temperature, with an initial ratio SH:PFB:DBU = 1:1:1 and $[thiol]_0$ *= 0.075 mol·L*$^{-1}$ *in THF. The figure is adapted from Ref. [189] with the permission of The Royal Society of Chemistry.*

The comparison, highlighted in Figure 4.7c and d, shows a good agreement between simulated and experimental SEC traces. Thus, it was concluded that the side reaction does not take place when the fluorinated linker is present in the reaction mixture. Notably, the model is able to predict the experimental data and to follow the evolution of each species during PFTR. The rate coefficient for PFTR, performed under the abovementioned conditions, is equal to $2.5\ 10^2$ L·mol^{-1} s^{-1}. The combination of these findings, together with those related to the absence of multiple substitutions, makes the PFTR a suitable ligation system for polymer network formation as also no side reactions arising from the disulfide bond formation were observed.

Reactivity of structurally different thiols

Herein, a selection of commercially available small molecule thiol derivatives were employed for PFTR in combination with the three-armed fluorinated linker, **3PFB**. The variety of thiols was chosen in order to resemble the structure of the polystyrenic thiol employed in section 3.3. Accordingly, the aliphatic thiols are intended to mimic the aliphatic backbone of the polymer, while the aromatic thiols the pendant benzylic ring derived from styrene (monomer). For each category, aliphatic and aromatic, both a primary and a secondary thiol were selected, as depicted in Figure 4.8.

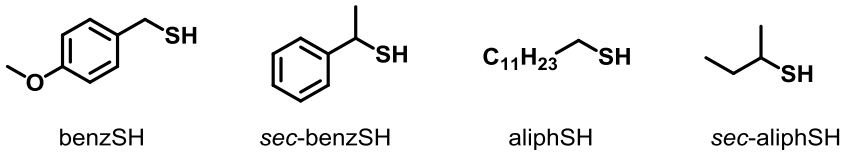

Figure 4.8 – List of small molecules thiol derivatives used for the kinetic study. From left to right 4-methoxy-α -toluenethiol (benzSH), 1-phenylethyl mercaptan (sec-benzSH), dodecanethiol (aliphSH) and 2-butanethiol (sec-aliphSH).

The same study presented for aliphSH was repeated for each thiol derivatives shown in Figure 4.8. Starting from benzSH, the disulfide bond formation was performed under identical conditions to those employed for aliphSH. Contrary to the previous case, for benzSH the presence of disulfide bond formation is already detectable after 5 min and the rate coefficient for the side reaction was found to be equal to 1.5 10^{-3} L·mol^{-1} s^{-1}. The experimental and the simulated SEC traces are reported in Figure 4.9.

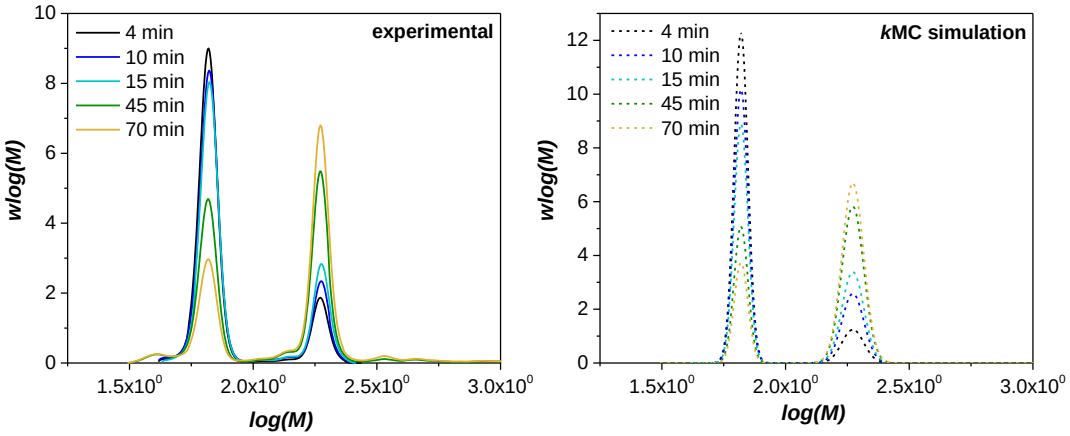

Figure 4.9 – Experimental (left) and simulated (right) SEC traces for the reaction of disulfide bond formation for benzSH. The reaction is performed using an initial ratio SH:base = 1:1 and a concentration of $[thiol]_0$ = 0.15 mol·L^{-1} The figure is adapted from Ref. [189] with the permission of The Royal Society of Chemistry.

Concerning the other thiol derivatives, it was not possible to quantify the disulfide bond formation *via* SEC analysis due to instrument limitations. Thus, in a first approximation, the rate coefficient for the disulfide bond formation, necessary for the *k*MC simulation, for *sec*-aliphSH and *sec*-benzSH are assumed identical to the one of aliphSH and aromSH, respectively. A summary of all the rate coefficients of the disulfide bond formation for each thiol is shown in Table 4.1.

Table 4.1 – Summary of the rate coefficients of the disulfide bond formation (k_{disulf}) and the para-fluoro–thiol reaction (k_{PFTR}) for different thiol derivatives. The rate coefficients are assessed via kMC simulations based on the experimental data and reported in $L \cdot mol^{-1}s^{-1}$. The disulfide bond formation was performed using $[thiol]_0 = 0.15\ mol \cdot L^{-1}$, while PFTR using $[thiol]_0 = 0.075\ mol \cdot L^{-1}$. In both cases, THF was used as solvent. The table is adapted from Ref. [189] with the permission of The Royal Society of Chemistry.

Thiol	Solvent	k_{disulf}	k_{PFTR}
benzSH	THF	$1.5 \cdot 10^{-3}$	$2.5 \cdot 10^{-1}$
sec-benzSH	THF	$1.5 \cdot 10^{-3}$[(a)]	$2.5 \cdot 10^{-1}$
aliphSH	THF	$1.0 \cdot 10^{-5}$	$2.5 \cdot 10^{-2}$
sec-aliphSH	THF	$1.0 \cdot 10^{-5}$[(a)]	$6.0 \cdot 10^{-3}$

[(a)]in these cases, the experimental evaluation of the disulfide bond formation was not possible due to instrument limitations, thus these values are assumed for the *k*MC simulations

Next, the PFTR was performed in THF using **3PFB** and each of the listed thiol ($[thiol]_0 = 0.075\ mol \cdot L^{-1}$). The rate coefficient was assessed by *k*MC simulation based on the experimental functional group conversion over time, as calculated *via* ^{19}F NMR spectroscopy. The difference in reactivity of the different thiols is depicted in Figure 4.10.

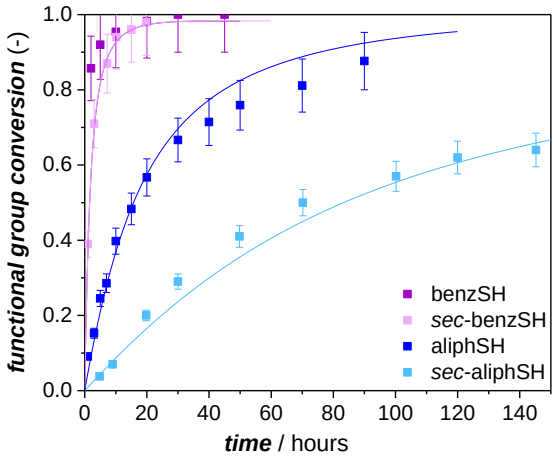

Figure 4.10 – Comparison of the functional group conversion over time for structurally different small molecule thiol derivatives during PFTR. The figure is adapted from Ref. [189] with the permission of The Royal Society of Chemistry.

The conversion over time plots (Figure 4.10) reveal that the reactivity is higher for aromatic thiols and that, in each case, primary thiol derivatives are more reactive than their secondary analogues. To summarize, the reactivity follows the order benzSH > *sec*-benzSH > aliphSH > *sec*-aliphSH. The increased reactivity can be attributed to the inherent acidity of the employed thiols, since aromatic thiols are more acidic than the aliphatic derivatives.[192] Even though previous literature does not determine the rate coefficient for each reaction, a comparable reactivity trend is observed.[98] A summary of the rate coefficient of the main and the side reaction for each thiol is reported in Table 4.1.

4.1.3 Presence of Ester Bonds

A disadvantage of the current approach is the synthesis of the **3PFB** linker *via* phase transfer catalysis (PTC), which requires a strong excess of the fluorinated starting material and results in low yield (≈ 35%, refer to Section 7.4). Contrary to that, a reaction involving the same starting material (2,3,4,5,6-pentafluobenzylbromide) and a carboxylic group results in yields of approximately 90% (see Section 7.4). Hence, the PFTR was studied for the case where pentafluorobenzyl moiety, previously proven to be selective towards the *para*- substitution only, is combined with the presence of an ester linkage, which often leads to multiple substitutions.[69] For this purpose, the same molecule containing three carboxylic acid groups was reacted with 2,3,4,5,6,-pentafluorophenylalcohol in one case and with 2,3,4,5,6-pentafluoro benzyl bromide in the second case. The outcome is a linker where the ester bond is connected to a pentafluoro phenyl group (**3aromCOOPFP**) in the former case, and a pentafluoro benzyl group (**3aromCOOPFB**) in the latter case. The chemical structure of the newly-synthesized linkers is depicted in Figure 4.11.

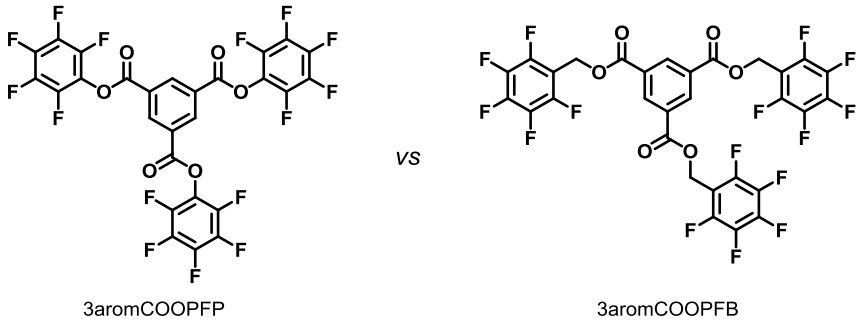

*Figure 4.11 – Chemical structure of the two fluorinated linkers used to investigate the selectivity of the nucleophilic aromatic substitution when the pentafluoro phenyl (left) or benzyl (right) group is directly connected to an ester group (**3aromCOOPFP** and **3aromCOOPFB**, respectively).*

The PFTR was performed employing aliphSH with either **3aromCOOPFP** or **3aromCOOPFB**. For both reactions, the initial molar ratio of SH:fluorinated group:base was fixed to 1:1:1. The reactions were performed in THF, with a $[thiol]_0 = 0.075\ mol \cdot L^{-1}$. As before, the crude product was analyzed *via* ^{19}F NMR spectroscopy after neutralization of the alkaline reaction mixture. The ^{19}F NMR spectra are reported in Figure 4.12, where they are compared to the unreacted linker and the homologous fluorinated alcohol, e.g. pentafluoro phenyl or benzyl alcohol.

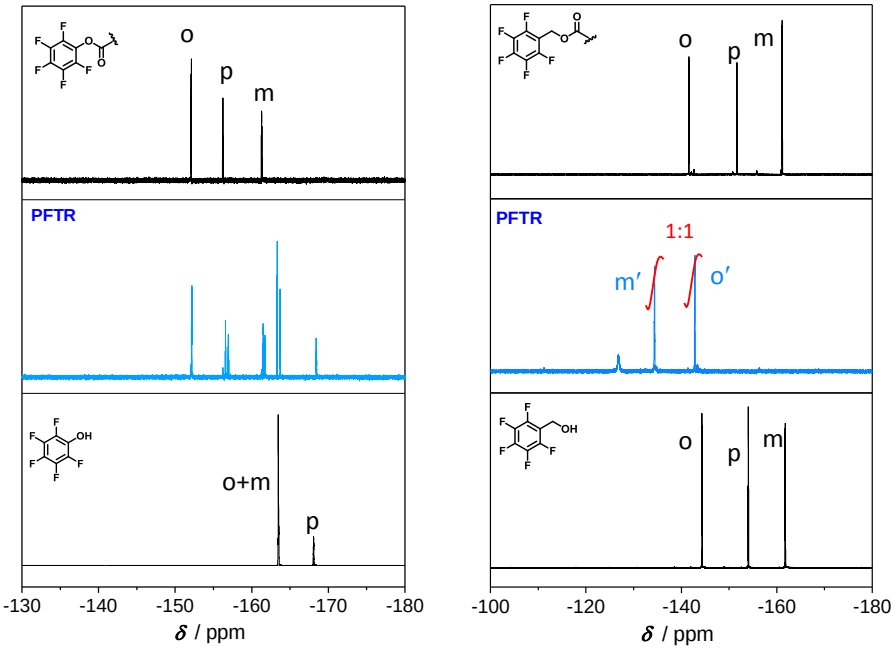

Figure 4.12 – ^{19}F NMR spectra ($CDCl_3$, 377 MHz*) of the **3aromCOOPFP** (left) and **3aromCOOPFB** linker (right) before and after PFTR (black and blue line, respectively). In each case, the ^{19}F NMR spectra of either the pentafluoro phenol (bottom panel, left) or pentafluoro benzyl alcohol (bottom panel, right) is reported for facilitating the peak assignment in case of cleavage of the fluorinated group.*

On the left side are reported the spectra for the PFTR performed in the presence of fluorinated phenyl groups. The ^{19}F NMR spectrum after PFTR (Figure 4.12, left, blue line) presents several resonances, which could not be assigned in detail due to the absence of data available in the literature. However, it is clear that part of the resonances can be attributed to the fluorinated linker still connected to the ester bond, due the similarity of the chemical shift with the parent linker (Figure 4.12, left, top). On the other hand, some of the resonances are comparable to the pentafluoro phenyl alcohol (Figure 4.12, left, bottom), suggesting the cleavage of the ester bond. The hypothesis of cleavage is based on literature data, where the PFP moiety directly attached to an ester bond is known to act as an activated ester, thus susceptible to cleavage.[93] No further detailed investigations have been performed in this direction as the main goal was

to perform PFTR in the absence of side reactions or degradation of the functional groups involved.

A different scenario is observed when the PFTR was performed with a fluorinated linker having the same core but PFB rather than PFP functional groups. Herein, the ^{19}F NMR spectrum, reported in Figure 4.12 right, depicts the resonances typical for PFTR at $\delta = -134.4$ (m') and $\delta = -142.8$ ppm (o').

It follows that the presence of just a single carbon between the ester bond and the fluorinated aromatic ring is sufficient for PFTR to occur selectively at the *para*- position.

As a drawback, the high content of aromatic rings leads to solubility issues in common organic solvents such as DMF. This can be easily overcome by switching to an aliphatic, rather than aromatic, core structure. Therefore, following a similar procedure to the one adopted for the synthesis of **3aromCOOPFB**, a three- and a four-armed linker (**3COOPFB** and **4COOPFB**, respectively) were prepared bearing an aliphatic core structure (refer to Section 7.4). The accessibility to a four-armed linker is important for the fabrication of networks, as it resemble the four crosslinking point generating upon crosslinking reaction using a bifunctional monomer during free radical polymerization (FRP). Thus, only in the case of a four-armed linker a direct comparison between the same network synthesized either *via* the end-linking strategy and FRP is possible (more details will follow in **Chapter 5**).

To complete the study, the reactivity of aliphSH towards PFTR was investigated using the newly synthesized **3COOPFB** and **4COOPFB** linkers, depicted in Figure 4.13, right. The data are compared with those obtained for **3PFB** in Figure 4.13, left.

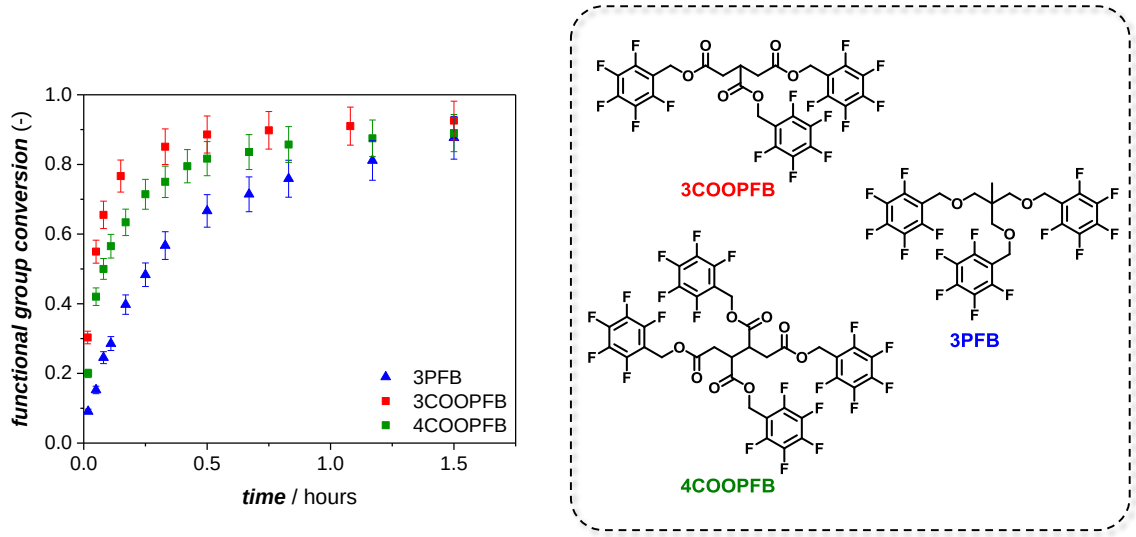

*Figure 4.13 – Left: Functional group conversion over time for the reaction between aliphSH and either **3PFB**, **3COOPFB** or **4COOPFB**. Right: Chemical structure for **3PFB, 3COOPFB** and **4COOPFB**. The reactions were performed using an initial molar ratio of SH:PFB:DBU = 1:1:1 and [thiol]$_0$ = 0.075 mol·L^{-1}.*

As depicted in Figure 4.13, the functional group conversion over time during PFTR is similar in all the three reported cases. Small differences are visible only in the first hour of the reaction, where a faster conversion of the functional group (*para*-fluorine atom) was observed when using ester bond containing linkers (red and green symbols). This is probably associated to the electronegative effect of the ester bond, which may cause the aromatic fluorinated linker to be even more electron-poor, thus more susceptible to nucleophilic attack. Nonetheless, the differences are minor and become negligible with proceeding reaction times ($t \geq 1$ h).

In summary, after elucidation of the reaction mechanism using a model reaction between aliphSH and **3PFB**, a variety of characterization tools have been presented. Among others, the most diagnostic analysis is, with no doubt, the ^{19}F NMR spectroscopy. The first advantage is the possibility of analyzing the crude mixture, as no interference of the protons coming from the thiol structure or the solvent will occur during the measurements. Moreover, upon comparison of the integrals of the resonances arising from the PFTR adduct with those of the parent linker, the conversion at any reaction time can be calculated from the ^{19}F NMR spectrum using Equation 4.1. In this section, particular attention was set on the selectivity to ensure the absence of multiple substitution on the fluorinated aromatic ring, as for network formation it is important that the reaction proceed according to the proposed reaction pathway. Thus, after having proved the suitability of the pentafluoro benzyl moieties (PFB), the influence of different parameters on the reaction rate of the PFT reaction were investigated. For example, increasing the concentration of the functional group or the acidity of the employed thiol results in faster reaction rates. Moreover, the selectivity of the PFB moieties, in terms of directing the nucleophilic attack only to the *para* position is preserved when ester bond are included in the linker core structure (e.g. **3COOPFB**). This is particularly relevant as it allows for the synthesis of the desired linker through synthetic protocols that allow high yields and mild reaction conditions (e.g. esterification).

The selectivity and the absence of the side reaction during PFTR, as well as the easy quantification of the conversion *via* ^{19}F NMR spectrum, opens the door for the application of the selected ligation to more complex architectures. Thus, in the next section, the performance of the reaction when polymeric thiol derivatives are used as nucleophile was investigated.

4.2 Polymeric Thiol Derivatives

4.2.1 Kinetic Study

Herein, the reactivity of polymeric thiol derivatives towards PFTR was investigated employing a polystyrene based polymer. Starting from a commercially available RAFT agent such as 2-(((dodecylthio)carbonothioyl)thio)propanoate (DoPAT), the polymerization of styrene was performed *via* RAFT polymerization (yielding intermediate **PSa**). Next, the polymeric thiol (**PSa-SH**) was achieved by removal of the trithiocarbonate group present at the polymer chain end. The reaction scheme is presented in Figure 4.14 (top) and the success of the aminolysis is shown *via* SEC and ESI-MS analysis (Figure 4.14, bottom). The molecular weight for **PSa**, as determined by SEC, is 4000 g mol^{-1} ($Đ$ = 1.1) before aminolysis, and 3800 g mol^{-1} ($Đ$ = 1.1) afterwards, due to the loss of the aliphatic chain and the trithiocarbonate group (Figure 4.14). The SEC trace of the polymer is important to show the absence of disulfide adducts after aminolysis, while for a more precise elucidation of the chemical structure, the ESI-MS spectra are reported in Figure 4.14 (bottom right, the full ESI-MS spectra in the range m/z = 1500-4000 is reported in Appendix, Figure 8.5). The ESI-MS spectra were recorded in negative ion mode, thus the molecule is present as $[M+Cl]^-$ or $[M+I]^-$ adduct. Herein, it can be noticed that the difference in mass (Δm) between two consecutive peaks within the same distribution is equal to 104.063, which refers to the molecular weight of the styrene, used as monomer (repeating unit). Moreover, when considering **PSa** with, for instance, 23 repeating units (n), the difference in the *m/z* before and after aminolysis is equal to Δm = 244.126, corresponding to the molar mass of the aliphatic chain and the thiocarbonate group removed during the post-modification reaction. This result, in particular shows the success of the reaction and the formation of the desired polymeric thiol derivative (**PSa-SH**). The ^{1}H and ^{13}C NMR spectra of **PSa** and **PSa-SH** were also recorded and are reported in Appendix (Figure 8.3 and Figure 8.4, respectively). Here, since the focus is set on understanding the reactivity of polymeric thiol derivatives, polystyrene was selected as thiol derivative in order to avoid functional groups on the repeating unit that might interfere with the PFT reaction. However, the procedure for obtaining thiol polymers is generally applicable to polymer produced by RAFT polymerization and not specific to polystyrene.[55]

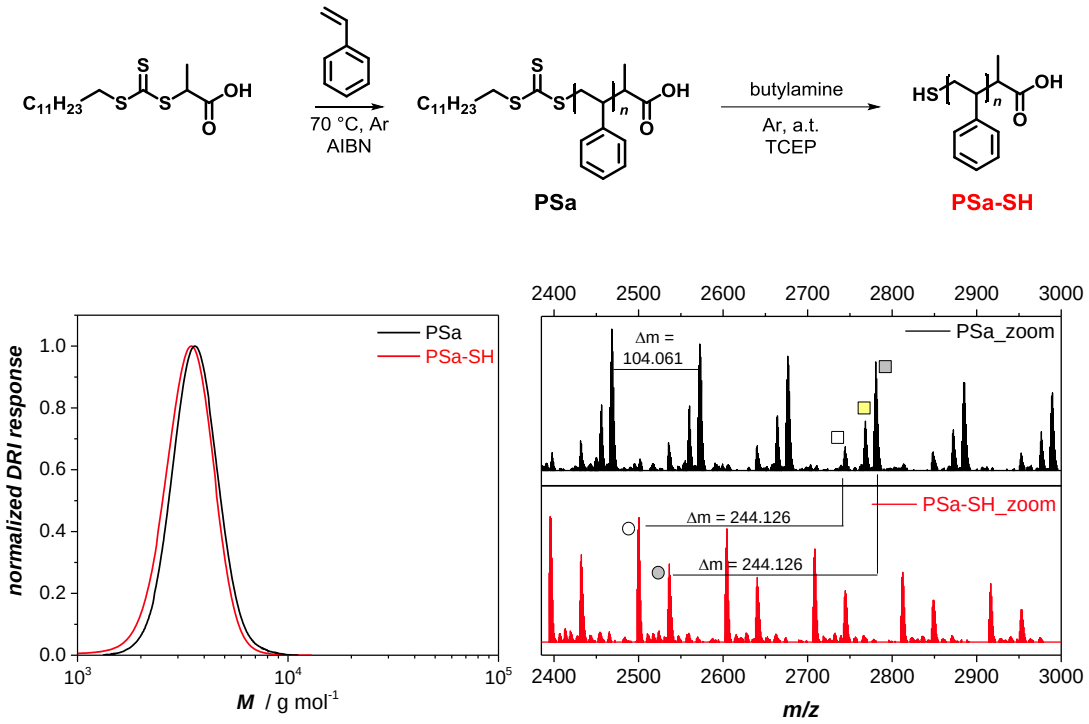

Figure 4.14 – Top: reaction scheme for the synthesis of the polymeric thiol derivative ***PSa-SH****. Bottom: SEC traces (left) and the corresponding (−)ESI-MS spectra (right) for* ***PSa*** *(black) and* ***PSa-SH*** *(red). For the ESI-MS spectra: Δm = 104.061, corresponds to the mass of the styrene and Δm = 244.126 indicate the loss of the aliphatic chain and the trithiocarbonate upon aminolysis. The figure is adapted from Ref. [189] with the permission of The Royal Society of Chemistry.*

Table 4.2 – Comparison of the experimental and the theoretical m/z ratio for the peak highlighted in the ESI-MS spectra in Figure 4.2. Herein, n refers to the number of styrene repeating units in the considered peak and Δm is the difference between the theoretical and the experimental value. The table is adapted from Ref. [189] with the permission of The Royal Society of Chemistry.

	structure	*n*	*m/z* (exp)	*m/z* (theo)	*Δm*
■	$[PSa+Cl]^-$	23	2780.534	2780.554	0.020
■	$[PSa+I]^-$	22	2768.409	2768.428	0.019
□	$[PSa]^-$	23	2744.559	2744.578	0.019
●	$[PSa\text{-}SH+Cl]^-$	23	2536.408	2536.422	0.014
○	$[PSa\text{-}SH]^-$	23	2500.433	2500.447	0.014

Additionally, for the polymeric system, the influence of the solvent polarity was explored by comparing the functional group (PFB) conversion in THF and DMF. As for small molecule thiol derivatives, the disulfide bond formation was first investigated in an isolated way. Here, the polymeric thiol and the base (i.e. DBU) were used with an initial ratio of 1:1 and an initial concentration of thiol equal to 0.075 mol·L^{-1}. At different reaction times, aliquots of the reaction mixture were analyzed *via* SEC analysis to evaluate whether there is formation of disulfide bond. If present, the heights of the peaks corresponding to **PSa-SH** and the disulfide were compared with each other. As in the previous section (refer to Section 4.1.2), *k*MC simulations were

used to support the experimental data, and to assess the rate coefficient of each reaction. The results of both the experimental and the simulated SEC traces are compared in Figure 4.15.

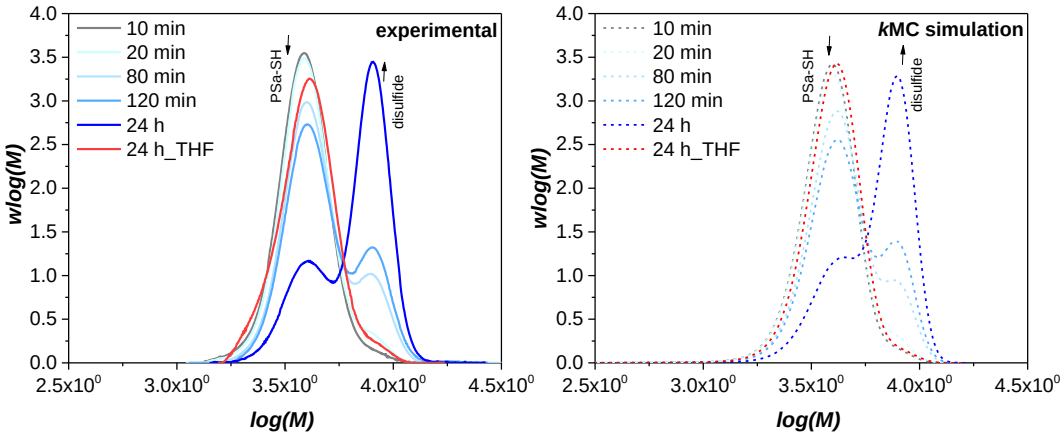

Figure 4.15 – Experimental (left) and simulated (right) SEC traces for the disulfide bond formation employing ***PSa-SH*** *as polymeric thiol derivative and using an initial molar ratio of SH:DBU = 1:1 and* $[thiol]_0$ *= 0.075 mol·L*$^{-1}$ *in THF (red, 24h) or DMF (blue). The figure is adapted from Ref. [189] with the permission of The Royal Society of Chemistry.*

For the reaction in THF, only minor or no disulfide bond formation was observed after 24 hours of reaction time, thus only the 24 h SEC trace is shown in Figure 4.15 (red line). In contrast, when performing the same reaction in DMF a small percentage of disulfide is already visible after short reactions times, e.g. after t = 5 and 10 min (Figure 4.15, blue lines). The different reactivity of the thiolate ion based on the solvent polarity is in agreement with published data. The low ability of THF, and other non-polar solvents, to promote reactions involving thiolates is reported for other reactions such as thiol-ene and thiol-ester exchange reactions.[193] Moreover, the *k*MC simulations indicated that an equilibrium reaction needs to be introduced for the disulfide bond formation in DMF at longer reaction times to simulate at best the results obtained experimentally. Thus, the rate coefficients were determined for the forward ($k_{disulf,f}$) and the reverse ($k_{disulf,r}$) reactions resulting in $k_{disulf,f}$ = 1.5 10^{-3} L·mol^{-1} s^{-1} and $k_{disulf,r}$ = 1.5 10^{-6} s^{-1}, respectively.

Next, PFTR was performed using an initial molar ratio of SH:PFB:DBU = 1:1:1 and an initial concentration of functional group equal to 0.075 mol·L^{-1}, in both THF and DMF. Without performing any purification, except for the removal or neutralization of the base, the crude mixture was analyzed *via* ^{19}F NMR spectroscopy and SEC. The results, in terms of functional group conversion (^{19}F NMR) and formation of mono- di- and trisubstituted linker (SEC traces) over time, are shown in Figure 4.16 top and bottom, respectively.

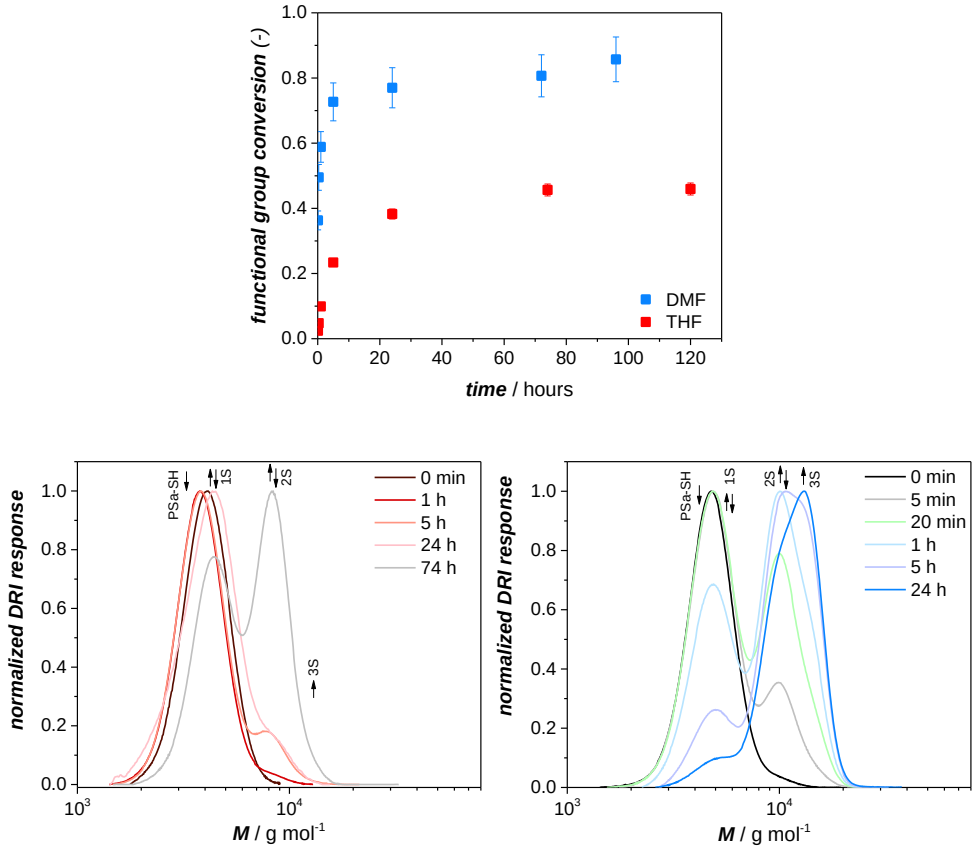

*Figure 4.16 – Top: Functional group conversion over time for PFTR performed employing **PSa-SH**, an initial molar ratio of SH:PFB:DBU = 1:1:1 and $[thiol]_0$ = 0.075 mol·L^{-1} in either THF (red) or DMF (blue). Bottom: Experimental SEC traces at selected intervals of time (see legend) for the PFTR in THF (left) or DMF (right). The figure is adapted from Ref. [189] with the permission of The Royal Society of Chemistry.*

Similar to what was observed for the side reaction (i.e. the disulfide bond formation), the reactivity of the thiolate ions towards PFTR is enhanced in DMF. Specifically, when the reaction was performed in THF, a maximum of 45% conversion is obtained after 72 h, while the same conversion is reached within 1 h when the reaction was performed in DMF. As a comparison, after a reaction time of 72 h in DMF, the conversion is equal to almost 90%, which is twice the amount achieved in THF within the same time frame. Subsequently, the experimental data were compared to the *k*MC simulations. For the simulation, both the conversion values as obtained from ^{19}F NMR spectroscopic analysis and the information previously obtained about the side reaction were considered. Moreover, the shielding effect, which is the hindrance of the reaction centers due to the substitution degree (SD) of the linker molecule, and the possibility of diffusional limitations were taken into account. In order to include these parameters, apparent rate coefficients were introduced and the formula was modified as follows:

$$k_{\mathrm{PFTR,app},1} = k_{\mathrm{PFTR},0} \tag{4.3}$$

$$k_{\mathrm{PFTR,app},2} = f_{\mathrm{shielding},1} k_{\mathrm{PFTR},0} \left(x_{\mathrm{n,thiol}} x_{\mathrm{n,ligation},1}\right)^{-\alpha} \tag{4.4}$$

$$k_{\mathrm{PFTR,app},3} = f_{\mathrm{shielding},2} k_{\mathrm{PFTR},0} \left(x_{\mathrm{n,thiol}} x_{\mathrm{n,ligation},2}\right)^{-\alpha} \tag{4.5}$$

where $k_{\mathrm{PFTR,\,app},1}$, $k_{\mathrm{PFTR,\,app},2}$, $k_{\mathrm{PFTR,\,app},3}$ are the rate coefficient for the formation of mono- di- and trisubstituted linker, respectively. $f_{\mathrm{shielding}}$ takes into account the substitution degree of the linker and is defined as 1/*SD*. Moreover, $x_{\mathrm{n,thiol}}$ and $x_{\mathrm{n,ligation}}$ refer to the number average molecular weight of the polymeric thiol derivative and the mono- (1) or di- (2) substituted linker, respectively (for more details on $x_{\mathrm{n,thiol}}$ refer to Appendix). α accounts for diffusional limitations arising from the chain length of the polymeric derivatives. It can assume values from 0 to 1, with 0 being no diffusional limitation. During this study α was found to be equal to 0.7.

The results are shown for the reaction in DMF in Figure 4.17, where the fitting between the experimental and simulated conversion values over time (left) is displayed together with the simulated product spectrum for the reaction performed in DMF (right).

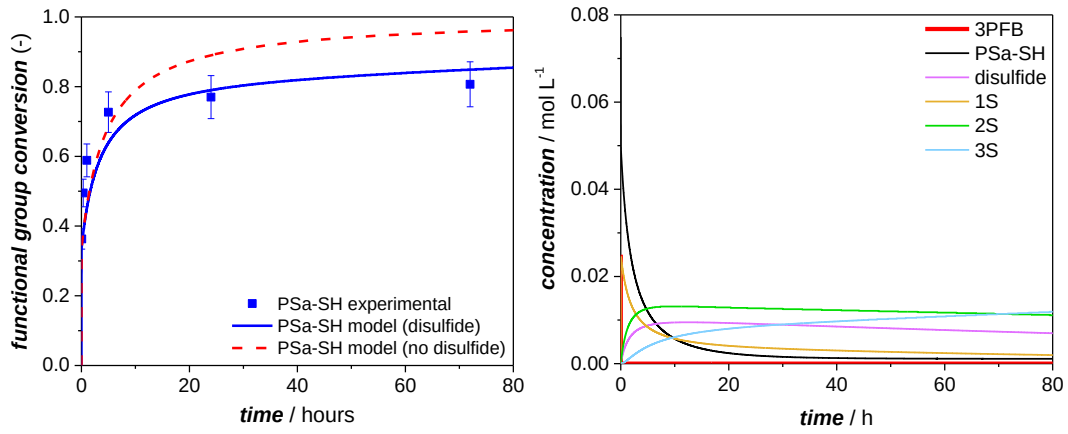

*Figure 4.17 – Left: experimental and simulated functional group conversion over time for PFTR employing **PSa-SH** and **3PFB** using a molar ratio of SH:PFB:DBU = 1:1:1 in DMF. The blue solid line refers to the simulation accounting for disulfide bond formation, while the red dashed line to the case where no disulfide are considered. Right: simulated product spectrum for the same reaction, obtained via kMC simulations, highlighting the concentration of each specie over time during the considered PFTR reaction. The figure is adapted from Ref. [189] with the permission of The Royal Society of Chemistry.*

In case of polymeric thiol, the product spectrum is of high importance since the molecular weight of the disulfide side product is similar to the one of the disubstituted linker (**2S**). The simulated product spectrum reported in Figure 4.17 (right), which shows the variation of the

concentration of each species present in the reaction mixture, suggests that part of the thiolates undergo disulfide bond formation, thus the peak marked as **2S** in the experimental SEC traces (Figure 4.16) is partially influenced by the disulfide adduct. The theoretical conversion in case no disulfide bonds were present is depicted in Figure 4.17 (left, red dashed line), indicating a deviation of the experimental data mostly after ≈10 h. Furthermore, to achieve an accurate fitting between experimental and simulated results, it was necessary to consider the chain length dependency during *k*MC simulation, while the influence of shielding was negligible. A comparison between the experimental and the simulated SEC traces (as obtained from the product spectrum in Figure 4.17) are reported in Appendix (Figure 8.8).

Presence of carboxylic groups

Before screening reaction conditions that can limit the formation of disulfides, the effect of the carboxylic group present as a chain-end of **PSa-SH** (Figure 4.14) was investigated. The reason is to understand the applicability of poly(acrylic acid) based polymeric thiol derivatives towards PFTR. Thus, the difference in reactivity between a polymeric thiol having a free (**PSa-SH**) and a protected (**PSb-SH**) carboxylic group as chain end was explored. **PSb-SH** was obtained by esterification of the RAFT agent (DoPAT) prior to polymerization. The thiol derivative was isolated following the same procedure adopted for **PSa-SH**. The chemical structure for **PSa-SH** and the newly synthesized **PSb-SH** are depicted in Figure 4.18. The full characterization for **PSb-SH**, such as SEC traces, ^{1}H NMR, ^{13}C NMR and ESI-MS spectra are reported in Appendix (Figure 8.9 to Figure 8.12). As before, the molecular weight for **PSb-SH** was determined *via* SEC analysis, using a polystyrene based calibration and resulted equal to 2800 g mol^{-1} ($Đ$ = 1.1).

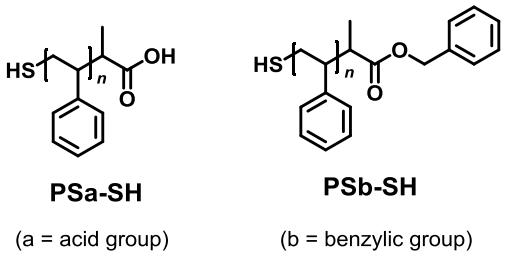

*Figure 4.18 Chemical structure for **PSa-SH** and **PSb-SH**, the two polymeric thiol derivatives used in this section. The label **a** and **b** serve as a reminder of the acid or benzylic group present as second chain-end.*

In order to compare the results with those obtained for **PSa-SH**, **PSb-SH** was reacted with **3PFB** employing an initial molar ratio of SH:PFB:DBU = 1:1:1 and a $[\text{thiol}]_0$ = 0.075 mol·L^{-1}

in both THF and DMF. The conversion values obtained for both polymers are depicted in Figure 4.19, while the SEC traces for **PSb-SH** are reported in Appendix (Figure 8.13).

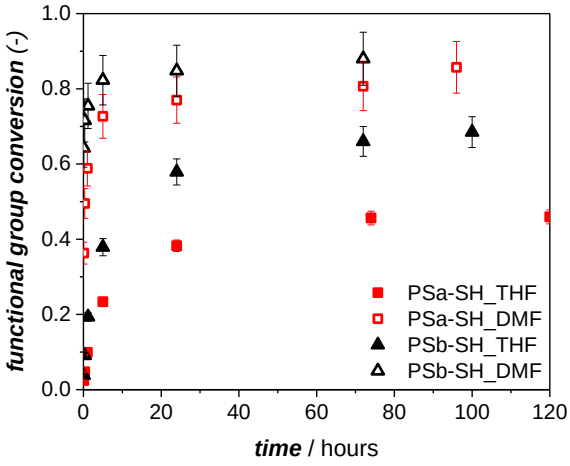

*Figure 4.19 – Functional group conversion over time for **PSa-SH** (red squares) or **PSb-SH** (black triangles) in either THF (full symbols) or DMF (empty symbols). In each case a molar ratio of 1:1:1 between thiol:PFB:base and a $[thiol]_0$ = 0.075 mol·L^{-1} was employed. The figure is adapted from Ref. [189] with the permission of The Royal Society of Chemistry.*

The results obtained for **PSb-SH** confirms that the reaction rates are faster in DMF compared to THF, highlighting the lower ability of the THF to promote PFTR, independently from the presence of carboxylic acid groups. Accordingly, for the reaction performed using **PSb-SH**, a conversion value of approximately 70% is reached within the first hour in DMF but only after 72h in THF. On the other hand, Figure 4.19 shows that, independently from the solvent used, protecting the carboxylic group allows for faster reaction times. Accordingly, upon performing PFTR in DMF for 5 min, a conversion of ~65% is achieved if the carboxylic group is protected, against ~35% when the free carboxylic group is present on the polymer chain. The difference in reactivity can arise from a partial neutralization of the base (i.e. DBU) for **PSa-SH** due to the presence of the acid functionality.

To further investigate this phenomenon, the results are compared with a commercially available small molecule thiol (COOH-SH). The new thiol was reacted with **3PFB** while keeping all the other parameters identical to the reactions discussed above, e.g. ratio between the functionality and solvent used. For a better visualization of the results, a zoom within the first 5 h of the reaction is displayed in Figure 4.20.

The reported data suggest a similar reactivity between the commercially available (blue) and the polymeric (red) thiol derivatives. On the one hand, the kinetics for both thiols overlap completely when THF is used as solvent (filled squares). On the other hand, if DMF is the solvent

of choice, the difference in reactivity are visible only within the first hour of reaction, with the polymeric thiol giving higher conversions. However, the effect is minimal and becomes negligible after the first hour and for longer reaction times (for the conversion values up to 100 h, refer to Appendix, Figure 8.14).

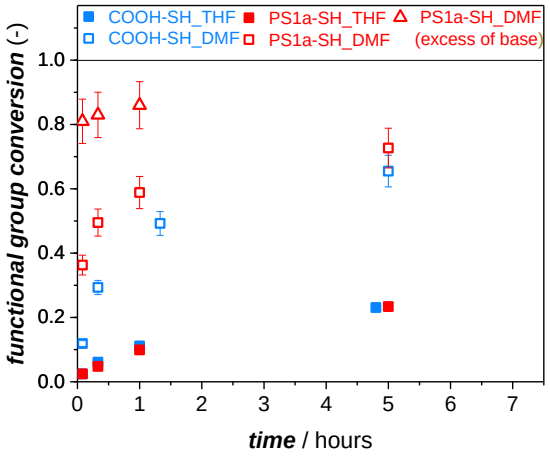

*Figure 4.20 – Functional group conversion over time for a polymeric (red) and a small molecule (blue) thiol derivative, both containing a free carboxylic acid group as second chain end. The reaction was performed in both THF (full symbol) and DMF (empty symbol) using a ratio SH:PFB:base equal to 1:1:1 (square) or 1:1:15 (triangle). The excess of base is applied only to **PSa-SH**. The figure is adapted from Ref. [189] with the permission of The Royal Society of Chemistry.*

Nonetheless, in order to overcome the slower reaction rates obtained with **PSa-SH** compared to **PSb-SH**, the PFTR was performed using an excess of base, e.g. a molar ratio of 1:15 = SH:base. The conversion values obtained within the first hour are reported in Figure 4.20. When using an excess of base, ≈80% of the PFB groups undergo nucleophilic substitution after 5 min, similarly to what was observed for **PSb-SH**, where almost 70% conversion was achieved within the same time frame. Notably, the excess of base is generally not a problem when performing polymer ligations, as the product can be easily isolated *via* precipitation. For a better comparison, a summary of the rate coefficients, determined *via k*MC simulations, for PFTR and disulfide bond formation concerning the employed polymeric thiol derivatives and the commercially available COOH-SH derivative is presented in Table 4.3.

The fitting between the experimental and simulated functional group conversion over time for the thiol derivatives used in this subsection is reported in Appendix (Figure 8.15Figure 8.8).

Table 4.3 – Summary of the rate coefficient values of the disulfide bond formation (k_{disulf}) and the para-fluoro–thiol reaction (k_{PFTR}) for different thiol derivatives. The rate coefficients are assessed via kMC simulations based on the experimental data and reported in $L \cdot mol^{-1} \cdot s^{-1}$ with the exception of $k_{disulf,r}$ which is reported in s^{-1}. Each reaction was performed using $[thiol]_0 = 0.075\ mol \cdot L^{-1}$. The table is adapted from Ref. [189] with the permission of The Royal Society of Chemistry.

Thiol	Solvent	$k_{disulf,f}$	$k_{disulf,r}$	$k_{PFTR,0}$[(b)]
PSa-SH	THF	$1.0 \cdot 10^{-5}$	N/A	$2.0 \cdot 10^{-2}$
PSa-SH	DMF	$1.5 \cdot 10^{-3}$	$1.5 \cdot 10^{-6}$	$7.5 \cdot 10^{-1}$
PSb-SH	THF	$1.0 \cdot 10^{-5}$[(a)]	N/A	$1.5 \cdot 10^{-2}$
PSb-SH	DMF	$1.5 \cdot 10^{-3}$[(a)]	$1.5 \cdot 10^{-6}$[(a)]	$1.5 \cdot 10^{0}$
COOH-SH	THF	N/A	N/A.	$8.0 \cdot 10^{-4}$
COOH-SH	DMF	N/A	N/A.	$2.0 \cdot 10^{-3}$

[(a)]assumed identical to **PSa-SH**

[(b)]refer to Equation 4.3 to 4.5

4.2.2 Investigation on Disulfide Bond Formation

Disulfide bonds are the product of the oxidation of the precursor thiols.[194] As such, two strategies are commonly adopted in the literature to suppress the reaction: the exclusion of oxygen from the reaction mixture or the addition of a reducing agent capable to prevent the disulfide bond formation and/or to cleave the disulfide bond once it has formed.[195]

Several reducing agents can be employed for this purpose. Among others, widely used in biochemistry are β-mercaptoethanol or dithiothreitol.[64, 196] However, both of above-mentioned reducing agents are thiol derivatives, which in this case is a limiting factor as the reactive species in PFTR is also a thiol. More suitable instead are phosphine-based reducing agents. In this study, tris(2-carboxyethyl)phosphine (TCEP) is used, due to its high efficiency in both basic and acidic media.[197]

In the current study, the combination of oxygen or argon atmosphere and the presence or absence of the reducing agent during disulfide bond formation performed using **PSa-SH** and DBU was explored. In order to have similar reaction conditions for all the listed options, a molar ratio SH:DBU:(TCEP) of 1:15:(6) and an initial thiol concentration $[thiol]_0 = 0.037\ mol \cdot L^{-1}$ in both THF and DMF was employed. The presence of the side reaction was evaluated *via* SEC analysis.

The absence of reducing agent, under atmospheric and inert conditions, did not lead to the successful suppression of disulfide bond formation (refer to Appendix, Figure 8.16). This is probably because the presence of oxygen is negligible when a strong excess of base is used (15 eq.). Contrary, the presence of the reducing agent in the reaction mixture led to a drastic reduction of the disulfide formation (refer to Appendix, Figure 8.16). In particular, the use of a

reducing agent under inert conditions resulted to be the most promising approach, as demonstrated by the SEC traces depicted in Figure 4.21, left (red line).

In the next step, PFTR was performed in presence of the reducing agent to investigate whether the generated thiolate is still reactive towards PFTR under these newly found conditions. The results, presented in terms of functional group conversion over time, are compared in Figure 4.21 (right, green squares) with those obtained when the same amount of base but no reducing agent is used (Figure 4.21, right, red squares).

The progress of PFTR in the presence of reducing agent (green squares) is significantly slower compared to the case where no TCEP was used (red squares). As concluded from the previous section, this is the result of a partial neutralization of the base due to the presence of the carboxylic acid moieties on the reducing agent. The TCEP molecule indeed, is composed of three carboxylic groups and it is commercially available as the corresponding hydrochloride salt (TCEP·HCl).

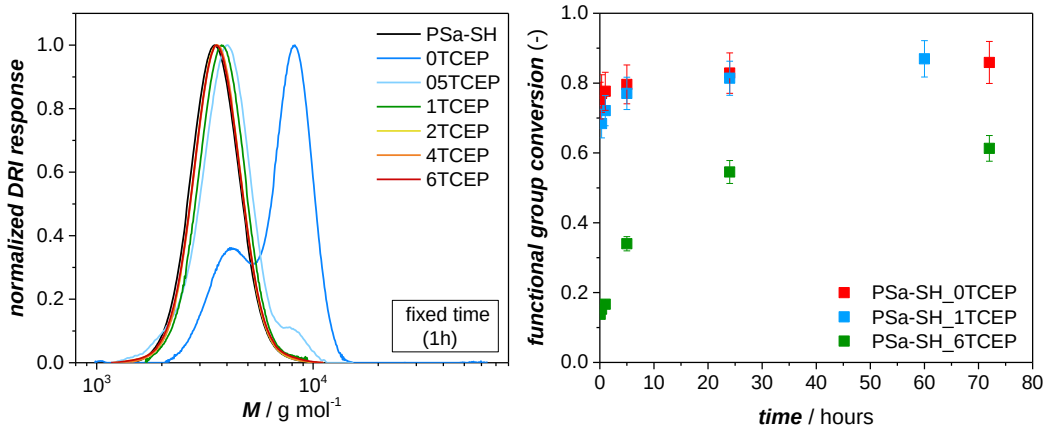

*Figure 4.21 – Left: experimental SEC traces for the evolution of disulfide bond formation after 1 h of reaction time when the reaction was performed using **PSa-SH** and different equivalents of base, as reported in the legend (SH:DBU = 1:15, $[thiol]_0$ = 0.037 mol·L^{-1} in DMF). Right: functional group conversion over time for PFTR using a molar ratio of SH:PFB:DBU = 1:1:15 and different amount of TCEP as highlighted in the legend ($[thiol]_0$ = 0.037 mol·L^{-1} in DMF). The figure is adapted from Ref. [189] with the permission of The Royal Society of Chemistry.*

Alternative routes to overcome the lower reaction rates of PFTR in the presence of the reducing agent are: increasing the amount of base or investigating whether a lower amount of TCEP will still block the disulfide bond formation. Even though the removal of the base after the reaction is not a problematic step, a strong excess was already used in the proposed procedure. Thus, while keeping the molar ratio of SH:DBU = 1:15, different amounts of TCEP were tested to find the minimal amount which can prevent the side reaction. As shown in Figure 4.21 (left), the amount of TCEP can be reduced up to an equimolar ratio SH:TCEP. Here, no disulfide

bond formation was observed in a time frame of 1 h. For lower amounts however, a small percentage of disulfide bond is detectable in the SEC traces. Nonetheless, even for under-stoichiometric amounts of TCEP, the disulfide bonds were cleaved if the reaction time was prolonged to 24 h (refer to Appendix, Figure 8.17). This scenario, however, is less ideal for the final purpose of polymer network formation.

Finally, PFTR was performed with a molar ratio SH:DBU:TCEP = 1:15:1 with a $[thiol]_0$ = 0.037 mol·L^{-1}. The kinetics reported in Figure 4.21 (right, light blue squares) show that the conversion values obtained are comparable to the case where PFTR was performed in the absence of TCEP, with the advantage of avoiding the disulfide bond formation. The SEC traces for PFTR using 6, 1 or 0 equivalents of TCEP are reported in Figure 8.18. Despite the advantages obtained when using TCEP as an auxiliary agent during the synthesis of three-armed star and/or block copolymers, its excessive use simultaneously leads to the formation of undesired by-products and elaborate synthetic effort to remove TCEP when encased in a polymer network. Thus, before adopting the above-reported procedure, the selectivity between the disulfide bond formation and PFTR is explored in supplementary experiments. For a better visualization of the results, a different system needs to be employed in order to overcome the fact that the disulfide and the disubstituted PFTR product will appear in the same position on the SEC trace. Hence, the polymeric thiol derivative was reacted with a monofunctional linker (**1COOPFB**) as depicted in Scheme 4.2.

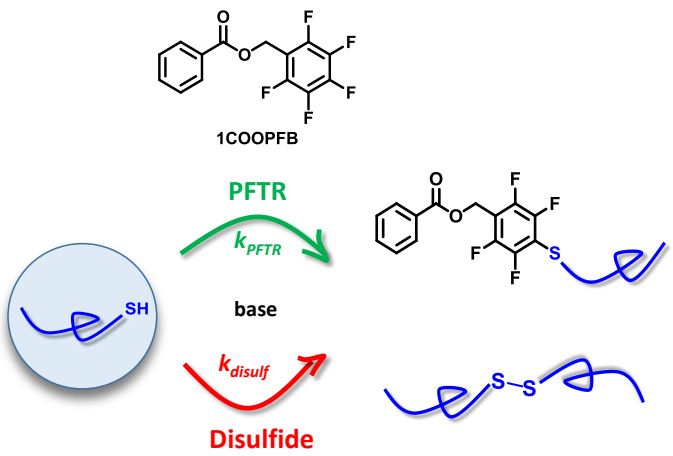

*Scheme 4.2 – The selectivity study is performed upon reaction of the polymeric thiol derivative (**PSa-SH**) and a monofunctional fluorinated linker (**1COOPFB**). PFTR can be visualized as end-capping of the polymer, thus the molecular weight does not vary significantly. On the contrary, if disulfides are formed, the molecular weight of the polymer is double the original value, which can be easily monitored by SEC analysis. The scheme is adapted from Ref. [189] with the permission of The Royal Society of Chemistry.*

In the proposed system (Scheme 4.2), if PFTR takes place, which is evaluated *via* ^{19}F NMR spectroscopy, the difference in terms of molecular weight with the pristine polymer is not significant enough to show a shift in the SEC traces. Contrary to that, if disulfide bond formation occurs, a clear shift of the peak to a position corresponding to double of its original molecular weight is observed in the SEC chromatogram. The reaction was performed employing **PSa-SH** and **1COOPFB**, with a molar ratio SH:DBU:PFB = 1:1:1 and $[\text{thiol}]_0$ = 0.075 mol·L^{-1} in DMF. The ^{19}F NMR spectrum recorded after 24 h and the SEC traces at different reaction times are reported in Figure 4.22.

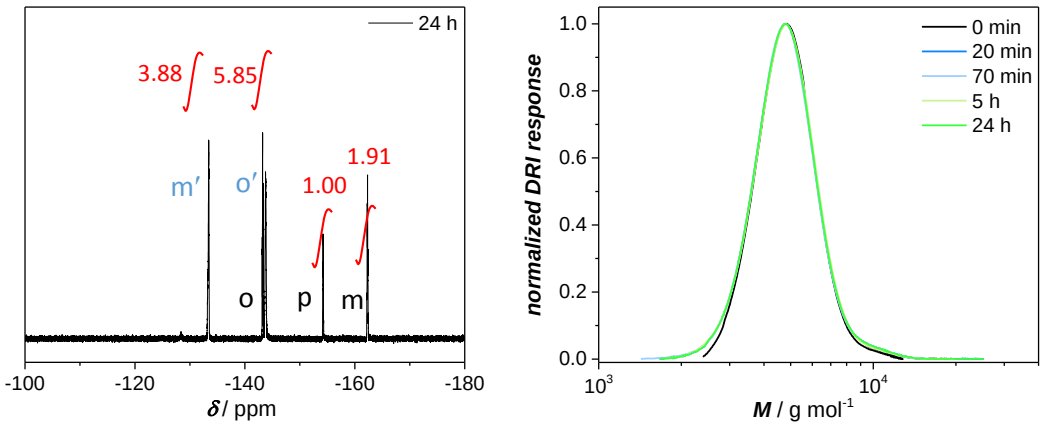

Figure 4.22 – ^{19}F NMR spectrum ($CDCl_3$*, 377 MHz, left) and SEC traces (right) for the para-fluoro–thiol reaction between **PSa-SH** and **1COOPFB**. The ^{19}F NMR spectrum was recorded after24 h of reaction time (~66%), while the SEC traces are reported for different reaction times and present no evidence of disulfide formation. The figure is adapted from Ref. [189] with the permission of The Royal Society of Chemistry.*

As shown in Figure 4.22 left, the conversion increases up to ~66% of reacted group within 24 h, while there is no clear evidence for the formation of disulfide bonds according to the SEC traces (Figure 4.22, right). In order to further prove these findings, ESI-MS was performed (after 24 h), and the recorded mass spectrum is depicted in Figure 4.23. Besides the recorded full spectrum, a comparison between the experimental and the simulated isotopic pattern is presented (Figure 4.23b). The ESI-MS analysis was performed in ion negation mode, thus the molecule is reported as $[M+nCl]^{n-}$. In the full ESI-MS spectrum (Figure 4.23a), both distributions are assigned to the product after PFTR (**PSa-PFB**). In detail, one corresponds to the double charged ($[\textbf{PSa-PFB}+2Cl]^{2-}$) and one to the single charged adduct (($[\textbf{PSa-PFB}+Cl]^{-}$). The excellent agreement between the experimental and simulated ESI-MS spectra for the $[\textbf{PSa-PFB}+Cl]^{-}$ adduct having 23 repeating units (*n*), confirms the success of PFTR (main reaction) over the disulfide bond formation (side reaction).

These results, apparently in contrast with the findings from the *k*MC simulations, can be explained by two hypotheses. The first one, is that disulfide bonds occur at a later stage of the kinetics, as observed also in the simulation in Figure 4.17. The second hypothesis, is that it may be that the presence of disulfide bonds is relevant only for more complex system such as star-shaped polymers. The former hypothesis is not an issue as the kinetic study already showed that high conversion can be achieved within the first 5 h of the reaction, mostly in the absence of free carboxylic groups. The latter hypothesis is challenging to prove experimentally as the interpretation of the SEC traces is complicated in the case of a multi-substituted linker.

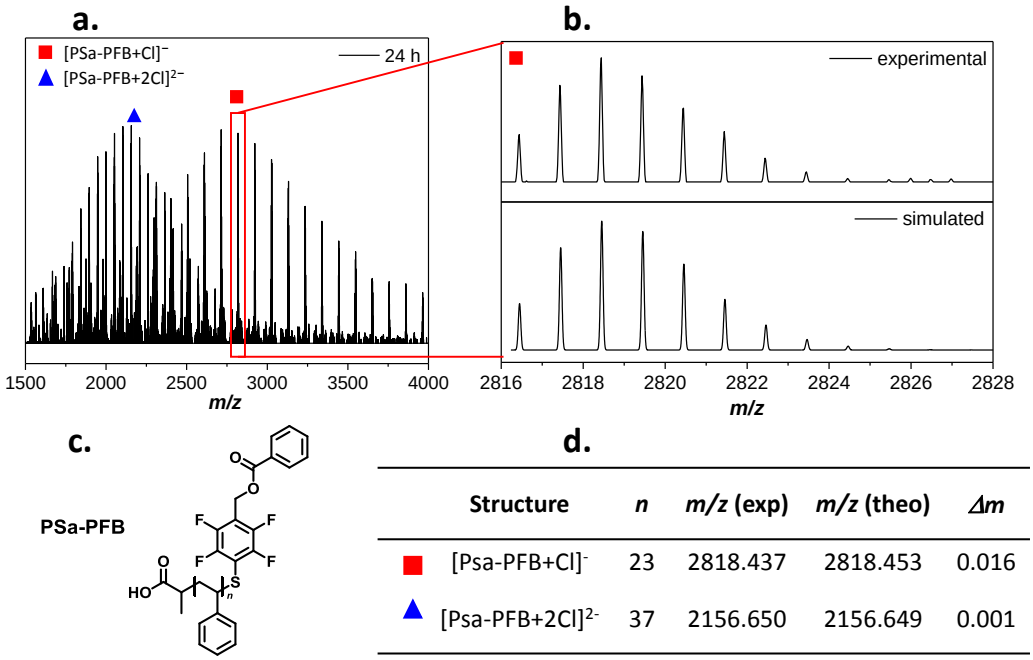

Structure	*n*	*m/z* (exp)	*m/z* (theo)	*Δm*
[Psa-PFB+Cl]⁻	23	2818.437	2818.453	0.016
[Psa-PFB+2Cl]²⁻	37	2156.650	2156.649	0.001

*Figure 4.23 – a. Full (−)ESI-MS spectra for **PSa-PFB** recorded in the range m/z = 1500-4000. b. Comparison between experimental and simulated isotopic pattern for **PSa-PFB** having n = 23 repeating units. c. Chemical structure of **PSa-PFB**, product of the PFTR reaction between **PSa-SH** and **1COOPFB**. d. comparison between the experimental and the simulated m/z ratio for a selected peak in the double (blue triangle) and single charged (red square) region of the (−)ESI-MS spectrum reported in Figure 4.23a. The figure is adapted from Ref. [189] with the permission of The Royal Society of Chemistry.*

In summary, within this section the kinetic study on the PFT reaction has been extended, for the first time, to polymeric thiols. Thiol-capped polymers are easily synthesized after cleavage of the thiocarbonate group (aminolysis) present as chain ends after RAFT polymerization of a selected monomer. Herein, the reactivity of the thiolate, generated upon addition of DBU as base, was studied during the synthesis of three-armed star polymers (mostly employing **PSa-SH** and **3PFB**). Moreover, the difference in reactivity of the thiolate after reaction in two different solvents (THF and DMF), and when the thiol polymer presents a carboxylic group as additional chain end was explored. As for small molecule derivatives, particular attention was given to the investigation of the disulfide bond formation (side reaction) both alone and in

combination with PFTR. The experimental data were complemented by *k*MC simulations in order to determine the rate coefficient of PFTR and the disulfide bond formation reactions. The findings revealed that the reactivity of the thiolate in THF is lower than the one in DMF. Furthermore, side reactions take place during the synthesis of three-armed star polymer in DMF, according to *k*MC simulations. However, disulfide formation is a reversible reaction and its rate coefficient is significantly lower than the one of the main reaction (refer to Table 4.3). Thus, disulfide formation participates in minor measure and PFTR still proceed to high yields. Conversion values up to 80% in DMF were achieved after 48 h of reaction time. Nonetheless, different protocols for performing PFTR while forcefully blocking the disulfide formation were tested. In particular, the combination of the addition of reducing agent and absence of oxygen revealed to be the most efficient solution. Finally, when the thiol polymer was reacted with a monofunctional linker, in order to quantify the presence of disulfide bonds *via* SEC analysis, no clear peak attributable to the disulfide adduct was visible. Thus, the side reaction occurs only during the synthesis of more complex architectures (e.g. three-armed star polymers) at longer reaction times. One possibility is also that the percentage of disulfides was minimal and not detectable according to the methods employed, which is still a good result for the final purpose of applying PFTR to network formation.

In both cases, the minor influence of the side reaction, and the high conversion achievable for PFTR, makes the ligation a suitable reaction to be used for network formation, as it will be investigated in the **Chapter 5**.

4.3 Self-propagated PFTR

Kinetic study

In a recent work, Park *et al.* proposed the organocatalyzed synthesis of fluorinated poly(aryl thioethers), involving the reaction between a silyl-protected thiol and a fluorinated aromatic group upon addition of a minimum amount of base.[198] The idea of a self-catalyzed mechanism is based on two facts: the elimination of a fluoride ion for each PFTR event, and the ability of the released fluoride ions (F^-) to deprotect the silyl groups. The combination of these two events allows for a continuous generation of thiolate ions throughout the entire reaction, first induced by low amounts of an external base and thereafter triggered by fluoride released during PFTR. Inspired from this work, the last point addressed during the in-depth investigation on the *para*-fluoro–thiol reaction was the possibility to introduce a self-propagated mechanism for PFTR, which can be beneficial in case of labile groups. Hence, PFTR was performed employing the non-protected aliphSH and **3COOPFB** with an under-stoichiometric amount of base, such as 0.5 or 0.1 equivalents (in respect to 1 eq. of thiol groups). The fundamental requirement for PFTR to be self-catalytic is that F^- must be able to deprotonate the thiol derivative. Thus, tetrabutylammonium fluoride (TBAF) was the first base used for this study. In addition, tetrabutylammonium hydroxide (TBAOH) and tetrabutylammonium bromide (TBABr) were chosen due to the similarity of their structure with TBAF, yet bearing different counter anions. TBAOH was used to expand the concept of the potential self-catalytic behaviour, as the basicity of the hydroxyl group is expected to deprotonate the thiol, while the counter ion tetrabutylammonium interacts with the generated fluoride to preserve it in its reactive form. Contrary, the bromide ion is not expected to have a sufficient basicity for the deprotonation of the thiol. Thus, TBABr was selected as a negative control compound to exclude possible effects arising from the tetrabutylammonium counter part. Finally DBU was also employed, being it a commonly used base for PFTR.[19]

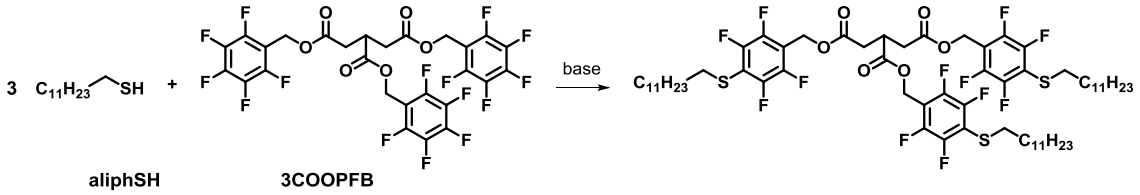

Scheme 4.3 – PTFR model reaction for the elucidation of the self-propagating PFTR mechanism. Herein, different bases were used in order to initiate PFTR such as TBAF, TBAOH and DBU. Each base was used in under-stoichiometric amount respect to the functional group, while the molar ratio of SH:PFB was kept equal to 1:1.

The results of the PFT model reactions using a 1:1 molar ratio between SH and PFB groups but under-stoichiometric amounts of the aforementioned bases, are reported in Figure 4.24 as functional groups conversion over time. The reaction was performed in THF-d_8 with a $[SH]_0$ = 0.075 mol·L^{-1} and followed *via* online ^{19}F NMR spectroscopic measurements.

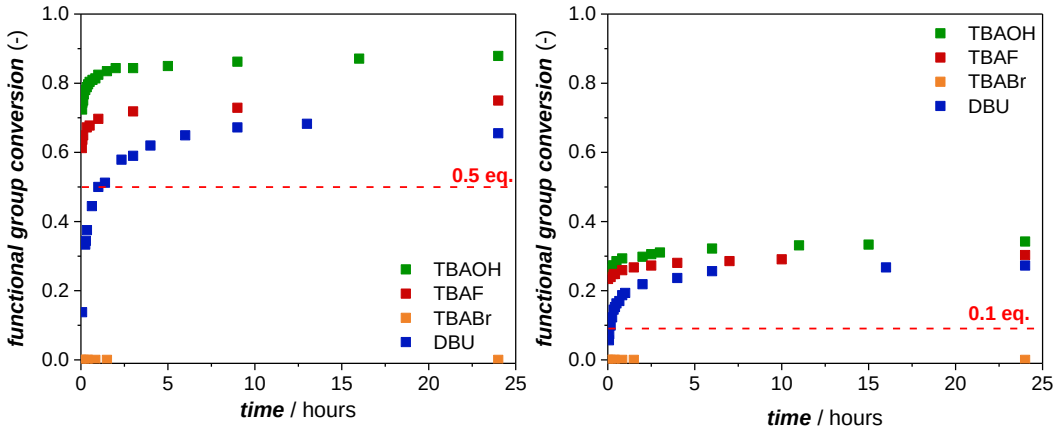

*Figure 4.24 – Functional group conversion over time for PFTR using aliphSH and **3COOPFB** (SH:PFB = 1:1) and either 0.5. (left) or 0.1 eq. (right) of base. In detail, each plot report the result for. TBAOH (green), TBAF (red), TBABr (orange) and DBU (blue). The reaction was performed using [thiol]$_0$ = 0.075 mol·L^{-1}, in THF-d_8 in order to monitor the conversion of the PFTR via online ^{19}F NMR measurements. The red dashed lines indicate the maximum theoretical conversion with respect to the amount of base used (excluding a self-propagating mechanism). Reproduced from Ref. [190] with the permission from John Wiley & Sons.*

Each reaction compared in Figure 4.24 shows conversion higher than the theoretical value. The theoretical value is calculated according to the amount of base used, excluding the possibility of a self-propagated mechanism and is represented by the red dashed line in Figure 4.24. In both graphs the reactivity follows the trend TBAOH > TBAF > DBU, while TBABr does not lead to any conversion. The results agree with the pK_a values of the employed bases. The pK_a values for the bases used in the current study are only available in DMSO in the literature and equal to 31.4, 15.0 and 13.9 for H_2O, HF and DBU-H$^+$, respectively.[199-201] Nevertheless, it is reasonable to assume that even if the absolute value is different, the relative trend of reactivity is still reflected also if THF was used as a solvent. With these values in hand, the difference in reactivity between TBAOH and TBAF is self-explicative, while the lower reactivity of DBU was ascribed to the different chemical structure of the base. To break it down to numbers, in case 0.1 eq. of base were used, the conversions are equal to approximately 30%, 25% and 20% after 2 h for TBAOH, TBAF and DBU, respectively. A further increase of ~5 % is obtained after 24 h. In a similar fashion, when 0.5 eq. of base were employed, conversions of 90%, 75% and 70% were observed after 24 h for TBAOH, TBAF and DBU, respectively. This preliminary investigation leads to two main conclusions: first, the fluoride ion (added as TBAF or generated

from PFTR events) is able to generate the reactive thiolates and second, all bases tested proved to be suitable for promoting, up to a certain extent, the self-propagated mechanism suggested in Scheme 4.4.

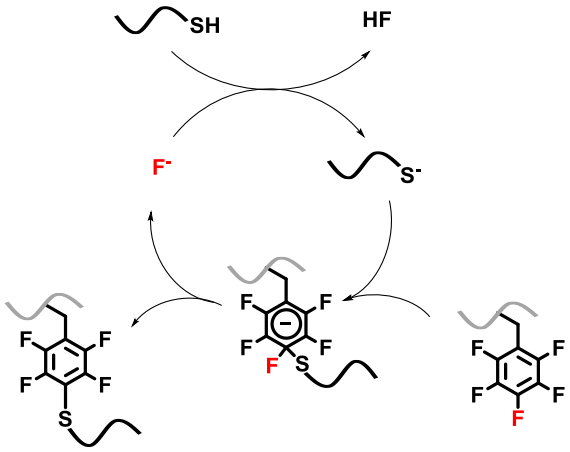

Scheme 4.4 – Proposed self-propagated mechanism for PFTR based on the assumption that the fluoride ions, produced at each reaction step (highlighted in red), is able to promote the next PFTR reaction event. Adapted from Ref. [190] with the permission from John Wiley & Sons.

Even though conversions are higher than the theoretical value, none of the kinetic experiments proceeded to full conversion. In order to assess these results, first some practical considerations were taken in account. Firstly, the fluoride ion is known to react with glass,[202] and thus potentially interact with the walls of the vessel. Thus, the same reaction was repeated in a plastic vial. Moreover, the effect of concentration and temperature was carefully evaluated in additional experiments. Accordingly, the PFTR was performed using both more diluted and more concentrated initial concentrations of functional groups, e.g. $[PFB]_0$ = 0.015 mol·L^{-1} and 0.15 mol·L^{-1} (SH:PFB = 1:1). Additionally, the PFTR was performed at 25 °C and 50 °C ($[PFB]_0$ = 0.075 mol·L^{-1}). The results of all the mentioned systems are summarized in Figure 4.25, where the conversion values obtained after a reaction time of 40 h are reported. This is because at longer reaction times, no further improvements are expected to occur based on the previous studies (refer to Figure 4.24). As evident in Figure 4.25, neither the material of the reaction vessel (glass or plastic), nor the concentration or the temperature have an impact on the final conversion. In each case, a conversion of approximately 25% to 30% is achieved.

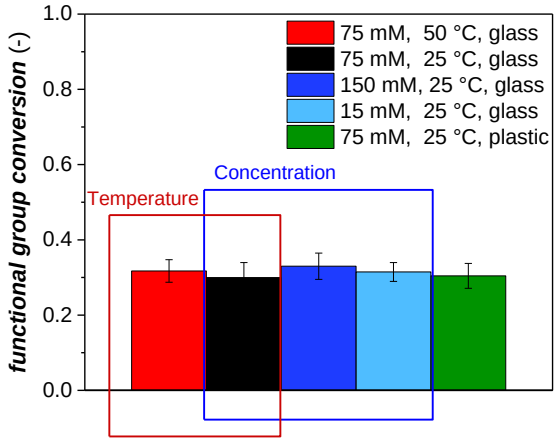

Figure 4.25 –Functional group conversion after a reaction time of 40 h for the PFTR between aliphSH and ***3COOPFB****. The reaction was performed at different temperatures (25 °C and 50 °C), concentrations ($[thiol]_0$ = 0.015, 0.075 and 0.15 mol·L^{-1}) or in different reaction vessels (glass or plastic) to investigate the impact of several parameters on the self-propagating mechanism. In each case the molar ratio of SH:PFB:TBAF = 1:1:0.1. Adapted from Ref. [190] with the permission from John Wiley & Sons.*

Influence of the addition of the base

Interestingly, in Figure 4.24 when 0.1 eq. of base are used a 2.5-fold increase in conversion respect to the base was achieved. Contrary, only a 1.5-fold increase resulted when 0.5 eq. of base were used. Thus, the effect of the same amount of fluoride added either step-wise or at once was compared to verify whether this strategy leads to higher conversion.

In detail, for the one-pot addition, aliphSH was exposed to either 0.1, 0.2 or 0.3 eq. of TBAF and the reaction was performed for 24 h. For the step-wise addition, PFTR was started using 0.1 eq. of TBAF, and each 24 h for two times 0.1 eq. of TBAF was added to the reaction mixture up to a total of 0.3 equivalents. In Figure 4.26, the impact on final conversion of a step-wise addition is displayed.

The results show a significant improvement in the case of a step-wise addition of TBAF. In detail, the addition of 0.1 eq. of base leads to approximately 2.8-fold increase in conversion respect to the base, as shown before. Moreover, when PFTR was performed with 0.2 eq. of TBAF, ≈45% conversion is reached if the base is added at once, in contrast to ≈57% if the same amount added in two consecutive steps. Eventually, another 0.1 eq. of TBAF were added to the previous reaction mixture. This resulted in a final conversion of ≈93%, which is significantly higher compared to the control experiment (65% conversion) where 0.3 eq. of TBAF were added “all at once” at the beginning of the reaction.

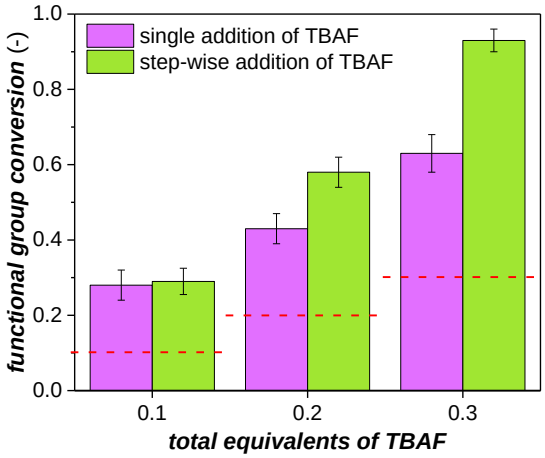

Figure 4.26 – Impact of the step-wise addition of base (TBAF) on the final conversion obtained after performing PFTR at ambient temperature employing a $[thiol]_0$ = 0.075 mol·L^{-1}. The step-wise addition of base (green bars) is compared to the final conversion obtained after using the same amount of base but added at once at the beginning of the reaction (purple bars). The amount of base used are reported along the x axis. Adapted from Ref. [190] with the permission from John Wiley & Sons.

To summarize, the results show that, at any stage, the step-wise addition of base appeared to be beneficial since almost full conversion is achieved after the addition of 0.1 eq. of base for three consecutive times. One hypothesis is associated with the solvation of the fluoride ions, which makes the produced fluoride ions no longer reactive. Thus, "freshly added" equivalents of F^- (TBAF) are more reactive. In each case, a significant influence of the self-propagating mechanism is evidenced, mostly when the experimental data are compared to the red dashed line, representing the theoretical value achievable with a given amount of base in case no self-propagating mechanism is taken in account.

Influence of structurally different thiol and of the solvent polarity

The only difference between the herein reported system and the one introduced by Park *et al.* is the presence of free thiol functional groups instead of a silyl-protected thiol analogous structure. Thus, even if the concept of pH is meant for aqueous system, one hypothesis for the lower performances of the herein introduced system could be associated with changes of the pH of the reaction mixture over the course of the reaction. Accordingly, the generation of HF during the reaction might lower the pH of the solution until a certain threshold is reached, where the thiol remains in its protonated state due to the acidity of the media. In order to verify this hypothesis, three structurally different thiols, thus having different pK_a values, were tested in terms of their reactivity towards PFTR. For each thiol, the PFTR was performed under the same reaction conditions (SH:PFB:TBAF = 1:1:0.1, $[thiol]_0$ = 0.075 mol·L^{-1}). The selected thiols are dodecanethiol (aliphSH), 4-methoxybenzyl mercaptan (benzSH) and thiophenol (phenSH),

which have, in the listed order, decreasing pKa values.[192] The expectation is that given the same environment, the more acidic thiol will reach higher conversion, as the formation of the thiolate is less dependent from minor changes in the pH values. The conversions over time obtained for the different thiols are compared in Figure 4.27.

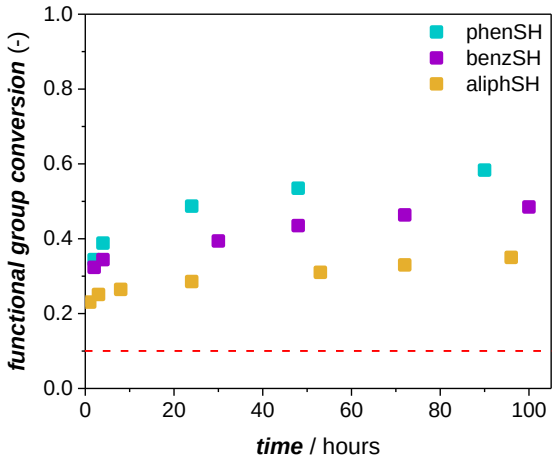

Figure 4.27 –Functional group conversion over time for the PFTR performed using thiol derivatives with decreased acidity in the order phenSH > benzSH > aliphSH. The reaction was performed using SH:PFB:TBAF = 1:1:0.1 and a $[thiol]_0$ *= 0.075 mol·L*$^{-1}$*. Adapted from Ref. [190] with the permission from John Wiley & Sons.*

The results plotted in Figure 4.27 are in line with the expectation. In detail, after the addition of 0.1 eq. of base to a mixture of thiol and fluorinated linker, conversion values of approximately 30%, 45 % and almost 60% for aliphSH, benzSH and phenSH, respectively, were observed. Thus, higher conversions are achieved when more acidic thiols were used.

Driven by this data, the influence of the solvent polarity was explored. As already observed for the previous kinetic study involving polymeric thiol derivatives, switching from THF to DMF led to significant improvement in terms of conversion and/or reaction times. Hence, the performances of the self-propagated behaviour in DMF were evaluated for each thiols. Furthermore, DMSO was also considered as a solvent due to its higher polarity, even though no reports about its ability to promote PFTR are reported in the literature yet. Aside the type of solvent, all the other parameters are kept constant, e.g. SH:PFB:TBAF = 1:1:0.1 and $[thiol]_0$ = 0.075 mol·L^{-1}. The results are depicted in Figure 4.28 where, in order to highlight the performances of the solvent, each graph compares the functional group conversion over time for a selected thiol tested in different solvents. Noteworthy, aliphSH was immiscible in DMSO, so the reaction could not be performed in this case.

In Figure 4.28a, the reactivity of aliphSH in both THF (blue squares) and DMF (orange squares) is displayed. In the case where DMF was used as a solvent, double the conversion was achieved

at any stage of the kinetic study. Approximately 70% of fluorinated groups have reacted with thiols after 48 h in DMF compared to only 30% when the reaction was performed in THF.

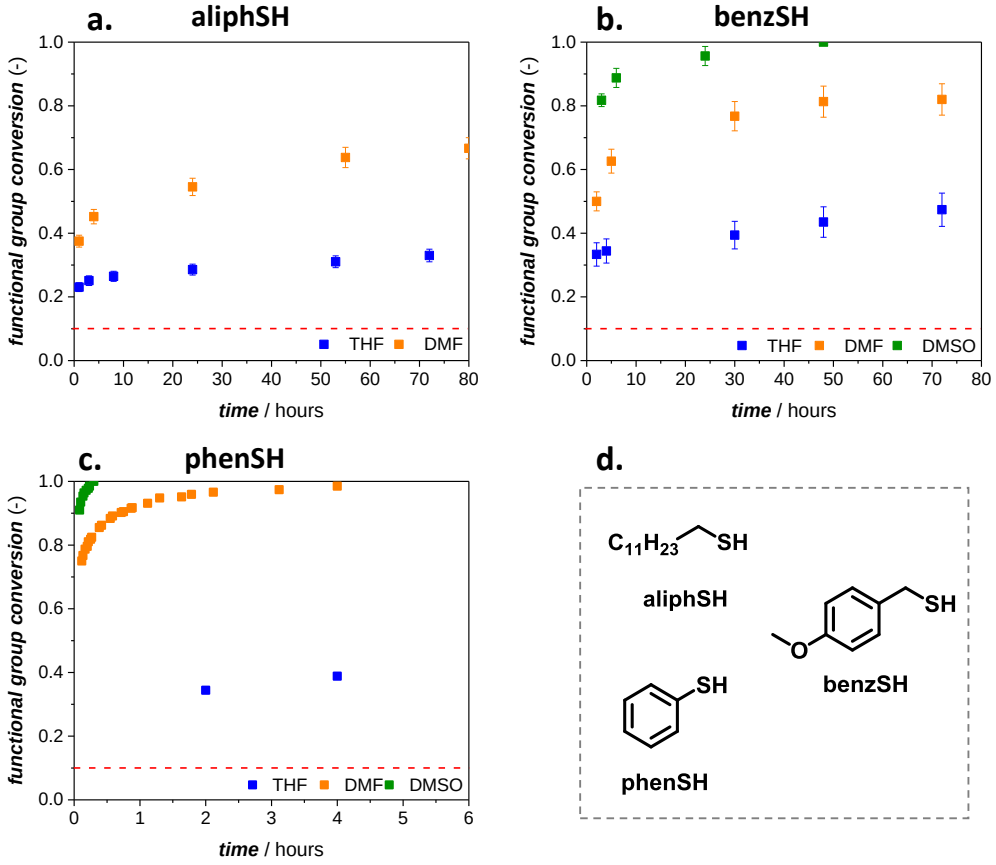

Figure 4.28 – Functional group conversion for PFTR using different combination of solvent and thiol. Each graph compares the reaction rates for a thiol in different solvents such as THF (blue), DMF (orange) and DMSO (green), (SH:PFB:TBAF = 1:1:0.1 and [thiol]$_0$ = 0.075 mol·L^{-1}). The thiol used is reported as headline of the graph, while its chemical structure is visible in the dashed box (d). The dashed red line is representative of the theoretical conversion, which should be achieved in case no self-propagating mechanism was possible. Adapted from Ref. [190] with the permission from John Wiley & Sons.

Similarly, when PFTR was performed using benzSH (Figure 4.28b), the conversion reaches values of 40% in THF (blue squares) and 80% in DMF (orange squares) after 48 h. Interestingly, within the same 48 h the reaction proceeds to quantitative conversion in DMSO (green squares). Lastly, when the reactivity of the more acidic phenSH is analyzed (Figure 4.28c), the reaction proceeded to quantitative conversion for both DMF and DMSO, with DMSO giving the fastest reaction rates. The reaction proceeded to completion after only 5 min in DMSO, while a reaction time of 4 h was necessary in DMF. In contrast, a maximum of 50% was achieved after 3 days when THF was used as a solvent. Since polar solvents promote the nucleophilic substitution events in PFTR,[203] the enhanced reactivity is attributed to the increased polarity when using DMF and DMSO compared to THF.[204]

4.4 Summary

The study presented in the last section proves the possibility to start PFTR with a source of fluoride ions, independently from the fact that fluoride is added to the solution (e.g., using TBAF as a base) or generated in situ as a by-product during the reaction. Moreover, even though the PFTR under the employed conditions cannot be defined as self-catalytic, the possibility for a self-propagating mechanism for PFTR was unambiguously demonstrated.

In the context of network formation, the possibility of a self-propagated mechanism it is of high relevance in case functional group sensitive to basic conditions are present within the bifunctional derivative or the crosslinker. Despite the presence of labile groups, it is without any doubt more efficient to perform PFTR using equimolar amount of base (i.e. DBU).

Importantly, a variety of fluorinated derivatives including three- and four-armed linkers, which allow for a selective mechanism for PFTR (i.e. no multiple substitution), were synthesized.

Concerning the disulfide bond formation, the *k*MC simulations revealed that the side reaction does not play a major role for small molecule thiol derivatives, while it does occur in small percentages during the synthesis of three-armed star polymer architectures in polar solvent (i.e. DMF). However, no evidence of the disulphide species was observed experimentally within the first 24 h for the reaction between **PSa-SH** and **1COOPFB**.

Notably, the presence of carboxylic acid groups partially neutralizes the base lowering the reaction yields. Nonetheless, as commonly reported in the literature, the problem can be overcome by employing a suitable protecting group, which upon PFTR can be removed to afford the desired poly(acrylic acid) based architectures.[47]

Remarkably, the main advantage of PFTR is most likely the possibility to follow the reaction *via* ^{19}F NMR spectroscopy without the need of additional purification before spectroscopic analysis. With these positive results in hand, the PFTR was applied, in the next step, to network formation.

5

Network Formation *via* *para*-Fluoro–Thiol Reaction

Polymeric networks were synthesized in the current chapter *via* the end-linking strategy (ELS), which is one of the most powerful approaches towards the achievement of more homogeneous networks according to the literature.[120, 152] This strategy is based on the reaction between a bifunctional precursor and a three- or four-armed linker bearing complementary functionalities, as displayed in Figure 5.1. In this way, the average mesh size and the macroscopic properties of the final network can be easily tuned by varying the molecular weight and the backbone of the bifunctional precursor, respectively.[152]

Importantly in the current work, the synthetic advantages of the end-linking strategy are completed with analytical advantages by using the *para*-fluoro–thiol reaction (PFTR), carefully studied and optimized in **Chapter 4**, as ligation for the crosslinking reaction (Figure 5.1). The idea is based on the fact that the presence of heteroatoms such as sulfur and fluorine, strategically located only at the crosslinking points, can lead to the identification and quantification of the unreacted moieties *via* non-destructive analysis such as ^{19}F NMR spectroscopy.

Furthermore, in the ^{19}F NMR spectrum, no interference by proton or carbon atoms will be present. Thus, the resonances associated with the fluorinated ring will be clearly displayed on the spectrum eliminating inaccuracy during integration of the signals.

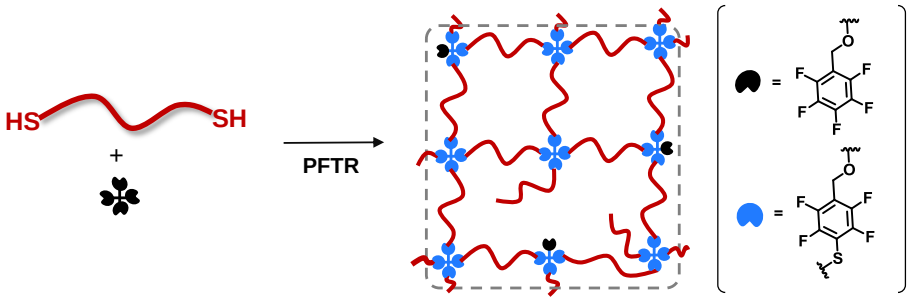

Figure 5.1 – Representation of a network obtained via end-linking strategy. The example displays the reaction of a bifunctional thiol and a four-armed fluorinated linker.

The main goal is to introduce the possibility to detect defects, where present, without the need to disassemble the network. With these broad advantages in mind, the following chapter discusses and explores the use of PFTR for the syntheses of disparate networks.

Initially, highly crosslinked networks, synthesized using bifunctional precursors with low molecular weight, were studied because of the high percentage of functional groups, which is a necessary condition to evaluate the expanded analytic toolbox facilitated by the presence of fluorine atoms.

Subsequently, the approach was adapted for the formation of networks starting from well-defined polymer precursors synthesized *via* RAFT polymerization followed by end-group modification.

The use of polymeric bifunctional precursors leads to networks with a lower degree of cross-linking. As a results of the larger mesh size, the networks present higher swellability, which is a relevant factor for some applications. The synthesis of network using PFTR was optimized for structurally different polymer precursors, e.g. polystyrene and poly(methacrylates), as discussed on detail in the current chapter.

Part of this chapter are reproduced from Ref. [188] with permission from The Royal Society of Chemistry.[188] The XPS and ToF-SIMS measurements were performed by Dr. Sven O. Steinmüller. The project was supervised by Prof. Dr. Leonie Barner.

The XPS and ToF-SIMS measurements in Section 5.2.1 were performed by Dr. Azmi Raheleh (KIT)

The ^{1}H NMR-relaxometry measurements were performed by Christoph Pfeifer (KIT).

The four-armed linker tetrathioltetraphenylmethane (4phenSH) was kindly provided by Matt Yannik (KIT)

The project was supervised by Prof. Dr. Leonie Barner.

5.1 Networks from Small Molecules

Initially, the three-armed fluorinated linker not containing any ester bond (**3PFB**), used in the previous kinetic study, was reacted with a bifunctional thiol derivative in order to achieve network rather than three-armed stars. The resultant networks present a high degree of crosslinking, due to the low molecular weight of the thiol employed. The high percentage of the fluorinated groups make them an ideal substrate for presenting the variety of analytical tools for the characterization of the final material.

Importantly, the reaction proceeded using a 1:1 stoichiometric ratio between the functionalities (i.e. aromatic fluorinated group and thiol) in order to avoid a large number of unreacted moieties, which cause defects in the network microstructure.

Initially, a representative network (Scheme 5.1) was obtained upon reaction of 1,4-phenylenedimethanethiol (PDT) with **3PFB** in THF ($[SH]_0$ = 1.8 M), using DBU (1 eq.) as base. Interestingly, the reaction mixture almost instantaneously turned into a gel, yielding the corresponding network (**PDT-N**) (Scheme 5.1). After 30 min, the soluble fractions were removed by washing the network with an excess of solvent (THF). The solvent was changed at least three times in order to remove completely the extractables from the crosslinked structure. Finally, the network was dried in a vacuum oven at 25 °C overnight, and characterized.

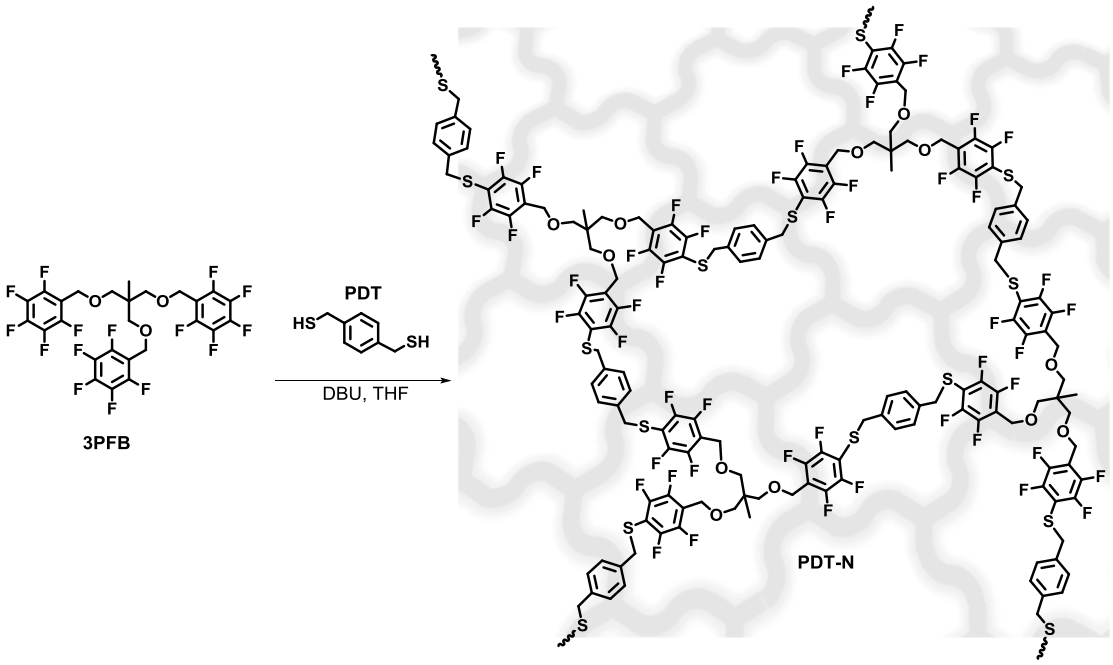

*Scheme 5.1 – Reaction scheme for network formation employing a three-armed fluorinated linker (**3PFB**) and a bifunctional thiol (PDT). The PFTR was performed using a molar ratio of SH:PFB:DBU equal to 1:1:1 in THF. The figure is adapted from Ref. [188] with the permission of The Royal Society of Chemistry.*

As shown in the previous chapter, ^{19}F NMR spectroscopy is a powerful tool for tracking the progress of the PFT reaction. Thus, the freshly obtained **PDT-N** network was placed in an NMR tube and swollen in $CDCl_3$ for analysis. Thereafter, the tube was placed into the auto sampler and the measurement was performed in the same way as for liquid samples. This procedure is named "gel-phase". In literature it is reported that the results obtained after measurements in the gel-phase are comparable to those recorded *via* solid-state NMR spectroscopy, confirming the validity of the approach.[117] The ^{19}F NMR spectrum for the synthesized network is reported in Figure 5.2 (bottom, blue line) and compared to the one of the **3PFB** linker used as starting material (Figure 5.2, top, black line).

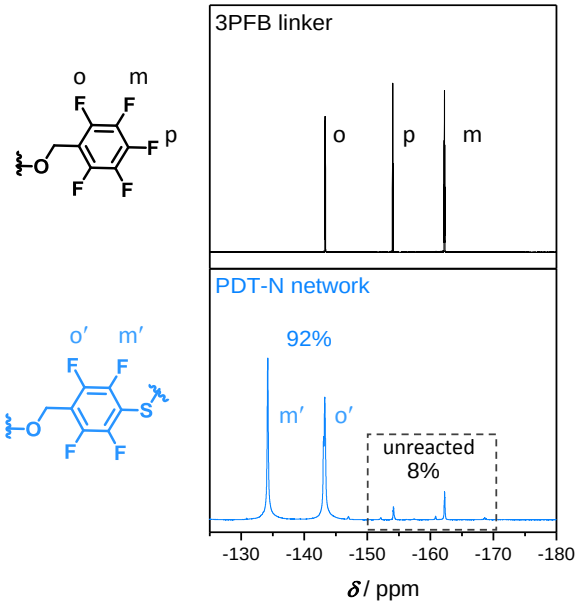

*Figure 5.2 – ^{19}F NMR spectra ($CDCl_3$, 377 MHz) of the fluorinated aromatic ring before (**3PFB** linker, black) and after (**PDT-N** network, blue) network formation via PFTR. The reaction was performed employing a 1:1 molar ratio between the functional groups and a $[PFB]_0$ = 1.8 mol·L^{-1} in THF, using DBU as base. The functional group conversion within the network resulted equal to 92%. The figure is adapted from Ref. [188] with the permission of The Royal Society of Chemistry.*

The ^{19}F NMR spectrum of **PDT-N** (Figure 5.2, bottom panel) delivers two main messages. First, the new resonances appearing at $\delta = -134.2$ and -142.2 ppm are ascribable to the *o′* and *m′* fluorine atoms after PFT reaction, as largely discussed in **Chapter 4**, which indicates the successful synthesis of the product according to the proposed reaction pathway (Scheme 5.1). Moreover, in the ^{19}F NMR spectrum of the gel (Figure 5.2, bottom) it is noticeable that a small fraction of unreacted fluorinated aromatic groups remains. The unreacted moiety were quantified by comparison of the integral of the resonances corresponding to the fluorine atoms before and after reaction, and resulted equal to 8%. Importantly, in contrast to the examples reported

in **Chapter 2** (section 2.3.4), the information regarding the number of reacted moieties (92%) is accessible without the need to disassembly the network structure, highlighting the analytical power of PFTR in combination with ^{19}F NMR spectroscopy.

To complement these ^{19}F NMR measurements, other analytical techniques were explored to collect further information on the synthesized network by taking advantage of the presence of heteroatoms (S and F), strategically located only at the junction points.

A common and simple analysis to perform on solid materials is the Attenuated Total Reflectance-Infrared Spectroscopy (ATR-IR). Due the large amount of data available in literature nowadays,[205] it is possible to assign the different bands present in a given IR spectrum to the corresponding functional group present in the analyzed molecule. For an accurate interpretation of the **PDT-N** IR spectrum, it is important to record also those of the starting materials, the **PDT** thiol and the **3PFB** linker. The mentioned IR spectra are compared in Figure 5.3.

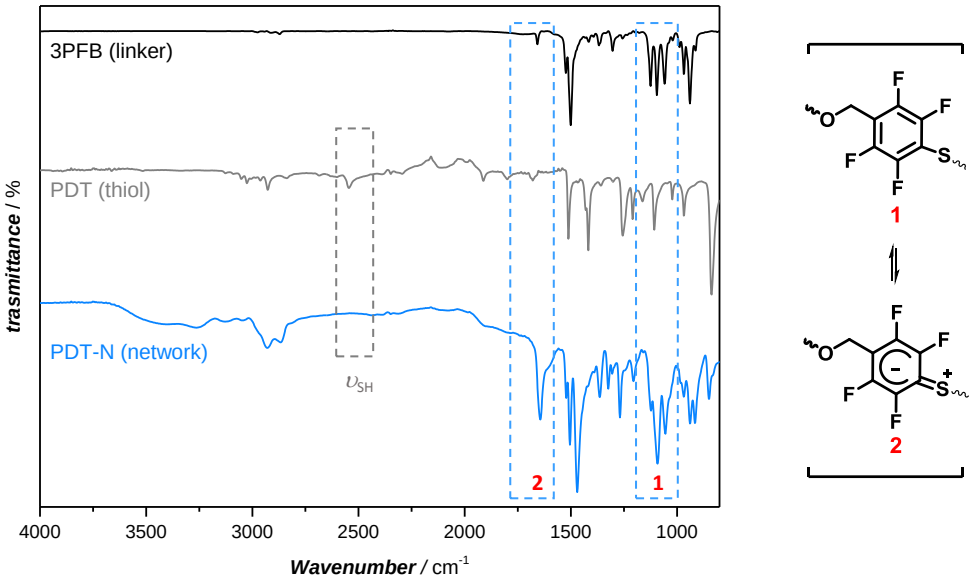

*Figure 5.3 – Left: ATR-IR spectra for, from top to bottom, the pristine linker (**3PFB**, black), the bifunctional thiol (PDT, gray), the synthesized network (**PDT-N**, blue). Right: the two resonance structures (**1** and **2**) for the fluorinated aromatic ring after ligation, responsible for the bands highlighted with blue boxes in the ATR-IR spectra. The gray box represents the disappearance of the stretching vibration assigned to the S-H bond. The figure is reproduced from Ref. [188] with the permission of The Royal Society of Chemistry.*

In the reported example (Figure 5.3), the stretching of the C_{arom}-H bond, arising from the aromatic ring of the **PDT** thiol, is visible at 3030 and 2900 cm^{-1} in both the network and the thiol precursor. However, more informative is the band at υ = 2650 cm^{-1} for **PDT** (Figure 5.3, gray box), which is ascribable to the S-H stretching. In particular, the presence of the latter band for the thiol precursor but not in the final network confirms the proposed reaction pathway as well as the high conversion detected *via* ^{19}F NMR spectroscopy.

Additionally, for the spectrum reported in Figure 5.3 (blue line), a band appears at $\upsilon = 1650\ cm^{-1}$, which is associated with the resonance structure of the newly formed aromatic ring. Accordingly, the PFT reaction involves the replacement of a fluorine with a sulfur atom, which is an electron-rich atom containing one lone pair of electrons. Hence, a resonance structure as the one labelled with the number **2** in Figure 5.3 (right) occurs. Less diagnostic but still relevant is the band arising from the resonance structure **1** (Figure 5.3, right), highlighted with a blue box (**1**) in the IR spectrum.

Subsequently, due to the presence of fluorine atoms, the chemistry of the crosslinking point was observed *via* X-ray Photoelectron Spectroscopy (XPS) and Time-of-Flight Secondary Ion Mass Spectrometry (ToF-SIMS).

Analysis of the surface *via* XPS permits to distinguish between different carbons present within a sample. This is possible because their binding energy is not identical, and can shift between approximately 285 to 294 eV depending on the chemical environment of the carbon itself (e.g. identity of X in a C-X bond).[206]

The C1s spectrum obtained after XPS analysis of the **3PFB** linker is displayed in Figure 5.4 (top, black line). Each spectrum was referenced at 285.0 eV (C-C, C-H) and peak fitting procedure was performed according to the literature.[207] In particular, four peaks were identified. First, the C-C and the C-O bonds present in the core of the linker are detectable (refer to Scheme 5.1). The other two peaks are associated with the C-F bond, with a particular differentiation between C-F_{o+m} and C-F_{para}, while the only carbon on the fluorinated aromatic ring not connected to a fluorine atom has a similar binding energy to C-O.[208] Next, the C1s spectrum of the **PDT-N** network is compared to the one of the linker in Figure 5.4 (bottom, blue line).

Here, some differences between the C1s spectrum of the network and the linker can be highlighted. First in the network spectrum, the C-C peak is now the peak with the highest intensity, due to the fact that many additional C-C bonds have been introduced after network formation from the thiol. For **3PFB** the main peak is the C-F_{o+m} peak, as expected from the chemical structure (Scheme 5.1). Next, a small shift from 286.5 eV to 286.2 eV is observed for the binding energy of the C-O peak. This is because this peak now has contributions from both the C-O and C-S bonds. A small difference in the binding energy is noticeable for C-F_{o+m} compared to C-$F_{o'+m'}$. Accordingly, the corresponding peak shifts from 288.6 eV (**3PFB** linker) to 287.8 eV (**PDT-N** network), which can be attributed to the replacement of an electron-withdrawing atom such as F with an electron-donating atom like sulfur.

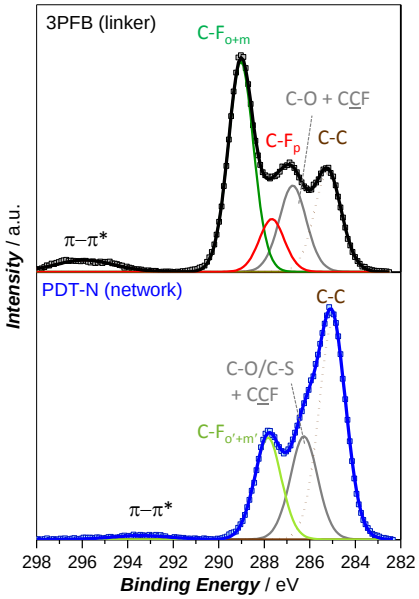

*Figure 5.4 – XP C1s spectra of the pristine linker (**3PFB**, top, black line) and the freshly synthesized network (**PDT-N**, bottom, blue line). The figure is adapted from Ref. [188] with the permission of The Royal Society of Chemistry.*

Finally, the surface of the network was analyzed *via* ToF-SIMS for the identification of specific fragments associated with the aromatic fluorinated group before and after PFTR. These fragments are $[C_7HOF_5]^-$ for the **3PFB** linker and $[C_7HSOF_4]^-$ for the formed network (**PDT-N**). The relative amount of the two above-mentioned fragments in the **3PFB** linker and the **PDT-N** network is depicted in Figure 5.5. For clarity, the color scale is an indication of the abundance of a given fragment, with brighter colors indicating a higher amount of the selected species.

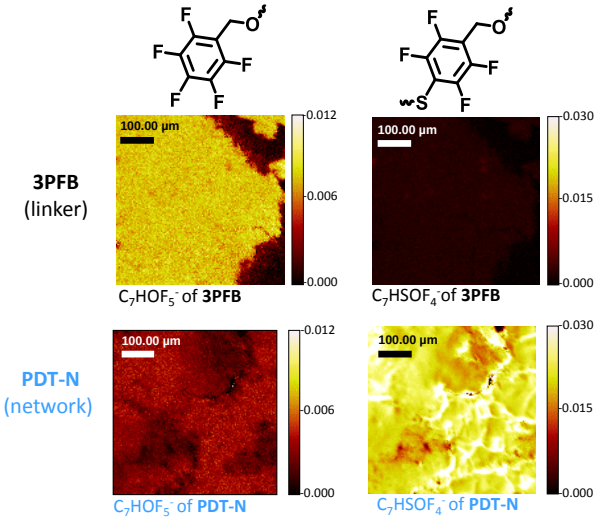

*Figure 5.5 – ToF-SIMS analysis of the precursor linker (**3PFB**, top) and the synthesized network (**PDT-N**, bottom). Highlighted is the relative abundance of the fluorinated aromatic ring before (left) and after (right) PFTR. Brighter colors indicate a higher abundance of the selected fragment. The figure is reproduced from Ref. [188] with the permission of The Royal Society of Chemistry.*

On the left side of Figure 5.5, the unreacted PFB fragment is displayed. According to the color scale, this fragment is detectable in high percentage in the **3PFB** linker (top) but not in the synthesized network (bottom). In contrast, the fragment corresponding to the fluorinated moiety after ligation is present in high percentage for the **PDT-N** network (bottom) but it is absent in the parent linker (top).

Clearly, all of the above analyses – ^{19}F NMR spectroscopy, XPS, ToF-SIMS, ATR-IR – support successful network formation with high conversion of the precursors within the synthesized network, and therefore affirming the synthetic and analytic advantages of network formation *via* the end-linking strategy employing PFTR.

In the next step, to demonstrate the versatility of the PFTR as crosslinking reaction, and in the view of its use for polymer network systems, a variety of alternative thiol derivatives were employed as bifunctional precursor, as shown in Figure 5.6. These include an aliphatic thiol (BT), mimicking a general polymer backbone, a thiol containing ether linkage (DODT), mimicking PEG-ylated polymers, and one possessing hydroxyl groups along the chain (DTT).

Herein, the same study performed for **PDT-N** was repeated for the listed thiols. The networks were synthesized using a molar ratio of SH:PFB:DBU equal to 1:1:1 and a $[\text{PFB groups}]_0 = 1.8\ \text{mol}\cdot\text{L}^{-1}$ in THF. As before, **3PFB** was used as fluorinated linker.

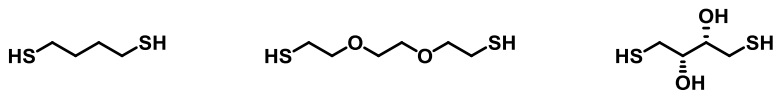

BT DODT DTT

Figure 5.6 – List of bifunctional thiol derivatives used for the synthesis of diverse networks via para-fluoro–thiol reaction (PFTR). List of abbreviations: butanedithiol (BT), 2,2'-(Ethylenedioxy)diethanethiol (DODT) and dithiothreitol (DTT).

In each case ^{19}F NMR and ATR-IR spectroscopy, as well as XPS and ToF-SIMS analysis were performed, with all data shown in Appendix. In detail, the ^{19}F NMR spectra for each network showed that the reaction proceeded as desired, with the appearance of the diagnostic resonances at $\delta = -134$ and -143 ppm (Figure 8.19), and a conversion higher than 95% in all cases. These values demonstrate the high efficiency of the reaction in the context of network formation. Similarly, ATR-IR measurements show the two diagnostic bands attributable to the fluorinated aromatic ring after nucleophilic substitution, along with the disappearance of the band corresponding to the stretching of the SH bond at $\upsilon = 2650\ \text{cm}^{-1}$ (Figure 8.20). Additionally, XPS and ToF-SIMS (refer to Appendix, Figure 8.21) results are comparable to those detailed for the **PDT-N** network, independently from the chemical structure of the thiol employed, underpinning the versatility of the approach.

Finally, the differences in the swelling and in the thermal behavior were investigated. For the latter, differential scanning calorimetry (DSC) analysis was performed on each network to identify the glass transition temperature (T_g). In the case of networks, the T_g is influenced by the degree of crosslinking (*DC*) and the rigidity of the wall of the pore. The values obtained after DSC analysis are summarized in Table 5.1.

Table 5.1 – Summary of the glass transition temperature (T_g) for the network obtained starting from structurally different thiols. The letter "-N" associated to the name of the thiol employed indicates that the result refer to the obtained network.

Network	**T_g (°C)**
PDT-N	54.7
DTT-N	50.2
DODT-N	40.2
BT-N	38.0

Herein, the T_g follows the trend **PDT-N** > **DTT-N** > **DODT-N** ≈ **BT-N**. Assuming the same *DC* – since the molecular weight of the thiol precursors is generally similar – the trend reflects the rigidity of the pore. Accordingly, the **PDT-N** is the most rigid one as the elastic chain consists of one aromatic ring. Similarly, the high T_g value observed for **DTT-N** suggests that the mentioned network possess a rigid structure, for instance arising from the presence of hydrogen bonds between neighboring hydroxyl groups.

Subsequently, the swelling behavior was tested for each network in two different solvents, THF and ethanol (EtOH). The obtained values are reported in Table 5.2.

Table 5.2 – Summary of the degree of swelling (w/w) obtained for different networks (-N) in THF and ethanol (EtOH).

Network	**Swelling ratio (w/w)**	
	THF	**EtOH**
PDT-N	1.7	0.3
DTT-N	0.3	0.4
DODT-N	2	0.6
BT-N	1.6	0.1

As mentioned in **Chapter 2**, the degree of swelling is influenced by the polymer/solvent interaction (mixing term) and the degree of crosslinking, *DC* (elastic term). Accordingly, the values reported in Table 5.2 indicate a higher affinity of the networks for THF compared to ethanol. The lower affinity towards ethanol is associated with the absence of functional groups on the elastic active chain able to create hydrogen bond with ethanol. Moreover, the increased degree

of swelling in the direction **DODT-N** > **PDT-N** ≈ **BT-N** >> **DTT-N** reflects the small differences in the core structure of the thiol derivatives. Noteworthy, in both solvents, an exception is observed for **DTT-N**. In line with results from DSC analysis, this is associated to the presence of hydrogen bonds between the hydroxyl group present along the elastic chain, which leads to higher degree of crosslinking. This hypothesis is further supported by the low intensity of the O-H stretching in the ATR-IR spectrum reported in Appendix (Figure 8.20).

In conclusion, this section develops the feasibility of PFTR as a ligation tool for network formation. Importantly, it was demonstrated that the synthesis of the networks *via* PFTR opens the door for the identification and quantification of the unreacted functionality simply by NMR measurements, thus without the need to destroy the network. Moreover, the variety of analytical tools for the qualitative analysis of the surface of the network was expanded to ATR-IR, XPS and ToF-SIMS analysis, with the presence of the fluorinated aromatic ring being a key feature for the successful employment of each analysis. Finally, the use of structurally different bifunctional thiols confirms the possibility to expand the PFTR to other thiol derivatives, potentially including polymeric thiols. Since the suitability of polymeric thiol towards PFTR was anticipated in **Chapter 4** for star shape polymer architecture, the following chapter explores the potential use of bifunctional α,ω–polymeric thiol derivatives for network formation.

5.2 Networks from Polymers

While for some application the crosslinking reaction occurs between small molecule derivatives as a considerably high degree of crosslinking is required, e.g. 3D printing,[209] for others, like desalination, it is important to achieve a reasonable degree of swelling.[182] In such cases, bifunctional polymer precursors are commonly used, allowing for easier tuning of properties such as swelling,[210] thermal[211] and mechanical.[154] Simply by changing the chemistry of the polymer, it is possible to obtain hydrophilic rather than hydrophobic networks, due to the different functional groups present along the polymer backbone, which lead to a different polymer/solvent interaction. After determining the most suitable backbone chemistry for a specific application, the mesh size, and thus the degree of swelling, can be tuned by modifying the average length of the polymer precursor, as shown in the following section (Figure 5.7). In the next session, three polymer precursors containing a different number of repeating units (*n*) will be synthesized to achieve "short" (*n* = 36), "medium" (*n* = 64) and "long" (*n* = 82) elastic chains in the final network.

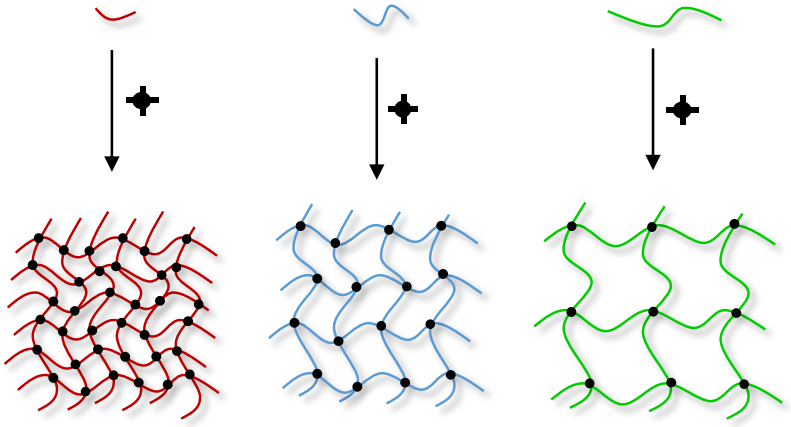

Figure 5.7 - Representation of three different networks synthesized via the end-linking strategy between a bifunctional polymer precursor and a four-armed linker. The impact of the chain length of the polymer precursor on the degree of crosslinking of the final polymer is highlighted.

Accordingly, the length of the polymer precursor determines the degree of crosslinking (*DC*) as follows:

$$DC = \frac{1}{M_c / M_{ru}} * 100 \tag{5.1}$$

where M_c and M_{ru} are the molecular weight of the elastic chain length (refer to Equation 2.26) and of the repeating unit of the polymer backbone, respectively.

For network formation, the two precursors must possess the suitable complementary functionalities: the thiol group and the fluorinated aromatic ring. However, no limitations on whether the thiol group is located on the bifunctional polymer or on the crosslinking agent are, in principle, present. Thus, both synthetic strategies will be evaluated in the following sections, starting from the use of thiol polymers, due to the large amount of knowledge gained in **Chapter 4**.

5.2.1 Polymeric Thiol Derivatives

As anticipated, in this section bifunctional polymeric thiol derivatives were used in order to achieve polymer networks. In particular, the polymer precursor was reacted with both a three- and a four-armed linker. The three-armed linker serves to link the polymeric networks to the results reported so far, while the four-armed linker serves as comparison of the network synthesized *via* the end-linking strategy (ELS) using PFTR with those synthesized *via* FRP, as the crosslinking agent in FRP leads to 4 crosslinking points.

The comparison between networks *via* FRP and ELS using PFT reaction is particularly important for verifying whether the ELS leads to a more homogeneous network microstructure.

It is important that the compared networks possess the same degree of crosslinking (*DC*). For ELS using a four-armed linker, the *DC* is calculated as reported in Equation 5.1, while for FRP the *DC* is determined by the molar ratio between the crosslinker and the monomer.

α,ω–Thiol polymers can be obtained *via* RAFT polymerization if the thiocarbonate moiety is present as chain end on both sides. Only in this case, upon cleavage (*via* aminolysis) the desired polymer precursor is achieved. For this purpose, a suitable bifunctional RAFT agent (**biDoPAT**) was obtained after esterification of the commercially available DoPAT (Figure 5.8, top), already used in **Chapter 4** (Section 4.2). The **biDoPAT**, which synthesis is reported in **Chapter 7** (Section 7.5), was employed for the polymerization of styrene, using a ratio of RAFT agent to monomer equal to 1:150, yielding the intermediate **PS(36)**, where 36 represents the number of repeating units in order to give an indication of the chain lengths of the polymer. In the next step, the polymer was subjected to aminolysis to achieve **biSH-PS(36)**. The reaction scheme is presented in Figure 5.8 (top). The molecular weight of the polymer (M_n), determined *via* SEC analysis, is 4500 g mol^{-1} ($Đ$ = 1.1) after polymerization and 3800 g mol^{-1} ($Đ$ = 1.1) after aminolysis. Importantly, the SEC trace of **biSH-PS(36)** shows the absence of disulfide bonds after aminolysis, which would cause a higher-molecular weight shoulder (Figure 5.8).

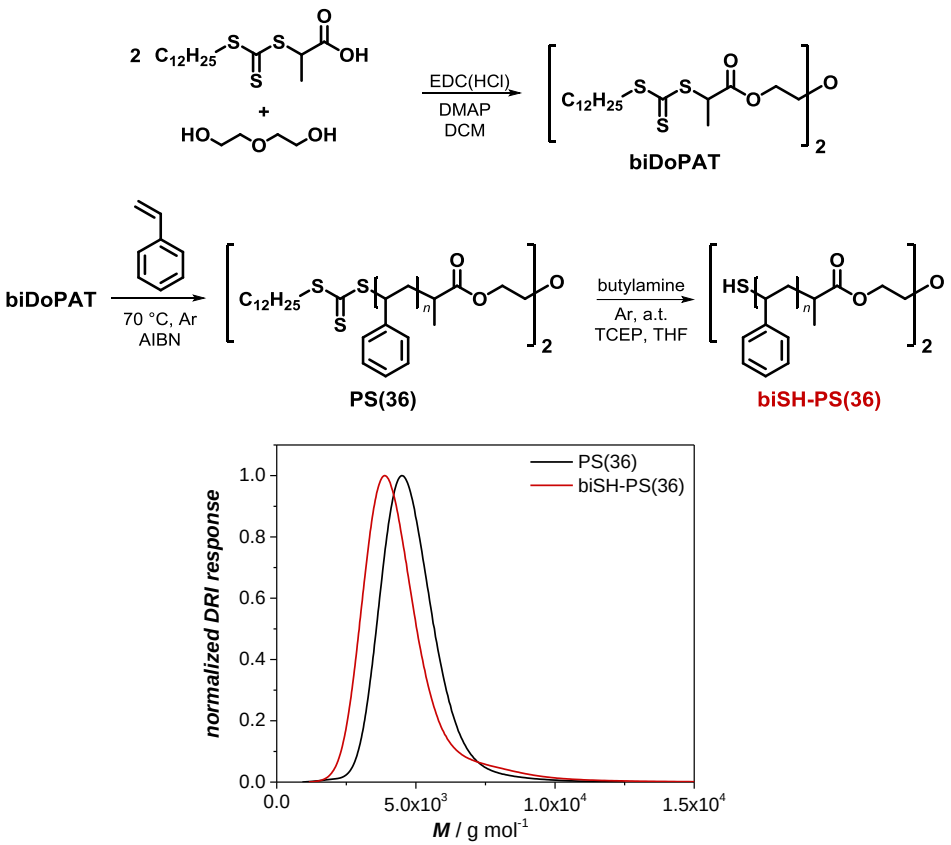

*Figure 5.8 – Top: Reaction scheme for the synthesis of a suitable bifunctional RAFT agent (**biDoPAT**), and of the desired polystyrene **biSH-PS(36)**. Bottom: SEC traces before (**PS(36)**, black line) and after aminolysis (**biSH-PS(36)**, red line).*

Next, ESI-MS analysis was performed to verify the end group fidelity and elucidate the chemical structure of the synthesized polymers. The ESI-MS spectra of the polymer before and after cleavage of the trithiocarbonate moieties are reported in Figure 5.9a. In addition, the ^{1}H and ^{13}C NMR spectra before and after aminolysis are reported in Appendix (Figure 8.23).

The ESI-MS spectra were recorded in negative ion mode, thus the molecule is present as the $[M+Cl]^-$ adduct. From Figure 5.9, the distance between two consecutive peaks within the same distribution correspond to the *m/z* ratio of the repeating unit. In this case, Δm is equal to 104.063, which refers to the molecular weight of the monomeric styrene unit (Figure 5.9b). Furthermore, the difference in mass of a polymer chain (e.g. with 24 repeating units as in example) before and after aminolysis corresponds to Δm = 488.265. This number corresponds to the molar mass of the aliphatic chain and the trithiocarbonate group removed during the post modification aminolysis reaction (Figure 5.9b and d and Table 5.3). Ultimately, the excellent agreement between the experimental and the simulated spectra (Figure 5.9c) confirms the synthesis of the desired **biSH-PS(36)**.

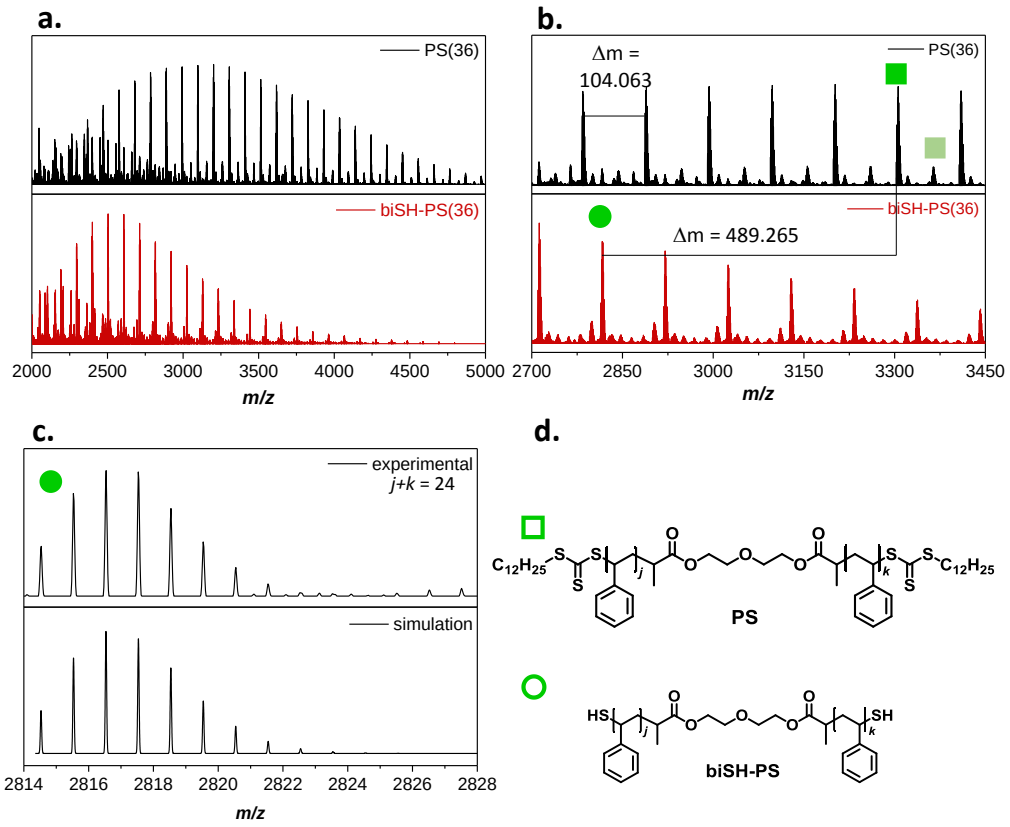

*Figure 5.9 – (–)ESI-MS analysis on **PS(36)** before (black) and after (red) aminolysis. a. Full spectra recorded in the range m/z = 2000-5000. b. Representative zoom in order to identify the species. Herein, Δm = 104.063 represents the styrenic repeating unit, while Δm = 489.265 the removal of the aliphatic chain and the trithiocarbonate group upon aminolysis. The assignments are summarized in Table 5.3. c. Experimental and simulated spectra for **biSH-PS(36)** with a total number of repeating units equal to 24. d. Chemical structure for the polystyrene sample before (square) and after (circle) aminolysis.*

Table 5.3 – Comparison of the experimental and the theoretical m/z ratio for the peak highlighted in the (–)ESI-MS spectra of Figure 5.9b. Herein, "j+k" refers to the total number of styrene repeating unit in the considered peak, according to Figure 5.9c. Δm is the difference between the theoretical and the experimental value.

	Structure	*j+k*	*m/z* (exp)	*m/z* (theo)	*Δm*
■	$[PS+Cl]^-$	24	3304.7944	3304.8003	0.0059
■	$[PS+NaCl+Cl]^-$	24	3363.7498	3363.7583	0.0091
●	$[biSH\text{-}PS+Cl]^-$	24	2816.5311	2816.5367	0.0056

In **Chapter 4**, PFTR was performed using an initial concentration of functional groups equal to 0.075 mol·L^{-1}. Since the molecular weight of the mono- (from **Chapter 4**) and bifunctional thiol polymers is similar, the same mass to solvent ratio (300 mg·mL^{-1}) can be used, effectively doubling the concentration of thiol functionalities without affecting the solubility of the polymer.

Moreover, in Section 4.2.2, it was demonstrated that the presence of disulfide bonds can be negligible within the first 24 h of the reaction, and that the conversion is mostly rising in the first 5 h from the addition of the base. Hence, the network formation was performed without addition of TCEP (used to reduce the disulfide bonds), at ambient temperature, and without removing oxygen from the reaction mixture. Here, **biSH-PS(36)** was reacted with **3COOPFB** in a ratio of 1:1 (SH:PFB) using 1eq. of base (i.e. DBU) and a concentration of 300 mg·mL^{-1}of polystyrene in DMF ([thiol]$_0$ = 0.150 mol·L^{-1}). After one hour, the solid and the liquid fractions were separated, and the solid fraction washed at least three time with THF to remove the extractables, which were combined for further analysis. The base was considered removed from the gel phase after the washing procedure, while the liquid phase was passed through a short column of basic alumina to remove the base. Finally, both fractions were dried in a vacuum oven at T = 35 °C overnight. After drying, the weight of each fraction was taken to assess their relative amount after PFTR. The same procedure was followed when the four-armed linker (**4COOPFB**) was employed, and each reaction was repeated three times in order to ensure reproducible and accurate data. The networks, obtained according to the reaction scheme reported in Scheme 5.2, are named **N3-36** and **N4-36**. The code is representative of the polymer used (**PS(36)**) and the crosslinker functionality (3 or 4).

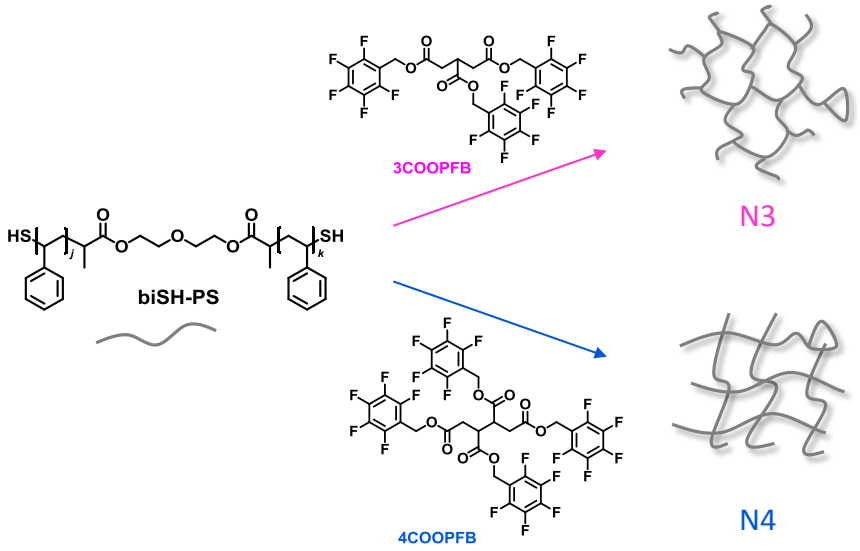

*Scheme 5.2 – Reaction scheme for the synthesis of **N3** or **N4** networks starting from **biSH-PS** and either a three- or a four-armed linker.*

The relative amount of solid and liquid fractions for **N3-** and **N4-36** was compared in Figure 5.10. In particular, the mean value from three independent syntheses, and its standard deviation, is reported.

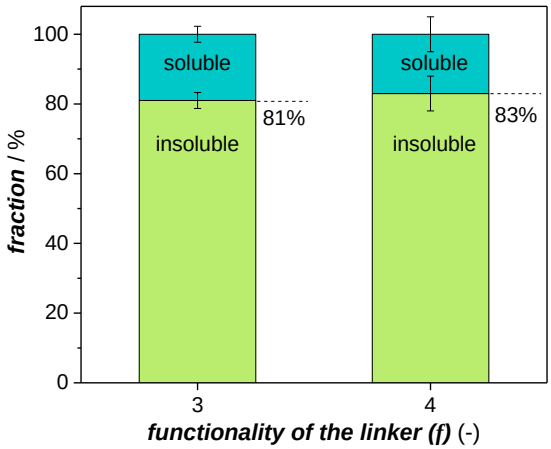

Figure 5.10 – Relative amount of soluble (extractables) and insoluble (network) fractions after PFT reaction between ***biSH-PS(36)*** *and either* ***3-*** *or* ***4COOPFB*** *(SH:PFB = 1:1, and a concentration equal to 300 mg·mL^{-1} in DMF).*

As depicted in Figure 5.10, the use of a three- rather than a four-armed linker does not significantly affect the overall yield of network. In both cases, high yields were achieved, with a relative amount of solid fraction equal to ~80%. Additionally, the soluble fractions were analyzed *via* SEC, and the results are displayed in Figure 5.11.

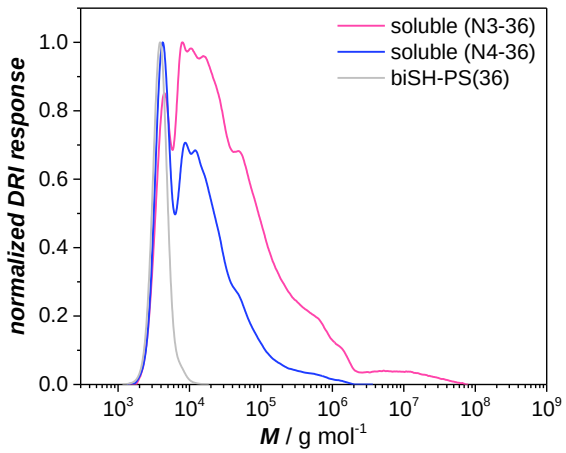

Figure 5.11 – Comparison of the SEC traces for the soluble fractions obtained after crosslinking between ***biSH-PS(36)*** *and either* ***3-*** *(pink) or* ***4COOPFB*** *(blue) (SH:PFB:DBU = 1:1:1, 300 mg·mL^{-1} of DMF). For clarity, the polymeric starting material* ***biSH-PS(36)*** *is reported (gray).*

The normalized SEC trace of the extractables obtained after crosslinking reaction using **3COOPFB** (Figure 5.11, pink) is characterized by higher molecular weight than the one obtained using **4COOPFB** (Figure 5.11, blue). This is because the three-armed linker creates less

connecting points than the four-armed one, thus more chains and crosslinking units need to interact with each other in order to achieve the gelation.

Next, both the soluble and insoluble fractions were analyzed *via* ^{19}F NMR measurements to determine the amount of unreacted functional groups. As before, the average values of three independent sets of data were considered and the average values are depicted in Figure 5.12.

On the one hand, the linker appears to be fully reacted within the network (empty symbols), or at least within the limit of detection of the NMR experiments for a complex system such as an organogel in gel phase, where the resonances become broad and the signal to noise ratio decreases. On the other hand, a higher amount of unreacted moieties is present in the soluble fractions. The average conversion value is approximately 75% for **N3-36** and 60 % in case for **N4-36**. Thus, slightly higher conversions seem to be achievable for the three-armed linker. One hypothesis is that the network obtained with a four-armed linker is more densely packed, thus the mobility of the chains and the probability of the end-groups to react with each other is lower at higher conversions, resulting in a higher amount of unreacted PFB groups.

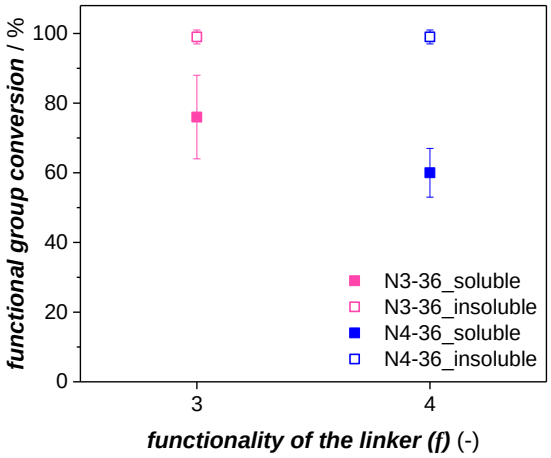

*Figure 5.12 – Functional group conversion, expressed as percentage of reacted fluorinated aromatic groups in the soluble (filled symbol) and insoluble (empty symbol) fractions for the networks obtained via PFTR employing **biSH-PS(36)** and either **3-** (pink) or **4COOPFB** (blue) (SH:PFB:DBU = 1:1:1, and a concentration of 300 mg·mL^{-1} in DMF).*

In order to prove the validity of the ^{19}F NMR measurements performed in the gel-phase, a selected network (**N4-36**) was degraded upon cleavage of the ester bond present on the linker structure (refer to Scheme 5.2). For the cleavage, the network was swollen in an excess of THF and an aqueous solution of 0.1 M NaOH was added to the mixture, as depicted in Scheme 5.3.

After stirring of the reaction mixture overnight (16 h), the organic and water phases were separated. The organic phases were concentrated under reduced pressure and analyzed. The results from the ^{19}F NMR and SEC analysis are reported in Figure 5.13.

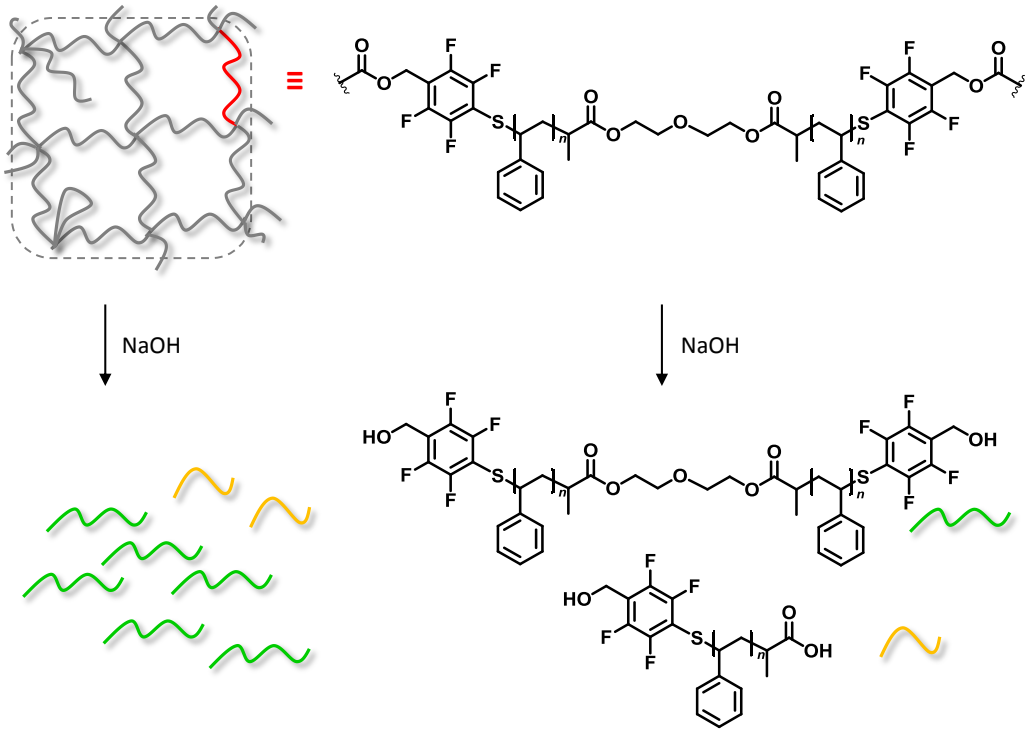

Scheme 5.3 – Reaction scheme for the degradation of a typical polystyrene network obtained via PFTR. The degradation was performed upon swelling of the network in a mixture of THF and an aqueous solution of NaOH 1 M overnight (16 h).

The ^{19}F NMR spectra before and after cleavage (Figure 5.13, left) are in good agreement with each other. As expected, after cleavage the signal to noise ratio is improved and the quantification more accurate. However, resonances at $\delta = -161.7$ ppm (unreacted *meta*- fluorine atom) are visible in both spectra.

In the SEC trace of the degraded **N4-36** network (Figure 5.13, right, green line), the main peak corresponds to the elastic chain. The position of the peak is shifted towards higher molecular weight compared to the polymer precursor, because of the incorporation of the fluorinated group at the end of the chain as a consequence of the crosslinking process ($M_c > M_n$). Moreover, small peaks at higher and lower molecular weight are visible. The former can be attributed to incomplete cleavage, while the latter to the cleavage of the elastic chain, which also contains an ester bond in the middle of the chain (refer to Scheme 5.3).

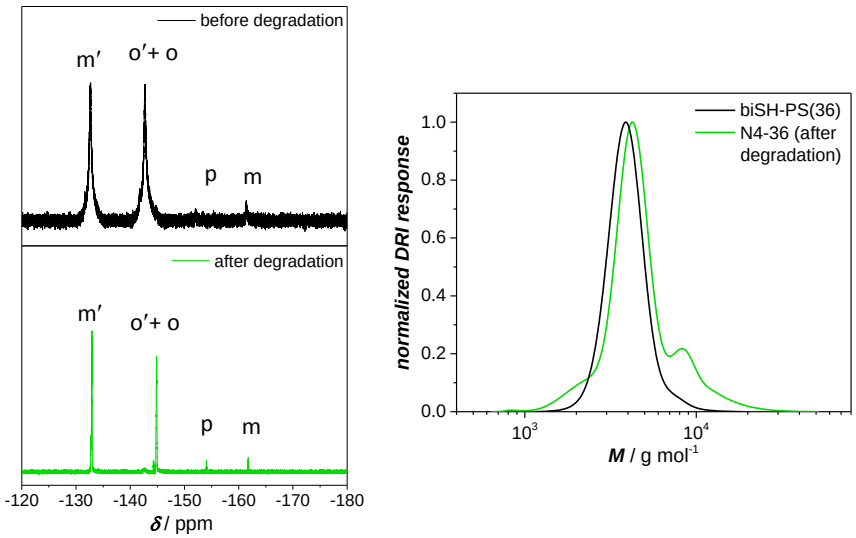

Figure 5.13 – Left: ^{19}F NMR spectra ($CDCl_3$, 377 MHz) *of **N4-36** before (top) and after (bottom) degradation. Right: SEC traces of the polymer precursor used for the synthesis of **N4-36** (**biSH-PS(36)**, black), and **N4-36** after degradation (green).*

Additionally, the networks were characterized *via* XPS and ToF-SIMS analysis. Here, it is worth to remember that the signal to noise ratio during the measurement, as well as the ionization is highly dependent on the roughness of the surface, with flat surfaces being a more suitable substrate. Hence, polymer networks with rough surfaces are not an ideal candidate for XPS and ToF-SIMS analysis. Moreover, the low percentage of aromatic fluorinated groups, present only at the crosslinking points in percentage of ~3%, made the use of these techniques challenging and less sensitive compared to the previous section (Section 5.1). Thus, only the results for **N4-36** as representative network are reported in Figure 5.14and Figure 5.15 for ToF-SIMS and XPS analysis, respectively.

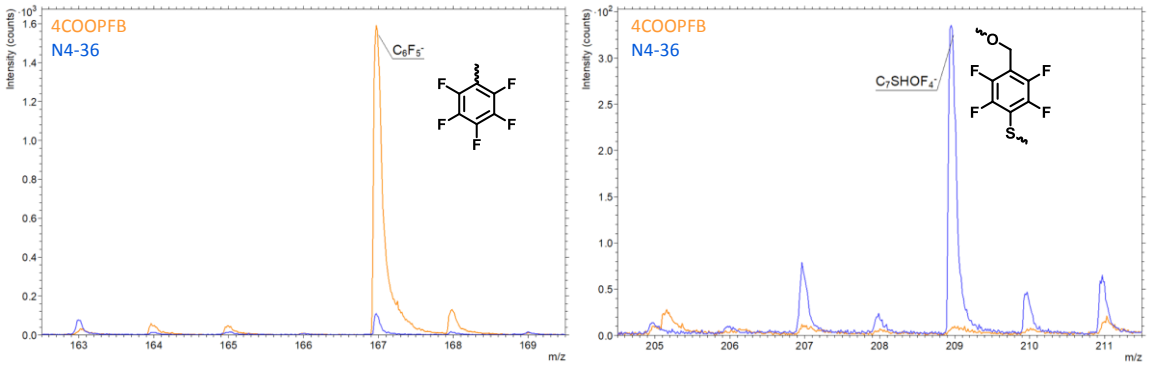

*Figure 5.14 – ToF-SIMS analysis on the precursor linker (**4COOPFB**, orange) and the synthesized network (**N4-36**, blue). Highlighted is the relative abundance of the fluorinated aromatic ring before (left) and after (right) PFTR.*

Upon ToF-SIMS analysis it can be noticed that the unreacted fragment ($[C_6F_5]^-$, *m/z* = 167) is characterized by a high intensity in the linker (**4COOPFB**) but it is almost absent in the polymeric network (**N4-36**). This and the high percentage of the reacted fragment ($[C_7SHOF_4]^-$, *m/z* = 209) indicate that the reaction has proceeded according to the proposed pathway, which is in agreement with the results obtained *via* ^{19}F NMR spectroscopy.

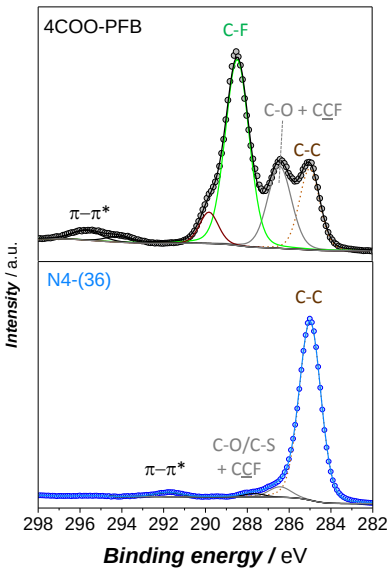

*Figure 5.15 – XP C1s spectra of the pristine linker (**4COOPFB**, top, black line) and the freshly synthesized network (**N4-36**, bottom, blue line).*

Concerning the XPS analysis instead, the C1s spectrum allows for the identification of the C-F peak in case of the linker precursor (**4COOPFB**, Figure 5.15, top) but not in case of the polymer network (**N4-36**, Figure 5.15, bottom). As previously mentioned this is mainly due to the roughness of the surface, and low percentage of the fluorine atoms within the sample in combination with the high percentage of the C-C bonds arising from the polymer backbone.

Notably, the decrease in sensitivity encountered for XPS and ToF-SIMS analysis is a minor issue, as they need to be considered as qualitative analysis. Accordingly, the main goal of accessing the amount of unreacted functionality is achievable *via* ^{19}F NMR spectroscopy, as shown in Figure 5.13.

Finally, the swellability – important for potential application of such networks – was tested. Herein, toluene was selected as solvent due to its favorable interactions with the polystyrene backbone. The experiments were performed by immersing a known amount of dry network (5-10 mg) in a solution of toluene (~5 mL). After the network was left swelling for 16 h, the gel was separated from the solution. Subsequently, the excess of solvent was removed from the outer surface of the material, and the weight of the swollen network was measured. The ratio

between the amount of solvent within the gel matrix and the dry network defines the swelling degree of a given gel according to Equation 2.22. The experiment was performed on three samples for each synthesis.

The average degree of swelling for the **N3-36** network is 6.4 ± 0.5, while it is 5.8 ± 0.2 for **N4-36**, thus the swelling degree is higher when a three-armed linker is used. This is expected since the polymer precursor used was identical but in the former case the crosslinker has a lower number of functionality (*f*), so a less crosslinked microstructure. The difference in the swellability in relation to the crosslinker functionality is also predicted by the phantom model theory (discussed in details in Section 2.3.2), where the pre-factor *A* of the elastic term includes the term *f* (Equation 2.21). For this reason, the phantom model was used for calculating the theoretical degree of swelling. For the calculation it is important to define the average molecular weight of the elastic chain (M_c), which resulted equal to 4277 g·mol^{-1} for **PS(36)**, according to Equation 2.26. Moreover, the concentration during the crosslinking process here equal to 300 mg·mL^{-1} (PS in DMF), needs to be expressed as volumetric ratio q_c. In this case, q_c was found to be 4.5 according to Equation 5.2.

$$q_c = \frac{m_{PS}\rho_{PS} + V_{DMF}}{m_{PS}\rho_{PS}} \tag{5.2}$$

where m_{PS} and ρ_{PS} (ρ_{PS} = 1.044 g·mL^{-1}) are the mass and the density of polystyrene, respectively, and V_{DMF} is the volume of solvent, here DMF. The predicted differences in Q_{eq} between **N3-36** and **N4-36** swollen in toluene (χ = 0.44[212]) is visualized in Figure 5.16.

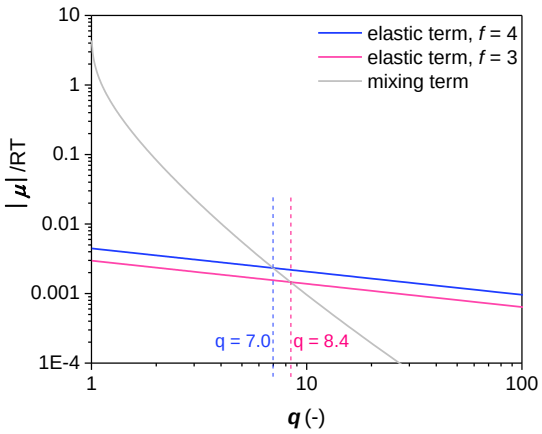

*Figure 5.16 – Graphical representation of the equation of state for a PS network swollen in toluene, highlighting the difference in the theoretical swelling behavior when using a three- (pink) and a four- (blue) armed linker but the same bifunctional polymer precursor (**PS(36)**). Here, χ = 0.44 (mixing term, Equation 2.20), while the elastic term (Equation 2.21) is evaluated using the phantom model (q_c = 4.5).*

The swelling values reported on the x axis of Figure 5.16 are expressed as volumetric ratio (q). The mass ratio is calculated from q by applying Equation 2.23, thus resulting in $Q_{eq,theo}$ = 6.1 and 5.0 for the three- and the four-armed linker, respectively. Hence, the deviation between the experimental and theoretical value, expressed as percentage and calculated according to Equation 5.3, is equal to 5% and 16% for **N3-36** and **N4-36**, respectively.

$$deviation\ \% = \left| \frac{Q_{\mathrm{eq,theo}} - Q_{\mathrm{eq,exp}}}{Q_{\mathrm{eq,theo}}} \right| * 100 \qquad (5.3)$$

The amount of solvent used during the crosslinking reaction needs to ensure the solubility of the precursor and favor inter- over intramolecular reactions. Accordingly, high dilutions lead more easily to loop formation (Figure 2.6), while high concentrations limit diffusion of the chains. Thus, **N4-36** was synthesized using different concentrations (150, 300 and 450 mg·mL^{-1}) during the crosslinking reaction.

As before, after reaction the soluble and the insoluble fractions were separated, washed with THF, and dried in vacuum. The percentage of each fraction is plotted in Figure 5.17 (left), while the conversion obtained after ^{19}F NMR measurements on both fractions is depicted in Figure 5.17 (right).

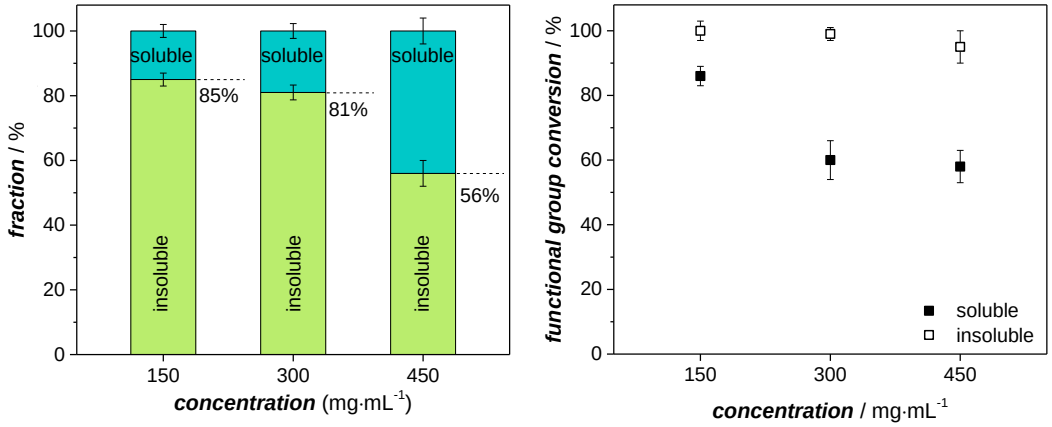

*Figure 5.17 – Left: Relative amount of the soluble and insoluble fractions, expressed as percentage. Right: Percentage of PFB groups reacted in the soluble (filled symbols) and insoluble (empty symbols) fractions of different networks. Each network was obtained employing **biSH-PFB(36)** and **4COOPFB** linker (SH:PFB = 1:1) but using different concentration of polymer in DMF during the crosslinking reaction. The concentration used is stated in the x axis.*

The relative amount of network obtained after reaction is higher for the network synthesized at 150 mg·mL^{-1} or 300 mg·mL^{-1} compared to the case where a concentration of 450 mg·mL^{-1}

was used (Figure 5.17, left). At 450 mg·mL^{-1}, only 55% of network is obtained. This is possibly a consequence of the limited diffusion of the chains, due to the high concentrations.

The results from the ^{19}F NMR measurements instead evidence almost full conversion within the insoluble fractions at all concentrations. For the soluble fractions, a similar conversion is achieved for the network synthesized at 450 and 300 mg·mL^{-1}, while a lower number of unreacted PFB group is visible when a concentration of 150 mg·mL^{-1} was used. These results are in agreement with the hypothesis that diffusion becomes more limited as the concentration increases.

Moreover, it is important to compare the experimental degree of swelling to the theoretical values in order to verify whether higher dilution led to the formation of primary loops. In fact, primary loops are elastically inactive chains and do not participate in the swelling, leaving the network structure more open (i.e. larger meshes), which results in a higher swelling ratio. The presence of loops, however, cannot be detected *via* ^{19}F NMR measurements as both the chain ends are reacted. Thus, the swelling behavior was evaluated for each network in toluene and the comparison between theoretical and experimental value is summarized in Table 5.4

*Table 5.4 – Summary of the experimental ($Q_{eq,exp}$) and theoretical ($Q_{eq,theo}$) degree of swelling (w/w ratio) for **N4-36** networks synthesized at different concentrations. The deviation percentage is calculated according to equation 5.3. q is the theoretical swelling (v/v ratio) using the phantom model.*

Concentration	q_c [(a)]	q	$Q_{eq,theo}$	$Q_{eq,exp}$	Deviation (%)
150 mg·mL^{-1}	8.0	8.3	6.1	7.0 ± 0.5	15
300 mg·mL^{-1}	4.5	7.0	5.0	5.8 ± 0.2	16
450 mg·mL^{-1}	3.3	6.4	4.5	5.5 ± 0.2	23

[(a)] q_c = concentration during the crosslinking reaction, calculated according to equation 5.2

As shown in Table 5.4, a deviation of approximately 15% from the theoretical value is observed for the networks synthesized at 150 and 300 mg mL^{-1}, while a slightly higher deviation (23%) is seen for the network synthesized at 450 mg mL^{-1}.

Hence, because of the higher deviations (Table 5.4) and the lower amount of network achievable (Figure 5.17, left), the latter concentration (450 mg·mL^{-1}) was excluded. Another important consideration is that polymer precursors with higher molecular weight will be used in the next step. This is relevant because for a given polymer to solvent ratio, the concentration of functional group is lower when longer polymer chains are used. Thus, the concentration choice is a compromise between ensuring a sufficiently high concentration of functional groups for efficient network synthesis (faster reaction rates and limited loop formation), while still facilitating

diffusion necessary for sufficient yields. With this in mind, a concentration of 300 mg·mL^{-1} was chosen as the standard concentration for network synthesis.

Thus, as anticipated, in the next step the average length of the elastic chain was varied to finely tune the degree of crosslinking. For this purpose, longer polymer chains were synthesized according to the procedure reported in **Chapter 7** (Section 7.5) but varying the RAFT agent to monomer ratios during the polymerization. In detail, the polymerization was performed employing molar ratios of 1:200, 1:250 (RAFT:monomer). This resulted in the synthesis of **PS(64)** and **PS(82)**, having M_n = 7300 ($Đ$ = 1.1) and 9300 g mol^{-1} ($Đ$ = 1.1), respectively. The corresponding SEC trace of the previous and the new polymers before (solid line) and after (dashed line) aminolysis are reported in Figure 5.18, while a summary of the different molecular weight is given in Table 5.5. The use of **PS(36)**, **PS(64)**, **PS(82)** leads to, respectively, short, medium and long elastic chains in the final polymer network. The number in brackets represents the number of repeating unit within the polymer chain.

The ^{1}H and ^{13}C NMR spectra of **PS(64)** and **PS(82)** before and after aminolysis are reported in Appendix (Figure 8.24 and Figure 8.25, respectively). The spectra are comparable to those obtained for PS-short (see Appendix, Figure 8.23), confirming the achievement of the targeted polymer.

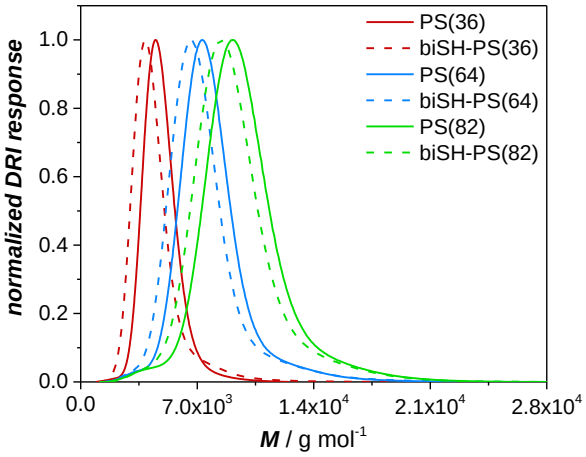

Figure 5.18 – SEC traces of the polystyrene precursors used for the synthesis of PS networks via PFTR.

The crosslinking reaction *via* PFTR was performed for each polymer precursor with both the three- and the four-armed linker. In each case, a concentration of 300 mg·mL^{-1} of polymer in DMF (q_c = 4.5) was used during the network formation. For clarity, a summary of the synthe-

sized networks, including the thiol/linker combination and their relative reaction codes is reported in Table 5.5. As example, the network **N3-36** refers to a network (**N**) synthesized using the three-armed linker (**3**) and characterized by elastic chains having 36 repeating units (**36**).

Table 5.5 – List of the bifunctional polymer precursors used in this section including their molecular weight (M_n), the dispersity index ($Đ$) and the molecular weight of the corresponding elastic chain after network formation (M_c). Moreover, a summary of the networks synthesized varying the thiol/linker combination is proposed including the relative network codes as cited in text.

Bifunctional thiol	M_n [(a)] (g·mol^{-1})	$Đ$ [(a)]	M_c [(b)] (g·mol^{-1})	**Fluorinated linker**	**Network**
biSH-PS(36)	3800	1.1	4277	3COOPFB	N3-36
biSH-PS(36)	3800	1.1	4277	4COOPFB	N4-36
biSH-PS(64)	6650	1.1	7127	3COOPFB	N3-64
biSH-PS(64)	6650	1.1	7127	4COOPFB	N4-64
biSH-PS(82)	8500	1.1	8977	3COOPFB	N3-82
biSH-PS(82)	8500	1.1	8977	4COOPFB	N4-82

[(a)] M_n and $Đ$ are determined *via* SEC based on polystyrene calibration.

[(b)] M_c is determined according to Equation 2.26.

At first, the relative ratio between the soluble and the insoluble fractions was investigated to evaluate whether any chain length dependency could be observed. The results for both three- (**N3-** series) and four-armed (**N4-** series) linker for each polymer precursor are compared in Figure 5.19.

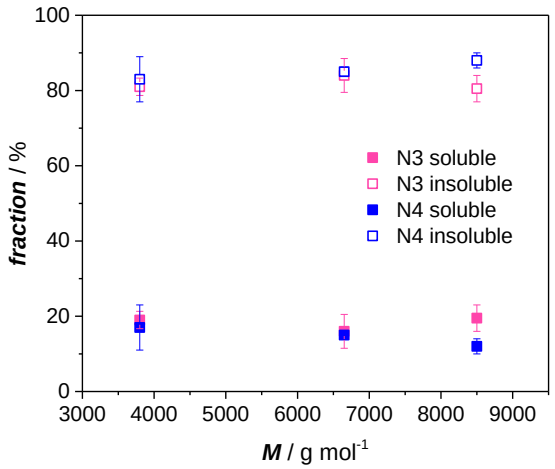

Figure 5.19 – Relative amount, expressed as percentage, of the insoluble (empty symbol) and soluble (filled symbol) fractions for polystyrene networks synthesized via PFTR. The reaction was performed using polymer precursors of different molecular weight (M_n is highlighted along the x axis), and either a three- (pink) or a four- (blue) armed linker.

All values reported in Figure 5.19 are rather similar to each other and small variations are well within the error bars. Thus, no clear trend in the yield of relative amount of soluble and insoluble fraction is observed regardless of whether a three- or a four-armed linker was used, nor when different polymer precursors were used. Next, the amount of unreacted functionality was calculated *via* ^{19}F NMR analysis. The results are depicted in Figure 5.20.

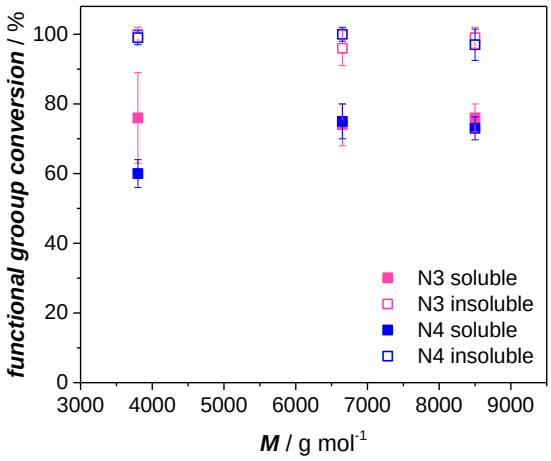

*Figure 5.20 – Functional groups conversion in the insoluble (empty symbol) and soluble (filled symbol) fractions as obtained via ^{19}F NMR measurements for different networks. The networks were obtained upon PFT reaction between a three- (**N3-** series, pink) or a four- (**N4-** series, blue) armed linker and several bifunctional thiol polymer precursors, which molecular weight is reported along the x axis.*

After comparison of the conversion in all the synthesized networks, the difference between the three- and the four-armed linker is less pronounced. In detail, nearly full conversion is achieved in each case. Interestingly, the unreacted moiety in the soluble fractions are rather low, reaching only ~25% of the total amount of PFB groups in most cases. The functional group conversion is largely the same regardless of the polymer chain length or whether a three- or a four-armed linker was used. The lowest conversion values are achieved for the soluble fraction when **PS(36)** is employed, probably associated with a higher degree of crosslinking, and thus the more tightly packed microstructure.

Nonetheless, the findings reveal that PFTR can be broadly applied to the fabrication of polymer networks. Positively, the performance of the reaction in terms of functional group conversion, was independent from the chain length of the tested polymer precursors, allowing for a broad use of the ligation and an easy tuning of the final properties.

In the final step, the swelling behavior of the different networks in toluene was tested. The adopted procedure is identical to the one described for **N4-36**. The experimental data are displayed in Figure 5.21 as degree of swelling against molecular weight of the polymer precursor

(M_n). A list of the experimental and theoretical swelling degree, as calculated using the phantom model, and the deviation between the two values is summarized in Table 5.6.

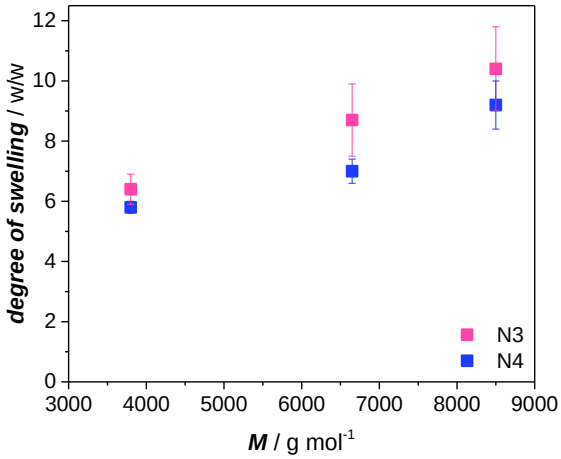

*Figure 5.21 – Degree of swelling for different networks obtained via PFTR employing a three- (**N3** series, pink) or a four- (**N4** series, blue) armed linker and several bifunctional thiol polymer precursors. The molecular weight of the polymer precursor used is reported along the x axis.*

Table 5.6 – Comparison between the theoretical (Q_{theo}) and experimental (Q_{exp}) degree of swelling (w/w ratio) for the polystyrene networks in toluene (χ = 0.44). The deviation between the two values is calculated according to Equation 5.3. q is the theoretical swelling (v/v ratio) as obtained using the phantom model.

Network	*q*	$Q_{eq,theo}$	$Q_{eq,exp}$	Deviation (%)
N3-36	8.4	6.1	6.4 ± 0.5	4.9
N4-36	7.0	5.0	5.8 ± 0.2	16.0
N3-64	10.8	8.1	8.7 ± 1.2	7.4
N4-64	8.9	6.5	7.0 ± 0.4	7.0
N3-82	12.0	9.1	10.4 ± 1.4	14.3
N4-82	9.9	7.4	9.2 ± 0.8	24.5

As expected, the degree of swelling increases for larger mesh size.

Both **N3** and **N4** series show a minor deviation (maximum 7.4 and 16%, respectively) from the theoretical value for short and medium chains, while larger deviation within each series are observed when **biSH-PS(82)** is the precursor (14.3% and 24.5% for **N3-82** and **N4-82**, respectively). Since this behavior is observed for both types of networks, independently from the crosslinker functionality, the reason for the larger deviation is likely to derive from the polymer precursor. One hypothesis is that longer chains lead to more defects due to the larger distance between the functional groups and thus the higher flexibility of the chain, which might increase the possibility of loop formation. However, no proof for this assumption can be achieved by

recording ^{19}F NMR spectroscopy, because both ends of the elastic chain involved in a loop are reacted, but its arrangement in space causes structural defects (i.e. loops cannot be distinct from regular meshes *via* ^{19}F NMR measurements). For analysis of loop formation, the network disassembly strategy (NDS) based on asymmetric cleavage of the elastic chain (discussed in Section 2.3.4) is the only valid option available so far.

Nonetheless, the main focus here was not the quantification of loops formed during the network synthesis, rather introducing a method for directly detect defects such as unreacted moieties. In addition, the understanding of whether the network obtained *via* the end-linking strategy (ELS), using PFTR ligation (and a four-armed linker), were more homogeneous than an equivalent network (same degree of crosslinking, *DC*) obtained *via* conventional free radical polymerization (FRP) was considered. In order to answer this question, networks having the same *DC* need to be synthesized *via* FRP approach. Thus, the FRP of styrene and divinylbenzene (DVB) was performed at 80 °C, employing AIBN (0.1 eq. with respect to styrene) as thermal initiator. Here, the molar ratio, expressed in percentage, between DVB and styrene defines the *DC*, which was adjusted to match the one of the networks synthesized *via* ELS (see Table 5.7). At first, the reaction was carried out at a concentration of 300 mg·mL^{-1} of styrene in DMF, as for the end-linking approach. However, this combination did not lead to any network formation in a time frame of three days. Further increasing the amount of AIBN from 0.1 eq. to 0.3 eq. was also not beneficial, thus the amount of solvent was significantly reduced and the networks were synthesized using an equal amount of monomer and solvent (q_c = 2). Upon reduction of the amount of solvent during the crosslinking process, the networks were achieved after a reaction time of 24 h. Subsequently, the networks were extensively washed to remove the extractables and after drying of the network, the swelling behavior in toluene was evaluated. The data are reported in Table 5.7, where the experimental values obtained for the networks synthesized *via* FRP and ELS are compared to the theoretical values. The theoretical values are calculated accounting for the different degree of crosslinking between the samples and the different amount of solvent used during the synthesis (q_c).

*Table 5.7 – Comparison of the theoretical ($Q_{eq,theo}$) and experimental ($Q_{eq,exp}$) degree of swelling (w/w ratio) in toluene for the polystyrene networks having different degree of crosslinking (DC) synthesized either via end-linking strategy (**N4**) using PFTR as ligation or via free radical polymerization (FRP). The theoretical values are obtained according to the phantom model (q, v/v ratio).*

Network	*DC*	*q* [(b)]	$Q_{eq,theo}$	$Q_{eq,exp}$	Deviation %
N4-36	2.7[(a)]	7.0	5.0	5.8 ± 0.2	16.0
FRP-36	2.7	5.5	3.7	5.0 ± 0.9	34.4
N4-64	1.6[(a)]	8.9	6.5	7.0 ± 0.4	7.0
FRP-64	1.6	6.9	4.9	8.1 ± 0.7	65.3
N4-82	1.2[(a)]	9.9	7.4	9.2 ± 0.8	24.5
FRP-82	1.2	7.7	5.5	10.8 ± 0.6	95.5

[(a)]calculated according to Equation 5.1

A visualization of the results, in terms of deviation between the experimental and theoretical degree of swelling, is depicted in Figure 5.22.

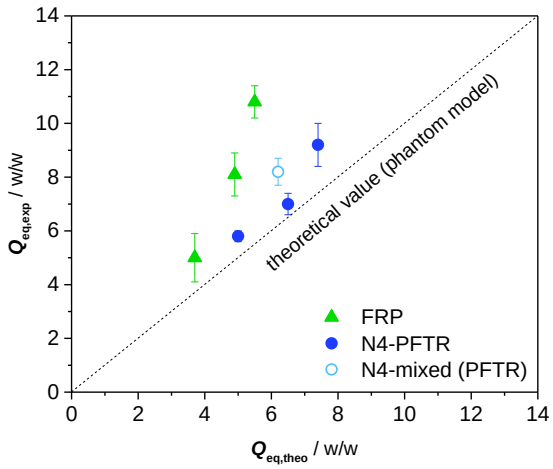

*Figure 5.22 – Visualization of the deviation between theoretical and experimental degree of swelling (w/w ratio) for the **N4-series** (blue) obtained via the end-linking strategy using PFTR as crosslinking reaction (q_c = 3.5) and FRP (green) networks (q_c=1). The different concentration used during synthesis is taken into account in the q_c parameter during calculation.*

Upon comparison of the experimental degree of swelling of the networks synthesized *via* FRP and ELS with the corresponding theoretical values, it is clear that higher deviations are observed for FRP. In details, as the degree of crosslinking decreases, the percentage error increases (Table 5.7), suggesting that defects are more probable with lower amount of crosslinking agent. One cause for the higher deviation observed in FRP samples is the crosslinking efficiency, which is influenced by the amount of solvent. Nonetheless, the experimental degree of swelling is double that of the predicted value for *DC* = 1.2 (**FRP-82**), indicating a strong preference for cyclization rather than crosslinking during synthesis.

Moreover, in Figure 5.22, one additional network is presented (empty circle). This network was synthesized *via* ELS using an equimolar mixture of polymer precursors having different chain lengths: **biSH-PS(36)** and **biSH-PS(82)**. The resultant network (**N4-mixed**) was characterized by a *DC* ~1.6, similar to **N4-64**. Despite the similarity, Figure 5.22 shows that higher deviations from the theoretical value are observed for the **N4-mixed** network compared to **N4-64,** 30% against 16%, respectively. Higher deviation can derive either from the usage of different polymer precursors, i.e. inhomogeneous average elastic chain lengths, or from the use of the long bifunctional thiol polymer **biSH-PS(82)** per se, which led to higher deviation already also when used individually during the synthesis of **N3-82** and **N4-82**. Additionally, the network **N4-mixed** represents an example of network with "controlled" inhomogeneity. In other words, the use of two different polymer precursors leads to the presence of both short and long elastic chains within the final structure, and thus to an inhomogeneous pore size distribution.

N4-mixed was intentionally synthesized to verify the ability of the ^{1}H NMR relaxometry, already used in **Chapter 3** to detect the presence of inhomogeneity within the network microstructure. Accordingly, the mobility of the elastic chains present in the resultant network is expected to be the sum or the average of the ones of the polymer precursors. The relaxation decay curves of **N4-mixed**, and of the networks **N4-36** and **N4-82** obtained by solely using **biSH-PS(36)** and **biSH-PS(82)**, respectively, are compared in Figure 5.23.

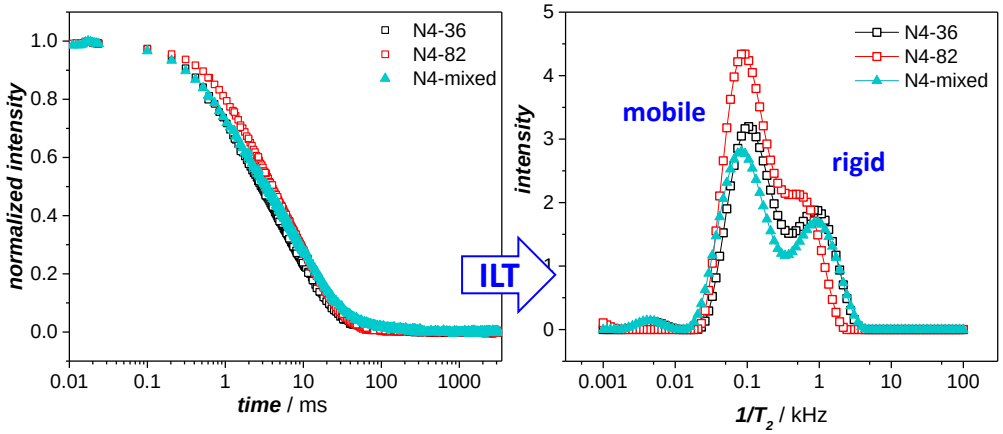

*Figure 5.23 – Left: T_2 relaxation curve for **N4-36** (black), **N4-82** (red) and **N4-mixed** (light blue). **N4-mixed** was synthesized using an equimolar ratio of functional groups arising from **PS(36)** and from **PS(82)**. Right: deconvoluted relaxation decay for **N4-36** (black), **N4-82** (red) and **N4-mixed** (light blue).*

In general, the rigidity increases with increasing the degree of crosslinking, thus for shorter elastic chain. From the relaxation decay reported in Figure 5.23 (left) it is visible that the net-

work **N4-36** is characterized by a higher rigidity. The higher rigidity is in line with the expectation as a shorter polymer precursor was used during the synthesis compared to **N4-82**. Concerning the relaxation decay of **N4-mixed** (Figure 5.23, light blue triangle), it can be seen that at short relaxation time (rigid part) the contribution of **PS(36)** is more significant, while at longer relaxation time (mobile part) the decay resemble more the one of **N4-82**. For an easier read-out of the results, the relaxation decay is deconvoluted via Inverse Laplace Transformation (ILT). The deconvolution of the signal of **N4-mixed** shows a contribution of both the long and the short chains, as the peak maximum of the two peaks appearing in the T_2 distribution match with those of **N4-36** or **N4-82**. However, the T_2 distribution of **N4-36** but mostly of **N4-36** indicates a pronounced inhomogeneity of the networks, despite the excellent agreement between the experimental and the theoretical degree of swelling. Notably, all the relaxation decays are similar to each other, indicating that the differences in molecular weights between the elastic chains are minor for the adopted method. It has to be mentioned that the method was adopted from the literature, where the optimization of the NMR relaxation experiment was performed on polyelectrolyte networks, thus on networks characterized by high degree of swelling. Therefore, it is possible that not all parameters for the NMR relaxation experiment are optimized for the polystyrene networks, which are characterized by low degree of swelling. For example, the network to solvent ratio used for the sample was equal to 1:5 *w/w*. The ratio is similar to the degree of swelling for **N4-36**, but is approximately half of the swelling degree for **N4-82**. The different level of stretching of the chains leads to differences in the relaxation decay. The temperature and the solvent used for analysis might also require optimization, and it will be part of future works.

Meanwhile, from the synthetic point of view, the attention was shifted to the synthesis of polymer networks more suitable for the targeted application, e.g. hydrophilic poly(acrylic acid) networks. Here, one important consideration is the need of using a protecting group strategy. This is because the presence of free carboxylic groups in acrylic acid lowers the reaction rate and the conversions achievable during PFTR, as discussed in **Chapter 4**. Thus, poly(*tert*-butylacrylate) was synthesized *via* RAFT polymerization using **biDoPAT** as RAFT agent. The polymerization kinetics showed the suitability of the RAFT agent for the polymerization of *tert*-butylacrylate as reported in Appendix (Figure 8.26). However, in the literature it is reported that performing aminolysis on (meth)acrylate polymers can lead to side reactions due to intramolecular backbiting reactions, as shown in Scheme 5.4.[213]

Scheme 5.4 – Side reaction occurring during the reaction of aminolysis of (meth)acrylate polymers.

The presence of backbiting reactions reduce the number of thiol groups available for PFTR. Thus, in the next step the use of α,ω–fluorinated rather than α,ω–thiol polymers will be evaluated as a potential strategy to overcome the backbiting reaction. This approach will still allow to take advantage of the PFTR as ligation for the crosslinking process, and to expand the applicability of PFTR to a larger library of polymer precursors. The suitability of PFTR for the synthesis of polymeric networks was indeed extensively demonstrated utilizing a variety of systems consisting of both three- and four-armed linkers. Importantly, the efficiency of the reaction was demonstrated, with yields of ~80% of network readily achievable, along with nearly full conversion quantified using ^{19}F NMR spectroscopy as a powerful analytical tool. The swelling behavior of the freshly synthesized network is in good agreement with the theoretical predicted value (phantom model), with smaller deviations observed for shorter elastic chains.

The networks were further characterized *via* XPS and ToF-SIMS, which resulted less sensitive in the detection of fluorine groups in case of polymeric networks due to the lower percentage of fluorinated group in combination with a high roughness of the surface. Nonetheless, the main goal was the quantification of unreacted moieties simply *via* ^{19}F NMR measurements, which has been achieved and extensively demonstrated.

With these positive results in hand, the use of PFTR, shown here to be a viable and potentially powerful tool (both synthetically and analytically), is expanded also to polymers that are sensitive to the aminolysis step. This is achieved by using well-defined α,ω–fluorinated polymer precursors and commercially available thiol linkers, as detailed in the next session.

5.2.2 Polymeric Fluorinated Derivatives

The current section discusses the introduction of pentafluorobenzyl (PFB) groups as chain ends, with two main advantages in mind. First, the use of commercially available thiol linkers, and second, the possibility of overcoming the step of aminolysis, which can cause issues such as backbiting reactions for some polymers as, for instance, (meth)acrylates.[213]

The first and easiest way to obtain α,ω–PFB-polymers is the synthesis of the desired polymer using a custom designed fluorinated RAFT agent. Accordingly, a suitable fluorinated RAFT agent (**biPFB**, Figure 5.24), which synthesis is reported in Section 7.5, was used for the RAFT mediated polymerization of styrene (Figure 5.24, top) employing a molar ratio of 1:150 **biPFB**:styrene. The product, **biPFB-PS**, presented a M_n = 7300 g mol^{-1} and $Đ$ = 1.1, according to SEC analysis (Figure 5.24, bottom).

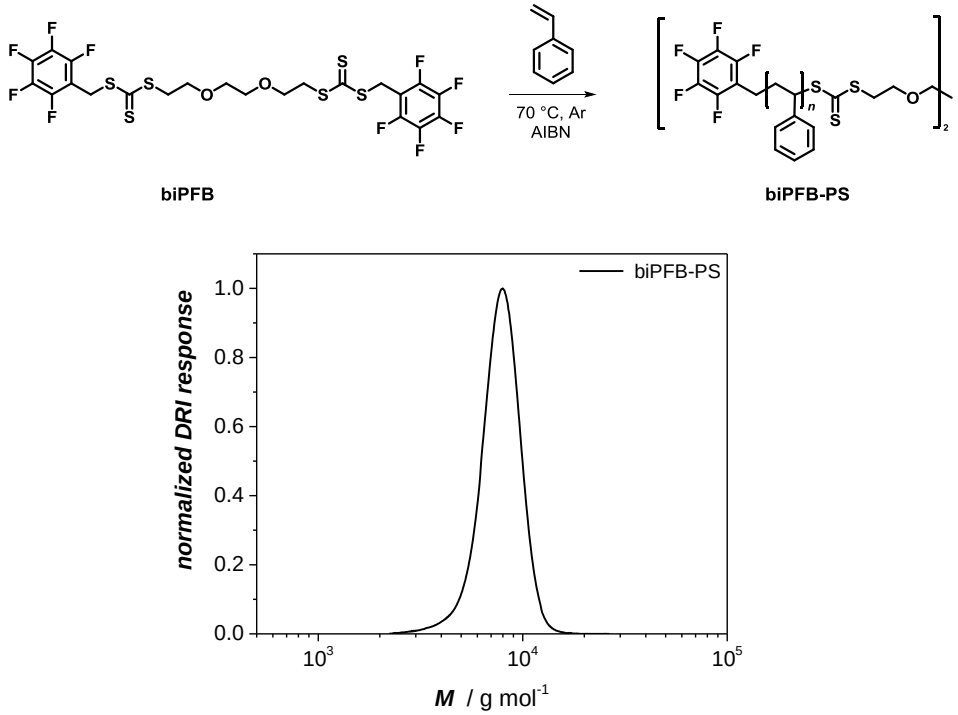

*Figure 5.24 – Top: Reaction scheme for the synthesis of bifunctional fluorinated polystyrene (**biPFB-PS**), starting from a custom designed RAFT agent. Bottom: SEC traces after the polymerization of styrene performed with a molar ratio of 1:150 RAFT agent:styrene, at 70 °C in bulk for 4 h..*

Initially, the possibility of performing PFTR was tested employing an aliphatic monofunctional thiol (aliphSH) and the synthesized **biPFB-PS**. For the reaction a 1:1:1 stoichiometric ratio of SH:PFB:DBU, and an initial concentration of $[PFB]_0$ = 0.15 g·mol^{-1} in DMF was used. After one hour, the crude reaction mixture was filtered through a short column of basic alumina for the removal of the base. The product was analyzed *via* ^{19}F NMR spectroscopy and SEC. Despite

the full conversion observed from the ^{19}F NMR spectrum (see Appendix, Figure 8.27), the SEC trace, displayed in Figure 5.25 together with the precursor polymer **biPFB-PS**, revealed a less ideal scenario.

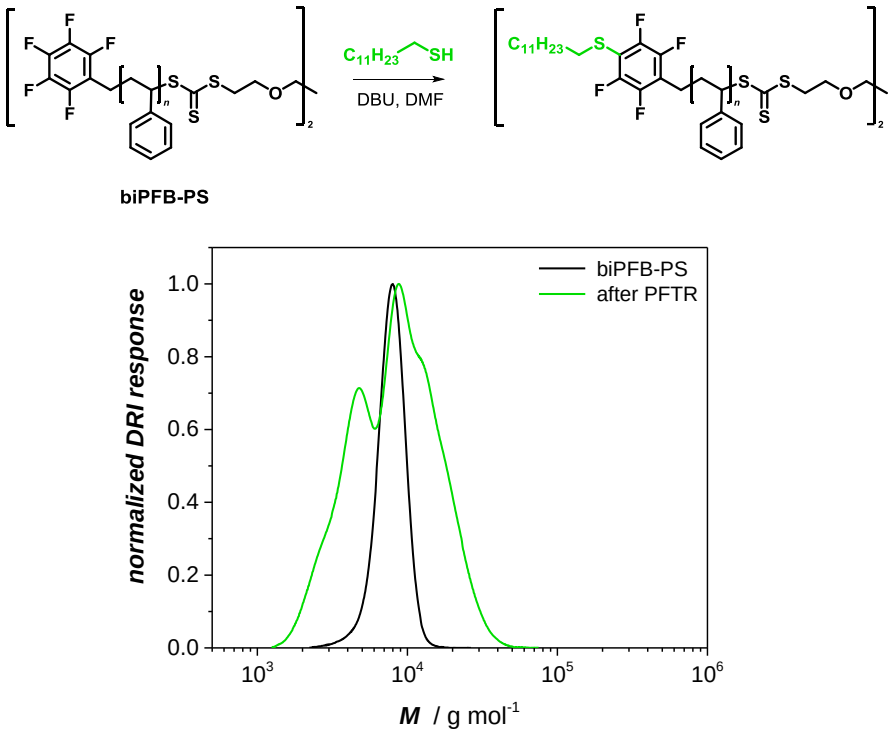

*Figure 5.25 – Top: Reaction scheme for PFTR between **biPFB-PS** and a monofunctional thiol (alipSH). The reaction was performed using an initial ratio SH:PFB = 1:1, and 1 eq. of DBU as base, $[PFB]_0$ = 0.15 g·mol^{-1} in DMF. Bottom: SEC traces before (black) and after (green) PFTR.*

Clearly, two main peaks can be observed in the SEC trace after PFTR (Figure 5.25, green). The main peak is ascribable to the desired PFTR product. The peak at lower molecular weight probably originates from a side reaction where the trithiocarbonate – being sensitive to nucleophiles (e.g. amines) – is attacked by the thiolate instead of at the fluorinated aromatic ring. Since the trithiocarbonate group is present in the middle of the polymer chain (Figure 5.25, top), its cleavage leads to a ´dead´ polymer having a molecular weight equal to approximately half of its original value and a newly formed thiol polymer, which can subsequently react *via* PFTR. This latter polymer is, in a first approximation, the reason for the shoulder observed at high molecular weight (Figure 5.25).

Thus, it is clear that this strategy does not appear to be viable without the sensitive trithiocarbonate moiety being protected or removed. Removal of the thiocarbonate group to prepare thiol polymers (aminolysis) has already been investigated in Section 5.2.1 and in **Chapter 4**. Another alternative, however, is the removal of the RAFT group *via* hetero-Diels–Alder (*h*DA)

reaction of a suitable thiocarbonate group with a photocaged diene (photoenol) (refer to **Chapter 2**, section 2.1.2).[66]

Here, a tailored photoenol bearing PFB groups (**PFB-PE**) serves both purposes: removing the sensitive thiocarbonate group and introducing the desired functional group (PFB) at the same time. The synthetic strategy is presented for a monofunctional polymer in Scheme 5.5, while the detailed synthesis of **PFB-PE** is described in Section 7.5.

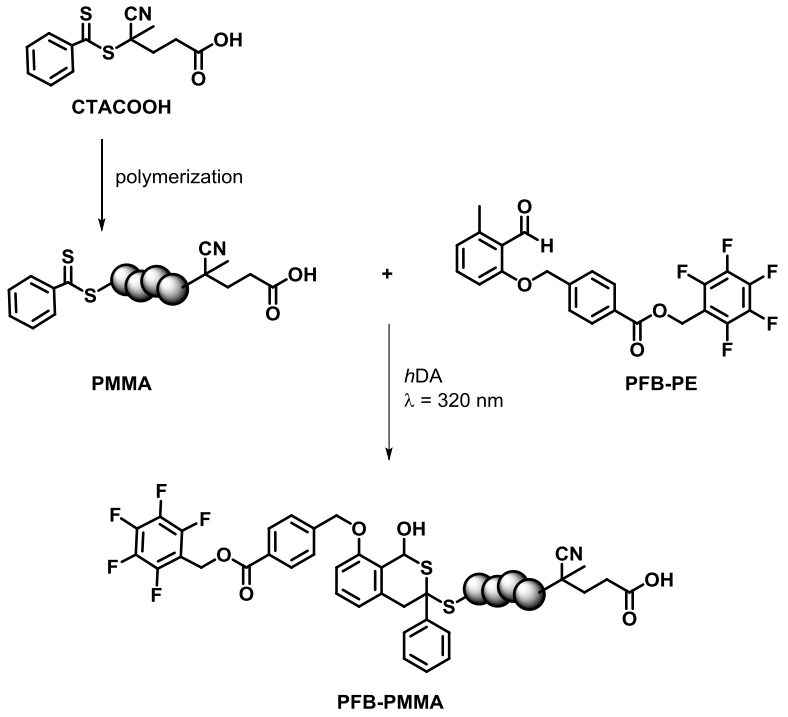

Scheme 5.5 – Reaction scheme for the one-pot removal of the sensitive thiocarbonate moiety and the introduction of the fluorinated group on the polymer chain

Given the possibility of simply esterifying **CTACOOH** to yield a symmetric RAFT agent (**biCTA**), the synthetic route presented in Scheme 5.5 can be used to prepare α,ω–PFB polymers from the bifunctional RAFT agent. Thus, **biCTA**, synthesized according to the procedure reported in Section 7.5, was used for the polymerization of methylmethacrylate as shown in Figure 5.26 (top). The RAFT polymerization was performed in dioxane at 70 °C employing a ratio of RAFT agent to monomer equal to 1:150 (for more details refer to section 7.5). The polymer is recovered by precipitation in a cold mixture of methanol:water (4:1). The precipitation was repeated several times until no monomer was left, as observed *via* ^{1}H NMR spectroscopy. This is particularly important in case of (meth)acrylate monomers as the double bond is an activated –ene (Michael type) and thus it is a substrate for *h*DA reaction

or nucleophilic attack. The final product (**biPMMA**) presented a molecular weight of 7000 g·mol^{-1} ($Đ$ = 1.2), according to SEC analysis (Figure 5.26, bottom, black).

Subsequently, **biPMMA** was functionalized with **PFB-PE** (as shown in Scheme 5.5) by irradiating the reaction mixture in a custom made photoreactor at λ = 320 nm for 1 h (refer to Section 7.5). The final product (**biPFB-PMMA**) was analyzed *via* SEC (Figure 5.26, bottom, light blue) and presented a M_n = 8100 g·mol^{-1} ($Đ$ = 1.2). The increase in the molecular weight compared to **biPMMA** precursor is due to the incorporation of the **PFB-PE** group at both ends.

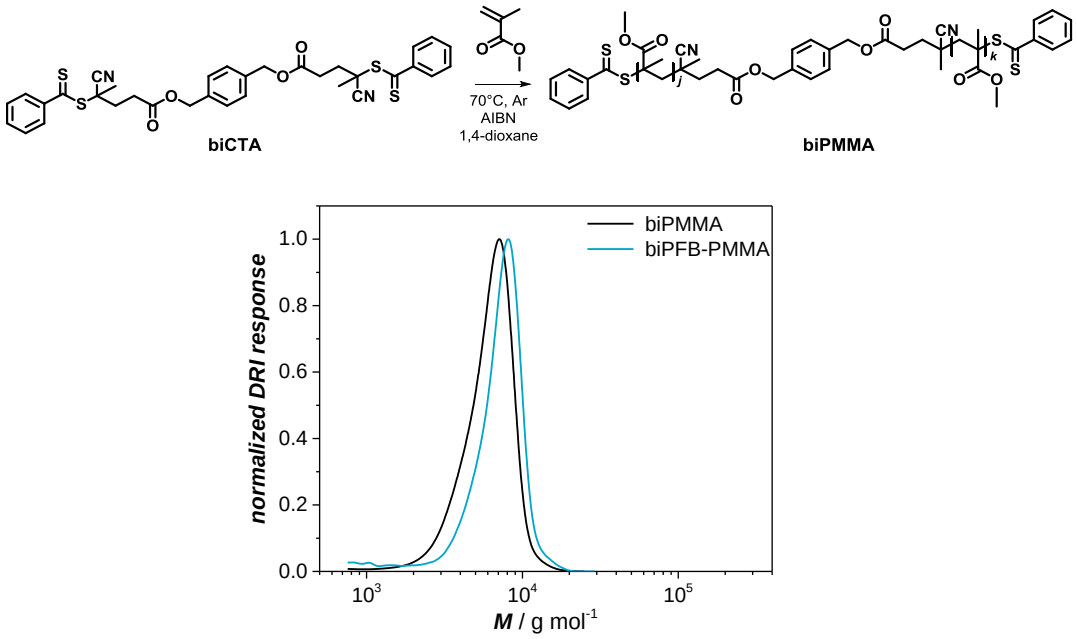

*Figure 5.26 – Top: Reaction scheme for the synthesis of **biPMMA** via RAFT polymerization, starting from a custom designed RAFT agent (**biCTA**). Bottom: SEC trace of the polymer as obtained after polymerization (**biPMMA**, black line), and after functionalization with **PFB-PE** (**biPFB-PMMA**, light blue line). M_n = 7000 g mol^{-1} ($Đ$ = 1.2) and 8100 g mol^{-1} ($Đ$ = 1.2) before and after functionalization, respectively.*

Furthermore, for a more precise elucidation of the chemical structure, the ESI-MS, ^{1}H and ^{19}F NMR spectra for **biPMMA** before and after functionalization were recorded. While the ^{1}H and ^{19}F NMR spectra are reported in Appendix (Figure 8.28), the ESI-MS spectra of the precursor and the product are reported in Figure 5.27. In detail, the ESI-MS spectra were recorded in positive ion mode, thus the molecule is present as $[M+nNa]^{n+}$ adduct.

In the full spectra (Figure 5.27a), recorded in the m/z = 1400-2700 range, the triple and double charged distributions are visible. Thus, a Δm = 100.053, corresponding to the molecular weight of the MMA used as monomer, is found each three or two consecutive peaks, respectively (Figure 5.27b). Moreover, the $\Delta m/z$ ratio of a selected polymer chain (e.g. having 57 repeating unit Figure 5.27b, red symbols) before and after functionalization with **PFB-PE** is equal to 300.060, where z = 3 and m = 900.179. The latter corresponds to the molecular weight of the

end group after functionalization. Overall, the excellent agreement between the experimental and simulated ESI-MS spectrum for **biPFB-PMMA** (Figure 5.27c, repeating unit = 57), confirms the synthesis of the desired α,ω–fluorinated poly(methyl methacrylate). Additionally, a selected list of peaks appearing in the ESI-MS spectra is listed in Table 5.8.

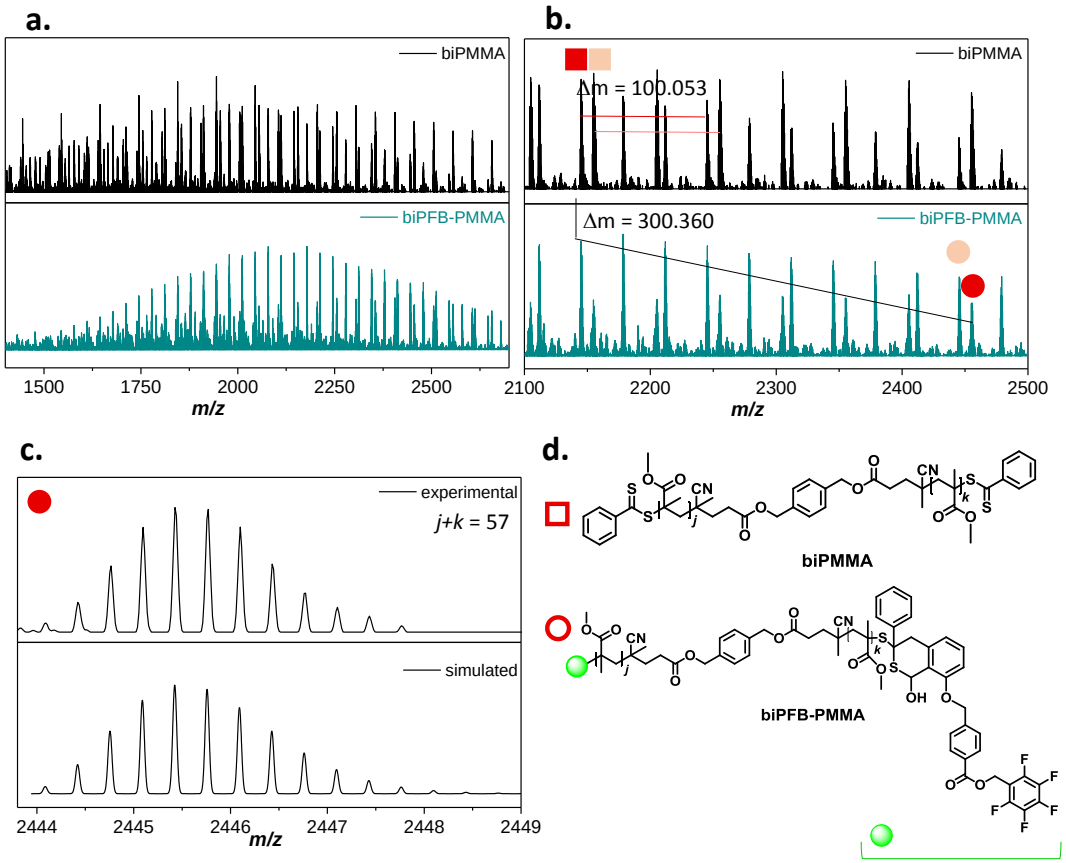

*Figure 5.27 – (+)ESI-MS analysis on **biPMMA** before (black) and after (blue) functionalization. a. Full spectra recorded in the m/z = 1400-2700 range. b. Representative zoom in order to identify the main species. Herein, Δm = 100.053 represents the repeating unit, methyl methacrylate. A selected list of peaks is summarized in Table 5.8. c. Experimental and simulated ESI-MS spectrum for **biPFB-PMMA** with a total of 57 repeating units (j+k). d. Chemical structure for **biPMMA** before (square) and after (circle) functionalization.*

Table 5.8 – Comparison of the mass to charge ratio (m/z) for the peak highlighted in Figure 5.27b. Herein, j+k represents the total number of repeating units and Δm the difference between the experimental and the theoretical m/z.

	Structure	*j+k*	*m/z* (exp)	*m/z* (theo)	*Δm*
■	$[biPMMA+2Na]^{2+}$	36	2154.5020	2154.4974	0.0046
■	$[biPMMA+3Na]^{3+}$	57	2144.3669	2144.3613	0.0056
●	$[biPFB\text{-}PMMA+2Na]^{2+}$	33	2455.5164	2455.5073	0.0091
●	$[biPFB\text{-}PMMA+3Na]^{3+}$	57	2444.4266	2444.4207	0.0059

In the following step, **biPFB-PMMA** was used for the synthesis of polymeric networks in combination with a four-armed, commercially available, thiol linker (pentaerythritol tetrakis(3-mercaptopropionate, 4COOSH). The reaction scheme is proposed in Scheme 5.6. The cross-linking reaction was carried out using an equimolar of SH:PFB, and a concentration of 300 mg·mL^{-1} in DMF, as for the previous section. Upon addition of DBU (i.e. base, 1eq.), the reaction mixture turned to a dark color, but no network formation was observed.

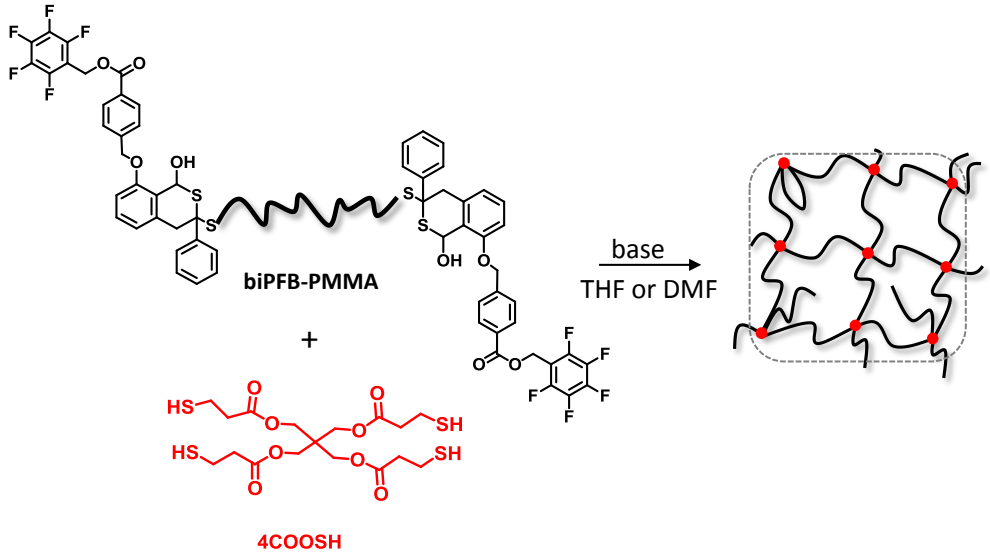

*Scheme 5.6 – Reaction scheme for the synthesis of polymeric network starting from **biPFB-PMMA** and a commercially available four-armed thiol linker (4COOSH).*

Hence, the crude mixture was analyzed *via* ^{19}F NMR spectroscopy, which indicated that the reaction proceeded with quantitative conversion, despite the absence of network. Notably, the resonances of the *ortho*- and *meta*- fluorine after PFTR appeared at $\delta = -138.0$ and -149.2 ppm instead of $\delta = -133.7$ and -141.6 ppm, respectively (Figure 5.28, middle).

Most likely, the difference in the chemical shift is associated with the degradation of the linker or bifunctional polymer, which inhibits network formation. The reaction was thus repeated in THF where the thiolate ions are less nucleophilic and potentially less likely to cause side reactions. After 1 h of reaction time however, no network was observed. The ^{19}F NMR spectra of the polymer precursor (top) and of the soluble fractions after PFTR for the reaction in both DMF (middle) and THF (bottom) are compared in Figure 5.28.

As already mentioned, for the reaction in DMF (middle), the resonances of the *ortho*- and *meta*-F atoms after PFTR do not correspond to those typical of PFTR reaction observed previously. Interestingly, when THF was used as a solvent, the characteristic resonances after PFTR are present but the conversion is equal to only 40% (Figure 5.28, bottom), which may be the reason why no network was observed.

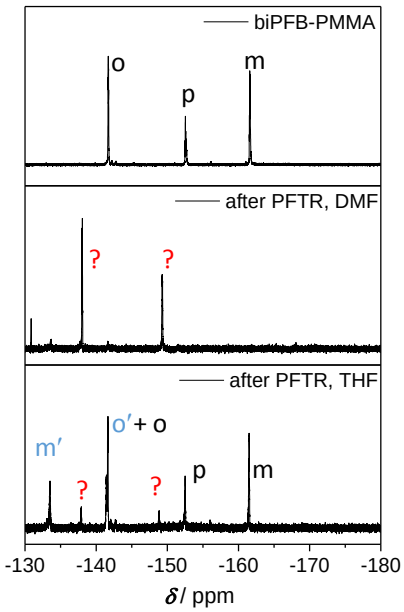

*Figure 5.28 – ^{19}F NMR spectra ($CDCl_3$, 377 MHz) of the reaction mixture before (top) and after PFTR between **biPFB-PMMA** and 4COOSH in DMF (middle) and THF (bottom). The reaction was performed using a ratio of 1:1:1 (SH:PFB:DBU) and a concentration of 300 mg·mL^{-1} in DMF.*

Notably, next to the expected resonances of the PFTR adduct, also those associated with the side product are observed in the ^{19}F NMR spectrum for the reaction with THF. Hence, further investigation was seemed necessary in order to identify the labile part of the system, which causes the undesired shift in the resonances. For this purpose, test reactions were performed on small molecule derivatives.

In **PFB-PE**, the fluorinated benzylic moiety contains ester bond directly attached to an aromatic group. Thus, a small molecule resembling this feature (**1COOPFB**) as well as **PFB-PE** were reacted with both 4COOSH and alipSH. Each reaction was performed with a molar ratio of SH:PFB:DBU = 1:1:1, and $[PFB]_0$ = 0.075 mol·L^{-1} in both DMF and THF. The ^{19}F NMR spectra were recorded in each case and no differences were observed between the same reaction performed in either DMF or THF. Thus, only the results for the reactions in DMF are displayed in Figure 5.29, showing the four possible reaction combinations.

According to the data reported in Figure 5.29, when the reaction is performed with alipSH rather than the 4COOSH, the resonances after PFTR appear at $\delta = -134$ and -142 ppm, highlighting the suitability of the fluorinated molecule (**PFB-PE**) towards PFTR. Contrary to that, the findings suggest an instability of the 4COOSH thiol under the adopted conditions (Figure 5.29, left), probably depending on the base used (i.e. DBU).

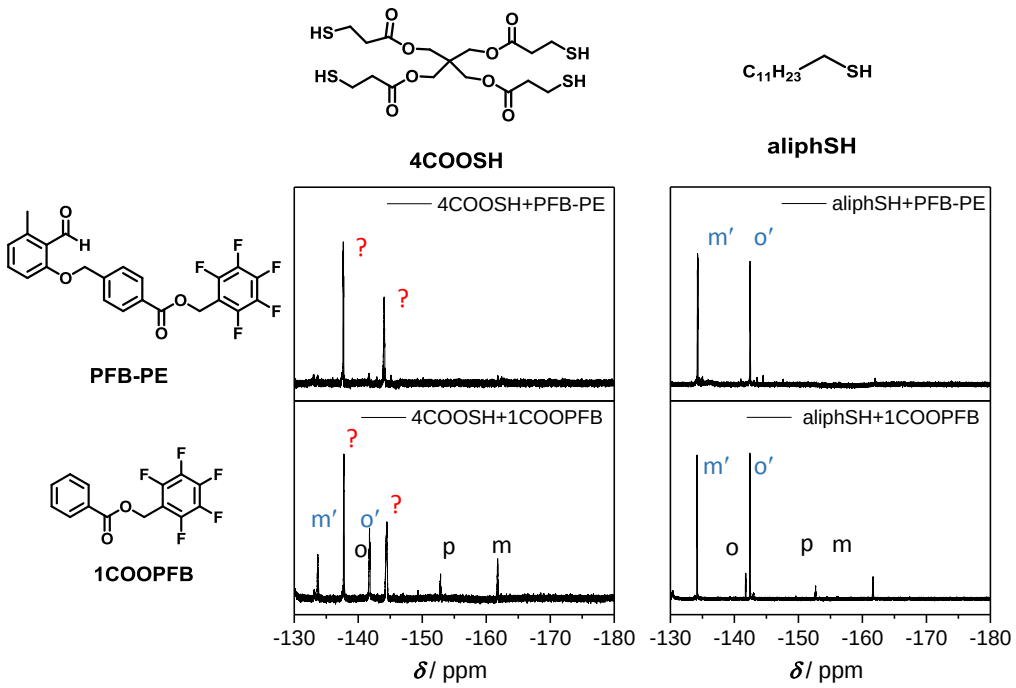

*Figure 5.29 – ^{19}F NMR spectra ($CDCl_3$, 377 MHz) for different PFTR reactions. The reactions were performed using a ratio of 1:1:1 SH:PFB:DBU. The PFB groups belong to either **PFB-PE** (top) or **1COOPFB** (bottom). The thiol groups belong to either 4COOSH (left) or alipSH (right). The resonances ascribed to the potential side reaction are highlighted with a red question mark in the ^{19}F NMR spectra.*

To overcome this issue, one possibility discussed in **Chapter 4**, is to take advantage of the self-propagated PFTR mechanism. Here, the use of a minimum amount of base can potentially reduce undesirable side reactions.

Thus, **PFB-PE** was reacted with **4COOSH** in DMF employing a ratio of SH:PFB = 1:1, while 0.3 eq. of TBAF as base were added dropwise. After two hours, the crude reaction mixture was analyzed *via* ^{19}F NMR spectroscopy, which indicated a conversion up to ~95% of the PFB group, and the resonances assigned to the side reaction were not present in the spectra (Figure 8.29, see Appendix). As further proof, ESI-MS analysis was performed (positive mode). The excellent agreement between the experimental and the simulated ESI-MS spectra (Figure 5.30, $\Delta m/z$ = 0.0034), together with the results from ^{19}F NMR measurements confirmed that success of the PFT reaction.

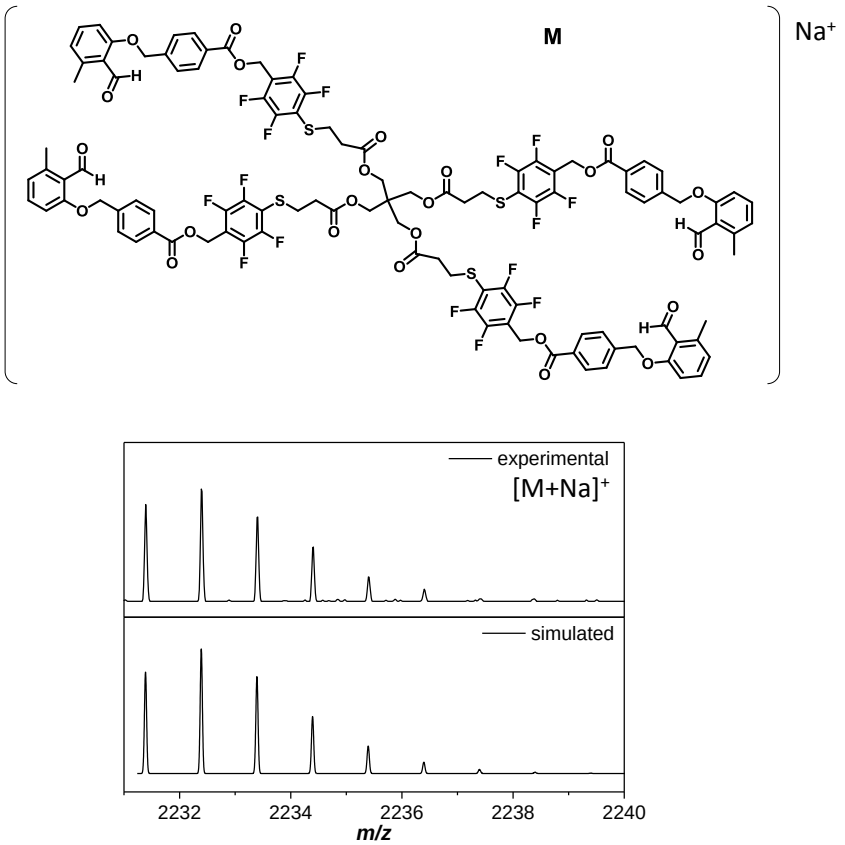

*Figure 5.30 – Top: Chemical structure of M, the molecule obtained after PFT reaction between 4COOSH linker and **PFB-PE**, performed using a ratio of 1:1 between SH and PFB group and 0.3 eq. of TBAF as base. Bottom: Experimental and simulated ESI-MS spectra for M, analyzed in positive ion mode. ($[M+Na]^+$). m/z_{exp} = 2232.3939, m/z_{theo}= 2232.3905, $\Delta m/z$ = 0.0034.*

Considering the positive results obtained after these test reactions, **biPFB-PMMA** was reacted with 4COOSH using a ratio of SH:PFB = 1:1 and 0.3 eq. of TBAF respect to the thiol groups as a base. However, the addition of TBAF caused, also in this case, color change in the reaction mixture, suggesting the presence of degradation products. Since the stability of the thiol linker was already demonstrated in the adopted conditions, the polymer was mixed with the base (0.3 eq. of TBAF respect to the PFB groups) in DMF. The mixture was stirred for 16 h (over-night) at ambient temperature, and analyzed the day after *via* ^{19}F NMR spectroscopy and SEC, with the results shown in Figure 5.31. In detail, the ^{19}F NMR spectrum of the polymer after degradation (Figure 5.31, left bottom) is compared to the one of the polymer precursor **biPFB-PMMA** (Figure 5.31, left top), with no observable differences. Similarly, the SEC trace of the crude mixture (Figure 5.31, right, red) is compared with the polymer before degradation (**biPFB-PMMA**, Figure 5.31,right, light blue), the polymer before functionalization with PFB groups (**biPMMA**, Figure 5.31, right, black) and the solvent in which the SEC trace was performed (Figure 5.31, right, gray). The latter is include to discriminate between peaks arising from the solvent and those from the polymer.

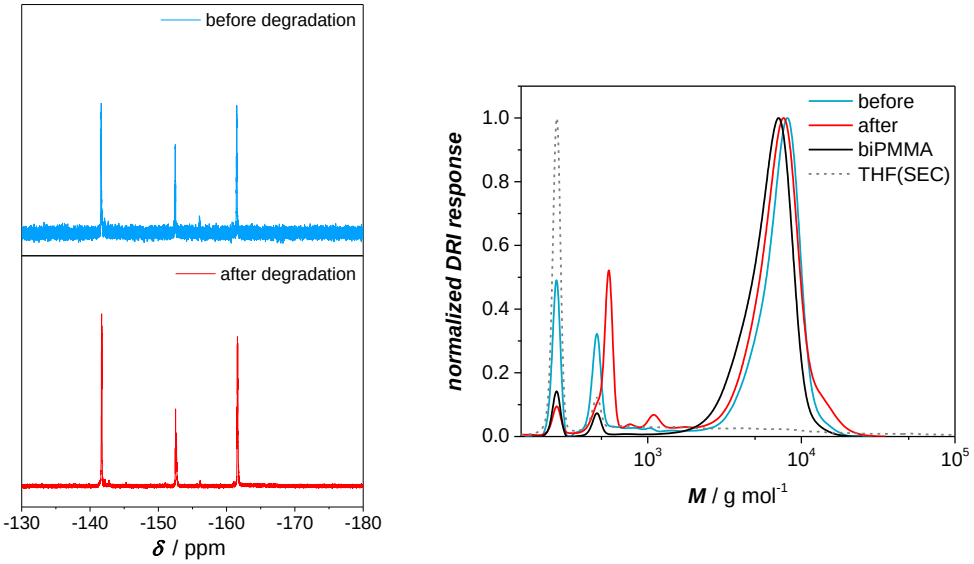

*Figure 5.31 – Left: ^{19}F NMR spectra ($CDCl_3$, 377 MHz) before (top) and after (bottom) the degradation test, performed by mixing **biPFB-PMMA** and TBAF (1:0.3 molar ratio) overnight, at ambient temperature in DMF (300 mg·mL^{-1}). Right: SEC traces of the polymer before (blue) and after (red) the degradation test. The SEC traces are compared with the parent **biPMMA** polymer (black) and the solvent used for SEC analysis (gray, dashed line). Despite the system peaks (present also in the blank, THF), a new peak appears after degradation.*

Contrary to the ^{19}F NMR spectrum (Figure 5.31, left), the SEC trace (Figure 5.31, right) of the polymer shows a shift towards lower molecular weight (red). The molecular weight of the degraded polymer (red) appears to be between that of the polymer before functionalization with a PFB moiety (black) and before base is added (blue). This indicates that some cleavage does indeed occur at the chain ends, ultimately proving the limitation of this route.

Accordingly, it appears that both DBU and TBAF are not suitable for the purpose. Thus, an alternative base – triethylamine (Et_3N) – was tested for its suitability in this work.

Since Et_3N is a milder base the reaction is often performed at 40 °C as reported in literature.[69, 98] In order to ensure the absence of side reactions, the stability of the **biPFB-PMMA** polymer in triethylamine at 40 °C was tested by stirring an equimolar ratio of polymer and the base in DMF (300 mg·mL^{-1}) for 16 hours. Subsequently, the crude mixture was analyzed *via* SEC (Figure 5.32). Positively, no change of the SEC trace after 16 hours are observed, which indicates that the polymer is stable under these conditions.

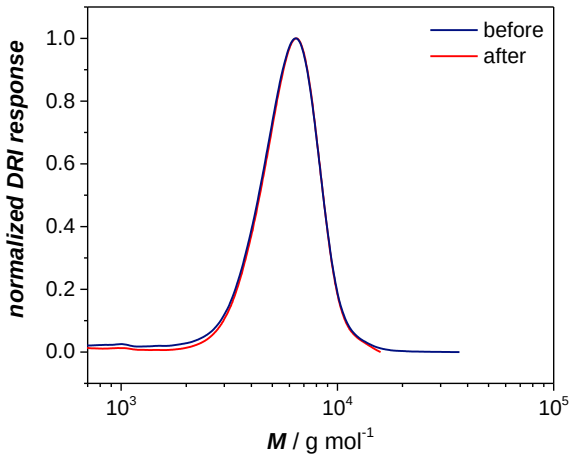

*Figure 5.32 – SEC traces before (blue) and after (red) degradation of **biPFB-PMMA** with triethylamine at 40 °C overnight. The reaction was performed using an initial molar ratio of SH:base = 1:1 and a concentration of 300 mg·mL^{-1} in DMF.*

Next, the crosslinking reaction was investigated employing the same conditions. Thus, an equimolar ratio of PFB and SH groups arising from **biPFB-PMMA** and 4COOSH were dissolved in DMF (300 mg·mL^{-1}), and heated to 40 °C. Next, triethylamine (1 eq. respect to the thiol groups) was added. However, network formation was not observed after 24 or 72 h, despite a 70% conversion *via* ^{19}F NMR analysis.

Ultimately, 4COOSH was replaced by a different four-armed thiol linker (4phenSH) and tested for network formation, as shown in Scheme 5.7. The network formation was performed in DMF (300 mg·mL^{-1}), separately employing DBU (1 eq.), TBAF (0.2 eq.) and Et_3N (1 eq.) as base. In the case of triethylamine the reaction was carried out at 40 °C instead of ambient temperature.

Successfully, after 16 hours, network formation was achieved for the reaction performed using Et_3N. Thus, the network was washed extensively with THF for the removal of the extractables. Afterwards, the soluble and insoluble phases were separated, and dried in vacuum overnight. The reaction yielded 75% of network by mass, with a functional group conversion of ~88% by ^{19}F NMR spectroscopy (refer to Appendix, Figure 8.30). The conversion in the soluble fraction was ~45% (refer to Appendix, Figure 8.31). The conversion within the network appears to be slightly lower than for thiol polymers with a fluorinated linker (section 5.2.1), however further development – as for the previous system – may allow optimization of this novel system.

As for those obtained from polymeric thiol precursors, the network was subjected to swelling tests in toluene. The resulted degree of swelling was equal to 5.2 ± 0.4 ($Q_{eq,exp}$), which corresponded to a deviation of 26% from the theoretical value ($Q_{eq,theo}$ = 7.1) as calculated using the phantom model for the elastic term and χ = 0.45 for the combination toluene/PMMA.[212] In

agreement with what was reported for the bifunctional thiol derivatives, the use of long chains leads to a deviation of approximately ~20%. However, the purpose of this strategy was to evaluate an alternative synthetic route for polymers that are sensitive to the aminolysis step and no further investigation of the effect of the elastic chain length were performed at present.

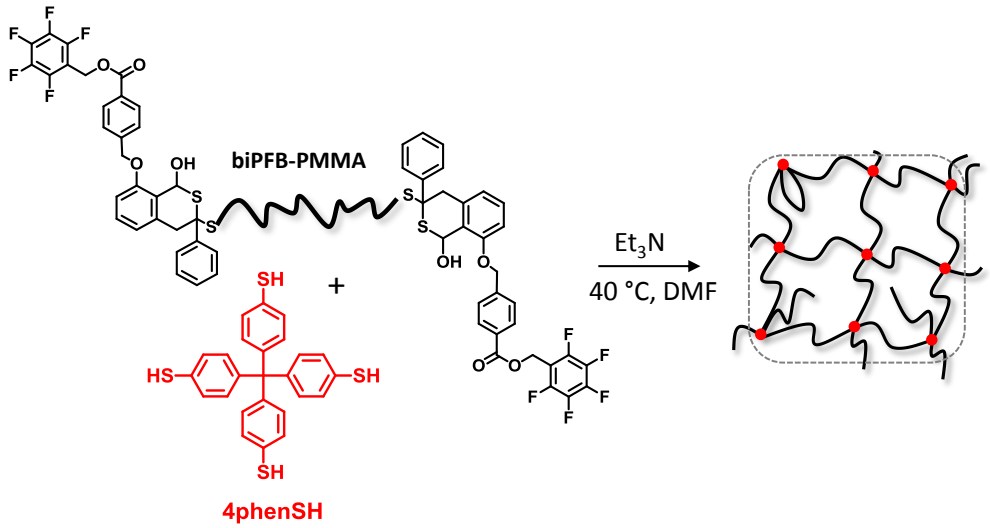

*Scheme 5.7 – Reaction scheme for the synthesis of networks via PFTR employing α,ω-fluorinated polymer (**biPFB-PMMA**) and 4phenSH at 40 °C in DMF (300 mg·mL^{-1}).*

In summary, a PFTR-based system using bifunctional fluorinated polymers and thiol linkers for the synthesis of polymer networks was successfully developed. However, in contrast to previous results (section 5.2.1), labile bonds present in both the commercially available 4COOSH linker and within the structure of the fluorinated polymer must be taken into account, limiting the choice of thiol linker and suitable bases. Nonetheless, after systematic exploration of this, the combination of a non-labile thiol linker (4phenSH) and bifunctional fluorinated polymer (**biPFB-PMMA**) with Et_3N as base was found to facilitate network formation, providing a platform for the synthesis of polymer networks from thiol linkers and fluorinated polymers. However, further development and optimization of these reaction conditions is needed to determine the maximum possible conversions and yields.

Most importantly, the dithiocarbonate RAFT agent used in the current section (**biCTA**) is suitable for the polymerization of methacrylates polymers, which upon deprotection can yield methacrylic acid polymers, necessary for applications such as the use of hydrogels as separation agent presented early on. Notably, the RAFT agent is also suitable for the direct polymerization of acrylic acid (refer to SEC traces in Appendix, Figure 8.32 and Table 8.6). However, the effect of free carboxylic acid groups during PFTR is potentially still problematic, yet not explored.

5.3 Summary

In the current chapter, the *para*-fluoro–thiol reaction between a thiol and a fluorinated aromatic group has been extensively studied as crosslinking reaction for the synthesis of networks *via* end-linking approach. The good agreement between the experimental and the theoretical degrees of swelling for the networks synthesized according to this strategy emphasizes the efficiency of the selected approach.

Synthetically, the networks can be achieved using both bifunctional thiol precursor in combination with three- or four-armed fluorinated linker or vice versa. In both cases, the polymer precursors can be precisely synthesized *via* RAFT polymerization. The first route is recommended for polymer not sensitive to the aminolysis step (e.g. polystyrene), while the second route is recommended for all monomers that can be polymerized with the reported RAFT agent, such as acrylic acid and methacrylates.

From the analytical point of view, the fluorine atoms – located at the crosslinking points – can be detected *via* XPS and ToF-SIMS when the concentration is sufficiently high, e.g. using small molecules bifunctional thiol precursors. On the other hand, ^{19}F NMR spectroscopy provides accurate data in each of the proposed examples, allowing the precise identification and quantification of the unreacted functionalities, providing a powerful tool for the direct quantification of structural defects. Thus, the identification of defects, detectable using nondestructive analytical method, was successfully achieved.

6
Conclusion and Outlook

Overall, the results described in the current thesis present a significant step towards achieving the long standing goal of developing advanced methodologies for the synthesis and characterization of polymer networks. By these means, a variety of potential pathways for the synthesis of more defined networks were successfully developed and in-depth explored. Namely, the RAFT-mediated polymerization of a mono- and a bifunctional monomer, and the use of highly efficient ligation techniques for the crosslinking of pre-formed well-defined bifunctional polymers with a suitable crosslinker unit. Firstly, the synthesis of poly(sodium acrylate) networks suitable for the desalination of salt water in a membrane-free process was performed *via* RAFT-mediated copolymerization of acrylic acid as monomer and *N,N´*–methylenebisacrylamide as crosslinking agent as described in **Chapter 3**. Significant differences between the polymerization techniques were visible during the crosslinking process already at early stage of the polymerization: at 5% conversion, for example, short and well-defined polymer chains were detected using the RAFT-mediated approach, in contrast to large and undefined chains for the conventional free radical polymerization (FRP). Moreover, the gelation was achieved after 30% conversion in the case of FRP compared to ~85% conversion in the presence of 0.17 molar % of RAFT agent. This difference clearly indicates that a high number of crosslinking points occur in solution for the RAFT mediated process, facilitating the diffusion of the growing chains before network formation, and potentially reducing the formation of entanglements. Furthermore, the macroscopic properties, e.g. swellability and rigidity of the network, were also affected by the presence of the RAFT agent. Briefly, the

networks obtained *via* RAFT approach showed higher degrees of swelling and higher mobilities of the network microstructure according to ^{1}H NMR relaxometry measurements compared to the analogous FRP networks. One reason for that is the reduced number of crosslinking points. However, understanding of whether the observed increase in mobility was also associated with a less efficient crosslinking process or with the reduced presence of entanglements and nanogels was challenging to evaluate. Moreover, both FRP and RAFT-mediated networks presented a heterogeneous mobility, indicating the presence of more mobile and more rigid parts within the networks, e.g. not homogeneous chain length. Further investigation regarding the quantification of the unreacted double bonds was not possible *via* NMR due to overlapping and broadening of the signal after network formation. Thus, with information about the network microstructure being difficult to assess, it follows that more advanced analytical tools as well as synthetic strategies are required to facilitate the identification of defects. Concerning ^{1}H NMR relaxometry measurements, the use of deuterated monomers, either located in the proximity of the crosslinking points or in the middle of the chain, provide a potential step towards the optimization of the method.

Based on the aforementioned limitations of the available analytical tools, the *para*-fluoro-thiol reaction (PFTR) was highlighted as a novel and potentially powerful tool in the quantification of network defects. The PFTR was proposed as crosslinking reaction between well-defined bifunctional polymer precursors and a three- or four-armed linker, i.e. end-linking strategy. Importantly, since each precursor contains complementary functionality, i.e. thiol and fluorinated groups, the resultant network bears the fluorine heteroatoms solely at the crosslinking point. Subsequently, since *via* ^{19}F NMR measurements it is possible to distinguish between the resonances of the fluorine atoms before and after PFTR, the identification and quantification of unreacted moieties becomes possible. Considering that, to the best of our knowledge, PFTR was never applied as a crosslinking reaction beforehand, a detailed study oriented towards the investigation of the optimal reaction conditions was carried out. In order to avoid defects during network formation in fact, it is important that the reaction proceeds selectively towards the desired product in nearly quantitative yields, and with minimal or no side reactions. The absence of multiple substitutions on the fluorinated aromatic ring was ensured by tailored design of the moiety itself. The importance of the overall chemical structure of the linker was highlighted in **Chapter 4**, with a pentafluoro-benzyl (PFB) rather than phenyl (PFP) moiety having a more suitable reactivity as PFB groups ensure the absence of the undesired multiple substitutions as proven by ^{19}F NMR spectroscopy. Moreover, since the PFT reaction involves the presence of thiolates, the disulfide bond formation was taken into account as a potential side reaction, and thus studied individually and in competition with PFTR. The

results showed that the oxidation to disulfides was negligible for small molecules and in general when the PFTR was performed in THF. In contrast, the side reaction occurred in small percentage during the formation of more complex polymeric architectures such as three-armed stars in DMF at long reaction times (> 24 h). Nonetheless, it was shown that the use of equimolar amounts of reducing agent (e.g. TCEP) and thiol groups avert the side reaction by reducing the disulfide bonds and regenerating free thiolates. Furthermore, the possibility of performing the reaction using under-stoichiometric amounts of base was developed as a reaction pathway in case labile groups are incorporated into the polymer backbone.

Finally, the networks were successfully synthesized, as previously suggested, upon using PFTR as crosslinking reaction for network formation *via* the end-linking approach. Notably, selecting the end-linking approach it was possible to accurately tune the mesh size of the final network by changing the length of the bifunctional precursor, from small molecule to polymeric derivatives, with the latter leading to larger mesh size and thus higher degrees of swelling. Moreover, the power of the end-linking strategy is highlighted by the ability to adjust the functionality of the bifunctional polymers and crosslinkers, depending on factors such as synthetic simplicity or commercial availability of the precursors. As extensively demonstrated in **Chapter 5**, the method has been optimized for both bifunctional thiol polymers, obtained upon aminolysis of the RAFT end-group, and bifunctional fluorinated polymers, which were prepared *via* reaction of the RAFT end-group with a photocaged diene possessing a pentafluoro benzyl moiety. Comparison of the degree of swelling of the final networks with the theoretical values (phantom model) led to minor deviation of approximately 5% to 25% when varying the length of the polymer precursor from 3800 $g \cdot mol^{-1}$ to 8500 $g \cdot mol^{-1}$.

For each network, the precise identification and quantification of the unreacted moiety was possible *via* direct analysis of the network using routine ^{19}F NMR measurements. The sensitivity of the analytical tool allowed for the detection of unreacted moieties, even if present only in low percentages.

For the identification of other types of defects, e.g. loops, significant progresses were made in the last couple of years.[5, 18, 126] The quantification of primary and secondary loops is indeed possible upon network disassembly procedure based on asymmetric cleavage of the elastic chains.[18] Nonetheless, a gap is still present for analyzing the mesh size distribution. One future option may be the optimization of analytical methods such as inverse-SEC.[214] The method is based on the combination of a column containing unknown porosity (synthesized network) with well-defined polymer samples (standards). The relation between the molecular weight of the employed polymer standards, their elution volume and the broadness of the resultant peak should give an indication of the pore size (and their distribution) of the prepared networks. This

method would require scalability of network synthesis, thus the RAFT mediated approach would be an ideal candidate for this purpose.

Concerning the salt rejection ability, the RAFT-networks showed a minimal improvement during the preliminary salt rejection experiments at low degree of crosslinking, showing an absolute increase of ~5% in the salt rejection ability. However, further advanced characterizations of the network are necessary to discriminate whether the minor differences observed were arising from a different microstructure, experimental deviations or inhomogeneity of the particle size distribution. Thus, an important point is to understand whether the homogeneity is desirable in terms of network microstructure or, more generally, of particle shape size and distributions. In order to relate any difference in performance to the microstructure the detection of defects is fundamental. In other words, it is necessary to precisely identify the amount of unreacted moieties, loops, as well as the mesh size distribution in order to understand the impact that each one of these defects have on the application. Concerning the particle shape instead, homogeneous particles could be achievable *via* suspension polymerization[215] or by using microfluidics.[216] Here, established analytical methods such as scanning electron microscopy (SEM) may assist in the determination of the most beneficial diameter and particle size distribution for following application.

Given the largely unexplored nature of the employed strategies, along with the difficulties and limitations of quantifying defects in polymer networks, the development of defect-free networks is inevitably a step-wise process.

In conclusion, the presented work achieves a number of goals and progresses towards the synthesis of more homogeneous networks. The precise quantification of defects *via* nondestructive, routine measurements was explored, as well as the impact of a RAFT agent in the early stage of the crosslinking process was elucidated. Building on these results, important further advancements will be facilitated by the development of tools for a more complete characterization of the synthesized networks. This will then allow for a more precise and tailored synthesis of polymer networks where the properties are introduced or removed on-demand, according to the requirements arising from the final application, by controlling the presence or absence of defects at best.

7 Experimental Section

7.1 Materials

Monomers:

Divinylbenzene (80% mixture of isomers, Alfa Aesar), styrene (stabilized, >99.0%, Merck), methyl acrylate (MA, stabilized, 99%, Sigma Aldrich) and methyl methacrylate (MMA, stabilized, 99%, Sigma Aldrich) were passed through a column loaded with basic alumina, while acrylic acid (AA, 99%, sigma Aldrich) was distilled prior to use.

Other chemicals:

Azobis(isobutylnitril) (AIBN, 98%, Merck) was recrystallized before use.

Aliquat® 336 (Sigma Aldrich), aluminium chloride ($AlCl_3$, 99%, Roth), aluminium oxide basic (Acros Organic), 4,4'-Azobis(4-cyanovaleric acid) (V-501, 98% Alfa Aesar), 1,3,5-benzenetricarboxylic acid (98%, Alfa Aesar), benzoic acid (BA, >99,5% Merck), 1,3-butanediol diacrylate (DAc, 98%, Sigma Aldrich), 1,4-butanedithiol (BT, >95%, TCI), 1,2,3,4-butanetetracarboxylic acid (> 98%, Alfa Aesar), 2-butanethiol (*sec*-aliphSH, ≥95%, Sigma Aldrich), butylamine (>99%, Alfa Aesar), carbon disulfide (CS_2, ≥ 99%, Sigma Aldrich), cesium carbonate (Cs2CO3, 99% Sigma Aldrich), copper sulfate pentahydrate ($CuSO_4$ $5H_2O$, Merck, for synthesis), 4-cyano-4-(phenylcarbonothioylthio)pentanoic acid (CTACOOH, Sigma Aldrich), 1,8-diazabicyclo[5.4.0]undec-7-ene (DBU, ≥98%, Merck), α,α´-dibromo-*p*-xylene (97%, Sigma Aldrich), diethylene glycol (99%, Alfa Aesar), *N*,*N*-diisopropylethylamine (DIPEA, ≥ 99%,

Sigma Aldrich), 4-(dimethylamino)pyridine (DMAP, ≥ 99%, Sigma Aldrich), 2,3-dimethylanisole (97%, Alfa Aesar), 3,6-dioxa−1,8-octanedithiol (DODT, 95%, Sigma Aldrich), dithiothreitol (DTT, molecular biology grade, AppliChem), 1-dodecanethiol (aliphSH, 98%, ABCR), 2-(((dodecylthio)carbonothioyl)thio)propanoate (DoPAT, Lanxess GmbH), 2,2′-(ethylenedioxy)diethanethiol (> 95%, Sigma Aldrich), 1-Ethyl-3-(3-dimethylaminopropyl)carbodiimide hydrochloride (EDC(HCl), ≥ 99%, Roth),magnesium sulfate (Mg_2SO_4, ≥99.8%, Roth), *N*,*N*´-Methylenebisacrylamide (MBA, ≥ 99.5%, Sigma Aldrich), methyl 4-(bromomethyl) benzoate (98%, Sigma Aldrich), 4-methoxy-α-toluenethiol (benzSH, 90%, Sigma Aldrich), 1-phenylethyl mercaptan (*sec*-benzSH. 98%, Alfa Aesar), 1,4-phenylenedimethanethiol (PDT, >98%, TCI), pentaerythritol tetrakis(3-mercaptopropionate) (4COOSH, > 95%, Sigma Aldrich), 2,3,4,5,6-Pentafluorobenzyl bromide (PFB-Br, 98%, Alfa Aesar), pentafluorophenol (≥ 99%, Sigma Aldrich), potassium carbonate (K_2CO_3, Alfa Aesar, 99 %, anhydrous), potassium peroxodisulfate ($K_2S_2O_8$, Sigma Aldrich, 97), sodium carbonate (NaHCO3, ≥ 99.5, Roth), sodium chloride (NaCl, 99.9%, AnalaR, VWR), sodium hydroxide (NaOH, ≥99%, Roth), tetrabutylammonium bromide (TBABr, 99%, ABCR), tetrabutylammonium fluoride solution (TBAF, 1 M in THF, Sigma Aldrich), tetrabutylammonium hydroxide (TBAOH, 40% w/w in MeOH, Sigma Aldrich), thiolactic acid (COOH-SH, 95%, Sigma Aldrich), thiophenol (phenSH, ≥99%, Sigma Aldrich), triethylamine (Et_3N, ≥ 99%, Sigma Aldrich), tricarballylic acid (98%, Alfa Aesar), tris(2-carboxyethyl)phosphine (TCEP, 98 %, Alfa Aesar), 1,1,1-tris(hydroxymethyl)ethane (99%, Sigma Aldrich), and 18-crown-6 (99%, Acros Organic) were used as received.

Solvents:

Cyclohexane (CH, AnalaR, VWR), dichloromethane (DCM, AnalaR, VWR), *N*,*N*-dimethylformamide (DMF, AnalaR, VWR), dry DMF (99+%, Acros Organic), ethanol (99.8%, AnalaR, VWR), ethylacetate (EA, AnalaR, VWR), methanol, tetrahydrofuran (THF, AnalaR, VWR), dry THF (99.5%, stabilized, Acros Organic), toluene (≥ 99.5%, AnalaR, VWR) were employed as solvents as used as received.

Deuterated solvents:

$CDCl_3$ (> 99.8%), DMSO-d_6 (99.8%), DMF-d_7 (99.5%), THF-d_8 (99.5%) D_2O (99.9%) were purchased from Eurisotop.

7.2 Methods

Size-exclusion chromatography (SEC) – system 1 (used in Chapter 4)

SEC traces were recorded using a TOSOH Eco-SEC HLC-8320 GPC System, comprising an auto sampler, a SDV 5 µm bead-size guard column (50 x 8 mm, PSS) followed by three SDV 5 µm columns (300 x 7.5 mm, subsequently 100 Å, 1000 Å and 10^5 Å pore size, PSS), a differential refractive index (DRI) detector and an UV detector. THF was used as eluent at 30 °C with a flow rate of 1 mL·min^{-1}. The SEC system was calibrated using linear polystyrene (PS) standards ranging from 2.66 10^2 to 2.52 10^6 g·mol^{-1}. Calculation of the absolute molar mass proceeded *via* the Mark-Houwink-Sakurada (MHS) parameters in THF at 30 °C, K = 13.63 10^{-3} mL g^{-1}, α = 0.714.[217]

Size-exclusion chromatography (SEC) – system 2 (used in Chapter 3 and 5)

SEC measurements were performed on an Agilent 1200 system, consisting of an autosampler, a Plgel 5 µm bead-size guard column (50 × 7.5 mm), one Plgel 5 µm Mixed E column (300 × 7.5 mm), three Plgel 5 µm Mixed C columns (300 × 7.5 mm), a differential refractive index detector and a UV detector. THF was used as eluent at 35 °C with a flow rate of 1 mL min^{-1}. The SEC system was calibrated using linear poly(styrene) standards ranging from 370 to 2.5 × 10^6 g mol^{-1} or poly(methyl methacrylate) standards ranging from 800 to 2.2 × 10^6 g mol^{-1}. Typically, 100 µL of a 2.0 mg·mL^{-1} polymer solution was injected into the columns. Calculation of the absolute molar mass proceeded *via* the Mark-Houwink-Sakurada (MHS) parameters in THF at 30 °C, K = 13.63 10^{-3} mL g^{-1}, α = 0.714.[217]

Aqueous size-exclusion chromatography (SEC)

SEC measurements were performed on a SECcurity GPC System - Polymer Standards Service GmbH, Mainz - Agilent Technologies 1260 Infinity, comprising an autosampler, a Suprema 5 µm bead-size guard column (8 x 50 mm, PSS) followed by a Suprema linear S mixed-bed 5 µm column (8 x 300 mm, PSS), a differential refractive index (DRI) detector and a UV detector. The measurements were performed using disodium hydrogen phosphate 0.07M in water as the eluent at room temperature with a flow rate of 1 mL·min^{-1}. The SEC system was calibrated using linear poly(acrylic acid) sodium salt standards (PSS) ranging from 1250 g·mol^{-1} to 115 000 g·mol^{-1}.

Nuclear Magnetic Spectroscopy (NMR)

High field

NMR measurements were performed on a Bruker Avance III Microbay 400 at an operating frequency of 400 MHz (^{1}H), 101 MHz (^{13}C) and 377 MHz (^{19}F), respectively.

For cross-linked material, ~10 mg of the gel were placed in the NMR tube and swollen in $CDCl_3$. Thereafter, a NMR spectrum was recorded following the common procedure as employed for liquid samples; all other compounds were dissolved prior to recording the spectrum. All spectra were recorded in $CDCl_3$ at 25 °C, unless differently specified. The residual solvent signals were employed for shift correction (for $CDCl_3$, ^{1}H NMR spectra at δ = 7.26 ppm, for ^{13}C NMR at δ = 77.16 ppm). Abbreviations used in the compound description include singlet (s), doublet (d), triplet (t), multiplet (m), and their combinations. For the ^{19}F NMR spectra, the baseline was corrected with the multipoint baseline correction function.

Low field:

T_2-relaxometry measurements were recorded with the benchtop spectrometer minispec NF (Bruker, Karlsruhe, Germany) at low field (19.95 MHz). The sample temperature was controlled by a BVT3000 unit (Bruker) and kept constant at 30 °C. For all hydrogels, the magnetic field was matched and the pulse lengths were determined prior to the start of the actual experiment.

Sample preparation: The dry polymer was swollen in D_2O in a ratio of 1:9 and transferred to the bottom of a 10 mm glass tube. The tube was sealed with a cap and the hydrogel was allowed to equilibrate for 2 days before the measurement.

T_2 relaxation measurements:

The procedure was adapted from the literature.[160] In detail, the relaxation curve was measured using: one MSE was recoded for 50 μs, followed by a XX4 sequence with a pulse separation of τ = 50 μs and three CPMG/XY16 experiments, having τ = 0.04, 0.1 and 1 ms, respectively. If the decay of the curve was steep at short relaxation times an additional XX4 sequence with τ = 5 μs was measured to increase the point density in the crucial region. A recycle delay of 1 s and no dummy scans were used. Of the XY16 cycle every 8th cycle was recorded, while of the XX4 all cycles were traced. The parameters are summarized in Table 7.1.

Table 7.1 – List of parameters used for measuring the T_2 relaxation decay. In detail, the number of acquired scans (ns), the number of dummies scans (ds), the echo time (τ), the number of dummies echoes (de), the recycle delay (rd) and the number of acquired echoes (ne) are reported.

Parameter	MSE	XX4	XY16_short	XY16_middle	XY16_long
ns (-)	1024	1024	1024	1024	1024
ds (-)	0	0	0	0	0
τ (ms)	-	0.05	0.04	0.1	1
de (-)	-	0	7	7	7
rd (s)	1	1	1	1	1
ne (-)	-	100	100	100	100

Inverse Laplace Transformation:

The Inverse Laplace Transformation was used for deconvoluting the relaxation decay and the mathematical elaboration of the data was performed in agreement with previous literature.[9, 161] The smoothing factor was set equal to 10 and the number of data points to 100 points, logarithmically spaced in the range from 0.01 – 1000 ms.

Electron Spray Ionization Mass Spectroscopy (ESI-MS)

ESI-MS measurements were performed on a Q Exactive (Orbitrap) mass spectrometer (Thermo Fisher Scientific, San Jose, CA, USA) equipped with a HESI II probe. The instrument calibration was carried out in the *m/z* range 74 – 1822, using calibration solutions from Thermo Scientific. A constant spray voltage of 3.6 kV and a dimensionless sheath gas of 5 were applied. The capillary temperature and the S-lens RF level were set to 320 °C and 62.0, respectively. Typically, the samples were dissolved in a THF:MeOH (3:2) mixture containing 100 μmol of sodium triflate and injected with a flow of 5 $\mu L \cdot min^{-1}$. For PS samples, the polymer was dissolved in DCM containing 100 μmol of sodium chloride and injected with a flow of 5 $\mu L \cdot min^{-1}$.

Attenuated Total Reflectance - Infrared Spectroscopy (ATR-IR)

Solid-state Fourier transform IR spectra were recorded using a Bruker Vertex 80 spectrometer, equipped with a tungsten halogen lamp, a KBr beam splitter, and a DTGS detector.

X-Ray Photoelectron Spectroscopy (XPS)

XPS was performed with a K-Alpha+ XPS instrument (Thermo Fisher Scientific, East Grinstead, England). At least three random points for each sample were analysed using a micro-focused, monochromated Al Kα X-ray source (400 μm spot size). The K-Alpha+ charge compensation system was employed during analysis, using electrons of 8 eV energy and low-energy argon ions to prevent any localized charge build-up. Spectra were fitted with several Voigt

profiles (binding energy uncertainty of +/- 0.1 eV). The analyzer transmission function, Scofield sensitivity factors[218] and effective attenuation lengths (EALs) for photoelectrons were applied for quantification. EALs were calculated using the standard TPP-2M formalism.[219] All spectra were referenced to the C1s peak (C-C, C-H) at 285.0 eV binding energy controlled by the means of the well-known photoelectron peaks of metallic Cu, Ag and Au.

Time-of-Flight Secondary Ion Mass Spectrometry (ToF-SIMS)

ToF-SIMS analysis was performed using a ToF-SIMS 5 instrument (ION-TOF GmbH, Muenster, Germany). Surface spectroscopy was carried out with Bi_3^+ as primary ion for secondary ion generation. Measurements were performed on two different positions of each sample obtaining surface images with high mass resolution. Surface charging was avoided by compensation with a low energy (<20 eV) electron beam. The recorded data was flight time corrected using the Advanced ToF Correction feature of the SurfaceLab 6.6 software of the instrument. All images show a recorded area of 500 x 500 µm with 128 x 128 data points obtaining a resolution of about 4 µm per measurement point. Images are normalized to the total ion intensity. Brighter colors indicate higher intensity values. Color scales of specific fragments have always the same values. For the measurement of polymeric networks 1000 Ar atoms with total energy of 10 keV with single positive charge, in delayed extraction mode, were used as primary ions instead of Bi_3^+ clusters.

Different Scanning Calorimetry (DSC)

DSC experiments were carried out under nitrogen atmosphere using 40 µL aluminium crucibles with a DSC821e (Mettler Toledo) calorimeter, using sample mass in the range of 8–15 mg. For analysis the following method was employed: the first heating proceeded from -75 °C to 300 °C with a heating rate of 10 °C min^{-1}; a cooling step was performed from 300 °C to -75 °C with a heating rate of 10 °C; the second heating run was recorded from -75 °C to 300 °C with a heating rate of 10 °C min^{-1}. The glass transition temperature, T_g, is reported as the midpoint of the heat capacity change in the first heating scan.

Photoreactor

The hetero-Diels–Alder (*h*DA) reaction was performed in a custom-built photoreactor (refer to Figure 7.1), employing a contact lamp (ARIMED B6, 36 W, λ_{max} = 320 nm, for emission spectra refer to Figure 7.2). For details concerning the experimental procedure refer to Section 7.5.

Figure 7.1 – Picture of the employed photoreactor for the hetero-Diels–Alder reaction.

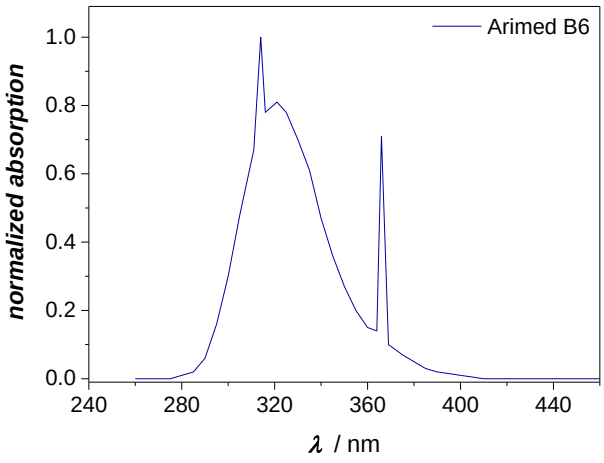

Figure 7.2 – Emission spectra of the Arimed B6 lamp used for the hetero-Diels–Alder reaction.

Swelling

*For organic solvents (performed in **Chapter 5**)*

Swelling experiment in toluene, THF or ethanol were performed by immersing a known amount of gel (5 – 10 mg) into a vial filled with solvent (~5 mL). After the gel was allowed to equilibrate overnight, the swollen gel was collected from the solution, and the excess of solvent on its surface was removed. Finally, the gel was weighted (m_s) and the degree of swelling was calculated according to Equation 2.22.

For water absorbency:

For the water absorbency tests, the procedure was adapted from previous literature.[9]
In detail, the dried polymer with a mass (m_0) of about 10 mg was placed on a metal sieve (120 μm mesh size and mass equal to m_{sieve}). The sieve containing the polymer was placed in an excess of the NaCl solution (10 $g \cdot L^{-1}$), where the solution is in contact to the polymer only through the sieve, as shown in Figure 7.3. After the gel was allowed to swell overnight (16 h), the sieve with the swollen hydrogel was collected, gently pressed onto a paper towel to remove excess solution and weighted ($m_{s+sieve}$). The swelling degree was determined by comparing the weight of the swollen (m_s) and the dry polymer (m_0) according to Equation 2.22.

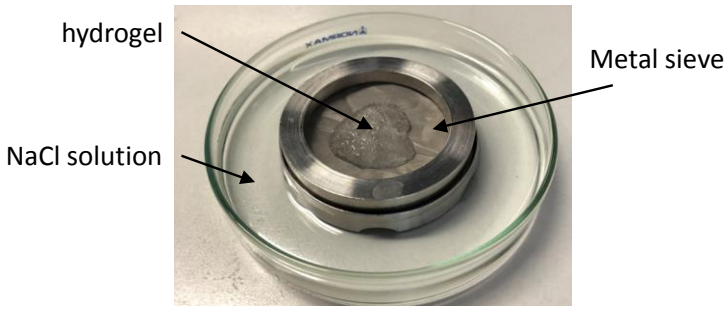

Figure 7.3 – Water absorbency test in order to determine the degree of swelling of poly(acrylic acid) and poly(sodium acrylate) networks

In each case (swelling in either aqueous or organic solvent), the measurements were repeated three times. Thus, the reported value refers to the mean value, and the standard deviation is indicated as error bars.

Rheometer

Sample preparation: For the rheological measurements, disk-shaped specimens were required, which were obtained *via* the following procedure. 1.4 mL of the reaction solution were poured in a 7 mL head-space vial. After degassing for 15 min, the vial was placed in a heating block at 70 °C overnight (16 h). The next day, the glass was broken for collecting the sample, which was then used for rheological measurements ("*as prepared*" state).

Figure 7.4 – Adopted set-up for the rheological measurements. A disk-shaped specimen was placed in between the two plates of the ARES-G2 rheometer.

The oscillatory shear measurements were carried out on the strain controlled rotational rheometer Ares G2 (TA Instruments, Eschborn, Germany). Plate-plate geometries made from aluminum with a diameter of either 13 or 25 mm were used. The temperature was controlled to 20 ± 0.1 °C by a Peltier element (Advanced Peltier System, TA Instruments).

For the analysis, the sample (disk) was placed in between two plates, where the upper one was stationary, while the lower one was able to rotate. As a general remark, by rotating the lower plate a sinusoidal shear strain (γ), having amplitude γ_0 and angular frequency ω, is applied to the sample, and the resulting stress (σ) is measured. In the linear viscoelastic (LVE) regime, from these parameters one can calculate the complex modulus (G^*), which indicates the rigidity of the hydrogel.[186]

$$G^* = \frac{\sigma}{\gamma} = G' + iG'' \qquad (7.1)$$

The complex modulus (G^*) is in turn composed by the storage modulus (G´), and the loss modulus (G´´), which indicate the elastic and the viscous contributions, respectively. The ratio between these two components represents the loss in the elastic behavior due to viscous contributions (loss factor, tan(δ)).[186] Accordingly, low values of tan(δ) are desirable.

$$G' = \frac{\sigma}{\gamma} cos\delta \tag{7.2}$$

$$G'' = \frac{\sigma}{\gamma} sin\delta \tag{7.3}$$

$$\tan(\delta) = \frac{G''}{G'} \tag{7.4}$$

On the first sample (**FRP-DC1**), an amplitude sweep was carried out by varying the strain from $\gamma_0 = 2 \cdot 10^{-5}$ to 10 with a constant frequency of $\omega = 1$ rad/s to find the linear viscoelastic (LVE) regime (Figure 7.5, left).

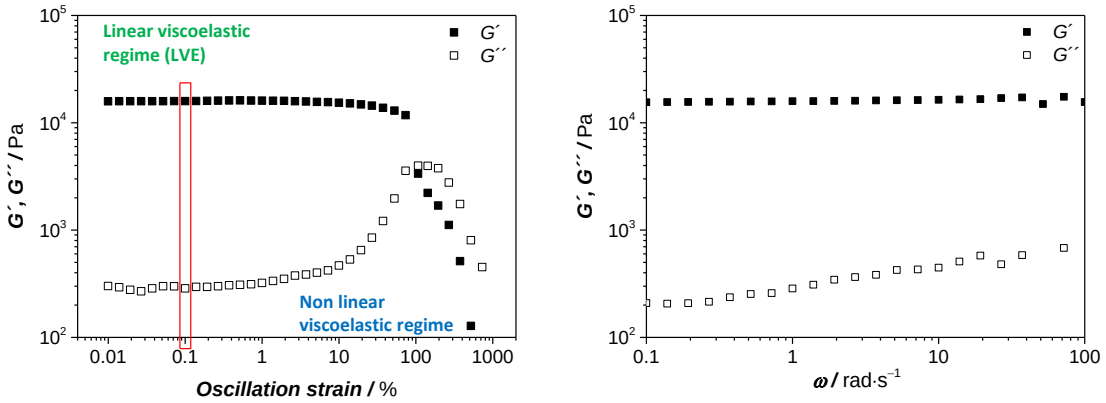

*Figure 7.5 – Left: Variation of G´ and G´´ during the oscillatory strain sweep on **FRP-DC1** at 1 rad/s. Right: Frequency sweep for **FRP-DC1** at 0.1% amplitude (this amplitude is highlighted with a red box in the graph on the left).*

In the next step, the amplitude (γ_0) was fixed at 0.1% (within LVE, Figure 7.5, red box) and a frequency sweep from 0.1 to 100 rad·s^{-1} was applied, as displayed in (Figure 7.5, right). This test was performed for each sample under the same described conditions.

The reproducibility of the method was tested upon multiple measurements on different samples of identical composition (same %RAFT and same *DC*). The results for three selected samples (**FRP-DC1**, **RAFT01-DC1** and **RAFT025-DC1**) are reported in Figure 7.6.

Minor deviations are expected when measuring different samples, mostly in the "*as prepared*" state since the extractables are not removed. Thus, the results reported in suggests that the method is reproducible over the whole analyzed range.

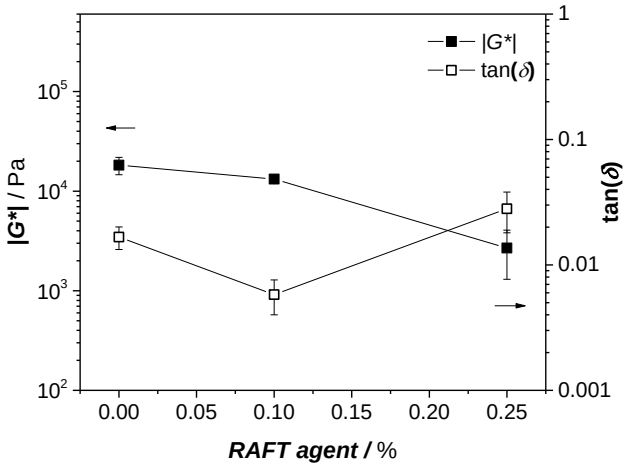

*Figure 7.6 – Variation on the mechanical properties for three selected poly(acrylic acid) hydrogels (**FRP-DC1**, **RAFT01-DC1** and **RAFT025-DC1**) prepared starting from different stock solutions, in order to verify the reproducibility of the results.*

Salt rejection experiments

Preliminary salt rejection experiments were performed by mixing a calculated amount of hydrogel in a solution of brine (10 g·L^{-1} NaCl). The total mass was set to 20 g, while Q_{rel} to 2 in order to have an equal distribution of the brine inside the gel and in the supernatant phase during the experiments. The amount of dry network (m_0) necessary to achieve these conditions was calculated according to Equation 7.6, and depends on the degree of swelling of the network itself. In detail,

$$Q_{\mathrm{rel}} = \frac{m_{\mathrm{brine}}}{Q_{\mathrm{eq}} m_0} \tag{7.5}$$

$$m_0 = \frac{m_{\mathrm{tot}}}{Q_{\mathrm{rel}} * \left(Q_{\mathrm{eq}} + 1\right)} \tag{7.6}$$

where m_0 is the total mass of dry polymer, m_{brine} the mass of the salt solution and m_{tot} is the overall mass (polymer plus brine). Moreover, Q_{eq} is defined by separate swelling experiment according to equation 2.22. The swelling experiments were performed using a solution having a salt content equal to the one employed for the salt rejection experiments ($c_{s,0}$). At any time, the salt concentration was determined by measuring the conductivity of the solution according to the formula:

$$c(NaCl) = A + B\sigma + C\sigma^2 + D\sigma^3 \tag{7.7}$$

where A = 0.0343159 g·L^{-1} , B = 0.579411 g·cm·L^{-1}·mS^{-1}, C = 3.23002 g·cm^2·L^{-1}·mS^{-2} and D = −5.87361 g·cm^3·L·mS^{-3}, σ is the conductivity as measured (SevenMulti, Mettler Toledo, Gießen, Germany).

The salt rejection ability, expressed as percentage, is determined by the difference in salt content of the supernatant phase before and after swelling, according to Equation 3.1

Donnan theory

The experimental results are compared to the theoretical values as calculated from the Donnan theory. The salt concentration of the mobile anions inside the gel (c_{in-}) was calculated according to: [182]

$$c_{\mathrm{in}-} = \sqrt{\left(\frac{DNc_{\mathrm{p}}}{2}\right)^2 + c_{\mathrm{out}}^2} - \frac{DNc_{\mathrm{p}}}{2} \tag{7.8}$$

where c_p is the molar concentration of the polymer (c_p = (ρ_{H2O}/94)(1/(1+Q_{eq}))), c_0 is the concentration of the bath 0.17 mol·L^{-1} (10 g·L^{-1}NaCl), DN is the degree of neutralization, and c_{out} is the concentration of salt in the supernatant phase, which is calculated by the following equation:

$$c_{\mathrm{out}} = \frac{Q_{\mathrm{rel}} * c_0 - c_{\mathrm{in}-}}{Q_{\mathrm{rel}} - 1} \tag{7.9}$$

Thus, the final theoretical salt rejection (SR_{Donnan}) resulted equal to:

$$SR_{\mathrm{Donnan}} = \left(\frac{c_{\mathrm{out}} - c_0}{c_0}\right) * 100 \tag{7.10}$$

7.3 Synthetic Protocols for Chapter 3

Synthesis of linear poly(methyl acrylate) polymers

The RAFT agent (DoPAT, 1.00 eq.), azobisisobutyronitrile (AIBN, 0.15 eq.) and methyl acrylate (MA, for equivalent refer to Table 7.2) were dissolved in 1,4-dioxane (20% w/w). The oxygen was removed by purging with argon for 15 min and then placed in a preheated oil bath at 70 °C. After 3 h, the polymerization was stopped *via* cooling with liquid nitrogen and opening the vial to air. The monomer and the solvent were evaporated under vacuum and subsequently the polymer was analyzed *via* SEC.

*Table 7.2 – Summary of the linear poly(methacrylate)s synthesized in **Chapter 3**, Section 3.1.*

RAFT agent(eq.)	monomer (eq.)
1	100
1	200
1	400
1	600
1	1000

Synthesis of poly(methyl acrylate) networks

AIBN as initiator (0.15eq.), DoPAT as RAFT agent (when needed, 1eq.) and 1,3 butanediol diacrylate (DAc) as crosslinking agent (1 mol% compared to the monomer) were dissolved in the desired volume of monomer (MA). The volume of monomer was determined according to the targeted molar ratio of RAFT agent:MA (1:600 or 1:1000). Afterwards, 1,4-dioxane (20:80 w/w ratio monomer to solvent) was added to the mixture and the solution was divided in different vials in order to stop the reaction at several intervals of time. Each vial was deoxygenated for 15 min by purging with argon and then heated up to 70 °C. The polymerization kinetics were investigated by cooling one vial at each desired reaction time in liquid nitrogen. The conversion was determined gravimetrically according to the following equation:

$$conversion\ (\%) = \frac{m_{\text{final}}}{m_{\text{initial}} * 0.2} \tag{7.11}$$

Where m_{initial} and m_{final} are the mass of the crude mixture before and after it was dried in a vacuum oven. Moreover, m_{initial} is multiplied by 0.2 in order to exclude the weight of the solvent (concentration during the synthesis).

Synthesis of linear poly(acrylic acid) polymers

The polymers were synthesized according to the procedure reported for the synthesis of linear poly(methyl acrylate) polymers.

In case of poly(acrylic acid), acrylic acid (AA) was used as monomer and TRITT as RAFT agent. The reaction was performed using distilled water as solvent (20% w/w) and thus a water soluble thermal initiator such as 4,4'-azobis(4-cyanovaleric acid) (V-501) was employed.

The molar ratio RAFT agent:monomer tested are identical to those reported in Table 7.2.

Synthesis of poly(acrylic acid) networks

Here, acrylic acid (AA) was used as monomer, *N,N´*–metylenbisacrylamide (MBA) as crosslinker, and TRITT as RAFT agent. In analogy to the synthesis of linear chains, the reaction was performed in distilled water (20%w/w) , thus V-501 was employed as initiator. The molar ratio V-501:TRITT was set to 0.15:1, while the molar ratio TRITT:AA and MBA:AA is specified in Table 7.3.

As a comparison, an analogous network was synthesized, in each case, also *via* free radical polymerization. In this case, the procedure is maintained identical (same *DC*) but no RAFT agent was employed.

Each reaction was carried out according to the procedure reported above for methyl acrylate based networks, with the exception that no kinetic investigation was performed. The reaction time was set to 16 h, subsequently the extractables were removed by washing the network extensively with an excess of solvent (water for PAA networks). Before changing the water, the network was allowed to swell for 24 h. The washing procedure was repeated at least two times. Eventually, the water inside the hydrogel was removed *via* lyophilization until the product was dried.

Table 7.3 – Summary of the poly(acrylic acid) networks synthesized via RAFT polymerization and via free radical polymerization (FRP). In detail, the reaction code, the ratio RAFT agent:monomer and the degree of crosslinking (expressed as molar ratio between the crosslinker and the monomer) are provided.

Sample	RAFT:AA	MBA:AA
FRP-DC1	no raft agent	0.01
RAFT005-DC1	1:2000	0.01
RAFT01-DC1	1:1000	0.01
RAFT017-DC1	1:600	0.01
RAFT025-DC1	1:400	0.01
RAFT05-DC1	1:200	0.01
RAFT1-DC1	1:100	0.01
FRP-DC06	no raft agent	0.006
RAFT01-DC06	1:1000	0.006
FRP-DC1.5	no raft agent	0.015
RAFT01-DC1.5	1:1000	0.015
RAFT025-DC1.5	1:400	0.015
FRP-DC3	no raft agent	0.03
RAFT01-DC3	1:1000	0.03
RAFT025-DC3	1:400	0.03
FRP-DC5	no raft agent	0.05
RAFT01-DC5	1:1000	0.05
RAFT025-DC5	1:400	0.05

From hydrogels to polyelectrolytes

Each of the PAA network synthesized was neutralized in order to achieve polyelectrolyte gels (PSA) suitable for the selected application, e.g. salt rejection.

The neutralization was performed by mixing a known amount of dry polymer with a calculated volume of 0.1 M $NaHCO_3$ (in distilled water) which allows for a ratio AA:Na^+ = 1:1.1, unless differently specified.

$$V_{\mathrm{NaHCO3}} = \frac{m_{\mathrm{dry\ network}}}{M_{\mathrm{AA}}} * \frac{1.1}{[NaHCO_3]} \qquad (7.12)$$

Where V is the volume of $NaHCO_3$ having a molarity [$NaHCO_3$] necessary for a given mass of dry network ($m_{\mathrm{dry\ network}}$), assuming a 1:1.1 ratio AA:Na. M_{AA} is the molecular weight of acrylic acid. The network was left in basic solution overnight (16 h). Afterwards, the polymer wash washed with distilled water until the pH of the solution was neutral. Eventually, the network was dried *via* lyophilization.

7.4 Synthetic Protocols for Chapter 4

Synthesis of trimethylolpropane tris(2,3,4,5,6-pentafluorobenzylether) (3PFB)

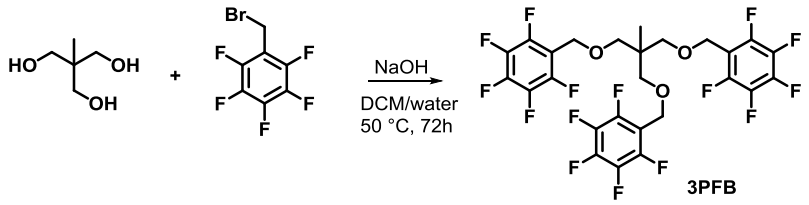

*Scheme 7.1 – Reaction scheme for the synthesis of trimethylolpropane tris(2,3,4,5,6-pentafluorobenzylether) (**3PFB**) via phase transfer catalysis (PTC).*

To a stirred aqueous solution of sodium hydroxide (9.0 eq., C_{NaOH} = 50 wt%), 1,1,1-tris(hydroxymethyl)ethane (10.0 mmol, 1.00 g, 1.0 eq) and tetrabutylammonium bromide (TBABr, 0.5 mmol, 0.32 g, 0.3 eq., phase transfer catalyst) were added. After stirring at ambient temperature for 2 h, a solution of 2,3,4,5,6-pentafluorobenzyl bromide (80.0 mmol, 12 mL, 8.0 eq) in dichloromethane (DCM, 10 mmol mL^{-1}) was added. Subsequently, the temperature was increased to 50 °C, and the reaction was allowed to proceed for 3 days. Eventually, the crude mixture was cooled to ambient temperature and washed with water (1x 50 mL), NaOH 0.1 M (2x 50 mL) and brine (1x 50 mL). The aqueous phases were collected and extracted with DCM (1x 100mL). The combined organic layers were dried over Mg_2SO_4. The solvent was removed under reduced pressure and the crude product was subjected to purification on a silica gel column (4:1, CH:DCM) to afford a white crystalline compound (yield 35%).

^{1}H NMR ($CDCl_3$, 400 MHz): δ = 0.88 (s, 3H, CH_3), δ = 3.3 (s, 6H, CH_2), δ = 4.54 (s, 6H, CH_2).

^{13}C NMR ($CDCl_3$, 101 MHz): δ = 17.2 (1C), δ = 40.7 (1C), δ = 60.2 (3C), δ = 72.8 (3C), δ = 111.4 (3C), δ = 136-147 (12C).

^{19}F NMR ($CDCl_3$, 377 MHz): δ = -143.2 (6F, *ortho*), -153.9 (3F, *para*), -162 (6F, *meta*).

(+)ESI-MS [M+Na]$^+$: m/z_{exp} = 683.0788, m/z_{theo}: 683.0789, Δm = 0.0001

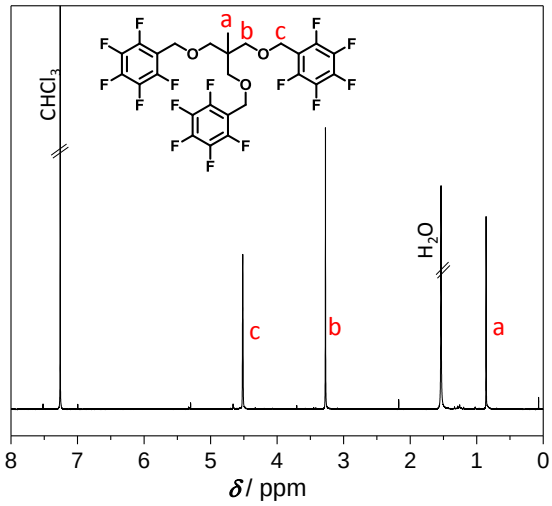

*Figure 7.7 – ^{1}H NMR spectrum ($CDCl_3$, 400MHz) of **3PFB.***

Synthesis of tris(2,3,4,5,6-pentafluorophenyl) benzene-1,3,5-tricarboxylate (3aromCOOPFP)

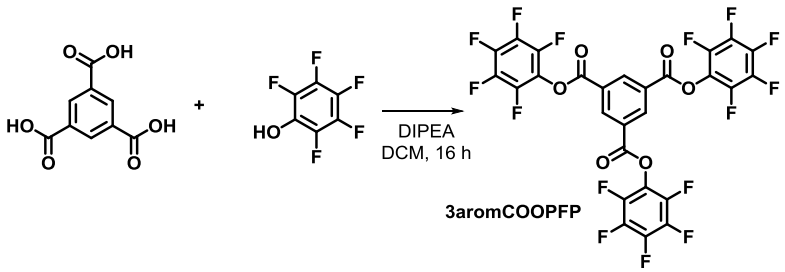

*Scheme 7.2 – Reaction scheme for the synthesis of tris(2,3,4,5,6-pentafluorophenyl) benzene-1,3,5-tricarboxylate (**3aromCOOPFP**) via esterification.*

1,3,5-Benzenetricarboxylic acid, (0.36 mmol, 0.075 g, 1.0 eq.), pentafluorophenol (1.18 mmol, 0.217 g, 3.3 eq.) and DIPEA (0.36 mmol, 0.065 mL, 1.0 eq.) were dissolved in DCM (3.6 mL). Subsequently, the solution was cooled to 0 °C in an ice bath prior to addition of EDC(HCl). Thereafter, the solution was allowed to warm up to ambient temperature and stirred overnight. Next, the crude mixture was washed with water (1x 10 mL). The organic layer was dried over MgSO4 and the solvent was removed in vacuo. The crude product was purified via column chromatography in CH:DCM = 4:4, to afford the product as a white solid compound.

Yield = 55%.

^{1}H NMR ($CDCl_3$, 400 MHz): δ = 9.28 (s, 3H)

^{19}F NMR ($CDCl_3$, 377 MHz): δ = -152.1 (6F, *ortho*), -156.2 (3F, *para*), -161.3 (6F, *meta*)

^{13}C NMR ($CDCl_3$, 101 MHz): δ = 160.3 (3C, COO), δ = 150 - 135(15C, CF), δ = 137.7 (3C, $\underline{C}_{arom}$-COO), δ = 129.5 (3C, $\underline{C}_{arom}$-H).

(−)ESI-MS [M+Cl]$^{+}$: m/z_{exp} = 742.9384, m/z_{theo}: 742.9373, Δm = 0.0011

Synthesis of tris(2,3,4,5,6-pentafluorobenzyl) benzene-1,3,5-tricarboxylate (3aromCOOPFB)

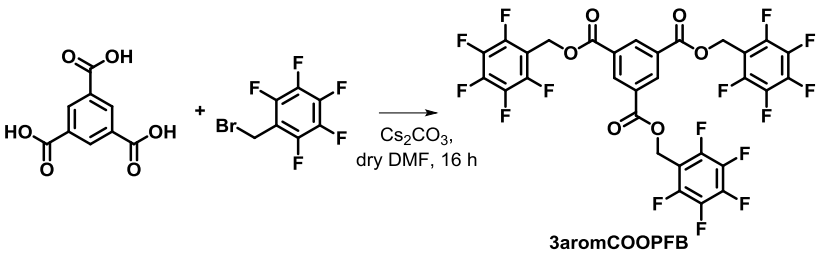

*Scheme 7.3 – Reaction scheme for the synthesis of tris(2,3,4,5,6-pentafluorobenzyl) benzene-1,3,5-tricarboxylate (**3aromCOOPFP**).*

In a pre-dried Schlenk flask, Cs_2CO_3 (13.5 mmol, 4.387 g, 4.5 eq.) was dispersed in dry DMF (20 mL, 0.45 M) under argon atmosphere before addition of the trimesic acid (3.0 mmol, 0.630 g, 1 eq.). After stirring for 30 min, 2,3,4,5,6-pentafluorobenzyl bromide (PFB-Br 8.55 mmol, 2.22 mL, 2.9 eq.) was added to the reaction mixture, which was then stirred overnight (16 h) at ambient temperature. The following day, Cs_2CO_3 was filtered off and the filtrate was diluted with water (1x 30 mL) and extracted with DCM (2x 30 mL). The collected organic phase was washed with brine (1x 40 mL), dried over $MgSO_4$, and concentrated under reduced pressure. The crude product was purified *via* column chromatography in CH:EA = 7:3, to afford the product as a white solid. Yield = 85%.

^{1}H NMR ($CDCl_3$, 400 MHz): δ = 8.80 (s, 3H, aromatic H), δ = 5.49 (s, 6H, CH_2).

^{13}C NMR ($CDCl_3$, 101 MHz): δ = 164.0 (3C, COO), δ = 150 - 135(12C, CF), δ = 135.2 (3C, $\underline{C}_{arom}$-COO), δ = 135.2 (3C, $\underline{C}_{arom}$-H), δ = 109.0 (3C, C_{arom}-CH_2), δ = 54.6 (3C, CH_2).

^{19}F NMR ($CDCl_3$, 377 MHz): δ = −141.6 (6F, *ortho*), −151.7 (3F, *para*), −161.1 (6F, *meta*).

(+)ESI-MS [M+Na]$^+$: m/z_{exp} = 773.0083, m/z_{theo}: 773.0052, Δm = 0.0031.

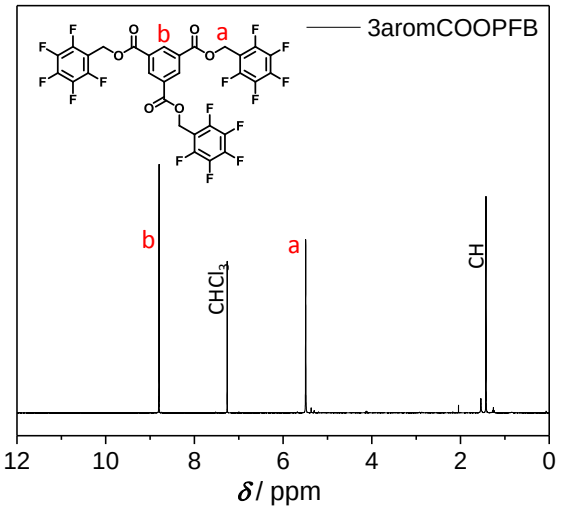

*Figure 7.8 – ^{1}H NMR spectrum ($CDCl_3$, 400MHz) of **3aromCOOPFB***

Synthesis of 2,3,4,5,6-pentafluorobenzyl benzoate (1COOPFB)

Here, an identical procedure to the one described for **3aromCOOPFB** was adopted for the synthesis of **1COOPFB**. For more details, refer to Table 7.4. The product was obtained as white solid in quantitative yield.

^{1}H NMR ($CDCl_3$, 400 MHz): δ = 5.45 (s, 2H, CH_2), δ = 7.44 (dt, 2H, CH), δ = 7.58 (tt, 1H, CH), δ = 8.00 (td, 1H, CH).

^{13}C NMR ($CDCl_3$, 101 MHz): δ = 55.83 (1C, aliphatic CH_2), δ = 109.59 (1C, C aromatic ring), δ = 128-134 (6C, C aromatic ring), δ = 137-147 (6C, aromatic fluorinated ring), δ = 165.86 (1C, ester).

^{19}F NMR ($CDCl_3$, 377 MHz): δ = −142.2 (2F, *ortho*), δ = −153.4 (1F, *para*), δ = −162.4 (2F, *meta*).

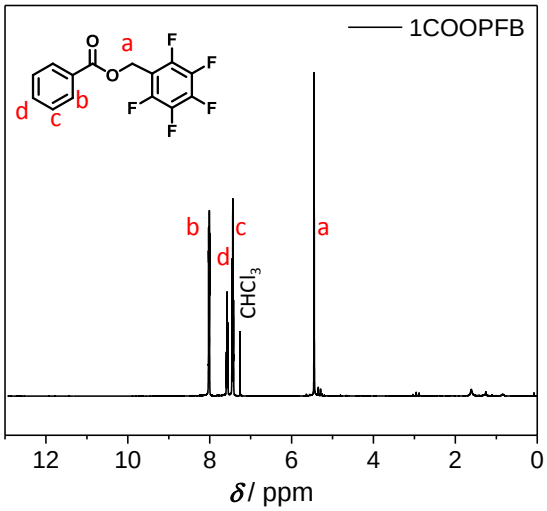

*Figure 7.9 – ^{1}H NMR spectrum ($CDCl_3$, 400MHz) of **1COOPFB.***

Synthesis of tris(2,3,4,5,6-pentafluorobenzyl)(1,2,3-propanetricarboxylate) (3COOPFB)

Here, an identical procedure to the one described for **3aromCOOPFB** was adopted for the synthesis of **3COOPFB**. For more details, refer to Table 7.4. The product was obtained as white solid. Yield = 90%.

^{1}H NMR ($CDCl_3$, 400 MHz): δ = 2.64 (dd, 2H, CH_2), δ = 2.78 (dd, 2H, CH_2), δ = 3.27 (p, 1H, CH), δ = 5.20 (m, 6H, CH_2).

^{13}C NMR ($CDCl_3$, 101 MHz): δ = 171.9 (1C, COO), δ = 170.4 (2C, COO), δ = 145.81 (CF_{meta}), δ = 142.9 (3C, CF_{para}), δ = 137.7 (6C, CF_{ortho}), δ = 109.0 (6C, C_{arom}), δ = 54.3 (2C, CH_2-O), δ = 53.8 (1C, CH_2-O), δ = 37.1 (1C, CH), δ = 34.7 (2C, CH_2).

^{19}F NMR ($CDCl_3$, 377 MHz): δ = −142.0 (6F, *ortho*), δ = −152.1 (3F, *para*), δ = −161.5 (6F, *meta*).

(+)ESI-MS, $[M+Na]^+$: m/z_{exp} = 739.0192, m/z_{theo}: 739.0208, Δm = 0.0016.

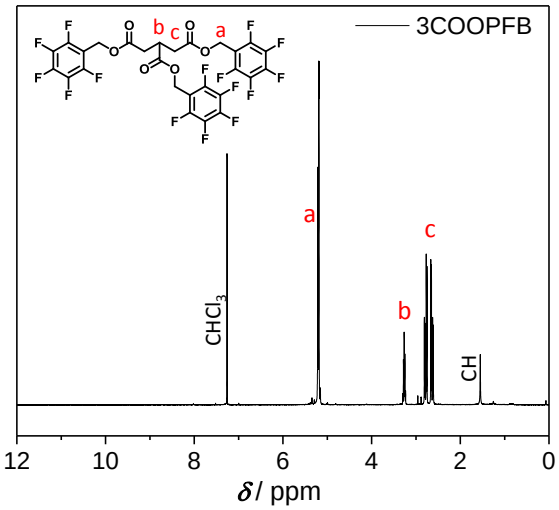

*Figure 7.10 – ^{1}H NMR spectrum ($CDCl_3$, 400MHz) of **3COOPFB.***

Synthesis of tetra(2,3,4,5,6-pentafluorobenzyl)(1,2,3,4-butanetetracarboxylate) (4COOPFB)

Here, an identical procedure to the one described for **3aromCOOPFB** was adopted for the synthesis of **4COOPFB**. For more details, refer to Table 7.4. The product was obtained as white solid. Yield = 90%.

^{1}H NMR ($CDCl_3$, 400 MHz): δ = 2.43 (dd, 2H, CH_2), δ = 2.78 (dd, 2H, CH_2), δ = 3.31 (m, 2H, CH) δ = 5.17 (s, 4H, CH_2), δ = 5.19 (s, 4H, CH_2).

^{13}C NMR ($CDCl_3$, 101 MHz): δ = 170.7 (2C, COO), δ = 170.2 (2C, COO), δ = 150 – 135 (CF), δ = 54.1 (2C, CH_2-O), δ = 53.8 (2C, CH_2-O), δ = 41.7 (2C, CH), δ = 35.8 (2C, CH_2).

^{19}F NMR ($CDCl_3$, 377 MHz): δ = −142.0 (8F, *ortho*), δ = −151.9 (2F, *para*), δ = −152.1 (2F, *para*) δ = −161.5 (8F, *meta*).

(+)ESI-MS, $[M+Na]^+$: m/z_{exp} = 977.0294, m/z_{theo}: 977.0262, Δm = 0.0032.

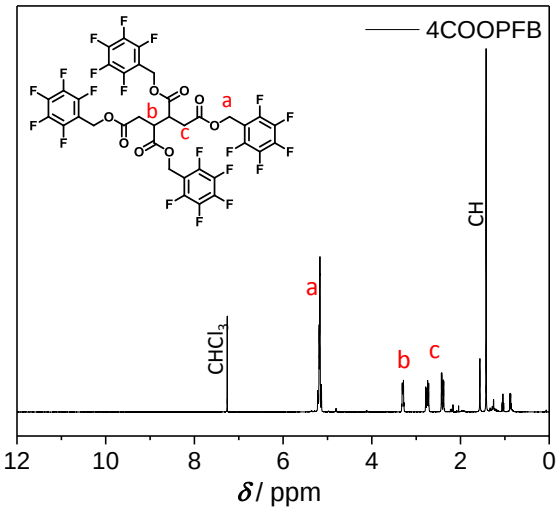

*Figure 7.11– ^{1}H NMR spectrum ($CDCl_3$, 400MHz) of **4COOPFB**.*

*Table 7.4 – List of the reagent for the synthesis of **1COOPFB**, **3COOPFB** and **4COOPFB**.*

Compound	Cs_2CO_3	Acid	PFB-Br
1COOPFB	1.5eq.	Benzoic acid, 1eq.	0.95eq.
3COOPFB	4.5eq.	Tricarballylic acid,1eq.	2.85eq.
4COOPFB	5.0eq.	1,2,3,4-butanetetracarboxylic acid, 1eq.	3.80eq.

Synthesis of benzyl 2-(((dodecylthio) carbonothioyl)thio) propanoate (DoPAT-OBz)

DoPAT-OBz was synthesized according to literature[58] to protect the carboxylic group of the RAFT agent DoPAT.

General procedure for the synthesis of PSa and PSb via RAFT polymerization

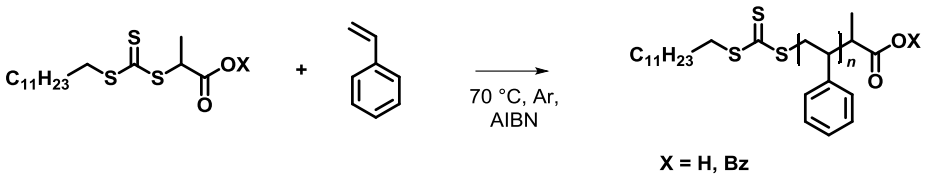

*Scheme 7.4 – Reaction scheme for the polymerization of polystyrene (PS) affording **PSa** and **PSb.***

In a typical procedure, RAFT agent (DoPAT or **DoPAT-OBz**, 1 eq.) and AIBN (0.1 eq.) were dissolved in styrene (150 eq.). The mixture was deoxygenated by purging with argon for 15 min and then heated at 70 °C for 6 h to afford **PSa** or **PSb**, respectively (M_n = 4000 g mol^{-1}, $Đ$ = 1.1; M_n = 3000 g mol^{-1}, $Đ$ = 1.1, respectively). In each case, the polymerization was stopped by exposing the mixture to oxygen and cooling in an ice bath. The product was isolated by precipitation in cold methanol, and collected by filtration. Characterization of the products was performed by NMR spectroscopy, SEC and ESI-MS analysis (see Appendix, Figure 8.3 to Figure 8.5 for **PSa**, and Figure 8.10 to Figure 8.12 for **PSb**). According to SEC, the number average molar mass of **PSa** and **PSb** was 4000 g mol^{-1} ($Đ$ = 1.1) and 3000 g mol^{-1} ($Đ$ = 1.1).

General procedure for the synthesis of PSa-SH and PSb-SH via aminolysis

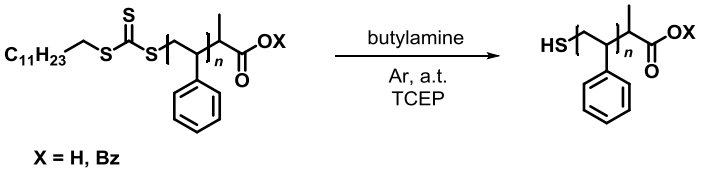

*Scheme 7.5 – Reaction scheme for the aminolysis of **PSa** and **PSb** to afford **PSa-SH** and **PSb-SH**, respectively.*

The procedure for aminolysis is adapted from the literature.[63] Polymers **PSa** or **PSb** (1 eq.) were dissolved in THF (100 mg mL^{-1}), and TCEP (3 eq.) was added to prevent disulfide formation. Subsequently, *n*-butylamine was added to the reaction mixture (60 eq.). The resulting mixture was stirred for 4 h at ambient temperature. The polymeric thiols were isolated by precipitation in cold methanol and filtration. Characterization of the product was performed by NMR spectroscopy, SEC and ESI-MS analysis in order to confirm the removal of the trithiocarbonate moiety (see Appendix, Figure 8.3 to Figure 8.5 for **PSa**, and Figure 8.10 to Figure 8.12 for **PSb**). Each analysis proved that the aminolysis successfully led to thiol polymers. According to SEC, the number average molar mass of **PSa-SH** and **PSb-SH** was 3800 g mol^{-1} ($Đ$ = 1.1) and 2800 g mol^{-1} ($Đ$ = 1.1), respectively.

General procedure for disulfide bond formation

In a vial, the thiol (1 eq.) was dissolved in THF or DMF ($[thiol]_0$ = 0.075 $mol \cdot L^{-1}$) at ambient temperature Subsequently, the base (DBU, 1 eq.) was added in order to start the reaction. At time 0 (before addition of the base) and at specific intervals of time, samples were withdrawn in order to follow the reaction *via* SEC analysis. Thus, a specific volume of reaction mixture corresponding to 4 mg was passed through a short column of basic alumina to remove the base. Thereafter, the sample is diluted with THF to a concentration of 2 $mg \cdot mL^{-1}$ and filtered prior to SEC analysis.

General procedure for PFTR

Both the thiol (1 eq.) and the fluorinated compound (PFB group = 1 eq.) were dissolved in either THF or DMF ($[thiol]_0$ = 0.075 $mol \cdot L^{-1}$, if not differently specified) at ambient temperature. Subsequently, DBU (1 eq.) was added to the reaction mixture in order to start the PFTR. Before addition of the base and at specific intervals of time, samples were withdrawn in order to follow the reaction *via* SEC analysis and ^{19}F NMR spectroscopy. For SEC analysis, the sample was prepared as described for disulfide bond formation. For ^{19}F NMR analysis, a volume of crude reaction mixture allowing for a final concentration of PFB groups $\geq$ 0.009 $mol \cdot L^{-1}$ in a NMR tube (V_{tot} = 0.5 mL) was withdrawn and the base neutralized with an excess of benzoic acid (4 eq. with respect to DBU) in order to stop the reaction.

For the self-propagated PFTR:

The base (DBU, TBAOH, TBABr or TBAF) was used in understoichiometric amount. The type and the amount of base, as well as the solvent used, is specified in the caption of the figure showing the results of the reaction itself.

In Figure 4.24 and Figure 4.28 (for phenSH in DMF and DMSO), the reaction was performed in a NMR tube using deuterated solvent (THF-d_8, DMF-d_7, DMSO-d_6, repectively) in order to allow for online ^{19}F NMR measurements.

General procedure for investigating the suppression of disulfide bond formation

The polymeric thiol (**PSa-SH**, 1 eq.) was dissolved in THF or DMF ($[thiol]_0 = 0.037$ mol·L^{-1}) at ambient temperature, with or without the presence of reducing agent (TCEP, 6 eq.). Subsequently, the base (DBU, 15 eq.) was added in order to start the reaction. Samples for SEC analysis were withdrawn at specific intervals of time following the procedure described earlier for disulfide bond formation.

The same procedure was repeated in a crimped vial in order to remove oxygen from the reaction mixture.

7.5 Synthetic Protocols for Chapter 5

General procedure for the synthesis of small molecules network

The **3PFB** linker (1 eq.) and the bifunctional thiol (1.5 eq.) were dissolved in a minimum amount of THF ($[SH]_0$ = 1.8 M). Subsequently, DBU (3 eq.) was added to start the reaction. After 30 min, the freshly formed network was washed with THF for at least three times to remove the extractables. Eventually, the network was dried in a vacuum oven overnight at 25 °C.

Synthesis of diethylene glycol di(2-(((dodecylthio) carbonothioyl)thio) propanoate) (biDoPAT)

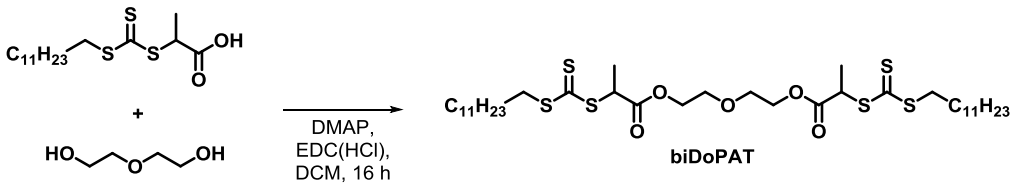

*Scheme 7.6 – Reaction scheme for the synthesis of diethylene glycol di(2-(((dodecylthio) carbonothioyl)thio) propanoate) (**biDoPAT**) via esterification.*

DoPAT (14.26 mmol, 5.0 g, 2.30 eq.), diethylene glycol (6.20 mmol, 0.589 mL, 1 eq.) and DMAP (2.85 mmol, 0.348 g, 0.46 eq.) were dissolved in DCM (30 mL, 0.5 M). Subsequently, the solution was cooled to 0 °C in an ice bath and EDC(HCl) (15.50 mmol, 2.972 g, 2.50 eq.) was added to the reaction mixture. The solution was allowed to warm up to ambient temperature and was stirred overnight (16 h). Afterwards, the crude mixture was washed with water (1x 60mL), $NaHCO_3$ (1x 60mL) and brine (1x 60mL). The combined organic layer was dried over $MgSO_4$ and the solvent was evaporated under reduced pressure. The crude product was purified *via* column chromatography (10:1 CH:EA) to afford the desired product as a yellow oil. Yield = 70%.

^{1}H NMR ($CDCl_3$, 400 MHz): δ = 0.88 (t, 6H, CH_3), δ = 1.25 (m, 38H, CH_2), δ = 1.40 (m, 4H, CH_2), δ = 1.62 (d, 6H, CH_3), δ = 1.69 (p, 4H, CH_2), δ = 3.33 (m, 4H, CH_2), δ = 3.70 (t, 4H, CH_2), δ = 4.29 (t, 4H, CH_2), δ = 4.85 (q, 2H, CH).

^{13}C NMR ($CDCl_3$, 101 MHz): δ = 171.1 (2C, COO), δ = 64-68 (4C, CO), δ = 53.4 (2C, CS), δ = 47.9 (2C, CS), δ = 37.5-14.0 (24C, CH_2 aliphatic chain and CH_3).

(+)ESI-MS $[M+Na]^+$: m/z_{exp} = 793.3135 m/z_{theo}: 793.3132, Δm = 0.0003.

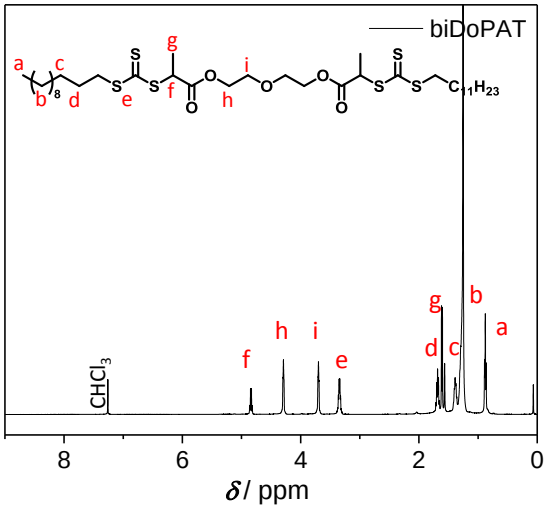

*Figure 7.12 – ^{1}H NMR spectrum ($CDCl_3$, 400MHz) of **biDoPAT**.*

General procedure for the synthesis of PS(x) and biSH-PS(x)

The polymerization is performed according to the procedure reported in section 7.4 for **PSa**. The three different polystyrene, with different molar mass, are obtained by varying the molar ratio of RAFT:styrene in the reaction mixture. In detail, a molar ratio of **biDoPAT**:styrene = 1:150, 1:200 and 1:250 was used to afford **PS(36)**, **PS(64)** and **PS(82)**, respectively.

The corresponding biSH-PS(x) were obtained after aminolysis, following the same procedure reported for **PSa-SH** (Section 7.4).

The characterization of the products was performed by NMR spectroscopy and SEC (see Appendix, Figure 8.23 (**PS(36)**), Figure 8.24 (**PS(64)**), and Figure 8.25 (**PS(82)**), for NMR spectroscopy, while the SEC traces are reported in **Chapter 5**, Figure 5.18). The ESI-MS was recorded for **PS(36)** only (Figure 5.9) due to the high molar mass of the other polymers combined with the low ionization of apolar polymers such as styrene.

Table 7.5 – List of the molecular weight (M_n) and the dispersity index (Đ) of the bifunctional polystyrene precursor used in Section 5.2.1 before and after aminolysis.

PS(x)	M_n (g·mol^{-1})	Đ	biSH-PS(x)	M_n (g·mol^{-1})	Đ
36	4500	1.1	36	3800	1.1
61	7300	1.1	64	6650	1.1
82	9150	1.1	82	8500	1.1

General procedure for the synthesis of PS network

Similar to what was reported for small molecules, the fluorinated linker (PFB group = 1 eq.) and the bifunctional polymeric thiol (**biSH-PS(x)** SH group = 1 eq.) were dissolved in DMF (300 $g \cdot mL^{-1}$). Subsequently, DBU (1 eq.) was added to start the reaction. The reaction mixture was allowed to react for 1 h. Afterwards, the gel was washed with an excess of THF for at least three times to remove the soluble fractions and the leftovers base. The extractables were passed through a short column of alumina basic in order to remove the base. Eventually, the sol and the gel were dried in a vacuum oven overnight at 25 °C. The following day, both the soluble and the insoluble phase were analyzed *via* ^{19}F NMR spectroscopy in order to determine the conversion.

Synthesis of 3,6-Dioxa−1,8-bis(2,3,4,5,6-pentafluorobenzylthiocarbonothioylthio)-octane (biPFB)

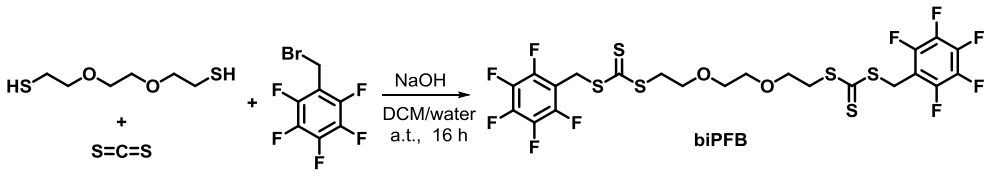

*Scheme 7.7 – Reaction scheme for the synthesis of 3,6-dioxa−1,8-bis(2,3,4,5,6-pentafluorobenzylthiocarbonothioylthio)-octane (**biPFB**) via phase transfer catalysis.*

In a round bottom flask, Aliquat® 336 (0.0035 mmol, 0.003 g, 0,024 eq.), 2,2′-(ethylenedioxy)diethanethiol (4.71 mmol, 0.77 mL, 0.33 eq.) and CS_2 (14,3 mmol, 1,088 g, 1 eq.) were added in this order. Subsequently, 7 mL of a 2M NaOH (aqueous solution) were added to the previous flask. After stirring for 2 h at ambient temperature, a 2 M solution of 2,3,4,5,6-pentafluorobenzylbromide (15 mmol, 2.26 mL, 1.1 eq.) in DCM (7 mL) was added to the solution. The reaction mixture was stirred overnight (16 h). Thereafter, the crude mixture was washed with water (3x 20 mL) and brine (1x 20mL). The organic layers were collected, dried over $MgSO_4$ and evaporated to dryness. The purification of the product was performed *via* column chromatography (7:3 DCM:CH) to afford the product as a yellow oil compound. Yield = 65%.

^{1}H NMR ($CDCl_3$, 400 MHz): δ = 3.63 (8H, CH_2), δ = 3.75 (4H, CH_2), δ = 4.68 (4H, CH_2).

^{13}C NMR ($CDCl_3$, 101 MHz): δ = 221.4 (2C, CS), δ = 150-130 (10C, CF), δ = 68-71 (4C, CO), δ = 36.8 (2C, CH_2**C**S), δ = 28.0 (2C, $\underline{C}H_2$-C_{arom}).

^{19}F NMR ($CDCl_3$, 377 MHz): δ = −140.1 (4F, *ortho*), δ = −153.6 (2F, *para*), δ = −161.3 (4F, *meta*).

(+)ESI-MS [M+Na]$^+$: m/z_{exp} = 716.9202, m/z_{theo}: 716.9213, Δm = 0.0011.

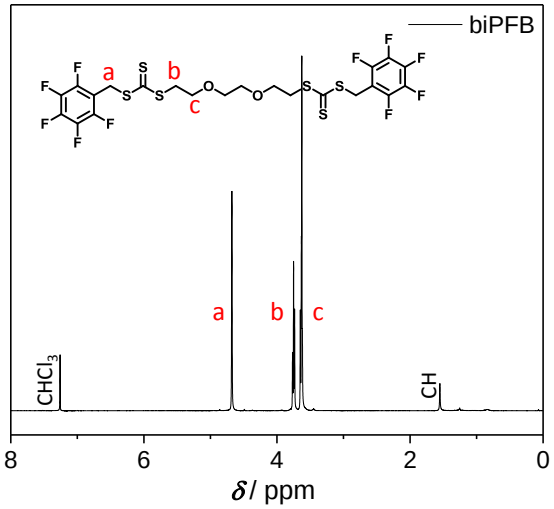

Figure 7.13 – ^{1}H NMR spectrum ($CDCl_3$, 400MHz) of ***biPFB.***

Synthesis of 1,4-phenylenebis(methylene) bis(4-cyano-4-(phenylcarbonothioylthio)pentanoate) (biCTA)

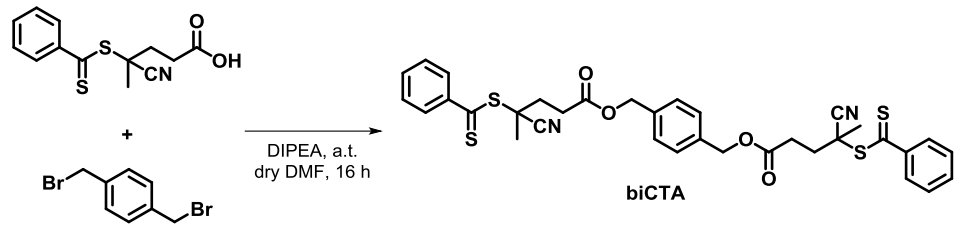

*Scheme 7.8 – Reaction scheme for the synthesis of 1,4-phenylenebis(methylene) bis(4-cyano-4-(phenylcarbonothioylthio)pentanoate) (**biCTA**) via esterification.*

In a pre-dried Schlenk flask, 4 cyano-4-(phenylcarbonothioylthio)pentanoic acid (4.0 mmol, 1.117 g, 1.0 eq.) was dissolved in dry DMF (8.00 mL, 0.5 M) under argon atmosphere. Subsequently, DIPEA (4.4 mmol, 0.766 mL, 1.1 eq.) was added. After stirring for 30 min, *α,α′*-dibromo-*p*-xylene (1.8 mmol, 0.475 g, 0.45 eq.) was added dropwise to the reaction mixture, which was allowed to stir overnight (16 h) at ambient temperature. Afterwards, the solvent was removed under reduced pressure and subsequently the crude product was dissolved in DCM and washed with water (2x 20 mL) and brine (1x 20 mL). The collected organic phases were dried over $MgSO_4$ and concentrated under reduced pressure. The crude product was purified *via* column chromatography (9:1-7:3 CH:EA) to afford the product as a pink viscous oil (yield 50%).

^{1}H NMR ($CDCl_3$, 400 MHz): δ = 1.93 (6H, CH_3), δ = 2.3-2.8 (8H, CH_2), δ = 5.15 (4H, CH_2), δ = 7.30-8.00 (14H, aromatic H).

^{13}C NMR ($CDCl_3$, 101 MHz): δ = 24.2 (2C, CH_3), δ = 29.9 (2C, CH_2), δ = 33.4 (2C, CH_2), δ = 45.7(2C, C), δ = 66.5 (2C, CH_2-O), δ = 118.5 (1C, CN), δ = 126-145 (18C, aromatic C), δ = 171.3 (2C, C=O).

(+)ESI-MS [M+Na]$^{+}$: m/z_{exp} = 683.1124, m/z_{theo}: 683.1137, Δm = 0.0013.

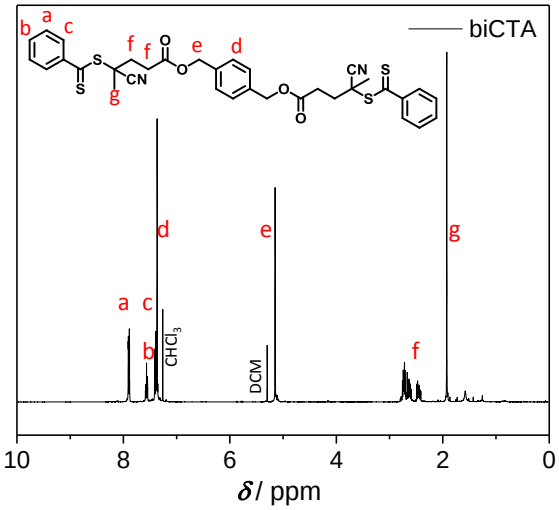

*Figure 7.14 – ^{1}H NMR spectrum ($CDCl_3$, 400MHz) of **biCTA**.*

General procedure for the synthesis of biPMMA via RAFT polymerization

In a crimped vial **biCTA** (1 eq.) as RAFT agent and AIBN (0.15 eq.) as initiator were dissolved in a mixture of monomer (MMA, 150 eq.) in ethylacetate (50% w/w). The solution was deoxygenated for 15 min by purging with argon and then heated at 70 °C for 3 h. The polymerization was stopped by cooling the mixture in liquid nitrogen and opening the vials to oxygen. The product was isolated by precipitation in a cold mixture of MeOH:water (4:1), and collected by filtration. Characterization of the products was performed by ^{1}H NMR spectroscopy (see Appendix Figure 8.28 top), SEC and ESI-MS analysis (see Figure 5.26 and Figure 5.27, respectively). M_n = 7000 g·mol^{-1} $Đ$ = 1.1

Synthesis of 2,3,4,5,6-pentafluorobenzyl 4-((2-formyl-3-methylphenoxy)methyl)benzoate (PFB-PE)

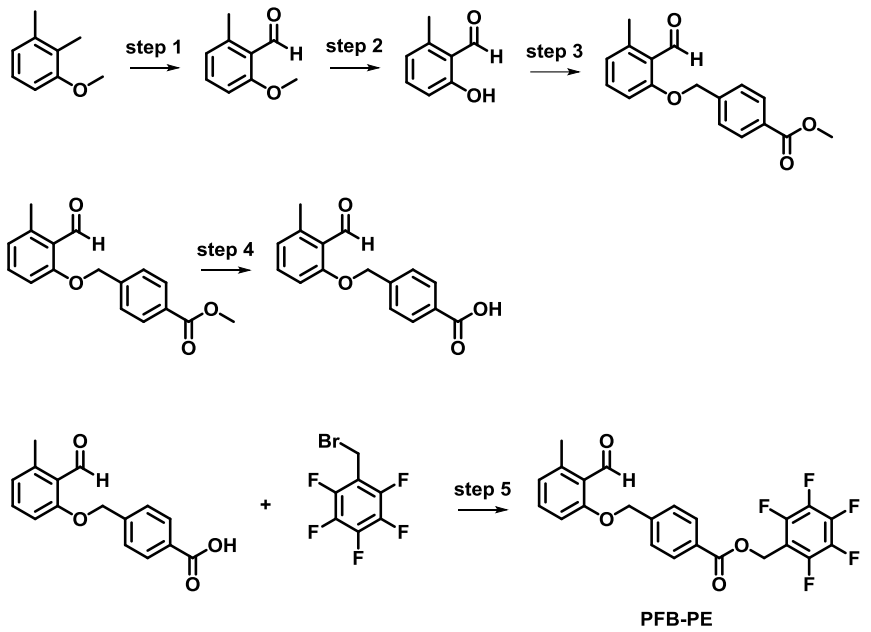

*Scheme 7.9 – Reaction scheme for the synthesis of 2,3,4,5,6-pentafluorobenzyl 4-((2-formyl-3-methylphenoxy)methyl)benzoate (**PFB-PE**).*

Step 1,[220] 2,[66] 3[221] and 4[221] were adapted from the literature.

<u>*Step 5:*</u> In a pre-dried Schlenk flask, Cs_2CO_3 (2.3 mmol, 0.740 g, 2.5 eq.) was dispersed in dry-DMF (5.00 mL) under argon atmosphere before addition of the acid, which was obtained from step 4, (1.0 mmol, 0.284 g, 1.1 eq.). After stirring for 30 min, 2,3,4,5,6-pentafluorobenzyl bromide (0.909 mmol, 0.137 mL, 1 eq) was added and the reaction mixture was stirred overnight at ambient temperature. Subsequently, Cs_2CO_3 was filtered off and the solvent removed under reduced pressure. Next, the crude product was diluted with water (1x 20 mL) and extracted with DCM (1x 20 mL). The collected organic phases were washed with brine (1x 40 mL), dried over $MgSO_4$ and concentrated under reduced pressure. The product was obtained as a yellow solid (quantitative yield).

^{1}H NMR ($CDCl_3$, 400 MHz): δ = 2.59 (s, 3H, CH_3), δ = 5.22 (s, 2H, CH_2), δ = 5.46 (s, 2H, CH_2), δ = 6.85 (d, 2H, CH), δ = 7.35 (t, 1H, CH), δ = 7.49 (d, 2H, CH), δ = 8.03 (d, 2H, CH), δ = 10.74 (s, 1H, CHO).

^{19}F NMR ($CDCl_3$, 377 MHz): δ = −141.6 (2F, *ortho*), δ = −152.3 (1F, *para*), δ = −161.4 (2F, *meta*).

(+)ESI-MS $[M+Na]^+$: m/z_{exp} = 473.0787, m/z_{theo}: 473.0783, Δm = 0.0004.

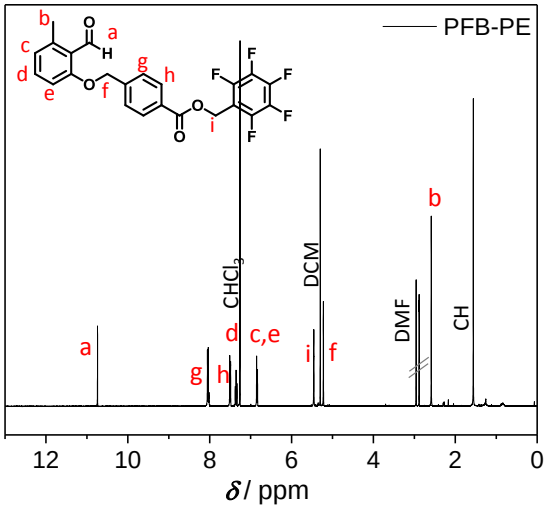

*Figure 7.15 – ^{1}H NMR spectrum ($CDCl_3$, 400MHz) of **PFB-PE.***

RAFT end group capping via hetero Diels-Alder reaction (hDA)

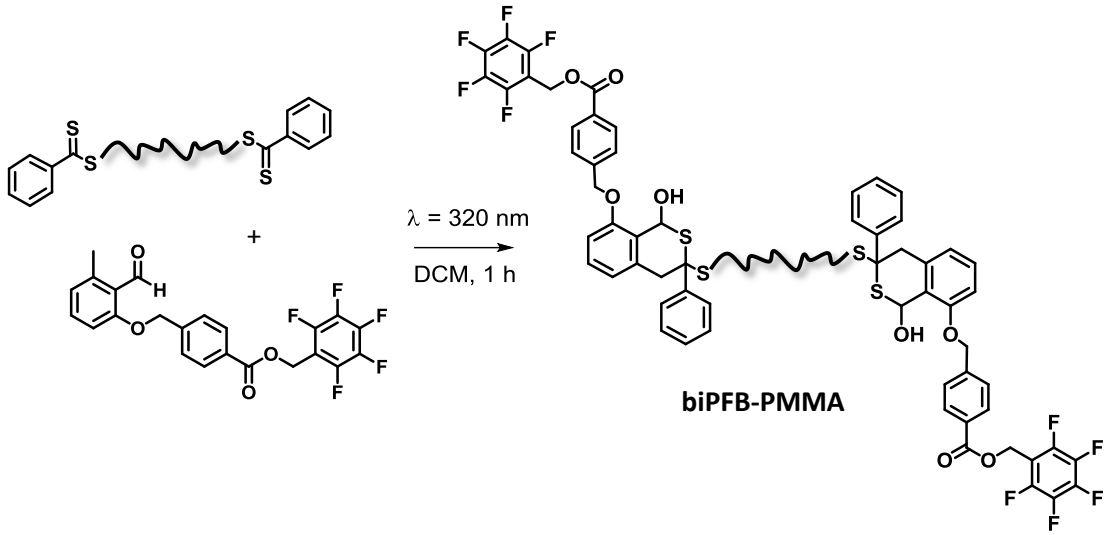

*Scheme 7.10 – Reaction scheme for the synthesis of **biPFB-PMMA** via RAFT end group capping of **biPMMA** with **PFB-PE** via hetero Diels-Alder reaction*

The procedure was adapted from the literature.[69] The polymer **biPMMA** (1 eq.) was dissolved in DCM ([RAFT end-group]$_0$ = 1 mmol·L^{-1}). To this, **PFB-PE** (1.3 eq.) was added and the solution was deoxygenated for 30 minutes. Afterwards, the flask was placed in a custom made photoreactor (refer to Figure 7.1) and irradiated at RT with one Arimed B6 lamp (λ_{max} = 320 nm, power density =14.7 mW·m^{-2}). After 1 h, DCM was removed under reduced pressure. Finally, the polymer was dissolved in a minimum amount of THF and recovered by precipitation in a cold mixture of MeOH:water (4:1), and recovered by filtration. End group

capping was confirmed *via* ^{1}H and ^{19}F NMR spectroscopy (Figure 8.28), SEC (Figure 5.26) and ESI-MS (Figure 5.27) analysis.

General procedure for the synthesis of PMMA based network

Here, an identical procedure to the one used for polystyrene networks was adopted. The type of base and linker used is detailed in **Chapter 5**. When triethylamine was used as a base, the reaction was performed at 40 °C.

Bibliography

[1] J. E. Mark, *Physical properties of polymers handbook*, 2nd ed., Springer, New York, NY, **2007**.

[2] S. Seiffert, *Polym. Chem.* **2017**, *8*, 4472-4487.

[3] M. Zhong, R. Wang, K. Kawamoto, B. D. Olsen, J. A. Johnson, *Science* **2016**, *353*, 1264-1268.

[4] R. Wang, M. K. Sing, R. K. Avery, B. S. Souza, M. Kim, B. D. Olsen, *Acc. Chem. Res.* **2016**, *49*, 2786-2795.

[5] R. Wang, J. A. Johnson, B. D. Olsen, *Macromolecules* **2017**, *50*, 2556-2564.

[6] F. L. Buchholz, A. T. Graham, *John Wiley & Sons, Inc, 605 Third Ave, New York, NY 10016, USA, 1998. 279* **1998**.

[7] P. C. Nicolson, J. Vogt, *Biomaterials* **2001**, *22*, 3273-3283.

[8] A. H. Shalla, Z. Yaseen, M. A. Bhat, T. A. Rangreez, M. Maswal, *Sep. Sci. Technol.* **2019**, *54*, 89-100.

[9] J. Höpfner, PhD thesis, KIT Scientific Publishing (Karlsruhe), **2013**.

[10] G. Singh, A. Mahajan, M. Kumar, *Global Journal of Engineering Science and Researches* **2015**, *2*, 1-4.

[11] Z. Gu, K. Huang, Y. Luo, L. Zhang, T. Kuang, Z. Chen, G. Liao, *WIREs Nanomed. Nanobiotechnol.* **2018**, *10*, e1520.

[12] Y. Liu, W. He, Z. Zhang, B. Lee, *Gels* **2018**, *4*, 46.

[13] M. Emma Parente, A. Ochoa Andrade, G. Ares, F. Russo, A. Jimenez-Kairuz, *Bioadhesive hydrogels for cosmetic applications, Vol. 37*, **2015**.

[14] G. Hild, *Polymer* **1997**, *38*, 3279-3293.

[15] A. Habicht, S. Czarnecki, T. Rossow, S. Seiffert, *J. Polym. Sci., Part B: Polym. Phys.* **2016**, *55*, 19-29.

[16] Y. Gu, K. Kawamoto, M. Zhong, M. Chen, M. J. A. Hore, A. M. Jordan, L. T. J. Korley, B. D. Olsen, J. A. Johnson, *PNAS* **2017**, *114*, 4875-4880.

[17] J. Wang, T.-S. Lin, Y. Gu, R. Wang, B. D. Olsen, J. A. Johnson, *ACS Macro Letters* **2018**, *7*, 244-249.

[18] H. Zhou, J. Woo, A. M. Cok, M. Wang, B. D. Olsen, J. A. Johnson, *PNAS* **2012**, *109*, 19119-19124.

[19] G. Delaittre, L. Barner, *Polym. Chem.* **2018**, *9*, 2679-2684.

[20] T.-S. Lin, R. Wang, J. A. Johnson, B. D. Olsen, *Macromolecules* **2018**, *51*, 1224-1231.

[21] R. G. Jones, J. Kahovec, R. Stepto, E. S. Wilks, M. Hess, T. Kitayama, W. V. Metanomski, *IUPAC* **2009**, 001-443.

[22] G. Odian, *Principles of polymerization*, 4th ed ed., Wiley-Interscience, Hoboken, NJ, **2004**.

[23] K. Matyjaszewski, T. P. Davis, *Handbook of radical polymerization*, Wiley-Interscience, Hoboken, **2002**.

[24] P. Nesvadba, *Encyclopedia of Radicals in Chemistry, Biology and Materials* **2012**.

[25] A. Rudin, P. Choi, in *The Elements of Polymer Science & Engineering (Third Edition)* (Eds.: A. Rudin, P. Choi), Academic Press, Boston, **2013**, pp. 341-389.

[26] T. Otsu, M. Yoshida, *Die Makromolekulare Chemie, Rapid Communications* **1982**, *3*, 127-132.

[27] T. Otsu, M. Yoshida, T. Tazaki, *Die Makromolekulare Chemie, Rapid Communications* **1982**, *3*, 133-140.

[28] D. Greszta, D. Mardare, K. Matyjaszewski, *Macromolecules* **1994**, *27*, 638-644.

[29] K. Matyjaszewski, in *Controlled/Living Radical Polymerization, Vol. 768*, American Chemical Society, **2000**, pp. 2-26.

[30] R. F. Storey, in *Fundamentals of Controlled/Living Radical Polymerization*, The Royal Society of Chemistry, **2013**, pp. 60-77.
[31] G. Moad, E. Rizzardo, S. H. Thang, in *Fundamentals of Controlled/Living Radical Polymerization*, The Royal Society of Chemistry, **2013**, pp. 205-249.
[32] J. Nicolas, Y. Guillaneuf, C. Lefay, D. Bertin, D. Gigmes, B. Charleux, *Prog. Polym. Sci.* **2013**, *38*, 63-235.
[33] G. Moad, E. Rizzardo, in *Nitroxide Mediated Polymerization: From Fundamentals to Applications in Materials Science*, The Royal Society of Chemistry, **2016**, pp. 1-44.
[34] K. Matyjaszewski, J. Xia, *Chem. Rev.* **2001**, *101*, 2921-2990.
[35] V. M. C. Coessens, K. Matyjaszewski, *J. Chem. Educ.* **2010**, *87*, 916-919.
[36] K. Matyjaszewski, J. Spanswick, in *Reference Module in Materials Science and Materials Engineering*, Elsevier, **2016**.
[37] M. Kamigaito, T. Ando, M. Sawamoto, *Chem. Rev.* **2001**, *101*, 3689-3746.
[38] S. H. Thang, Y. K. Chong, R. T. A. Mayadunne, G. Moad, E. Rizzardo, *Tetrahedron Lett.* **1999**, *40*, 2435-2438.
[39] S. Muthukrishnan, E. H. Pan, M. H. Stenzel, C. Barner-Kowollik, T. P. Davis, D. Lewis, L. Barner, *Macromolecules* **2007**, *40*, 2978-2980.
[40] J. Chiefari, Y. K. Chong, F. Ercole, J. Krstina, J. Jeffery, T. P. T. Le, R. T. A. Mayadunne, G. F. Meijs, C. L. Moad, G. Moad, E. Rizzardo, S. H. Thang, *Macromolecules* **1998**, *31*, 5559-5562.
[41] C. Barner-Kowollik, J. P. Blinco, M. Destarac, K. J. Thurecht, S. Perrier, *Encyclopedia of Radicals in Chemistry, Biology and Materials* **2012**.
[42] G. Moad, E. Rizzardo, S. H. Thang, *Aust. J. Chem.* **2012**, *65*, 985-1076.
[43] D. J. Keddie, G. Moad, E. Rizzardo, S. H. Thang, *Macromolecules* **2012**, *45*, 5321-5342.
[44] M. Destarac, *Polymer Reviews* **2011**, *51*, 163-187.
[45] G. Moad, *J. Polym. Sci., Part A: Polym. Chem.* **2018**, *57*, 216-227.
[46] S. Perrier, *Macromolecules* **2017**, *50*, 7433-7447.
[47] H. Mori, A. H. E. Müller, *Prog. Polym. Sci.* **2003**, *28*, 1403-1439.
[48] D. Kunkel, A. H. Müller, M. Janata, L. Lochmann, in *Makromolekulare Chemie. Macromolecular Symposia, Vol. 60*, Wiley Online Library, **1992**, pp. 315-326.
[49] T. E. Patten, K. Matyjaszewski, *Adv. Mater.* **1998**, *10*, 901-915.
[50] D. Benoit, V. Chaplinski, R. Braslau, C. J. Hawker, *J. Am. Chem. Soc.* **1999**, *121*, 3904-3920.
[51] C. Ramireddy, Z. Tuzar, K. Prochazka, S. Webber, P. Munk, *Macromolecules* **1992**, *25*, 2541-2545.
[52] J. Loiseau, N. Doërr, J. M. Suau, J. B. Egraz, M. F. Llauro, C. Ladavière, J. Claverie, *Macromolecules* **2003**, *36*, 3066-3077.
[53] U. C. Palmiero, A. Chovancová, D. Cuccato, G. Storti, I. Lacík, D. Moscatelli, *Polymer* **2016**, *98*, 156-164.
[54] R. O'Reilly, C. Hansell, *Polymers* **2009**, *1*, 3-15.
[55] H. Willcock, R. K. O'Reilly, *Polym. Chem.* **2010**, *1*, 149-157.
[56] O. I. Strube, L. Nothdurft, M. Drache, G. Schmidt-Naake, *Macromol. Chem. Phys.* **2011**, *212*, 574-582.
[57] A. Postma, T. P. Davis, R. A. Evans, G. Li, G. Moad, M. S. O'Shea, *Macromolecules* **2006**, *39*, 5293-5306.
[58] C. Heiler, J. T. Offenloch, E. Blasco, C. Barner-Kowollik, *ACS Macro Letters* **2017**, *6*, 56-61.
[59] W. Lv, L. Liu, Y. Luo, X. Wang, Y. Liu, *J. Colloid Interface Sci.* **2011**, *356*, 16-23.
[60] L. Michalek, K. Mundsinger, C. Barner-Kowollik, L. Barner, *Polym. Chem.* **2019**, *10*, 54-59.
[61] J. Hentschel, K. Bleek, O. Ernst, J.-F. Lutz, H. G. Börner, *Macromolecules* **2008**, *41*, 1073-1075.
[62] R. Nicolaÿ, Y. Kwak, K. Matyjaszewski, *Chem. Commun.* **2008**, 5336-5338.
[63] X.-P. Qiu, F. M. Winnik, *Macromol. Rapid Commun.* **2006**, *27*, 1648-1653.

[64] E. B. Getz, M. Xiao, T. Chakrabarty, R. Cooke, P. R. Selvin, *Anal. Biochem.* **1999**, *273*, 73-80.
[65] M. A. Tasdelen, *Polym. Chem.* **2011**, *2*, 2133-2145.
[66] K. K. Oehlenschlaeger, J. O. Mueller, N. B. Heine, M. Glassner, N. K. Guimard, G. Delaittre, F. G. Schmidt, C. Barner-Kowollik, *Angew. Chem. Int. Ed.* **2013**, *52*, 762-766.
[67] E. Espinosa, M. Glassner, C. Boisson, C. Barner-Kowollik, F. D'Agosto, *Macromol. Rapid Commun.* **2011**, *32*, 1447-1453.
[68] A. S. Goldmann, M. Glassner, A. J. Inglis, C. Barner-Kowollik, *Macromol. Rapid Commun.* **2013**, *34*, 810-849.
[69] D. Varadharajan, G. Delaittre, *Polym. Chem.* **2016**, *7*, 7488-7499.
[70] A. M. Schenzel, C. Klein, K. Rist, N. Moszner, C. Barner-Kowollik, *Advanced science (Weinheim, Baden-Wurttemberg, Germany)* **2016**, *3*, 1500361-1500361.
[71] K. K. Oehlenschlaeger, J. O. Mueller, J. Brandt, S. Hilf, A. Lederer, M. Wilhelm, R. Graf, M. L. Coote, F. G. Schmidt, C. Barner-Kowollik, *Adv. Mater.* **2014**, *26*, 3561-3566.
[72] S. Agar, E. Baysak, G. Hizal, U. Tunca, H. Durmaz, *J. Polym. Sci., Part A: Polym. Chem.* **2018**, *56*, 1181-1198.
[73] D. O'Hagan, *Chem. Soc. Rev.* **2008**, *37*, 308-319.
[74] L. Pauling, *The nature of the chemical bond and the structure of molecules and crystals : an introduction to modern structural chemistry*, 3. ed., 8. print. ed., Cornell Univ. Pr., Ithaca, NY, **1973**.
[75] D. G. Holland, G. J. Moore, C. Tamborski, *J. Org. Chem.* **1964**, *29*, 1562--1565.
[76] S. Chowdhury, E. P. Grimsrud, T. Heinis, P. Kebarle, *J. Am. Chem. Soc.* **1986**, *108*, 3630-3635.
[77] J. Weaver, S. Senaweera, *Tetrahedron* **2014**, *70*, 7413-7428.
[78] L. A. Wall, W. J. Pummer, J. E. Fearn, J. M. Antonucci, *Reactions of Polyfluorobenzenes With Nucleophilic Reagents, Vol. 67A*, **1963**.
[79] H. Pritchard, H. Skinner, *Chem. Rev.* **1955**, *55*, 745-786.
[80] C. Ott, R. Hoogenboom, U. S. Schubert, *Chem. Commun.* **2008**, 3516-3518.
[81] C. R. Becer, K. Babiuch, D. Pilz, S. Hornig, T. Heinze, M. Gottschaldt, U. S. Schubert, *Macromolecules* **2009**, *42*, 2387-2394.
[82] J. March, *Advanced organic chemistry : reactions, mechanisms, and structure*, 4. ed., Wiley, New York [u.a.], **1992**.
[83] C. E. Hoyle, A. B. Lowe, C. N. Bowman, *Chem. Soc. Rev.* **2010**, *39*, 1355-1387.
[84] H. Mutlu, E. B. Ceper, X. Li, J. Yang, W. Dong, M. M. Ozmen, P. Theato, *Macromol. Rapid Commun.* **2019**, *40*, 1800650.
[85] M. J. Kade, D. J. Burke, C. J. Hawker, *J. Polym. Sci., Part A: Polym. Chem.* **2010**, *48*, 743-750.
[86] H. Turgut, A. C. Schmidt, P. Wadhwani, A. Welle, R. Muller, G. Delaittre, *Polym. Chem.* **2017**, *8*, 1288-1293.
[87] E. A. Qian, A. I. Wixtrom, J. C. Axtell, A. Saebi, D. Jung, P. Rehak, Y. Han, E. H. Moully, D. Mosallaei, S. Chow, M. S. Messina, J. Y. Wang, A. T. Royappa, A. L. Rheingold, H. D. Maynard, P. Král, A. M. Spokoyny, *Nature Chemistry* **2016**, *9*, 333.
[88] J. Kvíčala, M. Beneš, O. Paleta, V. Král, *J. Fluorine Chem.* **2010**, *131*, 1327-1337.
[89] L. P. Hammett, *J. Am. Chem. Soc.* **1937**, *59*, 96-103.
[90] J. Burdon, W. B. Hollyhead, J. C. Tatlow, *J. Chem. Soc.* **1965**, 5152-5156.
[91] P. Robson, M. Stacey, R. Stephens, J. C. Tatlow, *J. Chem. Soc.* **1960**, 4754-4760.
[92] O. Exner, in *Correlation Analysis in Chemistry: Recent Advances* (Eds.: N. B. Chapman, J. Shorter), Springer US, Boston, MA, **1978**, pp. 439-540.
[93] A. Das, P. Theato, *Chem. Rev.* **2016**, *116*, 1434-1495.
[94] H. Turgut, G. Delaittre, *Chem.: Europ. J.* **2016**, *22*, 1511-1521.
[95] N. Cakir, U. Tunca, G. Hizal, H. Durmaz, *Macromol. Chem. Phys.* **2016**, *217*, 636-645.
[96] N. ten Brummelhuis, M. Weck, *ACS Macro Letters* **2012**, *1*, 1216-1218.
[97] J.-P. O'Shea, V. Solovyeva, X. Guo, J. Zhao, N. Hadjichristidis, V. O. Rodionov, *Polym. Chem.* **2014**, *5*, 698-701.
[98] J.-M. Noy, M. Koldevitz, P. J. Roth, *Polym. Chem.* **2015**, *6*, 436-447.

[99] C. Barner-Kowollik, F. E. Du Prez, P. Espeel, C. J. Hawker, T. Junkers, H. Schlaad, W. Van Camp, *Angew. Chem. Int. Ed.* **2011**, *50*, 60-62.
[100] S. Nishimura, A. Nagai, A. Takahashi, T. Narita, T. Hagiwara, H. Hamana, *Polym. J.* **1990**, *22*, 171.
[101] T. Cai, W. J. Yang, K.-G. Neoh, E.-T. Kang, *Polym. Chem.* **2012**, *3*, 1061-1068.
[102] S. Slavin, J. Burns, D. M. Haddleton, C. R. Becer, *Eur. Polym. J.* **2011**, *47*, 435-446.
[103] K. A. Gunay, N. Schuwer, H.-A. Klok, *Polym. Chem.* **2012**, *3*, 2186-2192.
[104] Y. Jin, K. H. Wong, A. M. Granville, *J. Colloid Interface Sci.* **2016**, *462*, 19-28.
[105] M. Álvarez-Paino, A. Muñoz-Bonilla, G. Marcelo, J. Rodríguez-Hernández, M. Fernández-García, *Polym. Chem.* **2012**, *3*, 3282-3288.
[106] K. Babiuch, R. Wyrwa, K. Wagner, T. Seemann, S. Hoeppener, C. R. Becer, R. Linke, M. Gottschaldt, J. Weisser, M. Schnabelrauch, U. S. Schubert, *Biomacromolecules* **2011**, *12*, 681-691.
[107] L. Dumas, E. Fleury, D. Portinha, *Polymer* **2014**, *55*, 2628-2634.
[108] K. Babiuch, C. R. Becer, M. Gottschaldt, J. T. Delaney, J. Weisser, B. Beer, R. Wyrwa, M. Schnabelrauch, U. S. Schubert, *Macromol. Biosci.* **2011**, *11*, 535-548.
[109] D. Varadharajan, H. Turgut, J. Lahann, H. Yabu, G. Delaittre, *Adv. Funct. Mater.* **2018**, *28*, 1800846.
[110] S. L. Cobb, C. D. Murphy, *J. Fluorine Chem.* **2009**, *130*, 132-143.
[111] A. Strunecka, J. Patocka, P. Connett, *Journal of Applied Biomedicine* **2004**, *2*, 141-150.
[112] P. Jeschke, *ChemBioChem* **2004**, *5*, 570-589.
[113] H. Teng, *Applied Sciences* **2012**, *2*, 496-512.
[114] S. C. Bushong, G. Clarke, *Magnetic Resonance Imaging-E-Book: Physical and Biological Principles*, Elsevier Health Sciences, **2013**.
[115] J. Gerig, *Biophysics Textbook Online* **2001**, 1-35.
[116] M. Drew, E. Orton, P. Krolikowski, J. M. Salvino, N. V. Kumar, *J. Comb. Chem.* **2000**, *2*, 8-9.
[117] M. Hourdin, G. Gouhier, A. Gautier, E. Condamine, S. R. Piettre, *J. Comb. Chem.* **2005**, *7*, 285-297.
[118] M. J. Shapiro, G. Kumaravel, R. C. Petter, R. Beveridge, *Tetrahedron Lett.* **1996**, *37*, 4671-4674.
[119] K. Dušek, M. Dušková-Smrčková, *Prog. Polym. Sci.* **2000**, *25*, 1215-1260.
[120] J. C. Hernández-Ortiz, E. Vivaldo-Lima, *Handbook of Polymer Synthesis, Characterization, and Processing* **2013**, 187-204.
[121] Y. N. Mata, M. L. Blázquez, A. Ballester, F. González, J. A. Muñoz, *J. Hazard. Mater.* **2010**, *178*, 243-248.
[122] J. Li, D. J. Mooney, *Nature reviews. Materials* **2016**, *1*, 16071.
[123] M. Akiba, A. S. Hashim, *Prog. Polym. Sci.* **1997**, *22*, 475-521.
[124] P. Milani, D. França, A. G. Balieiro, R. Faez, *Polímeros* **2017**, *27*, 256-266.
[125] J. Li, A. D. Celiz, J. Yang, Q. Yang, I. Wamala, W. Whyte, B. R. Seo, N. V. Vasilyev, J. J. Vlassak, Z. Suo, D. J. Mooney, *Science* **2017**, *357*, 378.
[126] Y. Gu, J. Zhao, J. A. Johnson, *Trends in Chemistry*.
[127] F. Ganji, F. S. Vasheghani, F. E. Vasheghani, **2010**.
[128] P. J. Flory, M. Gordon, P. J. Flory, N. G. McCrum, *Proc. R. Soc. Lond. A Math. Phys. Sci.* **1976**, *351*, 351-380.
[129] W. W. Graessley, *Macromolecules* **1975**, *8*, 186-190.
[130] W. Oppermann, in *Polyelectrolyte Gels*, American Chemical Society, **1992**, pp. 159-170.
[131] P. J. Flory, J. Rehner, *J. Chem. Phys.* **1943**, *11*, 512-520.
[132] H. H. Hooper, J. P. Baker, H. W. Blanch, J. M. Prausnitz, *Macromolecules* **1990**, *23*, 1096-1104.
[133] P. J. Flory, *Principles of polymer chemistry*, Cornell Univ. Pr., Ithaca, NY, **1953**.
[134] U. Schröder, W. Oppermann, in *Physical Properties of Polyelectrolyte Gels*, **1996**, pp. 19-38.
[135] Y. Akagi, J. P. Gong, U.-i. Chung, T. Sakai, *Macromolecules* **2013**, *46*, 1035-1040.
[136] H. M. James, E. Guth, *J. Chem. Phys.* **1943**, *11*, 455-481.

[137] H. M. James, E. Guth, *J. Chem. Phys.* **1947**, *15*, 669-683.
[138] G. Ronca, G. Allegra, *J. Chem. Phys.* **1975**, *63*, 4990-4997.
[139] S. F. Edwards, T. A. Vilgis, *Rep. Prog. Phys.* **1988**, *51*, 243-297.
[140] J. V. Alemán, A. V. Chadwick, J. He, M. Hess, K. Horie, R. G. Jones, P. Kratochvíl, I. Meisel, I. Mita, G. Moad, S. Penczek, R. F. T. Stepto, in *Pure Appl. Chem., Vol. 79*, **2007**, p. 1801.
[141] J. Zha, H. Roggendorf, *Adv. Mater.* **1991**, *3*, 522-522.
[142] M. Ebara, *Sci. Technol. Adv. Mater.* **2015**, *16*, 014804.
[143] H. Staudinger, W. Heuer, *Chem. Ber.* **1934**, 1174.
[144] T. Norisuye, T. Morinaga, Q. Tran-Cong-Miyata, A. Goto, T. Fukuda, M. Shibayama, *Polymer* **2005**, *46*, 1982-1994.
[145] N. Ide, T. Fukuda, *Macromolecules* **1997**, *30*, 4268-4271.
[146] A. J. Scott, A. Nabifar, A. Penlidis, *Macromol. React. Eng.* **2014**, *8*, 639-657.
[147] I. Bannister, N. C. Billingham, S. P. Armes, *Soft Matter* **2009**, *5*, 3495-3504.
[148] N. Ide, T. Fukuda, *Macromolecules* **1999**, *32*, 95-99.
[149] R. Henkel, P. Vana, *Macromol. Chem. Phys.* **2014**, *215*, 182-189.
[150] C. Norioka, A. Kawamura, T. Miyata, *Polym. Chem.* **2017**, *8*, 6050-6057.
[151] P. Ghosh, S. Katare, P. Patkar, J. M. Caruthers, V. Venkatasubramanian, K. A. Walker, *Rubber Chem. Technol.* **2003**, *76*, 592-693.
[152] G. Hild, *Prog. Polym. Sci.* **1998**, *23*, 1019-1149.
[153] H. Shih, C.-C. Lin, *Biomacromolecules* **2012**, *13*, 2003-2012.
[154] M. Chen, Y. Gu, A. Singh, M. Zhong, A. M. Jordan, S. Biswas, L. T. J. Korley, A. C. Balazs, J. A. Johnson, *ACS Central Science* **2017**, *3*, 124-134.
[155] C. Li, Q. Wang, *Polymer* **2016**, *99*, 594-597.
[156] S. Theis, A. Iturmendi, C. Gorsche, M. Orthofer, M. Lunzer, S. Baudis, A. Ovsianikov, R. Liska, U. Monkowius, I. Teasdale, *Angew. Chem. Int. Ed.* **2017**, *56*, 15857-15860.
[157] D. Estupiñán, C. Barner-Kowollik, L. Barner, *Angew. Chem. Int. Ed.* **2018**, *57*, 5925-5929.
[158] Y. Wang, C. I. Rivera Vera, Q. Lin, *Org. Lett.* **2007**, *9*, 4155-4158.
[159] Y. E. Shapiro, *Prog. Polym. Sci.* **2011**, *36*, 1184-1253.
[160] J. Höpfner, G. Guthausen, K. Saalwächter, M. Wilhelm, *Macromolecules* **2014**, *47*, 4251-4265.
[161] L. B. Arens, PhD thesis, KIT-Bibliothek (Karlsruhe), **2018**.
[162] O. Wichterle, D. LÍM, *Nature* **1960**, *185*, 117-118.
[163] F. Ullah, M. B. H. Othman, F. Javed, Z. Ahmad, H. M. Akil, *Mater. Sci. Eng. C* **2015**, *57*, 414-433.
[164] S. J. Buwalda, K. W. M. Boere, P. J. Dijkstra, J. Feijen, T. Vermonden, W. E. Hennink, *J. Controll. Release* **2014**, *190*, 254-273.
[165] E. S. Gil, S. M. Hudson, *Prog. Polym. Sci.* **2004**, *29*, 1173-1222.
[166] T. Miyata, N. Asami, T. Uragami, *Nature* **1999**, *399*, 766-769.
[167] B. E. Pollot, C. R. Rathbone, J. C. Wenke, T. Guda, *J. Biomed. Mater. Res. B* **2018**, *106*, 672-679.
[168] H. Park, K. Park, in *Hydrogels and Biodegradable Polymers for Bioapplications*, ACS Symposium Series, Vol. 627, **1996**, pp. 2-10.
[169] R. A. Batista, P. J. P. Espitia, J. d. S. S. Quintans, M. M. Freitas, M. Â. Cerqueira, J. A. Teixeira, J. C. Cardoso, *Carbohydr. Polym.* **2019**, *205*, 106-116.
[170] W. E. Hennink, C. F. van Nostrum, *Advanced Drug Delivery Reviews* **2002**, *54*, 13-36.
[171] F. L. Buchholz, *J. Chem. Educ.* **1996**, *73*, 512.
[172] W. Kuhn, B. Hargitay, A. Katchalsky, H. Eisenberg, *Nature* **1950**, *165*, 514-516.
[173] A. Katchalsky, I. Michaeli, *Journal of Polymer Science* **1955**, *15*, 69-86.
[174] K. Pulidindi, S. Chakraborty, **2018**, *https://www.gminsights.com/industry-analysis/superabsorbent-polymers-sap-market*.
[175] N. Orakdogen, T. Boyacı, *Soft Matter* **2017**, *13*, 9046-9059.
[176] F. G. Donnan, *Chem. Rev.* **1924**, *1*, 73-90.
[177] J. Ricka, T. Tanaka, *Macromolecules* **1984**, *17*, 2916-2921.
[178] G. S. Manning, *J. Chem. Phys.* **1969**, *51*, 924-933.

[179] G. S. Manning, *Biophys. Chem.* **1978**, *9*, 65-70.
[180] J. Skolnick, M. Fixman, *Macromolecules* **1977**, *10*, 944-948.
[181] J. Kucera, *Desalination: water from water*, John Wiley & Sons, **2014**.
[182] J. Höpfner, C. Klein, M. Wilhelm, *Macromol. Rapid Commun.* **2010**, *31*, 1337-1342.
[183] J. Höpfner, T. Richter, P. Košovan, C. Holm, M. Wilhelm, in *Intelligent Hydrogels*, Springer, **2013**, pp. 247-263.
[184] Q. Yu, M. Zhou, Y. Ding, B. Jiang, S. Zhu, *Polymer* **2007**, *48*, 7058-7064.
[185] K. Saalwachter, S. Seiffert, *Soft Matter* **2018**, *14*, 1976-1991.
[186] T. G. Mezger, *The rheology handbook: for users of rotational and oscillatory rheometers*, Vincentz Network GmbH & Co KG, **2006**.
[187] P. Fievet, in *Encyclopedia of Membranes* (Eds.: E. Drioli, L. Giorno), Springer Berlin Heidelberg, Berlin, Heidelberg, **2015**, pp. 1-3.
[188] F. Cavalli, H. Mutlu, S. O. Steinmueller, L. Barner, *Polym. Chem.* **2017**, *8*, 3778-3782.
[189] F. Cavalli, L. De Keer, B. Huber, P. H. M. Van Steenberge, D. R. D'Hooge, L. Barner, *Polym. Chem.* **2019**, *10*, 2781-2791.
[190] F. Cavalli, F. R. Bloesser, C. Barner-Kowollik, L. Barner, *Chem.: Europ. J.* **2019**, *25*, 10049-10053.
[191] P. H. M. Van Steenberge, D. R. D'hooge, M. F. Reyniers, G. B. Marin, *Chem. Eng. Sci.* **2014**, *110*, 185-199.
[192] J. P. Danehy, K. N. Parameswaran, *J. Chem. Eng. Data* **1968**, *13*, 386-389.
[193] B. T. Worrell, S. Mavila, C. Wang, T. M. Kontour, C.-H. Lim, M. K. McBride, C. B. Musgrave, R. Shoemaker, C. N. Bowman, *Polym. Chem.* **2018**, *9*, 4523-4534.
[194] H. F. Gilbert, in *Methods Enzymol., Vol. 251*, Academic Press, **1995**, pp. 8-28.
[195] R. Singh, G. M. Whitesides, in *Techniques in Protein Chemistry, Vol. 6* (Ed.: J. W. Crabb), Academic Press, **1995**, pp. 259-266.
[196] J. C. Lukesh, M. J. Palte, R. T. Raines, *J. Am. Chem. Soc.* **2012**, *134*, 4057-4059.
[197] O. Dmitrenko, C. Thorpe, R. D. Bach, *J. Org. Chem.* **2007**, *72*, 8298-8307.
[198] N. H. Park, G. d. P. Gomes, M. Fevre, G. O. Jones, I. V. Alabugin, J. L. Hedrick, *Nat. Commun.* **2017**, *8*, 166.
[199] F. G. Bordwell, *Acc. Chem. Res.* **1988**, *21*, 456-463.
[200] W. N. Olmstead, Z. Margolin, F. G. Bordwell, *J. Org. Chem.* **1980**, *45*, 3295-3299.
[201] A. Kütt, S. Selberg, I. Kaljurand, S. Tshepelevitsh, A. Heering, A. Darnell, K. Kaupmees, M. Piirsalu, I. Leito, *Tetrahedron Lett.* **2018**, *59*, 3738-3748.
[202] R. C. Specht, *Anal. Chem.* **1956**, *28*, 1015-1017.
[203] J. Chen, L. Dumas, J. Duchet-Rumeau, E. Fleury, A. Charlot, D. Portinha, *J. Polym. Sci., Part A: Polym. Chem.* **2012**, *50*, 3452-3460.
[204] C. Reichardt, T. Welton, *Solvents and solvent effects in organic chemistry*, John Wiley & Sons, **2011**.
[205] J. Coates, in *Encyclopedia of Analytical Chemistry*, John Wiley & Sons, Ltd, **2006**.
[206] P. van der Heide, in *X-Ray Photoelectron Spectroscopy*, **2011**, pp. 101-140.
[207] P. van der Heide, *X-Ray Photoelectron Spectroscopy* **2011**, 61-99.
[208] F. Chesneau, H. Hamoudi, B. Schüpbach, A. Terfort, M. Zharnikov, *The Journal of Physical Chemistry C* **2011**, *115*, 4773-4782.
[209] M. M. Zieger, P. Mueller, A. S. Quick, M. Wegener, C. Barner-Kowollik, *Angew. Chem. Int. Ed.* **2017**, *56*, 5625-5629.
[210] E. Mendes, P. Lindner, M. Buzier, F. Boué, J. Bastide, *Phys. Rev. Lett.* **1991**, *66*, 1595-1598.
[211] T. Kojima, M. Tsuchiya, K. Tago, *J. Therm. Anal.* **1997**, *49*, 149-154.
[212] R. A. Orwoll, P. A. Arnold, in *Physical Properties of Polymers Handbook* (Ed.: J. E. Mark), Springer New York, New York, NY, **2007**, pp. 233-257.
[213] J. Xu, J. He, D. Fan, X. Wang, Y. Yang, *Macromolecules* **2006**, *39*, 8616-8624.
[214] A. Sepsey, I. Bacskay, A. Felinger, in *Adv. Chromatogr.*, CRC Press, **2017**, pp. 205-227.
[215] E. Vivaldo-Lima, P. E. Wood, A. E. Hamielec, A. Penlidis, *Industrial & engineering chemistry research* **1997**, *36*, 939-965.
[216] S. Seiffert, *Macromol. Chem. Phys.* **2017**, *218*, 1600280.

[217] J. Brandrup, E. H. Immergut, E. A. Grulke, *Polymer handbook*, 4. ed. ed., Wiley, New York, **1999**.
[218] J. H. Scofield, *J. Electron. Spectrosc. Relat. Phenom.* **1976**, *8*, 129-137.
[219] S. Tanuma, C. J. Powell, D. R. Penn, *Surf. Interface Anal.* **1994**, *21*, 165-176.
[220] F. M. Hauser, S. R. Ellenberger, *Synthesis* **1987**, *1987*, 723-724.
[221] T. Pauloehrl, G. Delaittre, V. Winkler, A. Welle, M. Bruns, H. G. Börner, A. M. Greiner, M. Bastmeyer, C. Barner-Kowollik, *Angew. Chem. Int. Ed.* **2012**, *51*, 1071-1074.
[222] M. T. Erben, S. Bywater, *J. Am. Chem. Soc.* **1955**, *77*, 3710-3711.
[223] K. Hėberger, H. Fischer, *Int. J. Chem. Kinet.* **1993**, *25*, 249-263.
[224] M. G. Buback, Robert G.; Hutchinson, Robin A.; Klumperman, Bert; Kuchta, Frank-Dieter; Manders, Bart G.; O'Driscoll, Kenneth F. ; Russell, Gregory T. ; Schweer, Johannes *Macromol. Chem. Phys.* **1995**, *196*, 3267-3280.
[225] G. Johnston-Hall, M. J. Monteiro, *J. Polym. Sci., Part A: Polym. Chem.* **2008**, *46*, 3155-3173.
[226] P. Derboven, D. R. D'hooge, M.-F. Reyniers, G. B. Marin, C. Barner-Kowollik, *Macromolecules* **2015**, *48*, 492-501.
[227] G. B. Desmet, N. De Rybel, P. H. M. Van Steenberge, D. R. D'Hooge, M.-F. Reyniers, G. B. Marin, *Macromol. Rapid Commun.* **2018**, *39*, 1700403.
[228] M. Buback, B. Huckestein, F.-D. Kuchta, G. T. Russell, E. Schmid, *Macromol. Chem. Phys.* **1994**, *195*, 2117-2140.

8 Appendix

8.1 Appendix for Chapter 4

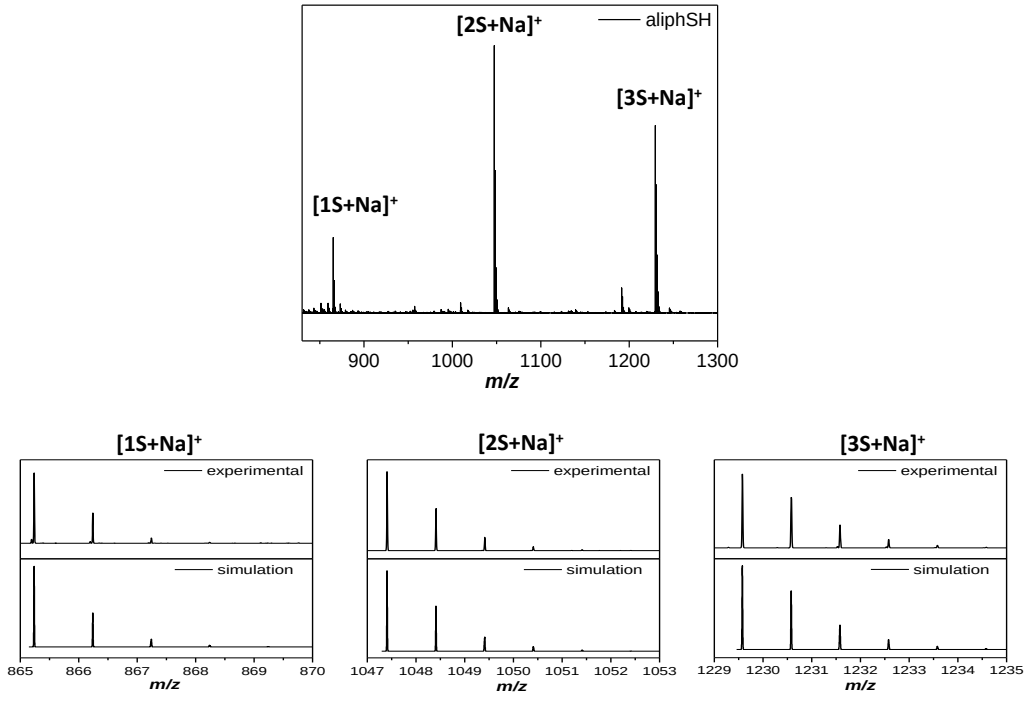

Figure 8.1 – Top: (+)ESI-MS spectrum of the model reaction after a reaction time of 5 min and removal of the base (SH:PFB = 1:1, $[SH]_0$=0.15 g·mol^{-1}). Bottom: the experimental and the simulated isotopic pattern are compared. The overview of the m/z ratio are reported in Table 8.1.

*Table 8.1 – List of the experimental and the theoretical m/z ratio for the mono- (**1S**) di- (**2S**) and trisubstituted (**3S**) fluorinated linker (**3PFB**) reported in Figure 8.1.*

Structure	*m/z*(exp)	*m/z*(theo)	*Δm*
$[1S+Na]^+$	865.2377	865.2367	0.0010
$[2S+Na]^+$	1047.4077	1047.4060	0.0017
$[3S+Na]^+$	1229.5774	1229.5753	0.0021

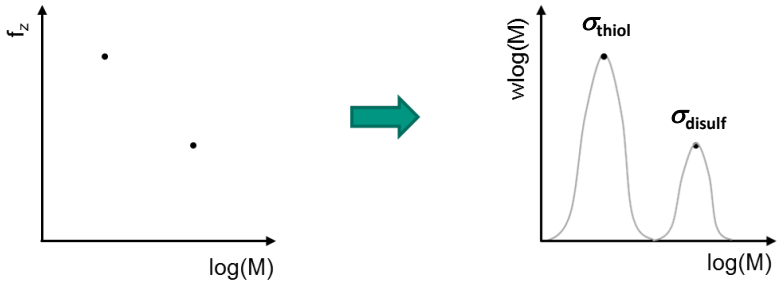

Figure 8.2 – The SEC broadening effect is accounted for in the kMC simulations by introducing a normal distribution on log scale having standard deviation (σ) = 0.03, for both thiol and disulfide in each solvent. The figure is adapted from Ref. [189] with the permission of The Royal Society of Chemistry.

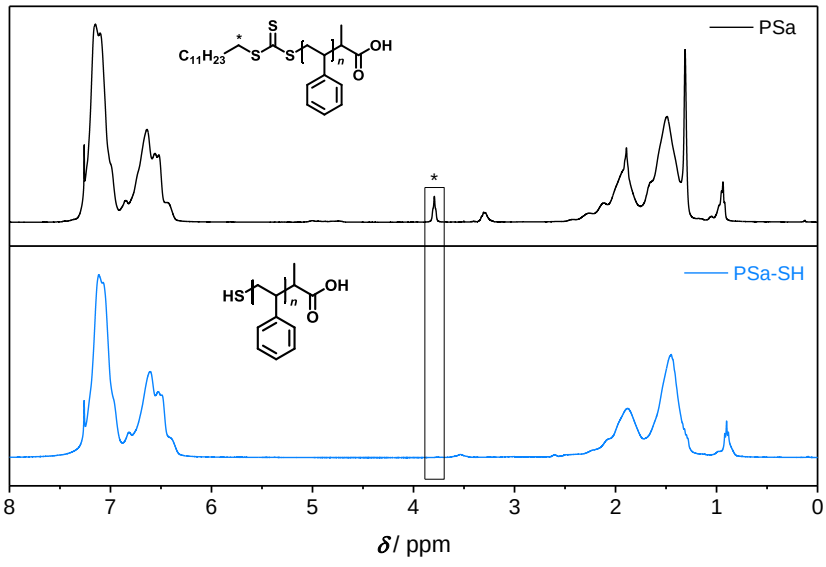

*Figure 8.3 – ^{1}H NMR spectra ($CDCl_3$, 400 MHz) for **PSa** (black) and **PSa-SH** (blue). In the box the disappearance of the –CH_2- marked in the structure (*) is highlighted. δ = 7.50 – 6.20 (m, ArH), 2.5 – 0.50 (m, aliphatic H). The figure is reproduced from Ref. [189] with the permission of The Royal Society of Chemistry.*

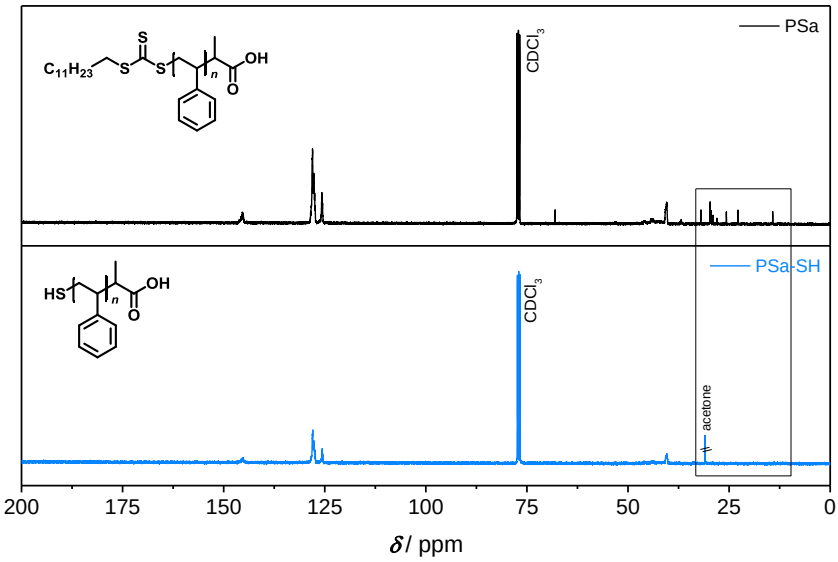

*Figure 8.4 – ^{13}C NMR spectra ($CDCl_3$, 101 MHz) for **PSa** (black) and **PSa-SH** (blue). The disappearance of the resonances corresponding to the aliphatic carbon chain of the RAFT agent is highlighted with a box. δ = 145.43(C, quaternary carbon in the styrene aromatic ring), δ = 128.33 and δ = 125,52 (-HC=CH-, unsaturated carbons, styrene ring), and δ = 40.30 (aliphatic C, aliphatic polymer backbone). The figure is reproduced from Ref. [189] with the permission of The Royal Society of Chemistry.*

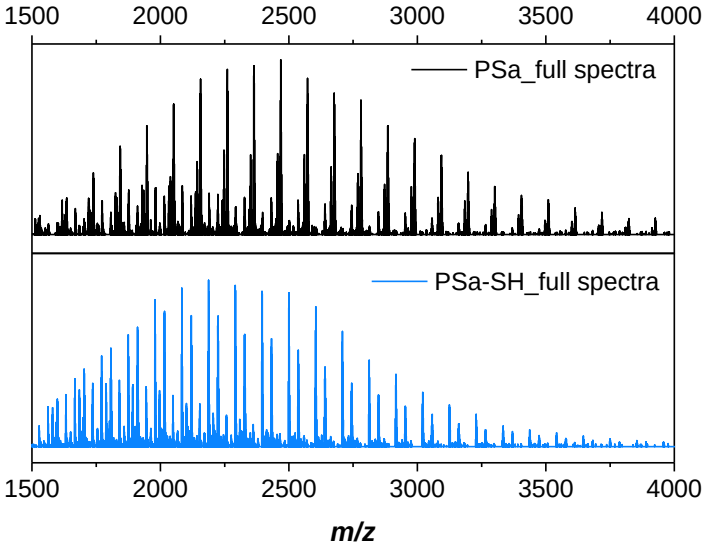

*Figure 8.5 – (−)ESI-MS spectra for **PSa** (black) and **PSa-SH** (blue) recorded in negative mode in the region m/z = 1500 to 4000. The figure is adapted from Ref. [189] with the permission of The Royal Society of Chemistry.*

The molecular weight of the polymer is the number or weight average of the molecular weight of each chain. Thus, in order to account for the distribution of the molecular weight during the *k*MC simulations, it is necessary to simulate the polymerization kinetics of the RAFT polymerization. In this way, the starting distribution of the polymer thiol is included accurately and diffusional limitations during PFTR can be accounted for. The following section, in which the kinetics of the RAFT polymerization are validated against experimental data, is thus necessary to demonstrate the ability of the *k*MC simulation to predict diffusional limitations.

The following information concerning the kinetic Monte Carlo simulation are reproduced from Ref. [189] with the permission of The Royal Society of Chemistry.

Simulations concerning the RAFT polymerization of PSa-SH and PSb-SH:

*Table 8.2 - Overview of the reactions and rate coefficients for **PSa-SH** and **PSb-SH** (monomer: styrene) with $I_2, I^\bullet, M, R_0^\bullet, R_i^\bullet, P_i, R_0X, R_iX$: conventional radical initiator, initiator fragment, monomer, RAFT leaving group, macroradical (chain length i≥1), dead polymer species, initial RAFT agent, dormant macrospecies; 70°C; for termination apparent rate coefficients with given value the one of $k_{t,app}^{1,1}$*

Reaction	Equation	k ((L mol^{-1}) s^{-1})	ref
Dissociation[(a)]	$I_2 \xrightarrow{f,k_{dis}} 2I^\bullet$	$4.4\ 10^{-5}$	[222]
Chain Initiation	$I^\bullet + M \xrightarrow{k_{pI}} R_1^\bullet$	$5.2\ 10^{3}$	[223]
	$R_0^\bullet + M \xrightarrow{k_{pR_0}} R_1^\bullet$	$5.2\ 10^{3}$	[223]
Propagation	$R_i^\bullet + M \xrightarrow{k_p} R_{i+1}^\bullet$	$4.8\ 10^{2}$	[224]
Termination by recombination	$R_0^\bullet + R_0^\bullet \xrightarrow{k_{tc,00}} P_0$	$2\ 10^{8.7}$	[225, 226]
	$R_0^\bullet + R_i^\bullet \xrightarrow{k_{tc,0}} P_i$	$2\ 10^{8.7}$	[225, 226]
	$R_i^\bullet + R_j^\bullet \xrightarrow{k_{tc,app}^{i,j}} P_{i+j}$	$2\ 10^{8.7}$	[225, 226]
RAFT exchange	$R_i^\bullet + R_0X \underset{k_{frag,1}}{\overset{k_{add,1}}{\rightleftarrows}} R_iXR_0 \underset{k_{add,2}}{\overset{k_{frag,2}}{\rightleftarrows}} R_iX + R_0^\bullet$	$3.3\ 10^{6}$ $3.5\ 10^{4}$ $5.3\ 10^{5}$	[227](b)
	$R_i^\bullet + R_jX \underset{k_{frag}}{\overset{k_{add}}{\rightleftarrows}} R_iXR_j \underset{k_{add}}{\overset{k_{frag}}{\rightleftarrows}} R_iX + R_j^\bullet$	$5.7\ 10^{4}$ $7.7\ 10^{4}$ $9.6\ 10^{4}$	[227](b)

[(a)](apparent) efficiency *f*, [(b)]values for 2-cyano-2-propyl dodecyl trithiocarbonate instead of DoPAT

Apparent termination rate coefficient

In order to accurately describe the diffusion-controlled mechanism of bimolecular termination in radical polymerization, the composite k_t model[4] [225] (aka RAFT-CLD-T model) was used.

This model allows to calculate an apparent homotermination rate coefficient ($k_{tc,app}^{i,i}$; *i*=chain length; only considering termination by recombination) dependent on the chain length *i* and the monomer conversion X_m:

For $i < i_{gel}$

$$k_{tc,app}^{i,i} = k_t^{1,1}\, i^{-\alpha_s} \qquad \text{for } i < i_{SL} \tag{8.1}$$

$$k_{tc,app}^{i,i} = k_t^{1,1}\, i_{SL}^{(\alpha_L-\alpha_s)}\, i^{-\alpha_s} \qquad \text{for } i \geq i_{SL} \tag{8.2}$$

For $i \geq i_{gel}$

$$k_{tc,app}^{i,i} = k_t^{1,1}\, i_{SL}^{(\alpha_{gel}-\alpha_s)}\, i^{-\alpha_{gel}} \qquad \text{for } i < i_{SL} \tag{8.3}$$

$$k_{tc,app}^{i,i} = k_t^{1,1}\, i_{SL}^{(\alpha_L-\alpha_s)}\, i^{(\alpha_{gel}-\alpha_L)}\, i^{-\alpha_{gel}} \qquad \text{for } i \geq i_{SL} \tag{8.4}$$

with $k_t^{1,1}$ the (apparent) termination rate coefficient for radicals with chain length 1, α_s the exponent for termination for termination of short chains in dilute solution, α_L the exponent for long chains in dilute solution, α_{gel} the exponent for chains in the gel regime, i_{SL} the crossover chain length between short- and long-chain behavior, i_{gel} the chain length at the onset of the gel-effect. An overview of these parameters can be found in Table 8.2.[225]

From the apparent homotermination rate coefficients, the apparent cross-termination rate coefficient $k_{tc,app}^{i,j}$ is calculated for simplicity using the geometric mean:

$$k_{tc,app}^{i,j} = \sqrt{k_{tc,app}^{i,i}\, k_{tc,app}^{j,j}} \tag{8.5}$$

An averaged (zero order) apparent termination rate coefficient can be calculated at any moment:

$$\langle k_{tc,app} \rangle = \frac{\sum_{i=1}^{\infty}\sum_{j=1}^{\infty} k_{tc,app}^{i,j}[R_i][R_j]}{(\sum_{i=1}^{\infty}[R_i])^2} \tag{8.6}$$

Table 8.3 – Parameters used for the composite k_t model.[225]

Monomer	***T*(K)**	$\boldsymbol{k_t^{1,1}}$	$\boldsymbol{\alpha_S}$	$\boldsymbol{i_{SL}}$	$\boldsymbol{\alpha_L}$	$\boldsymbol{\alpha_{gel}}$	$\boldsymbol{i_{gel}}$
Styrene	363	$2 \times 10^{8.7}$	0.53	30	0.15	$1.22X_m$-0.11	$3.30X_m{}^{-2.13}$

Apparent covalent initiator efficiency

An apparent conventional initiator efficiency f_{app} dependent on monomer conversion X_m can be calculated as described by Buback *et.al.*:[228]

$$f_{app} = \frac{D_I}{D_I + D_{term}} \tag{8.7}$$

with D_I the diffusion coefficient of the cyanoisopropyl radical and $D_{\mathrm{term}} = 5.3\ 10^{-10}\mathrm{m}^2\mathrm{s}^{-1}$ a correction factor related to the rate of termination between two cyanoisopropyl radicals. According to the free volume theory, D_I can be calculated *via*:

$$D_I = D_{0,I} \exp\left(-\frac{E_I}{RT}\right) \exp\left(\frac{-w_1 V_1^* \xi_{i2}/\xi_{12} + w_2 V_2^* \xi_{12}}{V_{FH}/\lambda}\right) \tag{8.8}$$

$$\frac{V_{FH}}{\lambda} = \frac{K_{11}}{\lambda} w_1 (K_{21} - T - T_{g1}) + \frac{k_{12}}{\lambda}\ w_2 (K_{22} + T - T_{g1}) \tag{8.9}$$

In Table 8.4 is presented an overview of the description and values of the parameters used.

Table 8.4 – Overview of the values to calculate the apparent initiator efficiency as described by Buback et al. for AIBN as conventional radical initiator and styrene as monomer.[228]

Parameter	Description	Value
$D_{0,I}\ (m^2 s^{-1})$	Pre-exponential factor for diffusion	$1.95\ 10^{-4}$
$E_I\ (kJ\ mol^{-1})$	Activation energy for diffusion	31
$R\ (J\ mol^{-1} K^{-1})$	Universal gas constant	8.314
$T\ (K)$	Temperature	$333 - 363$
$w_1\ (-)$	Mass fraction of monomer	0-1
$w_2\ (-)$	Mass fraction of polymer	0-1
$V_1^*\ (m^3 mol^{-1})$	Specific critical hole free volume of monomer	$9.46\ 10^{-7}$
$V_2^*\ (m^3 mol^{-1})$	Specific critical hole free volume of polystyrene	$8{,}50\ 10^{-7}$
$\frac{K_{11}}{\lambda}\ (m^3\ kg^{-1}\ K^{-1})$	Parameter for specific hole free volume monomer	$1.49\ 10^{-9}$
$\frac{K_{12}}{\lambda}\ (m^3\ kg^{-1}\ K^{-1})$	Parameter for specific hole free volume polymer	$5.82\ 10^{-10}$
$K_{21} - T_{g1}\ (K)$	Parameter for specific hole free volume monomer	-84
$K_{22} - T_{g1}\ (K)$	Parameter for specific hole free volume polymer	-327
$\xi_{i2}\ (-)$	Critical jumping unit volume ratio for cyanoispropyl radical to polymer	0.36
$\xi_{12}\ (-)$	Critical jumping unit volume ratio for monomer to polymer	0.59

The accuracy of the simulation is shown by the good fit obtained when comparing the calculated and the experimentally obtained monomer conversion and average molecular weight data, as displayed in Figure 8.6.

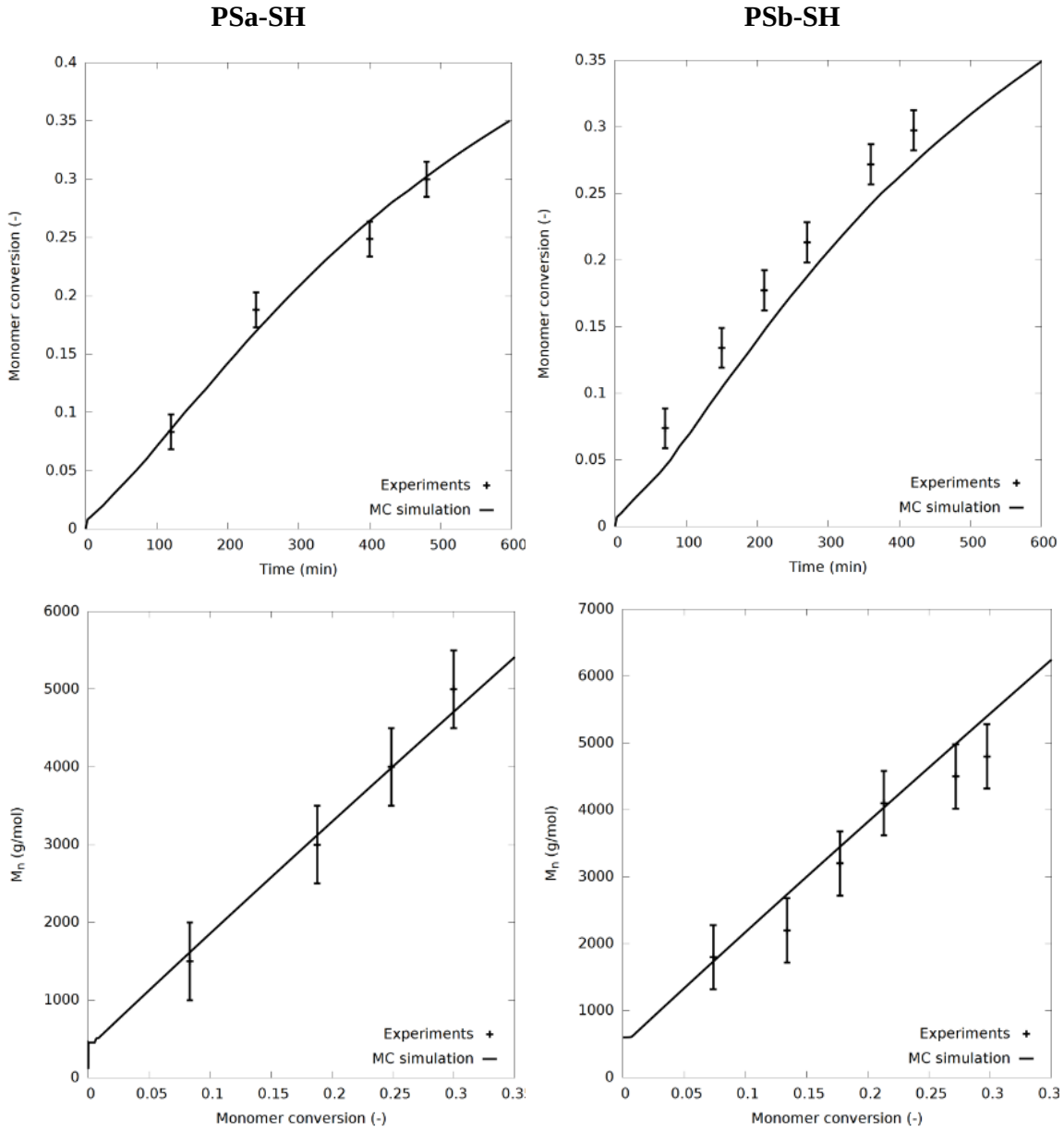

*Figure 8.6 – Comparison between the simulated (line) and the experimental (symbols) RAFT polymerization of styrene with DoPAT and **DoPAT-OBz** to achieve **PSa-SH** (left) and **PSb-SH** (right), respectively. Top: monomer conversion during time. Bottom: increasing of the molecular weight with the conversion.*

The SEC broadening for macromolecules is calculated as follows:

$$\sigma_{\mathrm{tot}}^2 = \sigma_{\mathrm{reac}}^2 + \sigma_{\mathrm{SEC}}^2 \qquad (8.10)$$

Where σ^2_{reac} is already considered during the simulation and it is associated with the molecular weight distribution of the synthesized polymer, while σ_{SEC} is relative to the Sec column and it is calculated according to eq. 8.11.

$$w_{\text{SEC}}(\log M) = \frac{1}{(2\pi)^{0.5}\sigma_{\text{SEC}}}\int_0^{+\infty} exp\left(-\frac{(log(M) - log(\widetilde{M}))^2}{2{\sigma_{\text{SEC}}}^2}\right) w(log\ \widetilde{M})\, dlog(\widetilde{M}) \qquad (8.11)$$

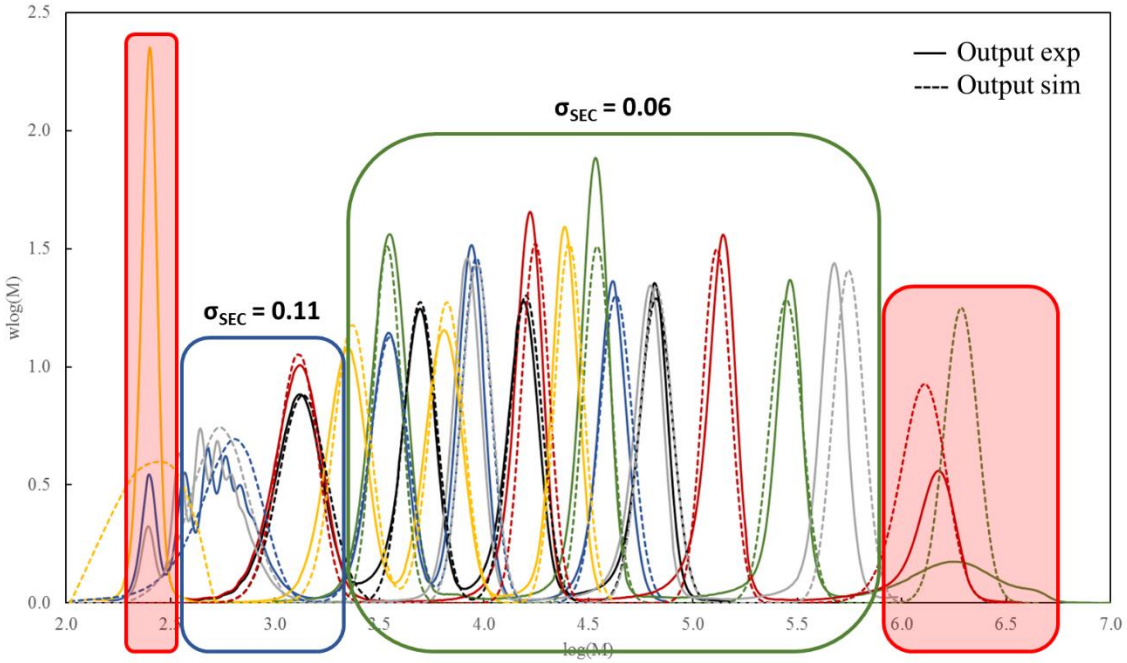

*Figure 8.7 – SEC broadening calculated for the polystyrene standards used to calibrate the THF SEC used for the kinetic study proposed in **Chapter 4**. The figure is reproduced from Ref. [189] with the permission of The Royal Society of Chemistry.*

(end of the *k*MC simulation section).

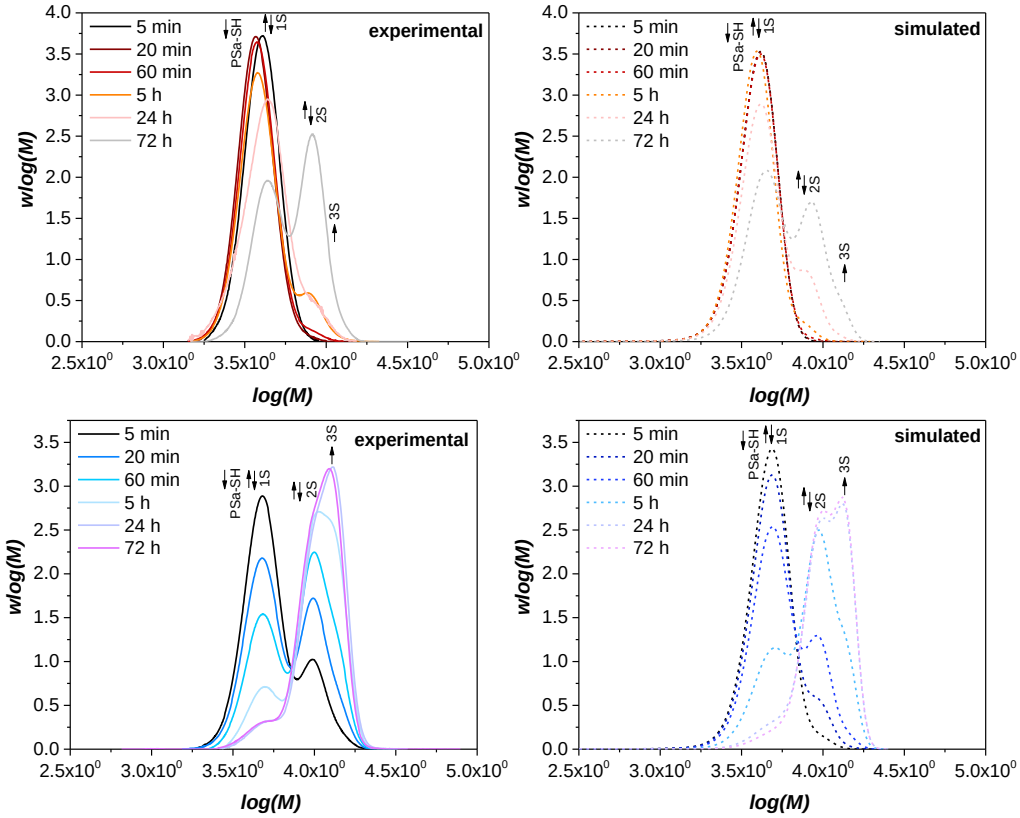

*Figure 8.8 – Experimental (full line) and simulated (dashed line) SEC traces for the PFTR reaction in THF (red) and DMF (blue) using **PSa-SH** and **3PFB**. (SH:PFB:DBU = 1:1:1, $[SH]_0$ = 0.075 g·mol^{-1}). The figure is reproduced from Ref. [189] with the permission of The Royal Society of Chemistry.*

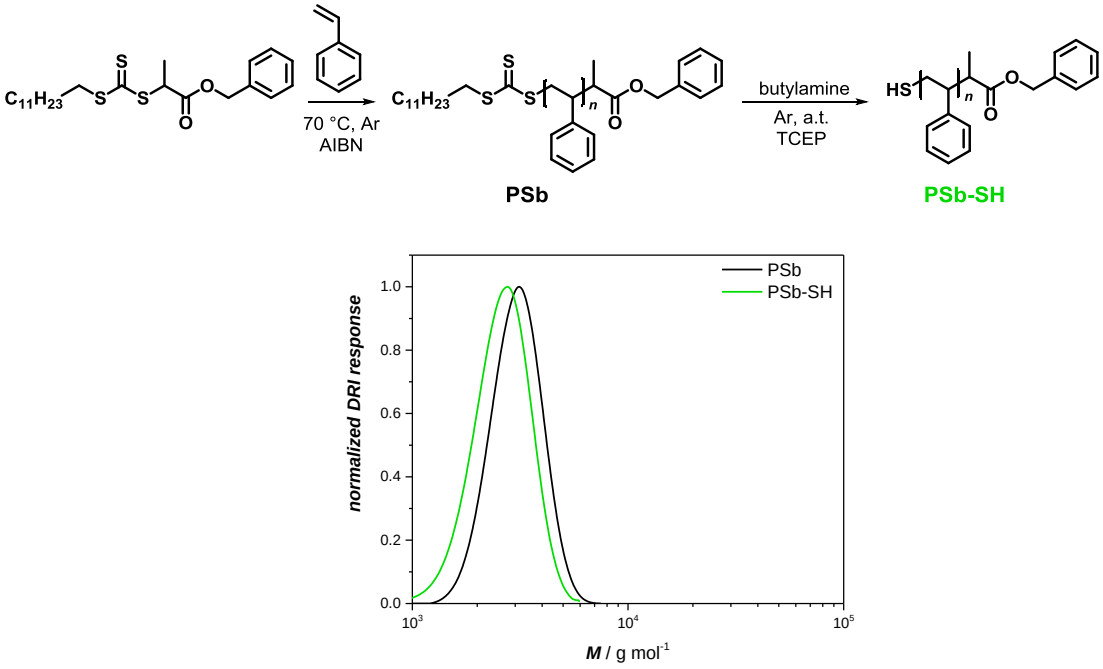

*Figure 8.9 – Top: Reaction scheme for the synthesis of **PSb** and **PSb-SH**. Bottom: SEC traces for **PSb** (black) and **PSb-SH** (green): The figure is reproduced from Ref. [189] with the permission of The Royal Society of Chemistry.*

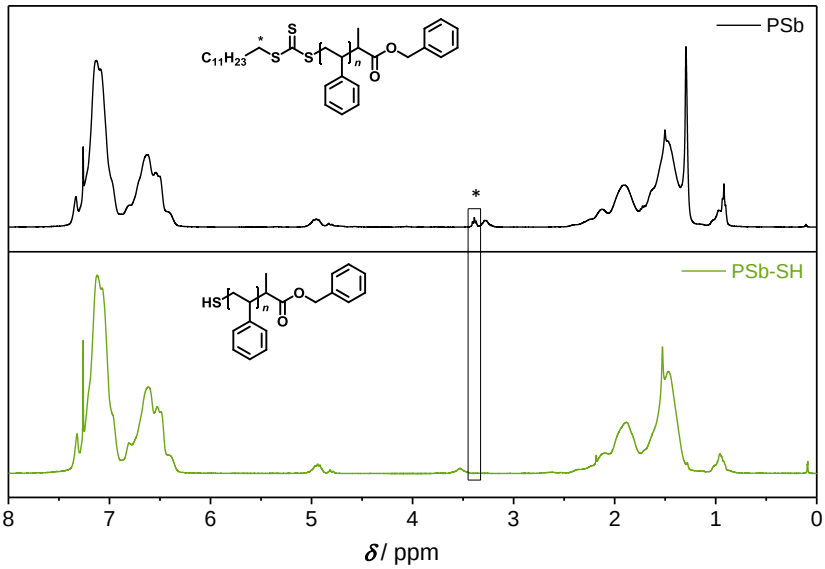

*Figure 8.10 – ^{1}H NMR spectra ($CDCl_3$, 400 MHz) spectra for **PSb** (black) and **PSb-SH** (green). In the box is highlighted the disappearance of the –CH_2- marked in the structure (*). δ = 7.50 – 6.20 (m, ArH), 2.5 – 0.50 (m, aliphatic H). The figure is reproduced from Ref. [189] with the permission of The Royal Society of Chemistry.*

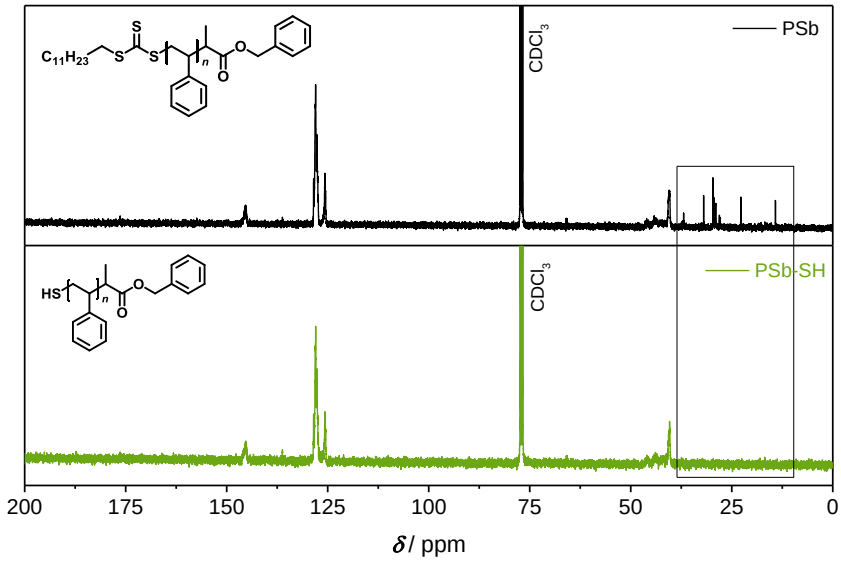

*Figure 8.11 – ^{13}C NMR spectra ($CDCl_3$, 101 MHz) for **PSb** (black) and **PSb-SH** (green). The disappearance of the resonances corresponding to the aliphatic carbon chain of the RAFT agent is highlighted with a box. δ = 145.43(C, quaternary carbon in the styrene aromatic ring), δ = 128.33 and δ = 125,52 (-HC=CH-, unsaturated carbons, styrene ring), and δ = 40.30 (aliphatic C, aliphatic polymer backbone). The figure is reproduced from Ref. [189] with the permission of The Royal Society of Chemistry.*

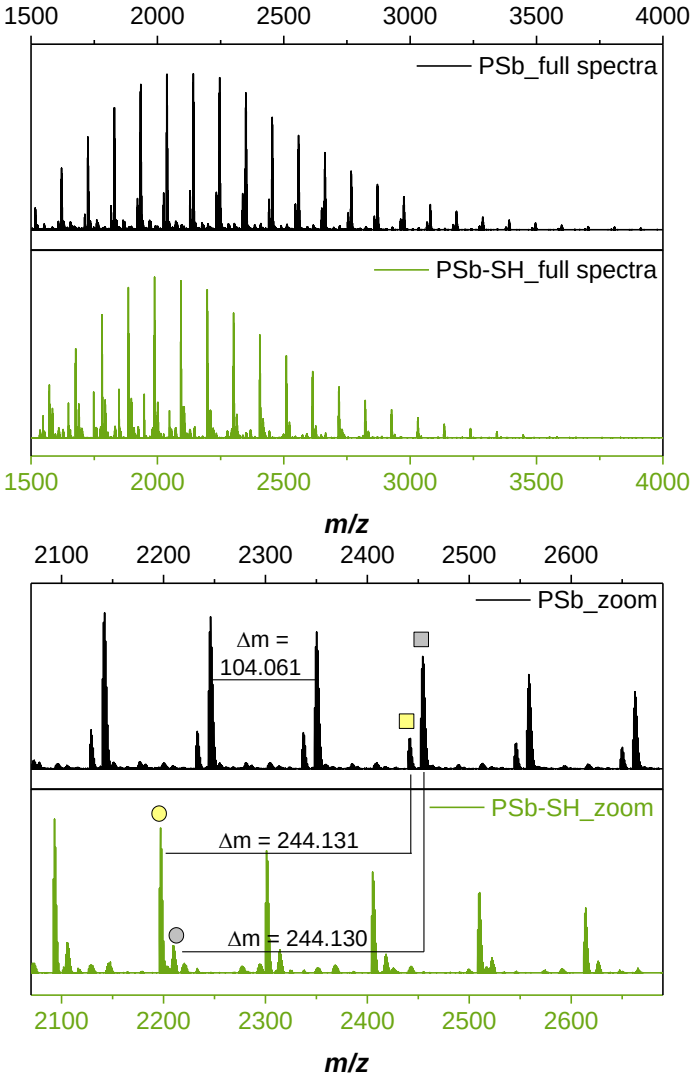

*Figure 8.12 – (−)ESI-MS spectra for **PSb** (black) and **PSb-SH** (green). Top: full spectra recorded in the region m/z = 1500-400. Bottom: zoom in a selected region of the spectra in order to highlight the Δm = 104.061, which refers to the styrenic monomer unit and Δm = 244.130 between **PSb** and **PSb-SH**, which refers to the loss of the aliphatic chain and the trithiocarbonate upon aminolysis. The figure is reproduced from Ref. [189] with the permission of The Royal Society of Chemistry.*

Table 8.5 – Comparison of the experimental and the theoretical m/z ratio for the peaks highlighted in Figure 8.12. The table is reproduced from Ref. [189] with the permission of The Royal Society of Chemistry.

	Structure	***n***	***m/z* (exp)**	***m/z* (theo)**	***Δm***
■	$[PSb + Cl]^-$	19	2454.3401	2454.3502	0.010
■	$[PSb + I]^-$	18	2442.2153	2442.2243	0.0090
●	$[PSb\text{-}SH + Cl]^-$	19	2209.2102	2209.2169	0.0067
●	$[PSb\text{-}SH + Cl]^-$	18	2197.0845	2197.0899	0.0054

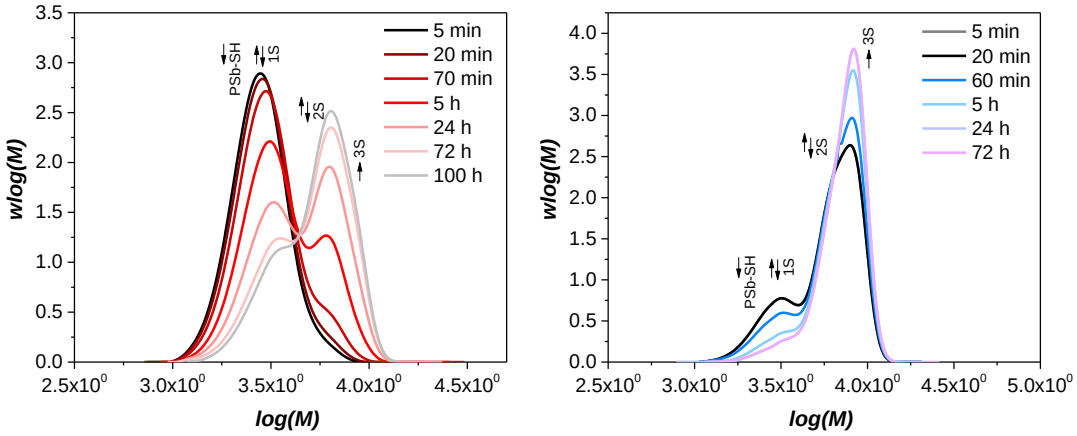

*Figure 8.13 – Experimental SEC traces for the PFTR reaction in THF (red) and DMF (blue) using **PSb-SH** and **3PFB**. (SH:PFB = 1:1, $[SH]_0$ = 0.075 g·mol^{-1}). The figure is reproduced from Ref. [189] with the permission of The Royal Society of Chemistry.*

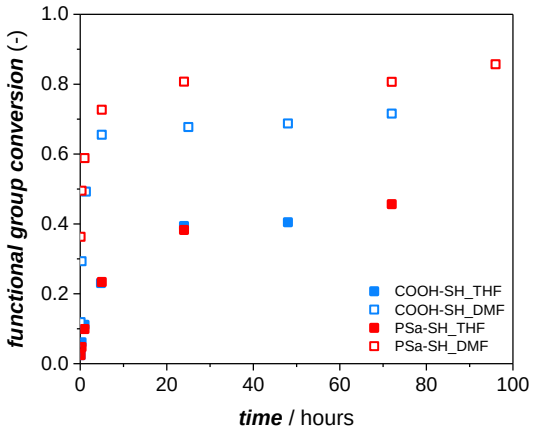

*Figure 8.14 – Experimental functional group conversion over time for the PFTR reaction using **3PFB** and either COOH-SH (blue) or **PSa-SH** (red) in THF (filled symbols) and DMF (empty symbols). (SH:PFB = 1:1 and $[SH]_0$ = 0.075 g·mol^{-1}). The figure is adapted from Ref. [189] with the permission of The Royal Society of Chemistry.*

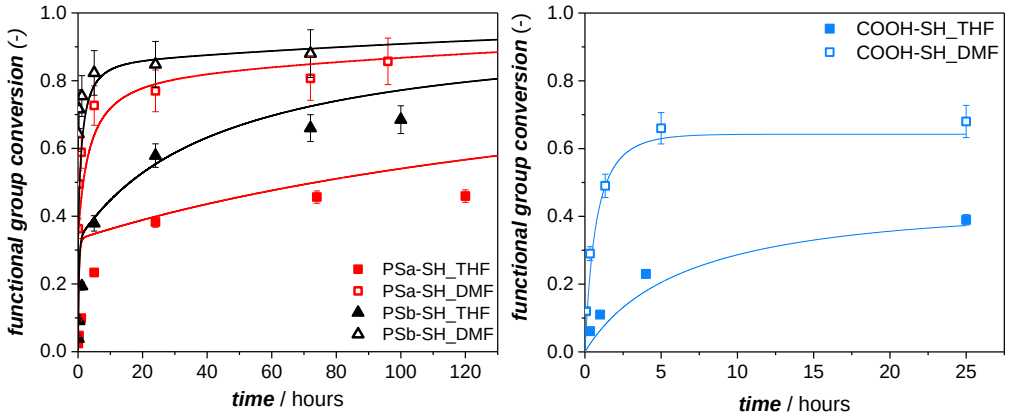

*Figure 8.15 – Comparison of the experimental (symbols) and simulated (line) functional group conversion over time for the PFTR in THF (full symbols) and DMF (empty symbols) (SH:PFB=1:1, $[SH]_0$ = 0.075 g·mol^{-1}). Left: The PFTR was performed using **3PFB** and either **PSa-SH** (red) or **PSb-SH** (black). Right: The PFTR was performed using **3PFB** and COOH-SH (blue). The figure is adapted from Ref. [189] with the permission of The Royal Society of Chemistry.*

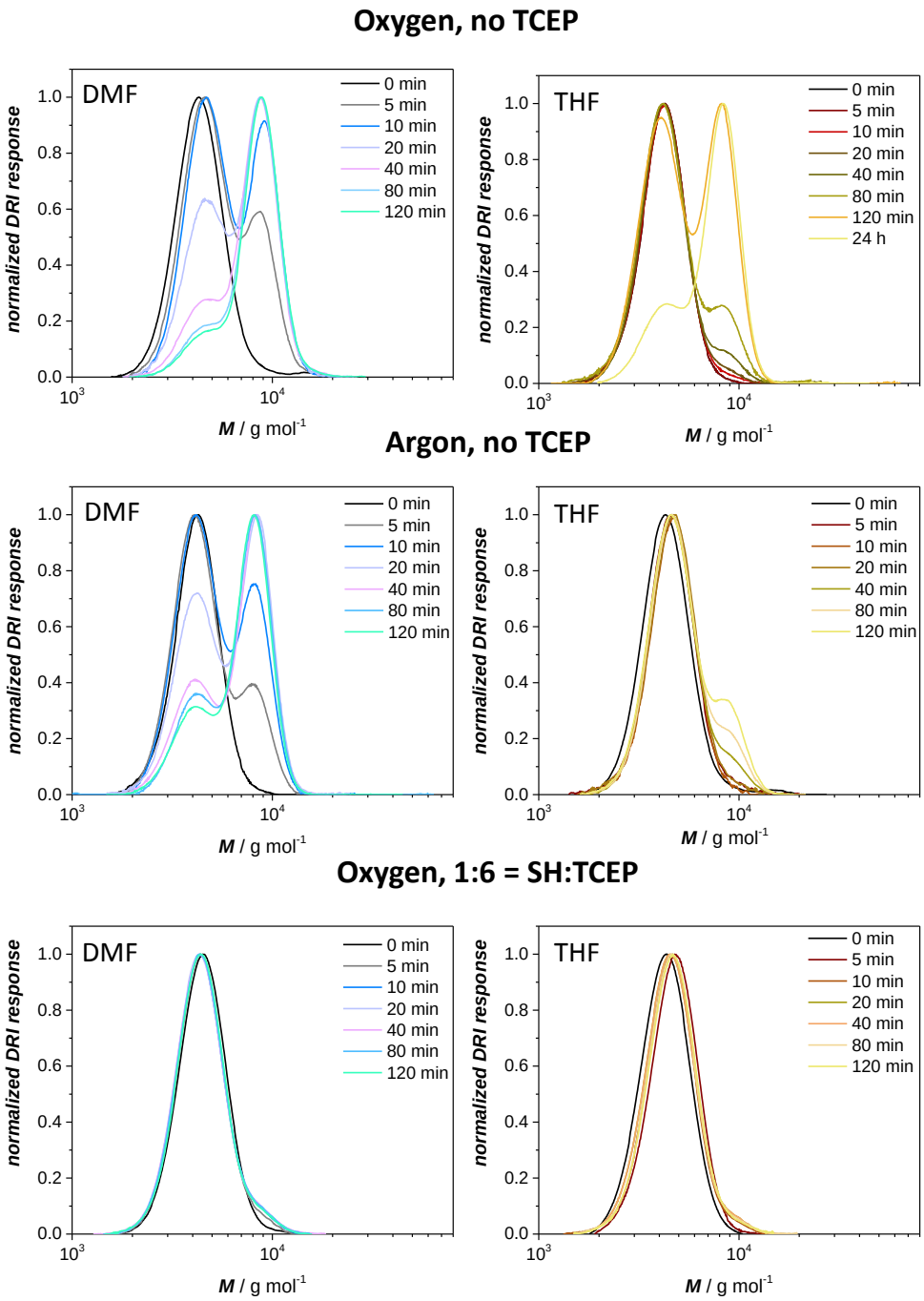

Figure 8.16 – SEC traces after investigation for the disulfide bond suppression. The reaction was performed using ***PSa-SH*** *as thiol derivative and a 1:15 molar ratio of SH:DBU, in different condition. Top: in the presence of oxygen and absence of TCEP. Middle: In the absence of oxygen (argon) and absence of TCEP. Bottom: in the presence of oxygen and 6eq. of TCEP with respect to the thiol groups.* $[SH]_0 = 0.037\ g{\cdot}mol^{-1}$. *The figure is reproduced from Ref. [189] with the permission of The Royal Society of Chemistry.*

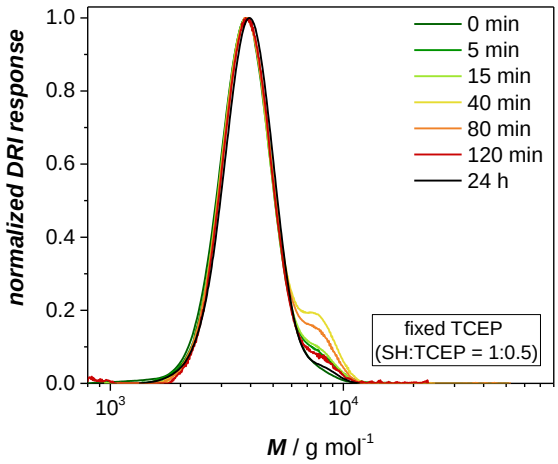

Figure 8.17 – SEC traces for the disulfide bond investigation in argon atmosphere, using a ratio of SH:TCEP = 1:1 and 15eq. of base (i.e. DBU). Aliquots of the reaction mixture were withdrawn at different intervals of time. After an initial phase, it is visible the cleavage of the disulfide bonds by the presence of the reducing agent. The figure is reproduced from Ref. [189] with the permission of The Royal Society of Chemistry.

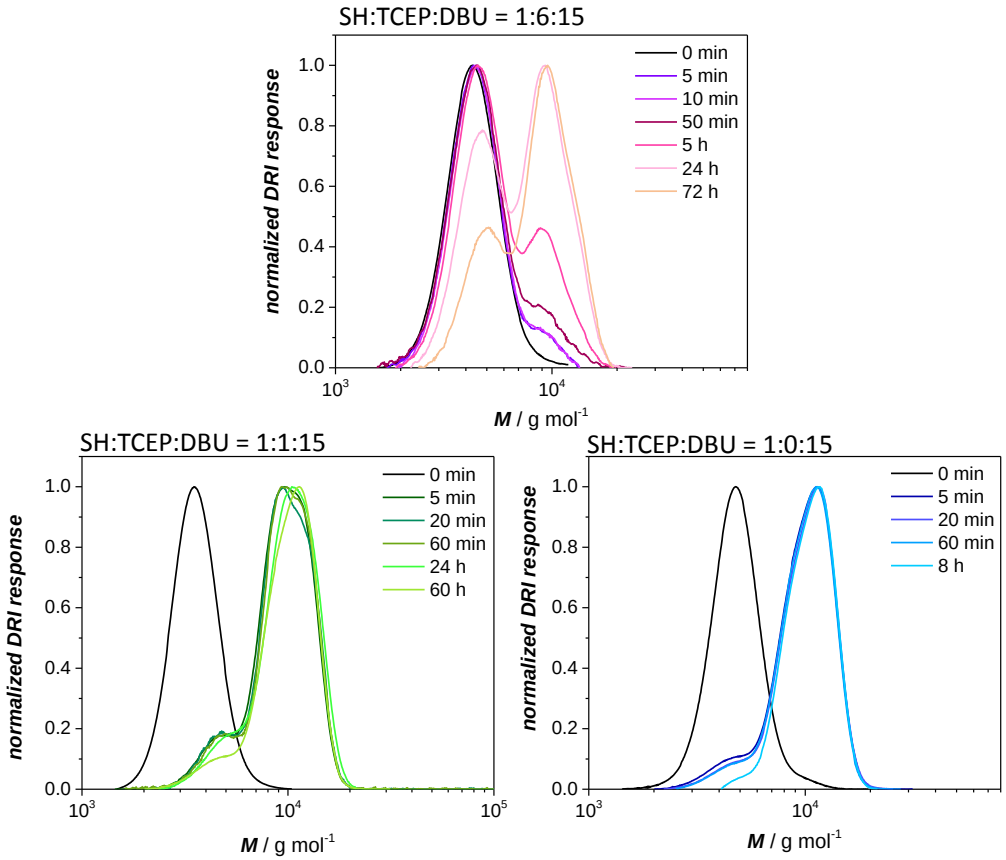

*Figure 8.18 – SEC traces for the PFTR reaction using **PSa-SH** and **3PFB** in DMF ($[SH]_0$ = 0.037 g·mol^{-1}). The molar ratio of SH:PFB:TCEP is stated in the legend, while the ratio of SH:DBU was fixed to 1:15. The figure is reproduced from Ref. [189] with the permission of The Royal Society of Chemistry.*

8.2 Appendix for Chapter 5

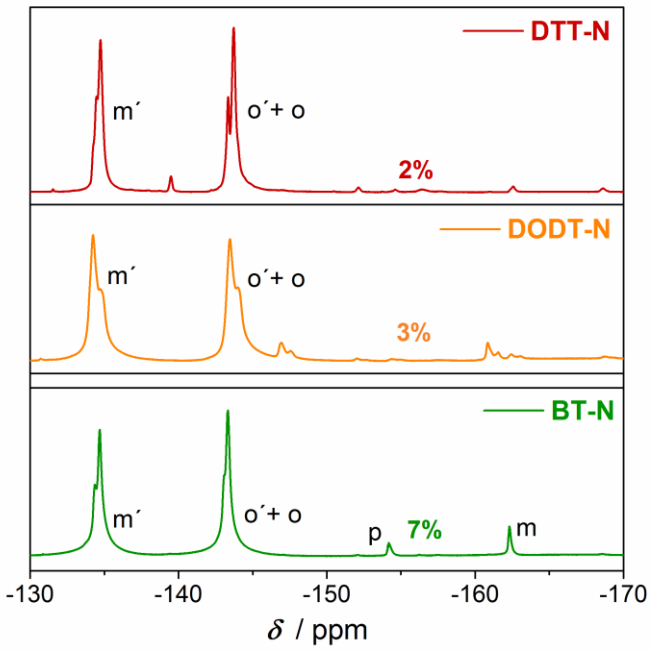

*Figure 8.19 – ^{19}F NMR spectra ($CDCl_3$, 377 MHz) for the networks obtained starting from small molecule bifunctional thiol derivatives and trifunctional fluorinated linker (**3PFB**). Thiol precursors: dithiothreitol (**DTT**), 2,2'-(Ethylenedioxy)diethanethiol (**DODT**) and butanedithiol (**BT**). The figure is adapted from Ref. [188] with the permission of The Royal Society of Chemistry.*

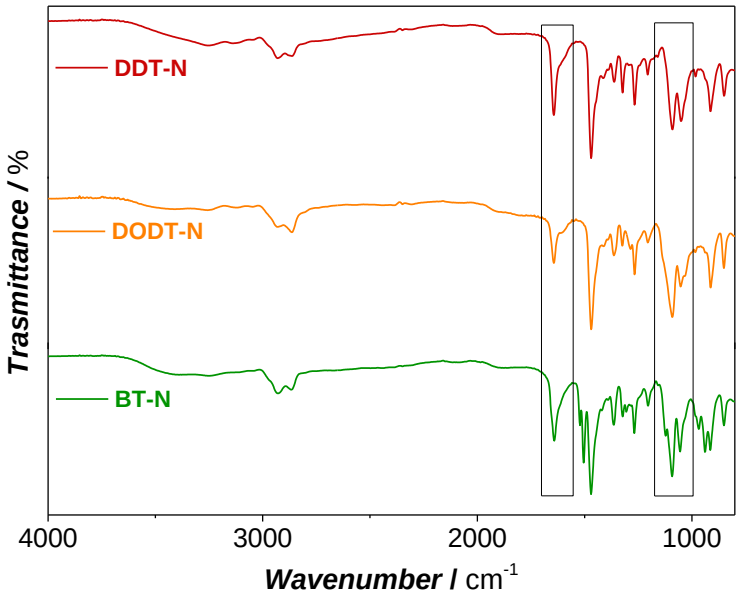

*Figure 8.20 – ATR-IR spectra for the networks obtained starting from small molecule bifunctional thiol derivatives and trifunctional fluorinated linker (**3PFB**). Thiol precursors: dithiothreitol (**DTT**), 2,2'-(Ethylenedioxy)diethanethiol (**DODT**) and butanedithiol (**BT**). The figure is adapted from Ref. [188] with the permission of The Royal Society of Chemistry.*

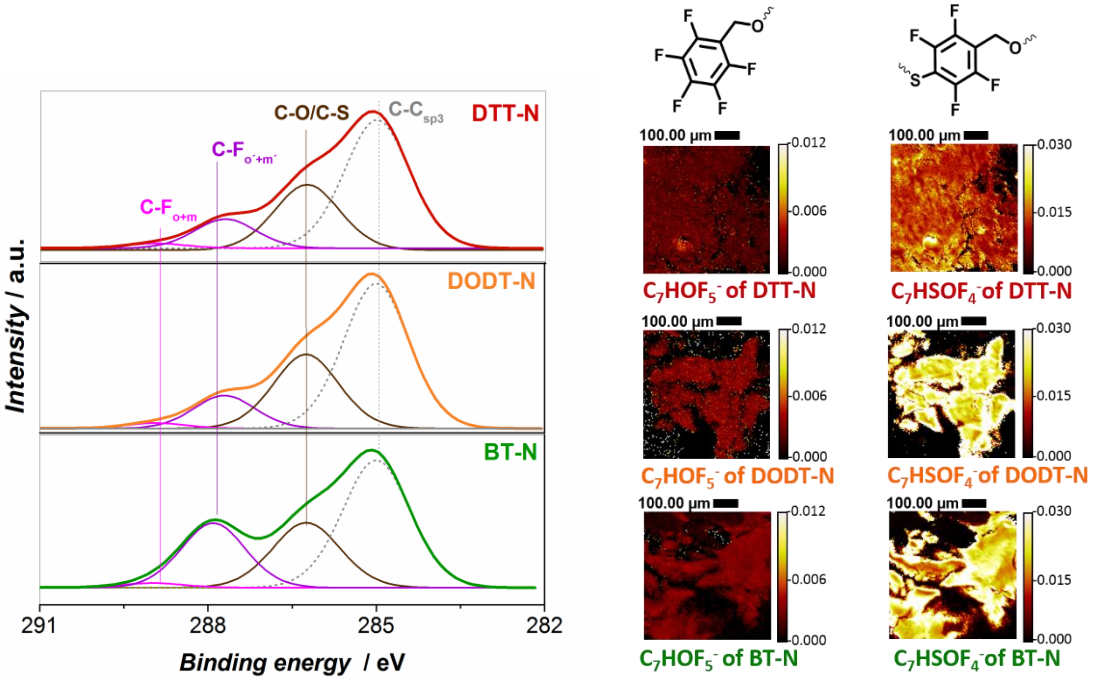

*Figure 8.21 – XP C1s (left) and ToF-SIMS (right) images for the networks obtained starting from small molecule bifunctional thiol derivatives and trifunctional fluorinated linker (**3PFB**). Thiol precursors: dithiothreitol (**DTT**), 2,2'-(Ethylenedioxy)diethanethiol (**DODT**) and butanedithiol (**BT**). The ToF-SIMS images show the relative abundance of the fragment before ($C_7HOF_5^-$) and after ($C_7HSOF_4^-$) PFTR. The figure is adapted from Ref. [188] with the permission of The Royal Society of Chemistry.*

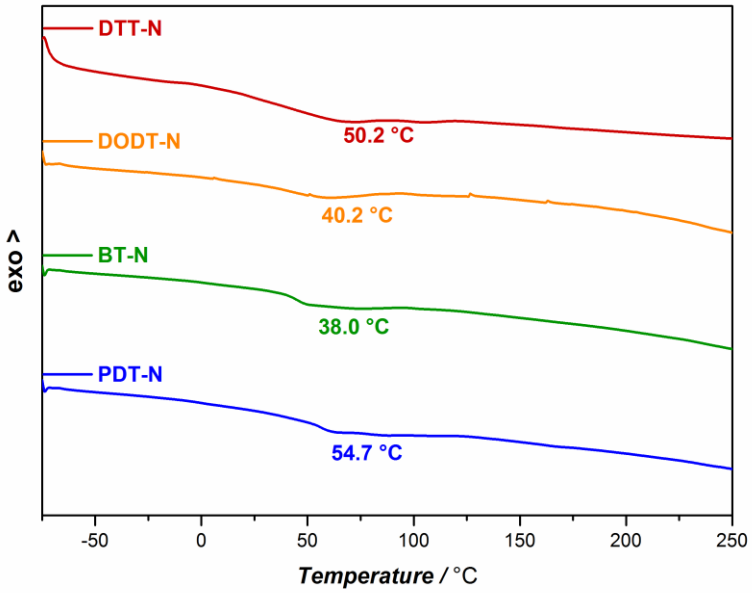

*Figure 8.22 – DSC curves for the networks obtained starting from small molecule bifunctional thiol derivatives and trifunctional fluorinated linker (**3PFB**). Thiol precursors: dithiothreitol (**DTT**), 2,2'-(Ethylenedioxy)diethanethiol (**DODT**), butanedithiol (**BT**) and 1,4-phenylenedimethanethiol (**PDT**). The figure is adapted from Ref. [188] with the permission of The Royal Society of Chemistry.*

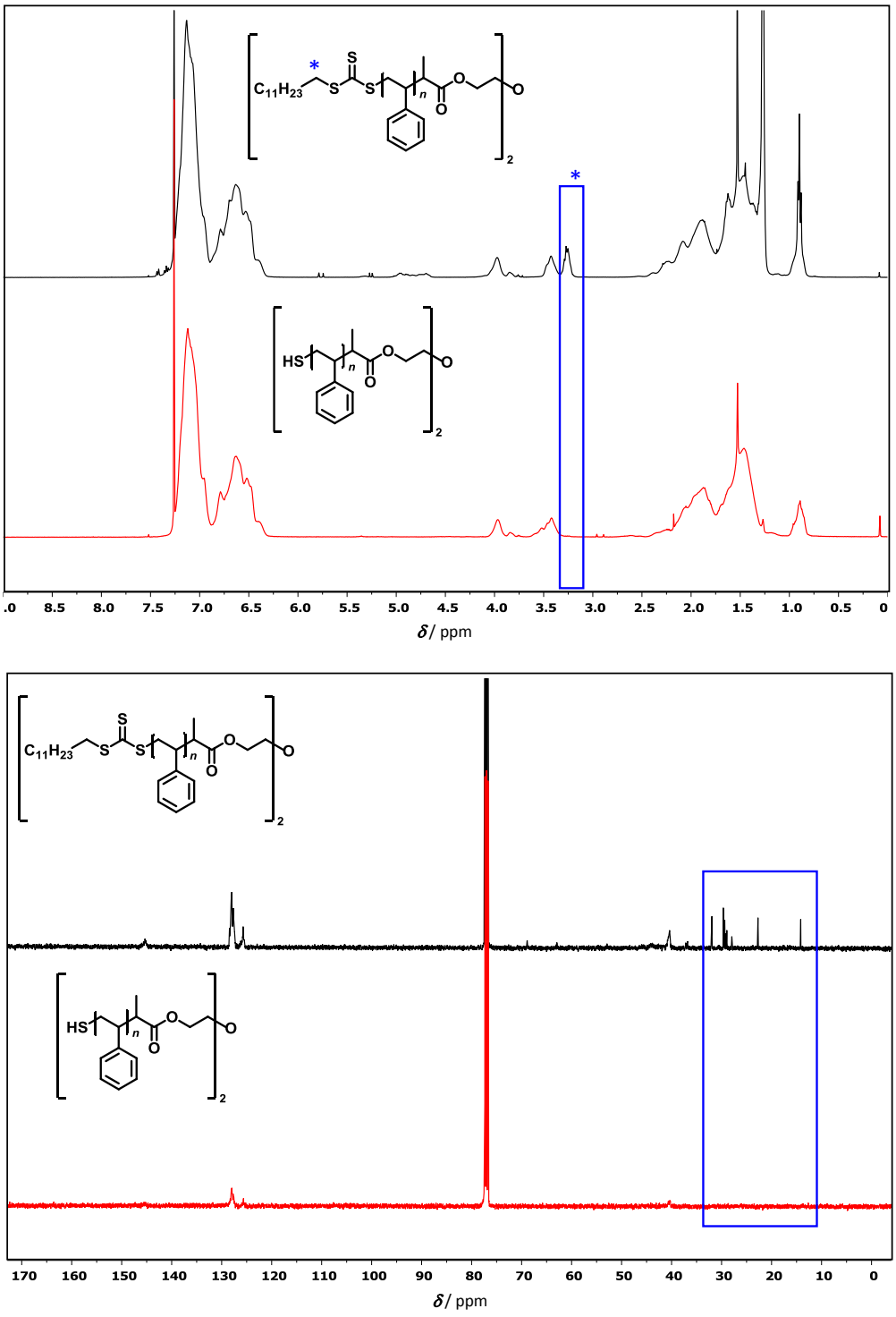

*Figure 8.23 – Top: ^{1}H NMR spectra ($CDCl_3$, 400MHz) for **PS(36)** (before aminolysis, black) and **biSH-PS(36)** (after aminolysis, red line). δ = 7.50 – 6.20 (m, ArH), 2.5 – 0.50 (m, aliphatic H). Bottom ^{13}C NMR spectra ($CDCl_3$, 101MHz) for **PS(36)** (before aminolysis, black) and **biSH-PS(36)** (after aminolysis, red line). δ = 145.4(C, quaternary carbon in the styrene aromatic ring), δ = 128.3 and δ = 125.5 (-HC=CH-, unsaturated carbons, styrene ring), and δ = 40.3 (aliphatic C, aliphatic polymer backbone) δ < 40 (aliphatic $C_{12}H_{25}$-adjacent to the trithiocarbonate moiety). In both cases: highlighted in the blue box is the diagnostic peaks confirming the removal of the aliphatic chain and the thiocarbonate moiety.*

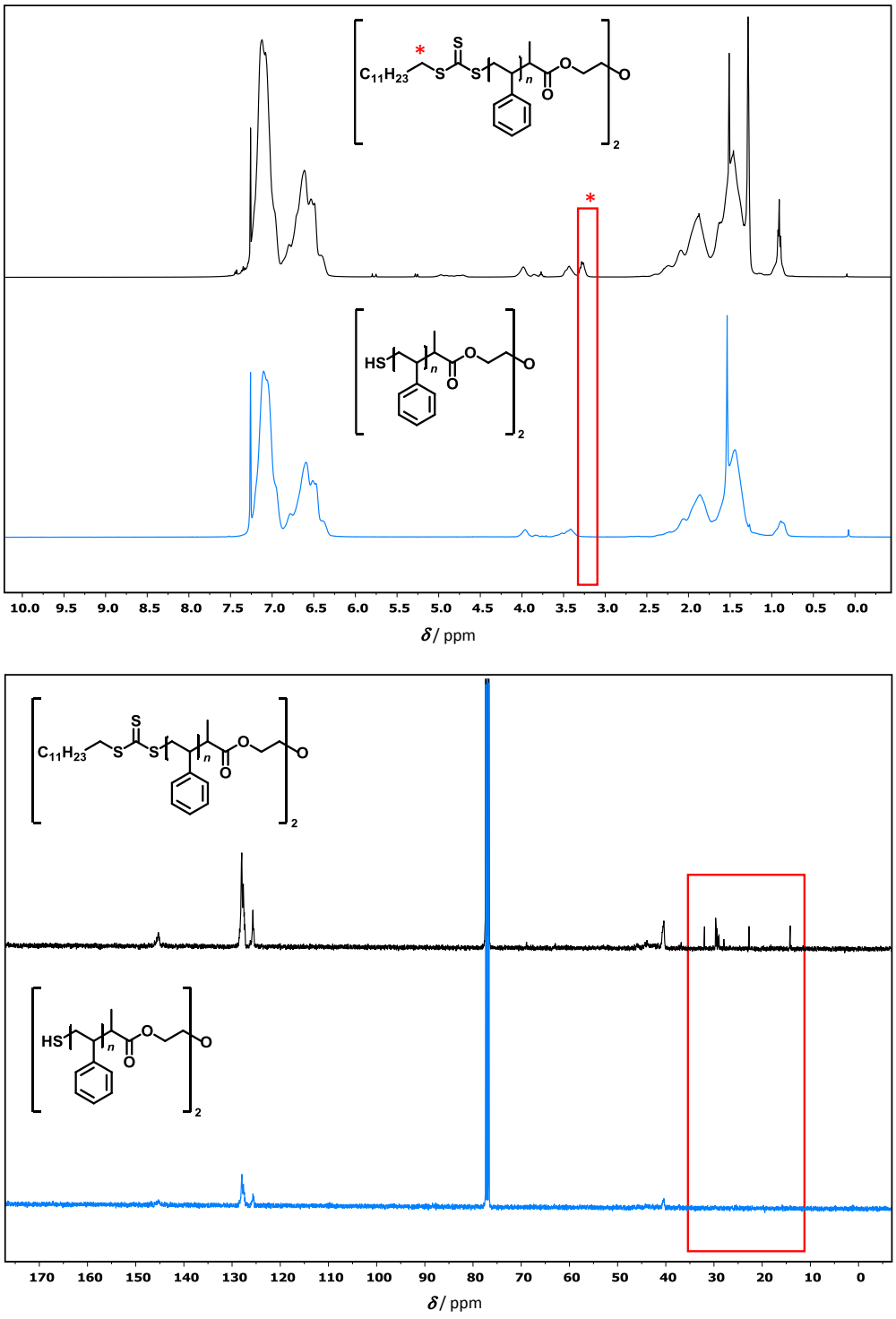

*Figure 8.24 – Top: ^{1}H NMR spectra ($CDCl_3$, 400MHz) for **PS(64)** (before aminolysis, black) and **biSH-PS(64)** (after aminolysis, blue line). δ = 7.50 – 6.20 (m, ArH), 2.5 – 0.50 (m, aliphatic H). Bottom: ^{13}C NMR spectra ($CDCl_3$, 101MHz) for **PS(64)** (before aminolysis, black) and **biSH-PS(64)** (after aminolysis, blue line). δ = 145.4(C, quaternary carbon in the styrene aromatic ring), δ = 128.3 and δ = 125.5 (-HC=CH-, unsaturated carbons, styrene ring), and δ = 40.3 (aliphatic C, aliphatic polymer backbone) δ < 40 (aliphatic $C_{12}H_{25}$- adjacent to the trithiocarbonate moiety). In both cases: highlighted in the blue box is the diagnostic peaks confirming the removal of the aliphatic chain and the thiocarbonate moiety.*

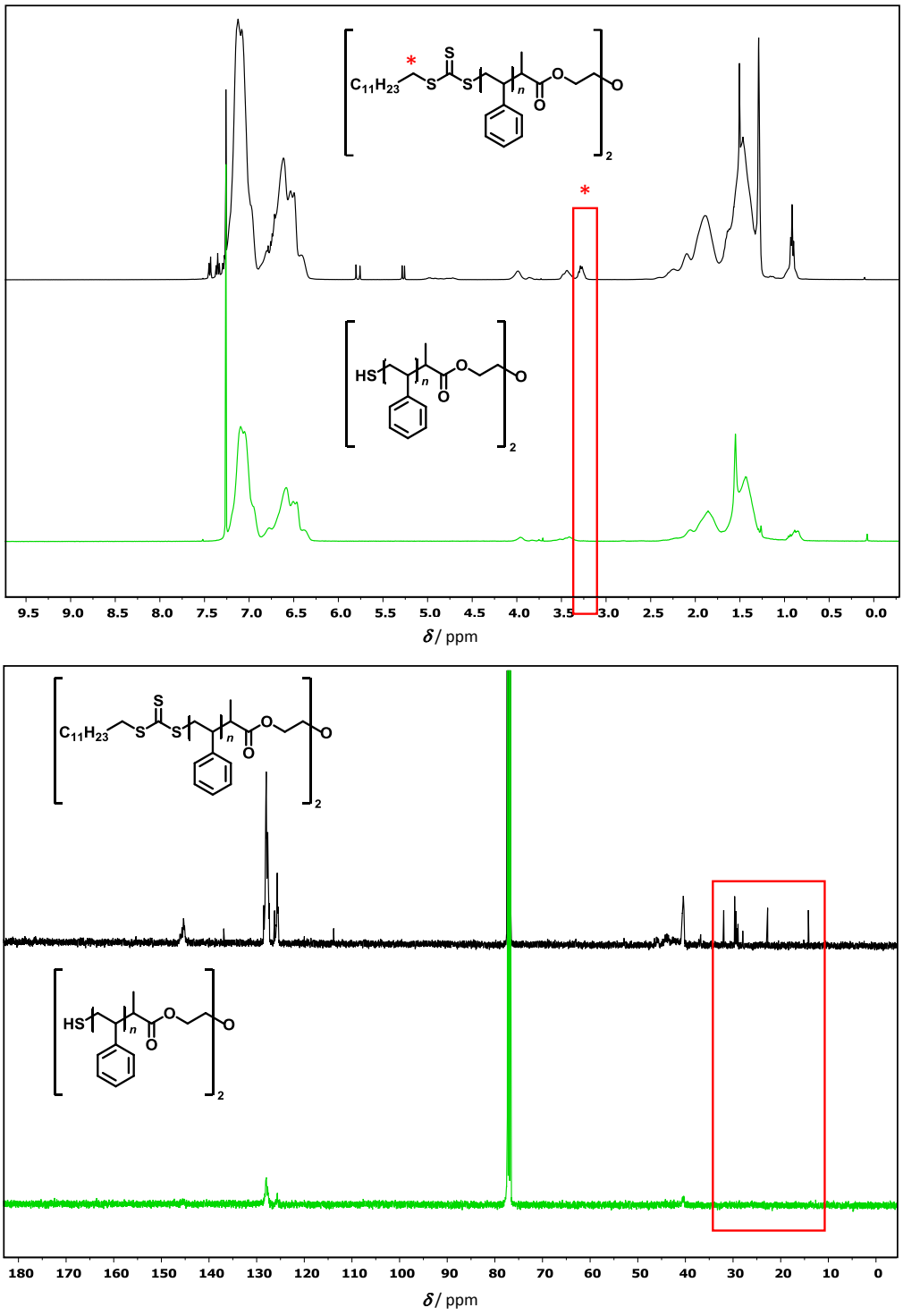

*Figure 8.25 – Top: ^{1}H NMR spectra ($CDCl_3$, 400MHz) for **PS(82)** (before aminolysis, black) and **biSH-PS(82)** (after aminolysis, green line). δ = 7.50 – 6.20 (m, ArH), 2.5 – 0.50 (m, aliphatic H). Bottom: ^{13}C NMR spectra ($CDCl_3$, 101MHz) for **PS(82)** (before aminolysis, black) and **biSH-PS(82)** (after aminolysis, green line). δ = 145.4(C, quaternary carbon in the styrene aromatic ring), δ = 128.3 and δ = 125.5 (-HC=CH-, unsaturated carbons, styrene ring), and δ = 40.3 (aliphatic C, aliphatic polymer backbone) δ < 40 (aliphatic $C_{12}H_{25}$- adjacent to the trithiocarbonate moiety). In both cases: highlighted in the blue box is the diagnostic peaks confirming the removal of the aliphatic chain and the thiocarbonate moiety.*

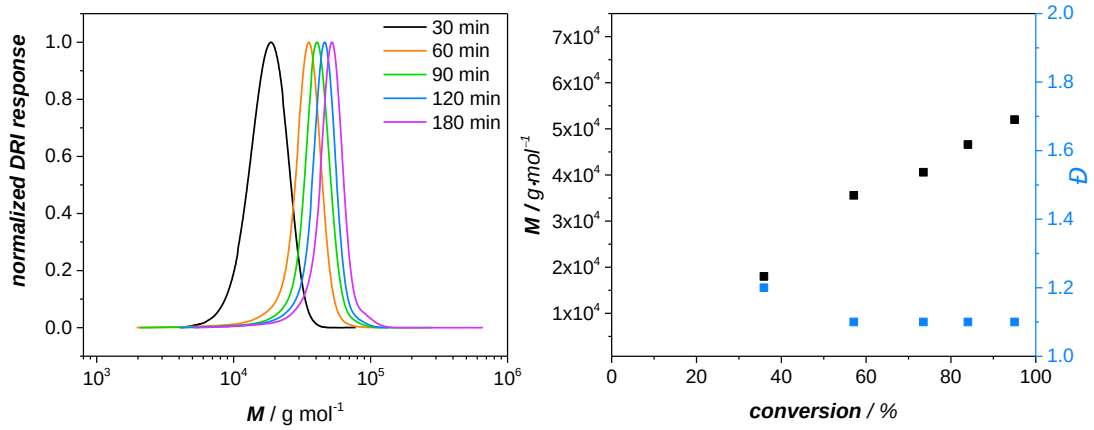

Figure 8.26 – Left: SEC traces recorded at different times during the polymerization of PTBMA. Right The molecular weight and the dispersity index (Đ) as determined via SEC are plotted against the concentration. A linear increase of M_n with the conversion, as well as low values for Đ, indicates a good control over the polymerization. DoPAT:TBMA:AIBN = 1:350:0.1 (molar ratio), T = 70 °C in toluene (50% w/w).

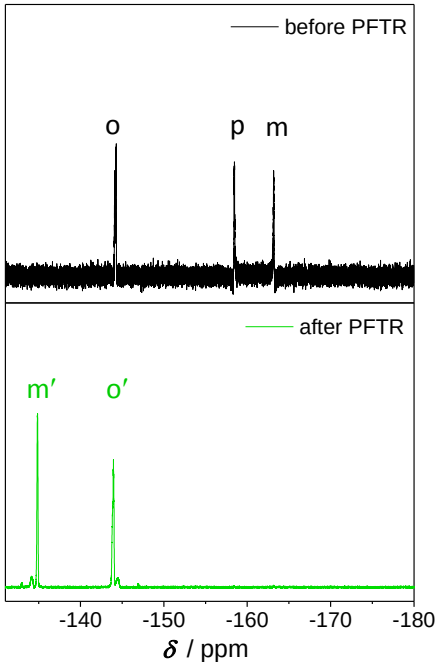

*Figure 8.27 – ^{19}F NMR spectra ($CDCl_3$, 377 MHz) of **biPFB-PS** before (black) and after (green) the PFTR reaction, performed between **biPFB-PS** and aliphSH using DBU as base (molar ratio of 1:1:1 = SH:PFB:DBU).*

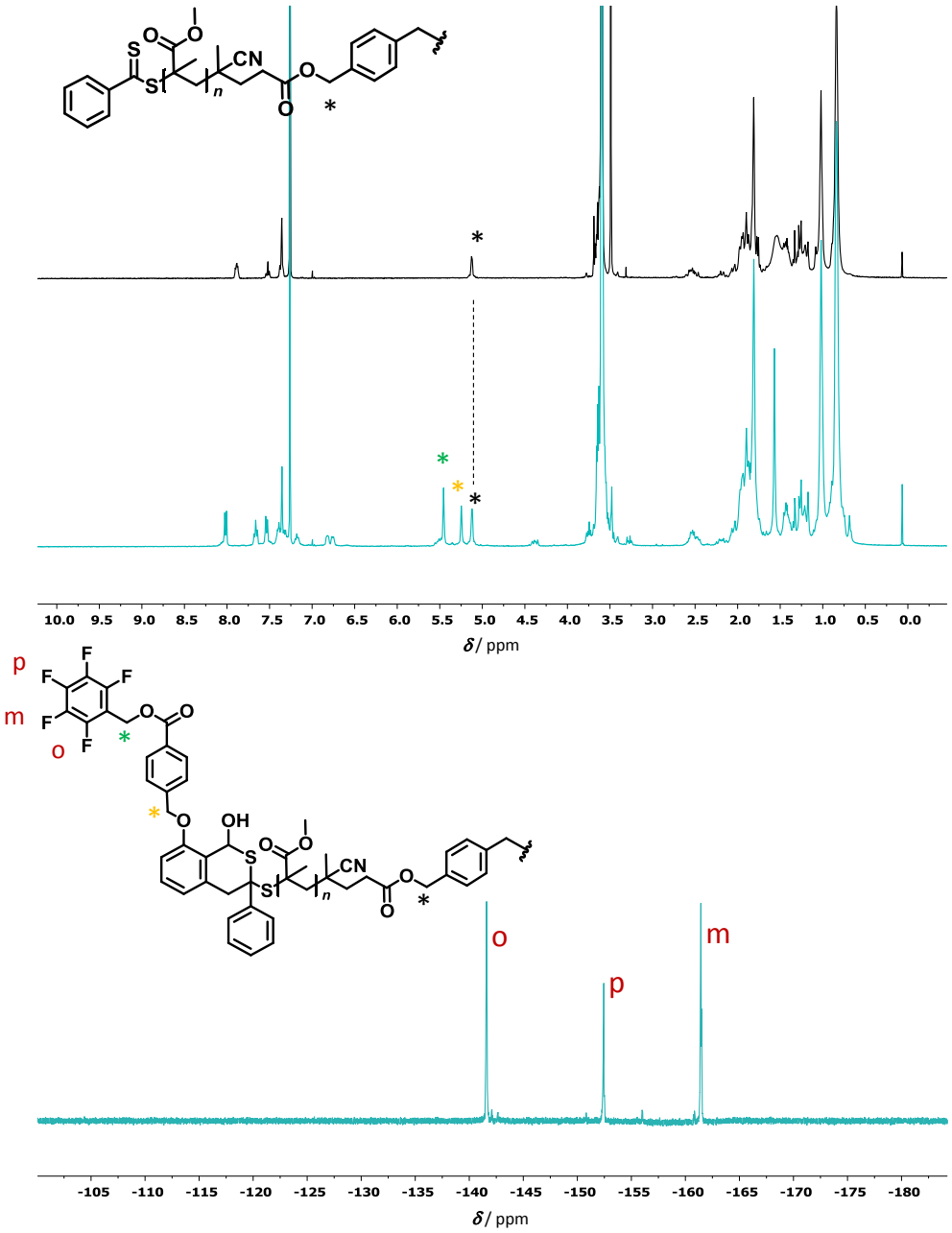

*Figure 8.28 – Top: ^{1}H NMR spectra ($CDCl_3$, 400 MHz) for **biPMMA** (before end-group capping, black) and **biPFB-PMMA** (after end-group capping, light blue line). Highlighted with colorful stars the protons diagnostic for the successful end-group functionalization. Bottom: ^{19}F NMR spectrum ($CDCl_3$, 377 MHz) for **biPFB-PMMA**, after end-group capping.*

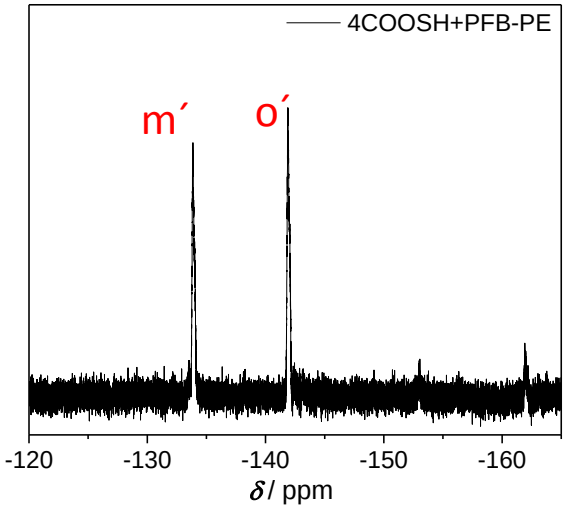

*Figure 8.29 – ^{19}F NMR spectrum ($CDCl_3$, 377 MHz) after PFTR reaction between 4COOSH and **PFB-PE**. SH:PFB = 1:1 stoichiometric ratio in DMF using TBAF (0.3eq.) as base.*

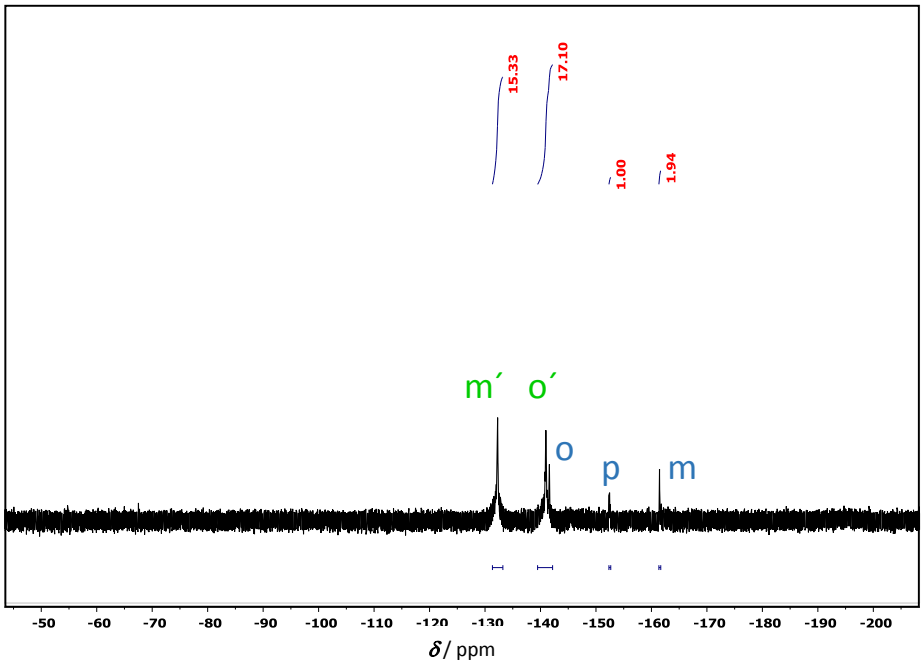

*Figure 8.30 – ^{19}F NMR spectrum ($CDCl_3$, 377 MHz, gel phase) of the poly(methacrylate) network obtained after PFTR reaction between **biPFB-PMMA** and 4phenSH, using a molar ratio of SH:PFB:Et_3N = 1:1:1 at 40 °C in DMF (300 mg·mL^{-1}).*

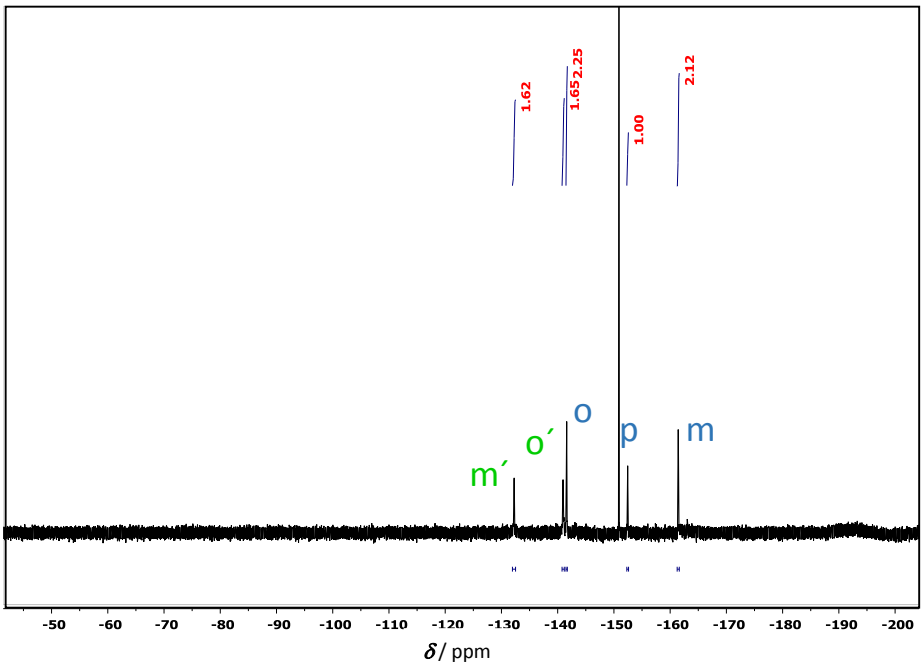

*Figure 8.31 – ^{19}F NMR spectrum ($CDCl_3$, 377 MHz) of the extractables of the poly(methacrylate) network obtained after PFTR reaction between **biPFB-PMMA** and 4phenSH, using a molar ratio of SH:PFB:Et_3N = 1:1:1 at 40 °C in DMF (300 mg·mL^{-1}).*

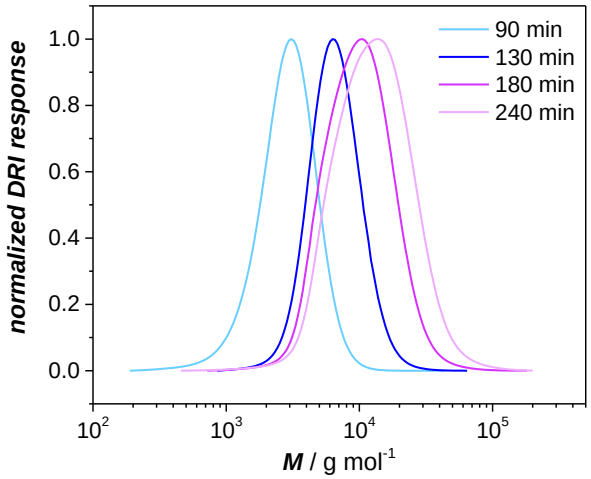

Figure 8.32 – SEC traces (aqueous SEC) after the polymerization of acrylic acid (AA) performed in dioxane (50% w/w ratio) and 70 °C using CTACOOH as RAFT agent in a stoichiometric ratio of 1:300 (CTA-COOH:AA).

Table 8.6 – Summary of the molecular weight and the dispersity index of the poly(acrylic acid) polymer reported in Figure 8.32

Reaction time / min	M_n / g·mol^{-1}	$Đ$
90	2500	1.3
130	5900	1.2
180	8400	1.3
240	10000	1.4

List of Abbreviations

Chemicals

AA	Acrylic acid
aliphSH	Dodecanethiol
AIBN	Azobis(isobutylnitril)
ATR-IR	Attenuated Total Reflectance - Infrared Spectroscopy
ATRP	Atom transfer radical polymerization
benzSH	4-Methoxy-α-toluenethiol
BA	Benzoic acid
BT	1,4-Butanedithiol
$CDCl_3$	Deuterated chloroform
CH	cyclohexane
COOH-SH	Thiolactic acid
CTA	Chain transfer agent
CPMG	Carr-Purcell-Meiboom-Gill (NMR pulse sequence)
DAc	1,3-Butanediol diacrylate
DBU	1,8-Diazabicyclo[5.4.0]undec-7-ene
DCM	Dichloromethane
DDT	Dithioerythritol
DEG	Diethyleneglycol
DIPEA	*N*,*N*-Diisopropylethylamine
DODT	2,2′-(Ethylenedioxy)diethanethiol
DoPAT	2-(((Dodecylthio)carbonothioyl)thio)propanoate
DMAP	4-Dimethylaminopyridine
DMF	*N*,*N*-dimethylformamide
DMSO	Dimethylsulfoxide
DSC	Differential scanning calorimetry
EDC	*N*-(3-Dimethylaminopropyl)-N′-ethylcarbodiimide
ELS	End-linking strategy
ESI-MS	Electron Spray Ionization Mass Spectroscopy
Et_3N	Triethylamine

FRP	Free radical (co)polymerization
*h*DA	Hetero Diels Alder
ILT	Inverse laplace transformation
*k*MC	Kinetic Monte Carlo
LVE	Linear viscoelastic (regime)
MA	Methyl acrylate (monomer)
MMA	Methyl methacrylate (monomer)
MBA	*N,N'*-methylenebisacrylamide (crosslinking agent)
MeOH	Methanol
MSE	Magic sandwich echo
NDS	Network disassembly strategy
NMR	Nuclear magnetic resonance
NMP	Nitroxide-mediated radical polymerization
PAA	Poly(acrylic acid)
PCT	Phase transfer catalysis
PDT	1,4-Phenylenedimethanethiol
phenSH	thiophenol
PFB	Pentafluoro benzyl
PFP	Pentafluoro phenyl
PFTR	*para*-fluoro–thiol reaction
PMMA	Poly(methyl methacrylate)
PS	Polystyrene
PSA	Poly(sodium acrylate)
RAFT	Reversible addition-fragmentation chain transfer
RDRP	Reversible-deactivation radical polymerization
SA	Sodium acrylate
SAP	Superabsorbent polymers
SEC	Size exclusion chromatography
sec-aliphSH	2-Butanethiol
sec-benzSH	1-Phenylethyl mercaptan
SR	Salt rejected
TBABr	Tetrabutylammonium bromide
TBAF	Tetrabutylammonium fluoride
TBAOH	Tetrabutylammonium hydroxide
TCEP	tris(2-carboxy-ethyl)phosphine

THF	Tetrahydrofuran
ToF-SIMS	Time-of-Flight Secondary Ion Mass Spectrometry
TRITT	*S*,*S*-di((2-methyl)propionic acid) trithiocarbonate
V-501	4,4'-Azobis(4-cyanovaleric acid
XPS	X-Ray Photoelectron Spectroscopy
XX4	Special phase cycling for CPMG pule sequence
XY16	Special phase cycling for CPMG pule sequence
4phenSH	Tetrathioltetraphenylmethane
4COOSH	Pentaerythritol tetrakis(3-mercaptopropionate)

Physical quantities

M_n	Number average molecular weight
M_w	Weight average molecular weight
$Đ$	Dispersity index
μ_{el}	Number of crosslinks
υ_{el}	Number of elastic chains
M_c	Molecular weight of the elastic chain
f	Functionality of the crosslinker
ξ	Cycle rank
DC	Degree of crosslinking
DN	Degree of neutralization
ΔG	Free energy of mixing
χ	Flory-Huggins (interaction) parameter
$\Delta\mu_{mix}$	Mixing contribution to the chemical potential
$\Delta\mu_{el}$	Elastic contribution to the chemical potential
$\Delta\mu_{ion}$	Electrostatic contribution to the chemical potential
N_A	Avogadro's number
m	Mass
m_0	Mass of dry polymer
Q_{eq}	Degree of swelling at equilibrium (w/w ratio)
q	Degree of swelling at equilibrium, theoretical (v/v ratio)
Q_{syn}	Degree of swelling during network formation (w/w ratio)
q_c	Degree of swelling during network formation (v/v ratio)
G^*	Complex shear modulus (rheology)

$G´$	Storage modulus (rheology)
$G´´$	Loss modulus (rheology)
$\tan(\delta)$	Loss factor (rheology)
T_2	Transverse relaxation (time) in NMR
ρ	Density
V	Volume
R	Reaction rate
k	Rate coefficient
X_n	Degree of polymerization

List of Figures

Figure 1.1 – General overview of the projects presented in the current thesis. Chapter 3: RAFT-mediated network formation as an advanced synthetic route for the control of the crosslinking process (compared to conventional polymer network formation via FRP). Chapter 4: In-depth investigation on PFTR for optimizing the reaction conditions using a (simplified) polymer model system. Chapter 5: Network formation via PFTR with precise characterization of PFTR-related traceable defects.....3
Figure 2.1 – Classification of RAFT agents in four different classes according to their chemical structures: dithioesters, trithiocarbonates, dithiocarbamates and xanthates. 13
Figure 2.2 – Guidelines for an appropriate RAFT agent selection, divided into the selection for R and Z groups, seperately. Solid lines represent good control over the polymerization, while dotted lines indicate poor control. List of abbreviations: MMA (methylmethacrylate), VAc (vinyl acetate), NVP (N-vinylpyrrolidone) and NVC (N-vinyl carbazole). The figure is adapted from "S. Perrier, Macromolecules **2017**, 50, 7433-7447".[46].....14
Figure 2.3 – Chemical structure of the two commercially available RAFT agents possessing a carboxylic acid group employed in **Chapter 5**. 16
Figure 2.4 – The influence of the different electronegativity of H and F on the electron density of the aromatic ring. In example benzene (left) and hexafluorobenzene (right). The electronegative values are in agreement with the relative scale of electronegativity of Pauling.[79].....19
Figure 2.5 – Examples of different polymer architectures: a linear chain (left), a branched polymer (middle) and a polymer network (right). 25
Figure 2.6 – Left: the definition of elastic chain (ν_{el}), cycle rank (ξ) and junction having functionality f are depicted for an ideal network. Right: defects such as dangling chains (1), cyclic loops (2) and intermolecular entanglements (3) are highlighted for a real network. 26
Figure 2.7 – The mixing (dashed lines) and the elastic term (solid lines) for polystyrene networks are depicted. For the mixing term (equation 2.20) the χ value is varied according to the legend. For the elastic term (equation 2.21) f = 4, so that A = 0.5 (phantom model), while q_c = 4 and the density of the elastic chain is determined by the degree of crosslinking (DC), which is varied according to the legend. 31
Figure 2.8 - Overview of the different strategies for the synthesis of polymer networks. In details, polymerization of a mono- and bi- unsaturated monomer via (a) free radical polymerization or (b) reversible-deactivation radical polymerization (RDRP), e.g. RAFT polymerization. (c) Synthesis of networks starting from pre-made polymer precursors: curing and end-linking approach. In both case the polymer chain is reacted with a small molecule acting as a crosslinking agent. 32
Figure 2.9 – Left: parent gel obtained via crosslinking reaction between the polymer containing the thrithiocarbonate moiety and the complementary linker. Right: newly synthesized network obtained after introduction of the new monomer (green) in the parent gel via RAFT polymerization. The figure is adapted from reference "M. Chen, Y. Gu, A. Singh, M. Zhong, A. M. Jordan, S. Biswas, L. T. J. Korley, A. C. Balazs, J. A. Johnson, ACS Central Science, **2017**, 3, 124−134."[154]. 36
Figure 2.10 – Fluoroscent network and susbsequent cleavage of the network after degradation of the trithiocarbonate moiety present on the elastic chain (green square). The quantification of the crosslinking point is achieved by measuring the fluorescence of the resulting solution and comparison with an appropriate calibration curve. The figure is

adapted from reference "D. Estupiñán, C. Barner-Kowollik, L. Barner, Angew. Chem. Int. Ed. **2018**, 57, 5925-5929.".[157] 37
Figure 2.11 – Left: Representation of the concept used for the quantification of the amount of primary loops within the network. Right: Plot correlating the value of the [LLL]:[LLS] ratio to the fraction of primary loops based on the statistical analysis of the soluble fractions after degradation. The figure is adapted from "H. Zhou, J. Woo, A. M. Cok, M. Wang, B. D. Olsen, J. A. Johnson, PNAS, **2012**, 109, 19119−19124".[18] 39
Figure 2.12 – Left: Full T_2-relaxation curve for a poly(sodium acrylate) network with DC = 3. Right: Deconvolution of the relaxation decay by using Inverse Laplace Transformation (ILT) showing the distribution of the relaxation rates $1/T_2$. 40
Figure 2.13 – Swelling for polyelectrolytes in contact with a salt solution. Herein, the uncharged water molecules can freely enter the network but the mobile ions are partially rejected due to the fixed charges present on the network structure (electrostatic repulsion). The figure is adapted from "Höpfner et al., Prog. Coll. Polym. Sci. **2013**, 140, 247". [183] 46
Figure 2.14 - Practical realization of the desalination based on a discontinuous three step approach using polyelectrolyte networks. 1. The dry hydrogel is placed in contact with the solution to swell until equilibrium is reached. 2. Removal of the supernatant phase enriched in salt content. 3. An external pressure is applied to recover the desalinated water from within the hydrogel matrix. The figure is adapted from "Höpfner et al., Prog. Coll. Polym. Sci. **2013**, 140, 247". [183] 46
Figure 3.1 –Theoretical charge distribution in a network having an inhomogeneous (left) and homogeneous (right) microstructure. 50
Figure 3.2 – Representation of the crosslinking process via FRP (top) or RAFT (bottom) polymerization between a mono- (blue) and a bifunctional (red) monomer, in the presence of initiator (green). The RAFT agent is represented by a yellow circle (bottom) but for simplicity not reported in the growing chains, while the polymer by the solid black lines. In a first approximation the overlap between the polymer chains is considered as a crosslinking point, independently of its nature (backbiting reaction, entanglement or crosslinking agent). The figure is adapted from "Henkel R., Vana P., Macromol. Chem. Phys. **2014**, 215, 182−189". [149] 51
Figure 3.3 – Top: Reaction scheme for the synthesis of poly(methyl acrylate) via RAFT polymerization. Bottom: SEC traces after polymerization using different molar ratios of RAFT agent (DoPAT) to monomer. The molar ratio used in each case is stated in the legend. 52
Figure 3.4 –The visual feedback for the network formation during the crosslinking reaction was obtained by twisting the vial upside down at selected intervals of time. The number on the vial corresponds to the reaction time (in minutes) at which the polymerization was stopped. Top: conventional free radical polymerization (FRP). Bottom: RAFT-mediated polymerization using 0.10 mol% of RAFT agent (DoPAT). 54
Figure 3.5 – SEC traces obtained at different conversion values for the crosslinking reaction between MA and DAc via FRP 55
Figure 3.6 – SEC traces obtained at different conversion values for the crosslinking reaction between MA and DAc via RAFT polymerization using 0.10 mol% of DoPAT. 56
Figure 3.7 – SEC traces obtained at different conversion values for the crosslinking reaction between MA and DAc via RAFT polymerization using 0.17 mol% of DoPAT. 56
Figure 3.8 – Comparison of the SEC traces obtained at 3% (left) and 50% (right) conversion during the crosslinking reaction between MA and DAc via FRP (gray) and RAFT polymerization with 0.10 (violet) and 0.17 (light blue) molar percentages of RAFT agent (DoPAT). 57
Figure 3.9 – Top: Reaction scheme for the RAFT polymerization of acrylic acid (AA) employing TRITT as RAFT agent. Bottom: SEC traces after RAFT polymerization performed using different molar ratio of TRITT:AA (reported in the legend). The results refer to a reaction time of 3 h (full conversion) 59
Figure 3.10 – Reaction mixture after the polymerization of AA (t = 16 h) in the presence of the crosslinking agent (MBA, 1 molar %) either via conventional free radical (FRP, first

vial on the left side) or RAFT polymerization using different amount of RAFT agent (yellow solutions). The molar ratio of RAFT agent:monomer used is reported on the vials. 61
Figure 3.11 – Theoretical number of crosslinking points per chain when using a molar ratio (TRITT:AA) of 1:100 (left), 1:200 (middle) and 1:400 (right). The crosslinking points are represented by vertical solid lines, while the RAFT agent is represented by the yellow circle. 61
Figure 3.12 – Increased number of crosslinking points per chain when using a molar ratio (TRITT:AA) of 1:200 and DC = 1 (left) or DC = 2 (right). The crosslinking points are represented by vertical solid lines, while the RAFT agent is represented by the yellow circle. 62
Figure 3.13 – Influence of the degree of neutralization (DN) on the swellability. The effect was studied on **FRP-DC1** as representative network. 63
Figure 3.14 - T_2 relaxation curve (left) and deconvoluted decay, using the Inverse Laplace Transformation, (ILT, right) for PSA hydrogels having DC = 1 and synthesized either via FRP or RAFT polymerization using different amount of RAFT agent (see legend). 65
Figure 3.15 – Absolute value of the complex modulus $|G^*|$(filled symbols) and the loss factor (tan (δ)) (empty symbols) for poly(acrylic acid) hydrogels in the "as prepared" state, synthesized via FRP (0% RAFT agent) or RAFT polymerization using different molar percentage of RAFT agent, as indicated along the x axis. 66
Figure 3.16 – Degrees of swelling, expressed as mass ratio, for poly(acrylic acid) hydrogels presenting different degree of crosslinking (DC) and synthesized via FRP polymerization (black symbols) or RAFT polymerization using 0.1 (red symbols) or 0.25 (orange symbols) molar percentage of RAFT agent. 67
Figure 3.17 – Left: T_2 relaxation curve (left) and deconvoluted decay using the inverse Laplace Transformation, (ILT, right) for poly(acrylic acid) hydrogels synthesized via RAFT polymerization (filled symbols) using 0.1 (top) or 0.25 (bottom) mol % of TRITT. In both cases the results are compared with an analogous network (same DC) but synthesized via FRP (empty symbols). 69
Figure 3.18 – Absolute value of the complex modulus $|G^*|$(filled symbols) and the loss factor (tan (δ)) (empty symbols) for networks synthesized either via FRP (black) or RAFT polymerization using 0.10 mol% of TRITT (red). 70
Figure 3.19 – Salt rejection experiments for networks synthesized via FRP or RAFT polymerization. The experimental results (symbols), expressed as percentage of salt rejected, are compared to theoretical values obtained from the Donnan theory (lines). 73
Figure 4.1 – Left: SEC traces of the crude reaction mixture at t = 0 (black) and t = 5 min (blue). Right: (+)ESI-MS spectrum of the reaction after 5 min is depicted. The peak were assigned according to the products shown in Scheme 4.1. The figure is adapted from Ref. [188] with the permission of The Royal Society of Chemistry. 78
Figure 4.2 – ^{1}H NMR spectra ($CDCl_3$, 400 MHz) of the reaction mixture at t = 0 and t = 5 min. The spectrum after 5 min of reaction is shown as crude reaction mixture (second panel) and after purification (bottom panel). Additionally, the ^{1}H NMR spectrum for the DBU-BA adduct is reported as guideline for the peak assignment. Mainly the shift of the resonance identified as **1** from δ = 2.68 ppm to δ = 2.95 ppm implies the success of the PFTR. The figure is adapted from Ref. [188] with the permission of The Royal Society of Chemistry. 79
Figure 4.3 – ^{19}F NMR spectra ($CDCl_3$, 377 MHz) of the fluorinated aromatic ring before (black) and after (blue)PFTR. Before reaction (black, **3PFB**) the resonances for the meta- (m), para- (p) and ortho- (o) fluorine atoms are present. After PFT reaction (blue) the new ortho- (o′) and meta- (m′) resonances appear. The comparison of the intensity of the resonances before and after reaction is used for calculating the conversion according to Equation

4.1. The figure is adapted from Ref. [188] with the permission of The Royal Society of Chemistry. 80
Figure 4.4 – Influence of time and concentration on the PFTR performed using an initial molar ratio of SH:PFB:DBU equal to 1:1:1. Left: The initial concentration is equal to 0.15 M in THF and the time is reported in the legend. Right: The reaction time is set to 5 min and the different concentrations tested are reported in the legend. The figure is adapted from Ref. [188] with the permission of The Royal Society of Chemistry. 81
Figure 4.5 – SEC (left) and ^{19}F NMR spectra (right, $CDCl_3$, 377 MHz) before and after PFTR employing 3PFB and either an equimolar (blue) or an excess (red) of aliphSH. The molar ratio of SH:base is kept equal to 1:1 and the $[PFB]_0 = 0.5$ M in both cases. The reported data refer to the analysis of the reaction mixture after 1 h of reaction time. The figure is adapted from Ref. [188] with the permission of The Royal Society of Chemistry. 82
Figure 4.6 – Experimental (left) and simulated (right) SEC traces for the disulfide bond formation for aliphSH. The reaction is performed with an initial ratio SH:DBU = 1:1 in THF ($[thiol]_0 = 0.15$ mol·L^{-1}). The fluorinated linker was not included in the reaction mixture in order to exclusively assess the rate coefficient of the side reaction. The figure is adapted from Ref. [189] with the permission of The Royal Society of Chemistry. 84
Figure 4.7 – a. Experimental and simulated data are compared in terms of functional group conversion over time. b. Simulated product spectrum showing the variation of the absolute concentration of each species over time during PFTR c. Experimental and d. Simulated SEC traces at selected intervals of time showing the evolution of each specie according to the product spectrum (b). The PFTR reaction was performed at ambient temperature, with an initial ratio SH:PFB:DBU = 1:1:1 and $[thiol]_0 = 0.075$ mol·L^{-1} in THF. The figure is adapted from Ref. [189] with the permission of The Royal Society of Chemistry. 85
Figure 4.8 – List of small molecules thiol derivatives used for the kinetic study. From left to right 4-methoxy-α -toluenethiol (benzSH), 1-phenylethyl mercaptan (sec-benzSH), dodecanethiol (aliphSH) and 2-butanethiol (sec-aliphSH). 86
Figure 4.9 – Experimental (left) and simulated (right) SEC traces for the reaction of disulfide bond formation for benzSH. The reaction is performed using an initial ratio SH:base = 1:1 and a concentration of $[thiol]_0 = 0.15$ mol·L^{-1} The figure is adapted from Ref. [189] with the permission of The Royal Society of Chemistry. 86
Figure 4.10 – Comparison of the functional group conversion over time for structurally different small molecule thiol derivatives during PFTR. The figure is adapted from Ref. [189] with the permission of The Royal Society of Chemistry. 87
Figure 4.11 – Chemical structure of the two fluorinated linkers used to investigate the selectivity of the nucleophilic aromatic substitution when the pentafluoro phenyl (left) or benzyl (right) group is directly connected to an ester group (**3aromCOOPFP** and **3aromCOOPFB**, respectively). 88
Figure 4.12 – ^{19}F NMR spectra ($CDCl_3$, 377 MHz) of the **3aromCOOPFP** (left) and **3aromCOOPFB** linker (right) before and after PFTR (black and blue line, respectively). In each case, the ^{19}F NMR spectra of either the pentafluoro phenol (bottom panel, left) or pentafluoro benzyl alcohol (bottom panel, right) is reported for facilitating the peak assignment in case of cleavage of the fluorinated group. 89
Figure 4.13 – Left: Functional group conversion over time for the reaction between aliphSH and either **3PFB**, **3COOPFB** or **4COOPFB**. Right: Chemical structure for **3PFB, 3COOPFB** and **4COOPFB**. The reactions were performed using an initial molar ratio of SH:PFB:DBU = 1:1:1 and $[thiol]_0 = 0.075$ mol·L^{-1}. 90
Figure 4.14 – Top: reaction scheme for the synthesis of the polymeric thiol derivative **PSa-SH**. Bottom: SEC traces (left) and the corresponding (−)ESI-MS spectra (right) for **PSa** (black) and **PSa-SH** (red). For the ESI-MS spectra: $\Delta m = 104.061$, corresponds to the mass of the styrene and $\Delta m = 244.126$ indicate the loss of the aliphatic chain and the trithiocarbonate upon aminolysis. The figure is adapted from Ref. [189] with the permission of The Royal Society of Chemistry. 93

Figure 4.15 – Experimental (left) and simulated (right) SEC traces for the disulfide bond formation employing **PSa-SH** as polymeric thiol derivative and using an initial molar ratio of SH:DBU = 1:1 and $[thiol]_0$ = 0.075 mol·L^{-1} in THF (red, 24h) or DMF (blue). The figure is adapted from Ref. [189] with the permission of The Royal Society of Chemistry. . 94
Figure 4.16 – Top: Functional group conversion over time for PFTR performed employing **PSa-SH**, an initial molar ratio of SH:PFB:DBU = 1:1:1 and $[thiol]_0$ = 0.075 mol·L^{-1} in either THF (red) or DMF (blue). Bottom: Experimental SEC traces at selected intervals of time (see legend) for the PFTR in THF (left) or DMF (right). The figure is adapted from Ref. [189] with the permission of The Royal Society of Chemistry. 95
Figure 4.17 – Left: experimental and simulated functional group conversion over time for PFTR employing **PSa-SH** and **3PFB** using a molar ratio of SH:PFB:DBU = 1:1:1 in DMF. The blue solid line refers to the simulation accounting for disulfide bond formation, while the red dashed line to the case where no disulfide are considered. Right: simulated product spectrum for the same reaction, obtained via kMC simulations, highlighting the concentration of each specie over time during the considered PFTR reaction. The figure is adapted from Ref. [189] with the permission of The Royal Society of Chemistry. . 96
Figure 4.18 Chemical structure for **PSa-SH** and **PSb-SH**, the two polymeric thiol derivatives used in this section. The label **a** and **b** serve as a reminder of the acid or benzylic group present as second chain-end. 97
Figure 4.19 – Functional group conversion over time for **PSa-SH** (red squares) or **PSb-SH** (black triangles) in either THF (full symbols) or DMF (empty symbols). In each case a molar ratio of 1:1:1 between thiol:PFB:base and a $[thiol]_0$ = 0.075 mol·L^{-1} was employed. The figure is adapted from Ref. [189] with the permission of The Royal Society of Chemistry. 98
Figure 4.20 – Functional group conversion over time for a polymeric (red) and a small molecule (blue) thiol derivative, both containing a free carboxylic acid group as second chain end. The reaction was performed in both THF (full symbol) and DMF (empty symbol) using a ratio SH:PFB:base equal to 1:1:1 (square) or 1:1:15 (triangle). The excess of base is applied only to **PSa-SH**. The figure is adapted from Ref. [189] with the permission of The Royal Society of Chemistry. 99
Figure 4.21 – Left: experimental SEC traces for the evolution of disulfide bond formation after 1 h of reaction time when the reaction was performed using **PSa-SH** and different equivalents of base, as reported in the legend (SH:DBU = 1:15, $[thiol]_0$ = 0.037 mol·L^{-1} in DMF). Right: functional group conversion over time for PFTR using a molar ratio of SH:PFB:DBU = 1:1:15 and different amount of TCEP as highlighted in the legend ($[thiol]_0$ = 0.037 mol·L^{-1} in DMF). The figure is adapted from Ref. [189] with the permission of The Royal Society of Chemistry..... 101
Figure 4.22 – ^{19}F NMR spectrum ($CDCl_3$, 377 MHz, left) and SEC traces (right) for the para-fluoro–thiol reaction between **PSa-SH** and **1COOPFB**. The ^{19}F NMR spectrum was recorded after24 h of reaction time (~66%), while the SEC traces are reported for different reaction times and present no evidence of disulfide formation. The figure is adapted from Ref. [189] with the permission of The Royal Society of Chemistry. ... 103
Figure 4.23 – a. Full (−)ESI-MS spectra for **PSa-PFB** recorded in the range m/z = 1500-4000. b. Comparison between experimental and simulated isotopic pattern for **PSa-PFB** having n = 23 repeating units. c. Chemical structure of **PSa-PFB**, product of the PFTR reaction between **PSa-SH** and **1COOPFB**. d. comparison between the experimental and the simulated m/z ratio for a selected peak in the double (blue triangle) and single charged (red square) region of the (−)ESI-MS spectrum reported in Figure 4.23a. The figure is adapted from Ref. [189] with the permission of The Royal Society of Chemistry. ... 104
Figure 4.24 – Functional group conversion over time for PFTR using aliphSH and **3COOPFB** (SH:PFB = 1:1) and either 0.5. (left) or 0.1 eq. (right) of base. In detail, each plot report the result for. TBAOH (green), TBAF (red), TBABr (orange) and DBU (blue). The reaction was performed using $[thiol]_0$ = 0.075 mol·L^{-1}, in THF-d_8 in order to monitor the conversion of the PFTR via online ^{19}F NMR measurements. The red dashed lines indicate the maximum theoretical conversion with respect to the amount of base used

(excluding a self-propagating mechanism). Reproduced from Ref. [190] with the permission from John Wiley & Sons. 107
Figure 4.25 –Functional group conversion after a reaction time of 40 h for the PFTR between aliphSH and **3COOPFB**. The reaction was performed at different temperatures (25 °C and 50 °C), concentrations ($[thiol]_0$ = 0.015, 0.075 and 0.15 $mol \cdot L^{-1}$) or in different reaction vessels (glass or plastic) to investigate the impact of several parameters on the self-propagating mechanism. In each case the molar ratio of SH:PFB:TBAF = 1:1:0.1. Adapted from Ref. [190] with the permission from John Wiley & Sons..... 109
Figure 4.26 – Impact of the step-wise addition of base (TBAF) on the final conversion obtained after performing PFTR at ambient temperature employing a $[thiol]_0$ = 0.075 $mol \cdot L^{-1}$. The step-wise addition of base (green bars) is compared to the final conversion obtained after using the same amount of base but added at once at the beginning of the reaction (purple bars). The amount of base used are reported along the x axis. Adapted from Ref. [190] with the permission from John Wiley & Sons..... 110
Figure 4.27 –Functional group conversion over time for the PFTR performed using thiol derivatives with decreased acidity in the order phenSH > benzSH > aliphSH. The reaction was performed using SH:PFB:TBAF = 1:1:0.1 and a $[thiol]_0$ = 0.075 $mol \cdot L^{-1}$. Adapted from Ref. [190] with the permission from John Wiley & Sons. 111
Figure 4.28 – Functional group conversion for PFTR using different combination of solvent and thiol. Each graph compares the reaction rates for a thiol in different solvents such as THF (blue), DMF (orange) and DMSO (green), (SH:PFB:TBAF = 1:1:0.1 and $[thiol]_0$ = 0.075 $mol \cdot L^{-1}$). The thiol used is reported as headline of the graph, while its chemical structure is visible in the dashed box (d). The dashed red line is representative of the theoretical conversion, which should be achieved in case no self-propagating mechanism was possible. Adapted from Ref. [190] with the permission from John Wiley & Sons..... 112
Figure 5.1 – Representation of a network obtained via end-linking strategy. The example displays the reaction of a bifunctional thiol and a four-armed fluorinated linker. 116
Figure 5.2 – ^{19}F NMR spectra ($CDCl_3$, 377 MHz) of the fluorinated aromatic ring before (**3PFB** linker, black) and after (**PDT-N** network, blue) network formation via PFTR. The reaction was performed employing a 1:1 molar ratio between the functional groups and a $[PFB]_0$ = 1.8 $mol \cdot L^{-1}$ in THF, using DBU as base. The functional group conversion within the network resulted equal to 92%. The figure is adapted from Ref. [188] with the permission of The Royal Society of Chemistry. 118
Figure 5.3 – Left: ATR-IR spectra for, from top to bottom, the pristine linker (**3PFB**, black), the bifunctional thiol (PDT, gray), the synthesized network (**PDT-N**, blue). Right: the two resonance structures (**1** and **2**) for the fluorinated aromatic ring after ligation, responsible for the bands highlighted with blue boxes in the ATR-IR spectra. The gray box represents the disappearance of the stretching vibration assigned to the S-H bond. The figure is reproduced from Ref. [188] with the permission of The Royal Society of Chemistry. 119
Figure 5.4 – XP C1s spectra of the pristine linker (**3PFB**, top, black line) and the freshly synthesized network (**PDT-N**, bottom, blue line). The figure is adapted from Ref. [188] with the permission of The Royal Society of Chemistry. 121
Figure 5.5 – ToF-SIMS analysis of the precursor linker (**3PFB**, top) and the synthesized network (**PDT-N**, bottom). Highlighted is the relative abundance of the fluorinated aromatic ring before (left) and after (right) PFTR. Brighter colors indicate a higher abundance of the selected fragment. The figure is reproduced from Ref. [188] with the permission of The Royal Society of Chemistry. 121
Figure 5.6 – List of bifunctional thiol derivatives used for the synthesis of diverse networks via para-fluoro–thiol reaction (PFTR). List of abbreviations: butanedithiol (BT), 2,2′-(Ethylenedioxy)diethanethiol (DODT) and dithiothreitol (DTT). 122
Figure 5.7 - Representation of three different networks synthesized via the end-linking strategy between a bifunctional polymer precursor and a four-armed linker. The impact of the

chain length of the polymer precursor on the degree of crosslinking of the final polymer is highlighted. 125
Figure 5.8 – Top: Reaction scheme for the synthesis of a suitable bifunctional RAFT agent (**biDoPAT**), and of the desired polystyrene **biSH-PS(36)**. Bottom: SEC traces before (**PS(36)**, black line) and after aminolysis (**biSH-PS(36)**, red line). 127
Figure 5.9 – (–)ESI-MS analysis on **PS(36)** before (black) and after (red) aminolysis. a. Full spectra recorded in the range m/z = 2000-5000. b. Representative zoom in order to identify the species. Herein, Δm = 104.063 represents the styrenic repeating unit, while Δm = 489.265 the removal of the aliphatic chain and the trithiocarbonate group upon aminolysis. The assignments are summarized in Table 5.3. c. Experimental and simulated spectra for **biSH-PS(36)** with a total number of repeating units equal to 24. d. Chemical structure for the polystyrene sample before (square) and after (circle) aminolysis. 128
Figure 5.10 – Relative amount of soluble (extractables) and insoluble (network) fractions after PFT reaction between **biSH-PS(36)** and either **3-** or **4COOPFB** (SH:PFB = 1:1, and a concentration equal to 300 $mg \cdot mL^{-1}$ in DMF). 130
Figure 5.11 – Comparison of the SEC traces for the soluble fractions obtained after crosslinking between **biSH-PS(36)** and either **3-** (pink) or **4COOPFB** (blue) (SH:PFB:DBU = 1:1:1, 300 $mg \cdot mL^{-1}$ of DMF). For clarity, the polymeric starting material **biSH-PS(36)** is reported (gray). 130
Figure 5.12 – Functional group conversion, expressed as percentage of reacted fluorinated aromatic groups in the soluble (filled symbol) and insoluble (empty symbol) fractions for the networks obtained via PFTR employing **biSH-PS(36)** and either **3-** (pink) or **4COOPFB** (blue) (SH:PFB:DBU = 1:1:1, and a concentration of 300 $mg \cdot mL^{-1}$ in DMF). 131
Figure 5.13 – Left: ^{19}F NMR spectra ($CDCl_3$, 377 MHz) of **N4-36** before (top) and after (bottom) degradation. Right: SEC traces of the polymer precursor used for the synthesis of **N4-36** (**biSH-PS(36)**, black), and **N4-36** after degradation (green). 133
Figure 5.14 – ToF-SIMS analysis on the precursor linker (**4COOPFB**, orange) and the synthesized network (**N4-36**, blue). Highlighted is the relative abundance of the fluorinated aromatic ring before (left) and after (right) PFTR. 133
Figure 5.15 – XP C1s spectra of the pristine linker (**4COOPFB**, top, black line) and the freshly synthesized network (**N4-36**, bottom, blue line). 134
Figure 5.16 – Graphical representation of the equation of state for a PS network swollen in toluene, highlighting the difference in the theoretical swelling behavior when using a three- (pink) and a four- (blue) armed linker but the same bifunctional polymer precursor (**PS(36)**). Here, χ = 0.44 (mixing term, Equation 2.20), while the elastic term (Equation 2.21) is evaluated using the phantom model (q_c = 4.5). 135
Figure 5.17 – Left: Relative amount of the soluble and insoluble fractions, expressed as percentage. Right: Percentage of PFB groups reacted in the soluble (filled symbols) and insoluble (empty symbols) fractions of different networks. Each network was obtained employing **biSH-PFB(36)** and **4COOPFB** linker (SH:PFB = 1:1) but using different concentration of polymer in DMF during the crosslinking reaction. The concentration used is stated in the x axis. 136
Figure 5.18 – SEC traces of the polystyrene precursors used for the synthesis of PS networks via PFTR. 138
Figure 5.19 – Relative amount, expressed as percentage, of the insoluble (empty symbol) and soluble (filled symbol) fractions for polystyrene networks synthesized via PFTR. The reaction was performed using polymer precursors of different molecular weight (M_n is highlighted along the x axis), and either a three- (pink) or a four- (blue) armed linker. 139
Figure 5.20 – Functional groups conversion in the insoluble (empty symbol) and soluble (filled symbol) fractions as obtained via ^{19}F NMR measurements for different networks. The networks were obtained upon PFT reaction between a three- (**N3-** series, pink) or a four-

(**N4-** series, blue) armed linker and several bifunctional thiol polymer precursors, which molecular weight is reported along the x axis. 140
Figure 5.21 – Degree of swelling for different networks obtained via PFTR employing a three- (**N3** series, pink) or a four- (**N4** series, blue) armed linker and several bifunctional thiol polymer precursors. The molecular weight of the polymer precursor used is reported along the x axis. 141
Figure 5.22 – Visualization of the deviation between theoretical and experimental degree of swelling (w/w ratio) for the **N4-series** (blue) obtained via the end-linking strategy using PFTR as crosslinking reaction (q_c = 3.5) and FRP (green) networks (q_c=1). The different concentration used during synthesis is taken into account in the q_c parameter during calculation. 143
Figure 5.23 – Left: T_2 relaxation curve for **N4-36** (black), **N4-82** (red) and **N4-mixed** (light blue). **N4-mixed** was synthesized using an equimolar ratio of functional groups arising from **PS(36)** and from **PS(82)**. Right: deconvoluted relaxation decay for **N4-36** (black), **N4-82** (red) and **N4-mixed** (light blue) 144
Figure 5.24 – Top: Reaction scheme for the synthesis of bifunctional fluorinated polystyrene (**biPFB-PS**), starting from a custom designed RAFT agent. Bottom: SEC traces after the polymerization of styrene performed with a molar ratio of 1:150 RAFT agent:styrene, at 70 °C in bulk for 4 h.. 147
Figure 5.25 – Top: Reaction scheme for PFTR between **biPFB-PS** and a monofunctional thiol (alipSH). The reaction was performed using an initial ratio SH:PFB = 1:1, and 1 eq. of DBU as base, $[PFB]_0$ = 0.15 g·mol^{-1} in DMF. Bottom: SEC traces before (black) and after (green) PFTR. 148
Figure 5.26 – Top: Reaction scheme for the synthesis of **biPMMA** via RAFT polymerization, starting from a custom designed RAFT agent (**biCTA**). Bottom: SEC trace of the polymer as obtained after polymerization (**biPMMA**, black line), and after functionalization with **PFB-PE** (**biPFB-PMMA**, light blue line). M_n = 7000 g mol^{-1} (Đ = 1.2) and 8100 g mol^{-1} (Đ = 1.2) before and after functionalization, respectively. . 150
Figure 5.27 – (+)ESI-MS analysis on **biPMMA** before (black) and after (blue) functionalization. a. Full spectra recorded in the m/z = 1400-2700 range. b. Representative zoom in order to identify the main species. Herein, Δm = 100.053 represents the repeating unit, methyl methacrylate. A selected list of peaks is summarized in Table 5.8. c. Experimental and simulated ESI-MS spectrum for **biPFB-PMMA** with a total of 57 repeating units (j+k). d. Chemical structure for **biPMMA** before (square) and after (circle) functionalization. 151
Figure 5.28 – ^{19}F NMR spectra ($CDCl_3$, 377 MHz) of the reaction mixture before (top) and after PFTR between **biPFB-PMMA** and 4COOSH in DMF (middle) and THF (bottom). The reaction was performed using a ratio of 1:1:1 (SH:PFB:DBU) and a concentration of 300 mg·mL^{-1} in DMF. 153
Figure 5.29 – ^{19}F NMR spectra ($CDCl_3$, 377 MHz) for different PFTR reactions. The reactions were performed using a ratio of 1:1:1 SH:PFB:DBU. The PFB groups belong to either **PFB-PE** (top) or **1COOPFB** (bottom). The thiol groups belong to either 4COOSH (left) or alipSH (right). The resonances ascribed to the potential side reaction are highlighted with a red question mark in the ^{19}F NMR spectra. 154
Figure 5.30 – Top: Chemical structure of M, the molecule obtained after PFT reaction between 4COOSH linker and **PFB-PE**, performed using a ratio of 1:1 between SH and PFB group and 0.3 eq. of TBAF as base. Bottom: Experimental and simulated ESI-MS spectra for M, analyzed in positive ion mode. ($[M+Na]^+$). m/z_{exp} = 2232.3939, m/z_{theo}= 2232.3905, Δm/z = 0.0034. 155
Figure 5.31 – Left: ^{19}F NMR spectra ($CDCl_3$, 377 MHz) before (top) and after (bottom) the degradation test, performed by mixing **biPFB-PMMA** and TBAF (1:0.3 molar ratio) overnight, at ambient temperature in DMF (300 mg·mL^{-1}). Right: SEC traces of the polymer before (blue) and after (red) the degradation test. The SEC traces are compared with the parent **biPMMA** polymer (black) and the solvent used for SEC analysis (gray,

dashed line). Despite the system peaks (present also in the blank, THF), a new peak appears after degradation. 156
Figure 5.32 – SEC traces before (blue) and after (red) degradation of **biPFB-PMMA** with triethylamine at 40 °C overnight. The reaction was performed using an initial molar ratio of SH:base = 1:1 and a concentration of 300 mg·mL^{-1} in DMF. 157
Figure 7.1 – Picture of the employed photoreactor for the hetero-Diels−Alder reaction. 171
Figure 7.2 – Emission spectra of the Arimed B6 lamp used for the hetero-Diels−Alder reaction. 171
Figure 7.3 – Water absorbency test in order to determine the degree of swelling of poly(acrylic acid) and poly(sodium acrylate) networks 172
Figure 7.4 – Adopted set-up for the rheological measurements. A disk-shaped specimen was placed in between the two plates of the ARES-G2 rheometer. 173
Figure 7.5 – Left: Variation of G´ and G´´ during the oscillatory strain sweep on **FRP-DC1** at 1 rad/s. Right: Frequency sweep for **FRP-DC1** at 0.1% amplitude (this amplitude is highlighted with a red box in the graph on the left). 174
Figure 7.6 – Variation on the mechanical properties for three selected poly(acrylic acid) hydrogels (**FRP-DC1**, **RAFT01-DC1** and **RAFT025-DC1**) prepared starting from different stock solutions, in order to verify the reproducibility of the results. 175
Figure 7.7 – ^{1}H NMR spectrum ($CDCl_3$, 400MHz) of **3PFB.** 181
Figure 7.8 – ^{1}H NMR spectrum ($CDCl_3$, 400MHz) of **3aromCOOPFB** 182
Figure 7.9 – ^{1}H NMR spectrum ($CDCl_3$, 400MHz) of **1COOPFB.** 183
Figure 7.10 – ^{1}H NMR spectrum ($CDCl_3$, 400MHz) of **3COOPFB.** 184
Figure 7.11– ^{1}H NMR spectrum ($CDCl_3$, 400MHz) of **4COOPFB**. 184
Figure 7.12 – ^{1}H NMR spectrum ($CDCl_3$, 400MHz) of **biDoPAT**. 189
Figure 7.13 – ^{1}H NMR spectrum ($CDCl_3$, 400MHz) of **biPFB.** 191
Figure 7.14 – ^{1}H NMR spectrum ($CDCl_3$, 400MHz) of **biCTA**. 192
Figure 7.15 – ^{1}H NMR spectrum ($CDCl_3$, 400MHz) of **PFB-PE.** 194
Figure 8.1 – Top: (+)ESI-MS spectrum of the model reaction after a reaction time of 5 min and removal of the base (SH:PFB = 1:1, $[SH]_0$=0.15 g·mol^{-1}). Bottom: the experimental and the simulated isotopic pattern are compared. The overview of the m/z ratio are reported in Table 8.1. 203
Figure 8.2 – The SEC broadening effect is accounted for in the kMC simulations by introducing a normal distribution on log scale having standard deviation (σ) = 0.03, for both thiol and disulfide in each solvent. The figure is adapted from Ref. [189] with the permission of The Royal Society of Chemistry. 204
Figure 8.3 – ^{1}H NMR spectra ($CDCl_3$, 400 MHz) for **PSa** (black) and **PSa-SH** (blue). In the box the disappearance of the –CH_2- marked in the structure (*) is highlighted. δ = 7.50 – 6.20 (m, ArH), 2.5 – 0.50 (m, aliphatic H). The figure is reproduced from Ref. [189] with the permission of The Royal Society of Chemistry. 204
Figure 8.4 – ^{13}C NMR spectra ($CDCl_3$, 101 MHz) for **PSa** (black) and **PSa-SH** (blue). The disappearance of the resonances corresponding to the aliphatic carbon chain of the RAFT agent is highlighted with a box. δ = 145.43(C, quaternary carbon in the styrene aromatic ring), δ = 128.33 and δ = 125,52 (-HC=CH-, unsaturated carbons, styrene ring), and δ = 40.30 (aliphatic C, aliphatic polymer backbone). The figure is reproduced from Ref. [189] with the permission of The Royal Society of Chemistry. 205
Figure 8.5 – (−)ESI-MS spectra for **PSa** (black) and **PSa-SH** (blue) recorded in negative mode in the region m/z = 1500 to 4000. The figure is adapted from Ref. [189] with the permission of The Royal Society of Chemistry. 205
Figure 8.6 – Comparison between the simulated (line) and the experimental (symbols) RAFT polymerization of styrene with DoPAT and **DoPAT-OBz** to achieve **PSa-SH** (left) and **PSb-SH** (right), respectively. Top: monomer conversion during time. Bottom: increasing of the molecular weight with the conversion. 209
Figure 8.7 – SEC broadening calculated for the polystyrene standards used to calibrate the THF SEC used for the kinetic study proposed in **Chapter 4**. The figure is reproduced from Ref. [189] with the permission of The Royal Society of Chemistry. 210

Figure 8.8 – Experimental (full line) and simulated (dashed line) SEC traces for the PFTR reaction in THF (red) and DMF (blue) using **PSa-SH** and **3PFB**. (SH:PFB:DBU = 1:1:1, $[SH]_0$ = 0.075 g·mol^{-1}). The figure is reproduced from Ref. [189] with the permission of The Royal Society of Chemistry. 211
Figure 8.9 – Top: Reaction scheme for the synthesis of **PSb** and **PSb-SH**. Bottom: SEC traces for **PSb** (black) and **PSb-SH** (green): The figure is reproduced from Ref. [189] with the permission of The Royal Society of Chemistry. 211
Figure 8.10 – ^{1}H NMR spectra ($CDCl_3$, 400 MHz) spectra for **PSb** (black) and **PSb-SH** (green). In the box is highlighted the disappearance of the –CH_2- marked in the structure (*). δ = 7.50 – 6.20 (m, ArH), 2.5 – 0.50 (m, aliphatic H). The figure is reproduced from Ref. [189] with the permission of The Royal Society of Chemistry. 212
Figure 8.11 – ^{13}C NMR spectra ($CDCl_3$, 101 MHz) for **PSb** (black) and **PSb-SH** (green). The disappearance of the resonances corresponding to the aliphatic carbon chain of the RAFT agent is highlighted with a box. δ = 145.43(C, quaternary carbon in the styrene aromatic ring), δ = 128.33 and δ = 125,52 (-HC=CH-, unsaturated carbons, styrene ring), and δ = 40.30 (aliphatic C, aliphatic polymer backbone). The figure is reproduced from Ref. [189] with the permission of The Royal Society of Chemistry. 212
Figure 8.12 – (−)ESI-MS spectra for **PSb** (black) and **PSb-SH** (green). Top: full spectra recorded in the region m/z = 1500-400. Bottom: zoom in a selected region of the spectra in order to highlight the Δm = 104.061, which refers to the styrenic monomer unit and Δm = 244.130 between **PSb** and **PSb-SH**, which refers to the loss of the aliphatic chain and the trithiocarbonate upon aminolysis. The figure is reproduced from Ref. [189] with the permission of The Royal Society of Chemistry. 213
Figure 8.13 – Experimental SEC traces for the PFTR reaction in THF (red) and DMF (blue) using **PSb-SH** and **3PFB**. (SH:PFB = 1:1, $[SH]_0$ = 0.075 g·mol^{-1}). The figure is reproduced from Ref. [189] with the permission of The Royal Society of Chemistry. 214
Figure 8.14 – Experimental functional group conversion over time for the PFTR reaction using **3PFB** and either COOH-SH (blue) or **PSa-SH** (red) in THF (filled symbols) and DMF (empty symbols). (SH:PFB = 1:1 and $[SH]_0$ = 0.075 g·mol^{-1}). The figure is adapted from Ref. [189] with the permission of The Royal Society of Chemistry. 214
Figure 8.15 – Comparison of the experimental (symbols) and simulated (line) functional group conversion over time for the PFTR in THF (full symbols) and DMF (empty symbols) (SH:PFB=1:1, $[SH]_0$ = 0.075 g·mol^{-1}). Left: The PFTR was performed using **3PFB** and either **PSa-SH** (red) or **PSb-SH** (black). Right: The PFTR was performed using **3PFB** and COOH-SH (blue). The figure is adapted from Ref. [189] with the permission of The Royal Society of Chemistry. 215
Figure 8.16 – SEC traces after investigation for the disulfide bond suppression. The reaction was performed using **PSa-SH** as thiol derivative and a 1:15 molar ratio of SH:DBU, in different condition. Top: in the presence of oxygen and absence of TCEP. Middle: In the absence of oxygen (argon) and absence of TCEP. Bottom: in the presence of oxygen and 6eq. of TCEP with respect to the thiol groups. $[SH]_0$ = 0.037 g·mol^{-1}. The figure is reproduced from Ref. [189] with the permission of The Royal Society of Chemistry. 216
Figure 8.17 – SEC traces for the disulfide bond investigation in argon atmosphere, using a ratio of SH:TCEP = 1:1 and 15eq. of base (i.e. DBU). Aliquots of the reaction mixture were withdrawn at different intervals of time. After an initial phase, it is visible the cleavage of the disulfide bonds by the presence of the reducing agent. The figure is reproduced from Ref. [189] with the permission of The Royal Society of Chemistry. 217
Figure 8.18 – SEC traces for the PFTR reaction using **PSa-SH** and **3PFB** in DMF ($[SH]_0$ = 0.037 g·mol^{-1}). The molar ratio of SH:PFB:TCEP is stated in the legend, while the ratio of SH:DBU was fixed to 1:15. The figure is reproduced from Ref. [189] with the permission of The Royal Society of Chemistry. 217
Figure 8.19 – ^{19}F NMR spectra ($CDCl_3$, 377 MHz) for the networks obtained starting from small molecule bifunctional thiol derivatives and trifunctional fluorinated linker (**3PFB**). Thiol precursors: dithiothreitol (**DTT**), 2,2′-(Ethylenedioxy)diethanethiol (**DODT**) and

butanedithiol (**BT**). The figure is adapted from Ref. [188] with the permission of The Royal Society of Chemistry. 218
Figure 8.20 – ATR-IR spectra for the networks obtained starting from small molecule bifunctional thiol derivatives and trifunctional fluorinated linker (**3PFB**). Thiol precursors: dithiothreitol (**DTT**), 2,2′-(Ethylenedioxy)diethanethiol (**DODT**) and butanedithiol (**BT**). The figure is adapted from Ref. [188] with the permission of The Royal Society of Chemistry. 218
Figure 8.21 – XP C1s (left) and ToF-SIMS (right) images for the networks obtained starting from small molecule bifunctional thiol derivatives and trifunctional fluorinated linker (**3PFB**). Thiol precursors: dithiothreitol (**DTT**), 2,2′-(Ethylenedioxy)diethanethiol (**DODT**) and butanedithiol (**BT**). The ToF-SIMS images show the relative abundance of the fragment before ($C_7HOF_5^-$) and after ($C_7HSOF_4^-$) PFTR. The figure is adapted from Ref. [188] with the permission of The Royal Society of Chemistry. 219
Figure 8.22 – DSC curves for the networks obtained starting from small molecule bifunctional thiol derivatives and trifunctional fluorinated linker (**3PFB**). Thiol precursors: dithiothreitol (**DTT**), 2,2′-(Ethylenedioxy)diethanethiol (**DODT**), butanedithiol (**BT**) and 1,4-phenylenedimethanethiol (**PDT**). The figure is adapted from Ref. [188] with the permission of The Royal Society of Chemistry. 219
Figure 8.23 – Top: ^{1}H NMR spectra ($CDCl_3$, 400MHz) for **PS(36)** (before aminolysis, black) and **biSH-PS(36)** (after aminolysis, red line). δ = 7.50 – 6.20 (m, ArH), 2.5 – 0.50 (m, aliphatic H). Bottom ^{13}C NMR spectra ($CDCl_3$, 101MHz) for **PS(36)** (before aminolysis, black) and **biSH-PS(36)** (after aminolysis, red line). δ = 145.4(C, quaternary carbon in the styrene aromatic ring), δ = 128.3 and δ = 125.5 (-HC=CH-, unsaturated carbons, styrene ring), and δ = 40.3 (aliphatic C, aliphatic polymer backbone) δ < 40 (aliphatic $C_{12}H_{25}$- adjacent to the trithiocarbonate moiety). In both cases: highlighted in the blue box is the diagnostic peaks confirming the removal of the aliphatic chain and the thiocarbonate moiety. 220
Figure 8.24 – Top: ^{1}H NMR spectra ($CDCl_3$, 400MHz) for **PS(64)** (before aminolysis, black) and **biSH-PS(64)** (after aminolysis, blue line). δ = 7.50 – 6.20 (m, ArH), 2.5 – 0.50 (m, aliphatic H). Bottom: ^{13}C NMR spectra ($CDCl_3$, 101MHz) for **PS(64)** (before aminolysis, black) and **biSH-PS(64)** (after aminolysis, blue line). δ = 145.4(C, quaternary carbon in the styrene aromatic ring), δ = 128.3 and δ = 125.5 (-HC=CH-, unsaturated carbons, styrene ring), and δ = 40.3 (aliphatic C, aliphatic polymer backbone) δ < 40 (aliphatic $C_{12}H_{25}$- adjacent to the trithiocarbonate moiety). In both cases: highlighted in the blue box is the diagnostic peaks confirming the removal of the aliphatic chain and the thiocarbonate moiety. 221
Figure 8.25 – Top: ^{1}H NMR spectra ($CDCl_3$, 400MHz) for **PS(82)** (before aminolysis, black) and **biSH-PS(82)** (after aminolysis, green line). δ = 7.50 – 6.20 (m, ArH), 2.5 – 0.50 (m, aliphatic H). Bottom: ^{13}C NMR spectra ($CDCl_3$, 101MHz) for **PS(82)** (before aminolysis, black) and **biSH-PS(82)** (after aminolysis, green line). δ = 145.4(C, quaternary carbon in the styrene aromatic ring), δ = 128.3 and δ = 125.5 (-HC=CH-, unsaturated carbons, styrene ring), and δ = 40.3 (aliphatic C, aliphatic polymer backbone) δ < 40 (aliphatic $C_{12}H_{25}$- adjacent to the trithiocarbonate moiety). In both cases: highlighted in the blue box is the diagnostic peaks confirming the removal of the aliphatic chain and the thiocarbonate moiety. 222
Figure 8.26 – Left: SEC traces recorded at different times during the polymerization of PTBMA. Right The molecular weight and the dispersity index (Đ) as determined via SEC are plotted against the concentration. A linear increase of M_n with the conversion, as well as low values for Đ, indicates a good control over the polymerization. DoPAT:TBMA:AIBN = 1:350:0.1 (molar ratio), T = 70 °C in toluene (50% w/w). 223
Figure 8.27 – ^{19}F NMR spectra ($CDCl_3$, 377 MHz) of **biPFB-PS** before (black) and after (green) the PFTR reaction, performed between **biPFB-PS** and aliphSH using DBU as base (molar ratio of 1:1:1 = SH:PFB:DBU). 223
Figure 8.28 – Top: ^{1}H NMR spectra ($CDCl_3$, 400 MHz) for **biPMMA** (before end-group capping, black) and **biPFB-PMMA** (after end-group capping, light blue line). Highlighted with

colorful stars the protons diagnostic for the successful end-group functionalization. Bottom: ^{19}F NMR spectrum ($CDCl_3$, 377 MHz) for **biPFB-PMMA**, after end-group capping. 224
Figure 8.29 – ^{19}F NMR spectrum ($CDCl_3$, 377 MHz) after PFTR reaction between 4COOSH and **PFB-PE**. SH:PFB = 1:1 stoichiometric ratio in DMF using TBAF (0.3eq.) as base. 225
Figure 8.30 – ^{19}F NMR spectrum ($CDCl_3$, 377 MHz, gel phase) of the poly(methacrylate) network obtained after PFTR reaction between **biPFB-PMMA** and 4phenSH, using a molar ratio of SH:PFB:Et_3N = 1:1:1 at 40 °C in DMF (300 mg·mL^{-1}). 225
Figure 8.31 – ^{19}F NMR spectrum ($CDCl_3$, 377 MHz) of the extractables of the poly(methacrylate) network obtained after PFTR reaction between **biPFB-PMMA** and 4phenSH, using a molar ratio of SH:PFB:Et_3N = 1:1:1 at 40 °C in DMF (300 mg·mL^{-1}). 226
Figure 8.32 – SEC traces (aqueous SEC) after the polymerization of acrylic acid (AA) performed in dioxane (50% w/w ratio) and 70 °C using CTACOOH as RAFT agent in a stoichiometric ratio of 1:300 (CTACOOH:AA). 226

List of Scheme

Scheme 2.1 – The free radical polymerization (FRP) process includes: i. the initiation, which generates active radicals; ii. the propagation, where the radical can grow in size after sequential addition of a monomer unit, and iii. the termination and/or transfer reactions, where the final polymer chain is produced. 7
Scheme 2.2 – Detailed overview of the RAFT mechanism. The initiation includes the decomposition of the initiator and the formation of the growing radical. The pre-equilibrium is established between the previously formed radical and the RAFT agent. The re-initiation refers to the incorporation of monomer units by the leaving R group of the RAFT agent. During the main equilibrium the propagating radical chain P_n is added to the RAFT unit and the polymer radical P_m is eliminated. The termination steps are drastically limited, yet not completely avoided. In the top box the general representation of a RAFT agent is depicted, while in the bottom box the overall reaction scheme is shown. 12
Scheme 2.3 – Reaction scheme for an alternative synthetic route towards the achievement of poly(acrylic acid) polymers. In the scheme, R corresponds to the protecting group, while A and X are the two chain ends, which nature is dependent on the polymerization approach employed. 15
Scheme 2.4 – Schematic representation of some possible modification reactions involving a typical RAFT end-group (red box). In red are highlighted the reaction used in this thesis. 17
Scheme 2.5 – General scheme for the para-fluoro thiol reaction (PFTR). The moieties involved are a thiol and a fluorinated aromatic ring. A base is used for the deprotonation of the thiol to generate the thiolate and promote the aromatic nucleophilic attack. 20
Scheme 2.6 – Schematic representation of the resonance structures for the nucleophilic substitution in monosubstituted perfluoraromatic compounds. According to the nature of the substituent Y either pathway A or B is followed. Mostly, pathway A occurs with the exception of strong electron donor group.[90] The figure is adapted from "J. Kvíčala, M. Beneš, O. Paleta, V. Král, J. Fluorine Chem., **2010**, 131, 1327−1337".[88] 21
Scheme 2.7 – PFTR reaction performed in the presence of two different substituents (Y), an oxygen and an aliphatic chain. The different reactivity is highlighted in the final product. 22
Scheme 3.1 – Reaction scheme for the synthesis of polymeric networks using methyl acrylate as monomer and 1,3-butanediol diacrylate (DAc) as crosslinking agent. The polymerization was performed at 70 °C with and without the presence of the RAFT agent (DoPAT). 53
Scheme 3.2 – Reaction scheme for the synthesis of poly(acrylic acid) networks using N,N´-methylenbisacrylamide (MBA) as crosslinker and TRITT as RAFT agent. The polymerization was performed in water (20% w/w) at 70 °C in presence of V-501 as initiator, with and without the presence of the RAFT agent (TRITT). 60
Scheme 4.1 – Reaction scheme for the para-fluoro–thiol reaction (PFTR) between dodecanethiol (aliphSH) and a fluorinated three-armed linker (**3PFB**). Top: The main reaction is displayed together with the targeted trisubstituted product (**3S**). Bottom: Possible by-products such as the mono- and disubstituted linker (**1S** and **2S**, respectively). 77
Scheme 4.2 – The selectivity study is performed upon reaction of the polymeric thiol derivative (**PSa-SH**) and a monofunctional fluorinated linker (**1COOPFB**). PFTR can be visualized as end-capping of the polymer, thus the molecular weight does not vary significantly. On the contrary, if disulfides are formed, the molecular weight of the polymer is double the original value, which can be easily monitored by SEC analysis. The scheme is adapted from Ref. [189] with the permission of The Royal Society of Chemistry. 102

Scheme 4.3 – PTFR model reaction for the elucidation of the self-propagating PFTR mechanism. Herein, different bases were used in order to initiate PFTR such as TBAF, TBAOH and DBU. Each base was used in under-stoichiometric amount respect to the functional group, while the molar ratio of SH:PFB was kept equal to 1:1. 106
Scheme 4.4 – Proposed self-propagated mechanism for PFTR based on the assumption that the fluoride ions, produced at each reaction step (highlighted in red), is able to promote the next PFTR reaction event. Adapted from Ref. [190] with the permission from John Wiley & Sons. 108
Scheme 5.1 – Reaction scheme for network formation employing a three-armed fluorinated linker (**3PFB**) and a bifunctional thiol (PDT). The PFTR was performed using a molar ratio of SH:PFB:DBU equal to 1:1:1 in THF. The figure is adapted from Ref. [188] with the permission of The Royal Society of Chemistry. 117
Scheme 5.2 – Reaction scheme for the synthesis of **N3** or **N4** networks starting from **biSH-PS** and either a three- or a four-armed linker. 129
Scheme 5.3 – Reaction scheme for the degradation of a typical polystyrene network obtained via PFTR. The degradation was performed upon swelling of the network in a mixture of THF and an aqueous solution of NaOH 1 M overnight (16 h). 132
Scheme 5.4 – Side reaction occurring during the reaction of aminolysis of (meth)acrylate polymers. 146
Scheme 5.5 – Reaction scheme for the one-pot removal of the sensitive thiocarbonate moiety and the introduction of the fluorinated group on the polymer chain 149
Scheme 5.6 – Reaction scheme for the synthesis of polymeric network starting from **biPFB-PMMA** and a commercially available four-armed thiol linker (4COOSH). 152
Scheme 5.7 – Reaction scheme for the synthesis of networks via PFTR employing α,ω-fluorinated polymer (**biPFB-PMMA**) and 4phenSH at 40 °C in DMF (300 $mg \cdot mL^{-1}$). 158
Scheme 7.1 – Reaction scheme for the synthesis of trimethylolpropane tris(2,3,4,5,6-pentafluorobenzylether) (**3PFB**) via phase transfer catalysis (PTC). 180
Scheme 7.2 – Reaction scheme for the synthesis of tris(2,3,4,5,6-pentafluorophenyl) benzene-1,3,5-tricarboxylate (**3aromCOOPFP**) via esterification..... 181
Scheme 7.3 – Reaction scheme for the synthesis of tris(2,3,4,5,6-pentafluorobenzyl) benzene-1,3,5-tricarboxylate (**3aromCOOPFP**). 182
Scheme 7.4 – Reaction scheme for the polymerization of polystyrene (PS) affording **PSa** and **PSb.** 185
Scheme 7.5 – Reaction scheme for the aminolysis of **PSa** and **PSb** to afford **PSa-SH** and **PSb-SH**, respectively. 185
Scheme 7.6 – Reaction scheme for the synthesis of diethylene glycol di(2-(((dodecylthio) carbonothioyl)thio) propanoate) (**biDoPAT**) via esterification. 188
Scheme 7.7 – Reaction scheme for the synthesis of 3,6-dioxa−1,8-bis(2,3,4,5,6-pentafluorobenzylthiocarbonothioylthio)-octane (**biPFB**) via phase transfer catalysis. 190
Scheme 7.8 – Reaction scheme for the synthesis of 1,4-phenylenebis(methylene) bis(4-cyano-4-(phenylcarbonothioylthio)pentanoate) (**biCTA**) via esterification. 191
Scheme 7.9 – Reaction scheme for the synthesis of 2,3,4,5,6-pentafluorobenzyl 4-((2-formyl-3-methylphenoxy)methyl)benzoate (**PFB-PE**). 193
Scheme 7.10 – Reaction scheme for the synthesis of **biPFB-PMMA** via RAFT end group capping of **biPMMA** with **PFB-PE** via hetero Diels-Alder reaction 194

List of Tables

Table 3.1 – Overview of the linear poly(methyl acrylate) polymers synthesized, displaying the amount of RAFT agent used during the polymerization (molar %), and the molecular weight ($M_{n,PMA}$) and the dispersity index (Đ) of the resulting polymer..... 53
Table 3.2 – Overview of the poly(acrylic acid) synthesized using different molar percentage of RAFT agent (%TRITT), including the molecular weight ($M_{n,PAA}$) and the dispersity index (Đ)..... 60
Table 3.3 – Summary of the PAA networks synthesized in the current section including the molar ratio of RAFT agent:AA, the molar % of TRITT, the % of network achieved and the relative reaction code..... 62
Table 3.4 – Summary of the degree of swelling, at DN = 0 or 100, for poly(acrylic acid) networks synthesizing via FRP or RAFT polymerization. 64
Table 3.5 – Percentage of salt-rejected (% SR) for a series of poly(sodium acrylate) networks having DC = 1 but a different amount of RAFT agent. For clarity, the values of the swelling at equilibrium are reported (Q_{eq}). 72
Table 4.1 – Summary of the rate coefficients of the disulfide bond formation (k_{disulf}) and the para-fluoro−thiol reaction (k_{PFTR}) for different thiol derivatives. The rate coefficients are assessed via kMC simulations based on the experimental data and reported in $L \cdot mol^{-1}s^{-1}$. The disulfide bond formation was performed using $[thiol]_0 = 0.15\ mol \cdot L^{-1}$, while PFTR using $[thiol]_0 = 0.075\ mol \cdot L^{-1}$. In both cases, THF was used as solvent. The table is adapted from Ref. [189] with the permission of The Royal Society of Chemistry. . 87
Table 4.2 – Comparison of the experimental and the theoretical m/z ratio for the peak highlighted in the ESI-MS spectra in Figure 4.2. Herein, n refers to the number of styrene repeating units in the considered peak and Δm is the difference between the theoretical and the experimental value. The table is adapted from Ref. [189] with the permission of The Royal Society of Chemistry..... 93
Table 4.3 – Summary of the rate coefficient values of the disulfide bond formation (k_{disulf}) and the para-fluoro−thiol reaction (k_{PFTR}) for different thiol derivatives. The rate coefficients are assessed via kMC simulations based on the experimental data and reported in $L \cdot mol^{-}1 \cdot s^{-1}$ with the exception of $k_{disulf,r}$ which is reported in s^{-1}. Each reaction was performed using $[thiol]_0 = 0.075\ mol \cdot L^{-1}$. The table is adapted from Ref. [189] with the permission of The Royal Society of Chemistry..... 100
Table 5.1 – Summary of the glass transition temperature (T_g) for the network obtained starting from structurally different thiols. The letter "-N" associated to the name of the thiol employed indicates that the result refer to the obtained network. 123
Table 5.2 – Summary of the degree of swelling (w/w) obtained for different networks (**-N**) in THF and ethanol (EtOH). 123
Table 5.3 – Comparison of the experimental and the theoretical m/z ratio for the peak highlighted in the (–)ESI-MS spectra of Figure 5.9b. Herein, "j+k" refers to the total number of styrene repeating unit in the considered peak, according to Figure 5.9c. Δm is the difference between the theoretical and the experimental value. 128
Table 5.4 – Summary of the experimental ($Q_{eq,exp}$) and theoretical ($Q_{eq,theo}$) degree of swelling (w/w ratio) for **N4-36** networks synthesized at different concentrations. The deviation percentage is calculated according to equation 5.3. q is the theoretical swelling (v/v ratio) using the phantom model. 137
Table 5.5 – List of the bifunctional polymer precursors used in this section including their molecular weight (M_n), the dispersity index (Đ) and the molecular weight of the corresponding

elastic chain after network formation (M_c). Moreover, a summary of the networks synthesized varying the thiol/linker combination is proposed including the relative network codes as cited in text. 139
Table 5.6 – Comparison between the theoretical (Q_{theo}) and experimental (Q_{exp}) degree of swelling (w/w ratio) for the polystyrene networks in toluene (χ = 0.44). The deviation between the two values is calculated according to Equation 5.3. q is the theoretical swelling (v/v ratio) as obtained using the phantom model. 141
Table 5.7 – Comparison of the theoretical ($Q_{eq,theo}$) and experimental ($Q_{eq,exp}$) degree of swelling (w/w ratio) in toluene for the polystyrene networks having different degree of crosslinking (DC) synthesized either via end-linking strategy (**N4**) using PFTR as ligation or via free radical polymerization (FRP). The theoretical values are obtained according to the phantom model (q, v/v ratio). 143
Table 5.8 – Comparison of the mass to charge ratio (m/z) for the peak highlighted in Figure 5.27b. Herein, j+k represents the total number of repeating units and Δm the difference between the experimental and the theoretical m/z. 151
Table 7.1 – List of parameters used for measuring the T_2 relaxation decay. In detail, the number of acquired scans (ns), the number of dummies scans (ds), the echo time (τ), the number of dummies echoes (de), the recycle delay (rd) and the number of acquired echoes (ne) are reported. 169
Table 7.2 – Summary of the linear poly(methacrylate)s synthesized in **Chapter 3**, Section 3.1. 177
Table 7.3 – Summary of the poly(acrylic acid) networks synthesized via RAFT polymerization and via free radical polymerization (FRP). In detail, the reaction code, the ratio RAFT agent:monomer and the degree of crosslinking (expressed as molar ratio between the crosslinker and the monomer) are provided. 179
Table 7.4 – List of the reagent for the synthesis of **1COOPFB**, **3COOPFB** and **4COOPFB**. .. 185
Table 7.5 – List of the molecular weight (M_n) and the dispersity index (Đ) of the bifunctional polystyrene precursor used in Section 5.2.1 before and after aminolysis. 189
Table 8.1 – List of the experimental and the theoretical m/z ratio for the mono- (**1S**) di- (**2S**) and trisubstituted (**3S**) fluorinated linker (**3PFB**) reported in Figure 8.1. 204
Table 8.2 - Overview of the reactions and rate coefficients for **PSa-SH** and **PSb-SH** (monomer: styrene) with $I2, I\bullet, M, R0\bullet, Ri\bullet, Pi, R0X, RiX$: conventional radical initiator, initiator fragment, monomer, RAFT leaving group, macroradical (chain length i≥1), dead polymer species, initial RAFT agent, dormant macrospecies; 70°C; for termination apparent rate coefficients with given value the one of $kt, app1,1$ 206
Table 8.3 – Parameters used for the composite k_t model.[225] 207
Table 8.4 – Overview of the values to calculate the apparent initiator efficiency as described by Buback et al. for AIBN as conventional radical initiator and styrene as monomer.[228] 208
Table 8.5 – Comparison of the experimental and the theoretical m/z ratio for the peaks highlighted in Figure 8.12. The table is reproduced from Ref. [189] with the permission of The Royal Society of Chemistry. 213
Table 8.6 – Summary of the molecular weight and the dispersity index of the poly(acrylic acid) polymer reported in Figure 8.32 226

Publications

Publications Arising from this Thesis

(1) *The para-Fluoro–Thiol Reaction as a Powerful Tool for Precision Network Synthesis*

F. Cavalli, H. Mutlu, S. O. Steinmueller, L. Barner*, *Polym. Chem.* **2017**, *8*, 3778−3782.

(2) *A Kinetic Study on the para-Fluoro–Thiol Reaction in view of its use in Materials Design*

F. Cavalli, L. De Keer, B. Huber, P. H. M. Van Steenberge, D. R. D´hooge*, L. Barner*, *Polym. Chem.* **2019**, *10*, 2781−2791.

(3) *Self-Propagated para-Fluoro–Thiol Reaction*

F.Cavalli,[#] F. R. Bloesser,[#] C. Barner-Kowollik*, L. Barner*, *Chem.: Europ. J.* **2019**, *25*, 10049−10053..

(4) *Analysis of the local mobility of RAFT mediated poly(acrylic acid) networks via low field ^{1}H-NMR tech-niques for investigation of the network topology*

F.Cavalli,[#] C.Pfeifer,[#] L.Arens, L.Barner*, M.Wilhelm*, *in preparation*.

[#]The authors contributed equally.

*corresponding author(s)

Conferences

(1) *Advanced Polymers via Macromolecular Engineering – APME2017*

Poster contribution: Expanding the toolbox of thiol-X chemistry: the thiol-*para*-fluoro reaction as an efficient approach for network formation

F. Cavalli, H. Mutlu, S. O. Steinmueller, L.Barner*

May 2017, Ghent, Belgium

(2) *International Conference on BioNano Innovation – ICBNI 2017*

Poster contribution: A novel strategy for precision network formation based on *para*- fluoro thiol ligation

F. Cavalli, H. Mutlu, S. O. Steinmueller, L.Barner*

September 2017, Brisbane, Australia

(3) *Emerging Polymer Technologies Summit – EPTS17*

Poster contribution: A novel strategy for precision network formation based on *para*- fluoro thiol ligation

F. Cavalli, H. Mutlu, S. O. Steinmueller, L.Barner*

November 2017, Melbourne, Australia

(4) *82nd Prague meeting on macromolecules, 24th polymer networks group meeting – 82PMM, 24PNG*

Oral presentation: A novel strategy for precision network formation based on *para*-Fluoro-Thiol ligation

F. Cavalli, L. De Keer, H. Mutlu, P.H.M. Van Steenberge, D.R. D´hooge, L. Barner*

June 2018, Prague, Czech Republic

(5) *Dimensional Control of Polymer Materials – From Synthesis to Function*

Poster contribution: A novel strategy for precision network formation based on *para*-Fluoro-Thiol ligatio

F. Cavalli, L. De Keer, H. Mutlu, P.H.M. Van Steenberge, D.R. D´hooge, L. Barner*, **September 2018**, Karlsruhe, Germany

Acknowledgements

The presented work would have not been possible without the support of many people, and my deepest thanks goes to everyone who walked by my side throughout this journey.

First of all, I would like to thank Prof. Manfred Wilhelm and Prof. Leonie Barner for giving me the opportunity to pursue my PhD, and to work on this challenging topic. I am extremely grateful for the fruitful discussions we had together, which helped me to grow as a scientist. I would like to thank prof. Manfred Wilhelm for your passion for science, and for the ever-present quote and take home message at the end of each meeting. In addition, my deepest gratitude goes to Prof. Leonie Barner, who supervised me directly throughout the whole project, even from the other side of the world. I am very thankful for all the motivating words you had during this journey. Your positive attitude and constant support have definitely been important and positively received. Moreover, I would like to acknowledge you for the amazing opportunity of spending some months of my PhD time in Australia.

An important acknowledgement goes to the Deutsche Forschungsgemeinschaft (DFG) for founding the SFB 1176 and the resulting funding during my PhD studies, which gave me the opportunity to join international conferences and financed my abroad stay.

Thank you to my collaboration partners I had the pleasure to share my working time with. To Hatice for helping me to start with "the right foot". To Christoph for sharing with me the world of hydrogels and networks. To Lies and Prof. Dagmar D´hooge for the constructive discussions, and for all the meetings and paper drafts we went through. To Fabian for all the side reactions we shared, keep it up with the second part of our project! To the organizers of the graduate school SFB 1176, the platform Z1 for analysis, and to all the SFB members for the funny time at the SFB retreats.
Last but not least, a special thanks goes to Diego, my faithful PhD companion. Simply thank you for always being there for me and having time to listen.

To my proofreaders (and supporters). My extreme gratitude to everyone that, at any stage, took part in the correction process. Thank you for your time and your precious inputs. A deserved

thanks goes to Lukas, for the countless times I knocked at your office with questions related to networks, hydrogels, numbers and formulas.

To the Soft Matter Lab (campus north), which has been my first home here in Germany. To its members Leonie, Hatice, Sylvain, Waldemar and Diego for making my start in this new country and group a bit easier. To Birgit, without whom the SML would not be running as smoothly as it does. Thanks for always having an open door for me. As I like to call you, you have definitely been my German mama.

Thanks to the important people that keep the group running: Prof. Christopher Barner-Kowollik, Dr. Anja Goldmann, Dr. Eva Blasco, Dr. Maria Schneider and Katharina Elies. To the whole Macroarc group for having welcomed me, for the nice and constructive working environment and for all the memories we shared. You have all been important, and I thank every single one of you, no one excluded. A separate thanks goes to my special Colleague Hendrik for all the motivating words, to David even though in three years I did not convince you not to put pineapple on pizza, to Hannah for the precious time, and to Divya, the other member of the not-german club. To the Australian node, Jordan, and to everyone that was in Australia with me for the amazing time, definitely the best of my PhD.

A coloro che ho lasciato in Italia ma che hanno sempre avuto un posto speciale. Senza i vostri messaggi corti, lunghi, frequenti o casuali, il viaggio non sarebbe stato lo stesso. Grazie soprattutto a voi che mi avete convinto a partire e che siete ancora al mio fianco. Un pensiero particolare va ad Andre, compagno a distanza di questa avventura che per mesi abbiamo fantasticato e immaginato. Da sempre una spalla su cui poter contare.

Alla “Happy Family”, le mie nonne e i miei zii materni, che seppur contrari ad ogni mia partenza o ripartenza mi hanno sempre sostenuta. Ai miei nonni che immancabilmente sono nei miei pensieri.

Ed infine, il mio grazie piú sentito va alla mia famiglia. Lasciarvi è stato difficile, ma nel tempo ho capito che non importa dove sono perché voi siete sempre al mio fianco. Non ci sono parole per esprimere la mia gratitudine, semplicemente *Grazie* per essere la certezza che siete da sempre.